Chapter 8

Scintillation Detector Principles

The detection of ionizing radiation by the scintillation light produced in certain materials is one of the oldest techniques on record. The scintillation process remains one of the most useful methods available for the detection and spectroscopy of a wide assortment of radiations. In this chapter we discuss the various types of scintillators available and the important considerations in the efficient collection of the scintillation light. The following chapters cover modern light sensors—photomultiplier tubes and photodiodes—required to convert the light into an electrical pulse, and the application of scintillation detectors in radiation spectroscopy.

The ideal scintillation material should possess the following properties:

1. It should convert the kinetic energy of charged particles into detectable light with a high scintillation efficiency.
2. This conversion should be linear—the light yield should be proportional to deposited energy over as wide a range as possible.
3. The medium should be transparent to the wavelength of its own emission for good light collection.
4. The decay time of the induced luminescence should be short so that fast signal pulses can be generated.
5. The material should be of good optical quality and subject to manufacture in sizes large enough to be of interest as a practical detector.
6. Its index of refraction should be near that of glass (~1.5) to permit efficient coupling of the scintillation light to a photomultiplier tube or other light sensor.

No material simultaneously meets all these criteria, and the choice of a particular scintillator is always a compromise among these and other factors. The most widely applied scintillators include the inorganic alkali halide crystals, of which sodium iodide is the favorite, and organic-based liquids and plastics. The inorganics tend to have the best light output and linearity, but with several exceptions are relatively slow in their response time. Organic scintillators are generally faster but yield less light. The intended application also has a major influence on scintillator choice. The high Z-value of the constituents and high density of inorganic crystals favor their choice for gamma-ray spectroscopy, whereas organics are often preferred for beta spectroscopy and fast neutron detection (because of their hydrogen content).

The process of *fluorescence* is the prompt emission of visible radiation from a substance following its excitation by some means. It is conventional to distinguish several other processes that can also lead to the emission of visible light. *Phosphorescence* corresponds to the emission of longer wavelength light than fluorescence, and with a characteristic time that is generally much slower. *Delayed fluorescence* results in the same emission spectrum as prompt fluorescence but again is characterized by a much longer emission time following excitation. To be a good scintillator, a material should convert as large a fraction as possible of the incident radiation energy to prompt fluorescence, while minimizing the generally undesirable contributions for phosphorescence and delayed fluorescence. Most of the emphasis in this chapter is on the pulse mode operation of scintillators. Here the light that can contribute to an output pulse is generally limited to the prompt fluorescence because the time constants of the measurement circuit are set much smaller than typical phosphorescence and delayed fluorescence decay times. This long-lived light is then spread out more-or-less randomly in time between signal pulses and arrives at the light sensor as individual photons that often may not be distinguished from random noise. In contrast, scintillators that are operated in current mode under constant illumination will produce a steady-state signal current that is proportional to the total light yield, and all the decay components will contribute in proportion to their absolute intensity. For this reason, the light yield measured from a scintillator operated in pulse mode may appear to be lower than that deduced from the steady-state current recorded from the same scintillator. Current mode scintillation detectors operated under conditions in which the radiation intensity changes rapidly will suffer from memory or "afterglow" effects if long-lived decay components are significant.

A number of general reviews of the basic theory and application of scintillators have been published, with the comprehensive book by Birks[1] as an outstanding example. A useful collection of fundamental papers on scintillators is available[2] that covers the period from the early investigation of many scintillation materials through recent reviews of scintillation mechanisms. In this chapter, we limit the discussions to those processes that are necessary to understand the differences in behavior of various types of scintillators, together with some of their important properties as practical radiation detectors.

I. ORGANIC SCINTILLATORS

A. Scintillation Mechanism in Organics

The fluorescence process in organics arises from transitions in the energy level structure of a single molecule and therefore can be observed from a given molecular species independent of its physical state. For example, anthracene is observed to fluoresce as either a solid polycrystalline material, as a vapor, or as part of a multicomponent solution. This behavior is in marked contrast to crystalline inorganic scintillators such as sodium iodide, which require a regular crystalline lattice as a basis for the scintillation process.

A large category of practical organic scintillators is based on organic molecules with certain symmetry properties which give rise to what is known as a π-electron structure. The π-electronic energy levels of such a molecule are illustrated in Fig. 8.1. Energy can be absorbed by exciting the electron configuration into any one of a number of excited states. A series of singlet states (spin 0) are labeled as $S_0, S_1, S_2, \ldots$ in the figure. A similar set of triplet (spin 1) electronic levels are also shown as $T_1, T_2, T_3, \ldots$ For molecules of interest as organic scintillators, the energy spacing between S_0 and S_1 is 3 or 4 eV, whereas spacing between higher-lying states is usually somewhat smaller. Each of these electronic configurations is further subdivided into a series of levels with much finer spacing that correspond to various vibrational states of the molecule. Typical spacing of these levels is of the order of 0.15 eV. A second subscript is often added to distinguish these vibrational states, and the symbol S_{00} represents the lowest vibrational state of the ground electronic state.

Because the spacing between vibrational states is large compared with average thermal energies (0.025 eV), nearly all molecules at room temperature are in the S_{00} state. In Fig. 8.1 the absorption of energy by the molecule is represented by the arrows pointing upward. In the case of a scintillator, these processes represent the absorption of kinetic

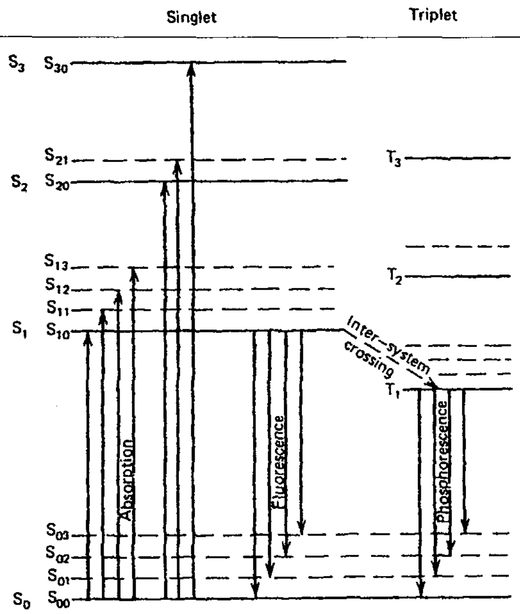

Figure 8.1 Energy levels of an organic molecule with π-electron structure. (From J. B. Birks, *The Theory and Practice of Scintillation Counting.* Copyright 1964 by Pergamon Press, Ltd. Used with permission.)

energy from a charged particle passing nearby. The higher singlet electronic states that are excited are quickly (on the order of picoseconds) de-excited to the S_1 electron state through radiationless internal conversion. Furthermore, any state with excess vibrational energy (such as S_{11} or S_{12}) is not in thermal equilibrium with its neighbors and again quickly loses that vibrational energy. Therefore, the net effect of the excitation process in a simple organic crystal is to produce, after a negligibly short time period, a population of excited molecules in the S_{10} state.

The principal scintillation light (or prompt fluorescence) is emitted in transitions between this S_{10} state and one of the vibrational states of the ground electronic state. These transitions are indicated by the downward arrows in Fig. 8.1. If τ represents the fluorescence decay time for the S_{10} level, then the prompt fluorescence intensity at a time t following excitation should simply be

$$I = I_0 e^{-t/\tau} \tag{8.1}$$

In most organic scintillators, τ is a few nanoseconds, and the prompt scintillation component is therefore relatively fast.

The lifetime for the first triplet state T_1 is characteristically much longer than that of the singlet state S_1. Through a transition called *intersystem crossing*, some excited singlet states may be converted into triplet states. The lifetime of T_1 may be as much as 10^{-3} s and the radiation emitted in a de-excitation from T_1 to S_0 is therefore a delayed light emission characterized as phosphorescence. Because T_1 lies below S_1, the wavelength of this phosphorescence spectrum will be longer than that for the fluorescence spectrum. While in the T_1 state, some molecules may be thermally excited back to the S_1 state and subsequently decay through normal fluorescence. This process represents the origin of the delayed fluorescence sometimes observed for organics.

Figure 8.1 can also be used to explain why organic scintillators can be transparent to their own fluorescence emission. The length of the upward arrows corresponds to those photon energies that will be strongly absorbed in the material. Because all the fluorescence transitions represented by the downward arrows (with the exception of $S_{10} - S_{00}$) have a lower energy than the minimum required for excitation, there is very little overlap between the optical absorption and emission spectra (often called the *Stokes shift*), and consequently little self-absorption of the fluorescence. An example of these spectra for a typical organic scintillator is given in Fig. 8.2.

The *scintillation efficiency* of any scintillator is defined as the fraction of all incident particle energy which is converted into visible light. One would always prefer this efficiency to be as large as possible, but unfortunately there are alternate de-excitation modes available to the excited molecules that do not involve the emission of light and in which the excitation is degraded mainly to heat. All such radiationless de-excitation processes are grouped together under the term *quenching*. In the fabrication and use of organic scintillators, it is often important to eliminate impurities (such as dissolved oxygen in liquid scintillators), which degrade the light output by providing alternate quenching mechanisms for the excitation energy.

In almost all organic materials, the excitation energy undergoes substantial transfer from molecule to molecule before de-excitation occurs. This energy transfer process is especially important for the large category of organic scintillators that involves more than one species of molecules. If a small concentration of an efficient scintillator is added to a bulk solvent, the energy that is absorbed, primarily by the solvent, can eventually find its way to one of the efficient scintillation molecules and cause light emission at that point. These "binary" organic scintillators are widely used both as liquid and plastic solutions incorporating a variety of solvents and dissolved organic scintillants.

A third component is sometimes added to these mixtures to serve as a "waveshifter." Its function is to absorb the light produced by the primary scintillant and reradiate it at a longer wavelength. This shift in the emission spectrum can be useful for closer matching to the spectral sensitivity of a photomultiplier tube or to minimize bulk self-absorption in large liquid or plastic scintillators. Birks and Pringle[3] have reviewed the energy transfer mechanisms in binary and tertiary organic mixtures together with their influence on scintillation efficiency and pulse timing characteristics.

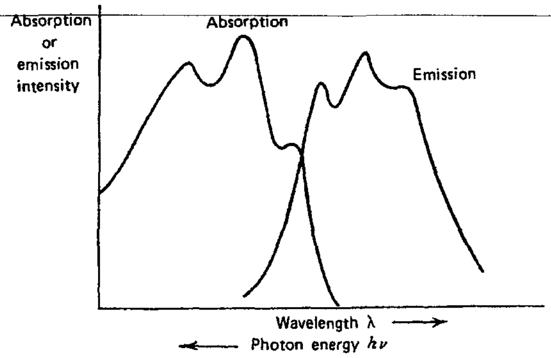

Figure 8.2 The optical absorption and emission spectra for a typical organic scintillator with the level structure shown in Fig. 8.1.

B. Types of Organic Scintillators

1. PURE ORGANIC CRYSTALS

Only two materials have achieved widespread popularity as pure organic crystalline scintillators. Anthracene is one of the oldest organic materials used for scintillation purposes and holds the distinction of having the highest scintillation efficiency (or greatest light output per unit energy) of any organic scintillator. Stilbene has a lower scintillation efficiency but is preferred in those situations in which pulse shape discrimination is to be used to distinguish between scintillations induced by charged particles and electrons (see the later discussion of this technique). Both materials are relatively fragile and difficult to obtain in large sizes. Also, the scintillation efficiency is known to depend on the orientation of an ionizing particle with respect to the crystal axis.[4] This directional variation, which can be as much as 20–30%, spoils the energy resolution obtainable with these crystals if the incident radiation will produce tracks in a variety of directions within the crystal.

2. LIQUID ORGANIC SOLUTIONS

A category of useful scintillators is produced by dissolving an organic scintillator in an appropriate solvent. Liquid scintillators can consist simply of these two components, or a third constituent is sometimes added as a wavelength shifter to tailor the emission spectrum to better match the spectral response of common photomultiplier tubes.

Liquid scintillators are often sold commercially in sealed glass containers and are handled in the same manner as solid scintillators. In certain applications, large-volume detectors with dimensions of several meters may be required. In these cases the liquid scintillator is often the only practical choice from a cost standpoint. In many liquids, the presence of dissolved oxygen can serve as a strong quenching agent and can lead to substantially reduced fluorescence efficiency. It is then necessary for the solution to be sealed in a closed volume from which most of the oxygen has been purged.

Because of their lack of a solid structure that could be damaged by exposure to intense radiation, liquid scintillators are expected to be more resistant to radiation damage effects than crystalline or plastic scintillators. This expectation is borne out by measurements,[5] and reasonable resistance to change up to exposures as high as 10^5 Gy has been demonstrated for some liquids.

Liquid scintillators are also widely applied to count radioactive material that can be dissolved as part of the scintillator solution. In this case, all radiations emitted by the source immediately pass through some portion of the scintillator and the counting efficiency can be almost 100%. The technique is widely used for counting low-level beta activity such as that from carbon-14 or tritium. This large field of *liquid scintillation counting* is described further in Chapter 10.

3. PLASTIC SCINTILLATORS

If an organic scintillator is dissolved in a solvent that can then be subsequently polymerized, the equivalent of a solid solution can be produced. A common example is a solvent consisting of styrene monomer in which an appropriate organic scintillator is dissolved. The styrene is then polymerized to form a solid plastic. Other plastic matrices can consist of polyvinyltoluene or polymethylmethacrylate. Because of the ease with which they can be shaped and fabricated, plastics have become an extremely useful form of organic scintillator.

Plastic scintillators are available commercially with a good selection of standard sizes of rods, cylinders, and flat sheets. Because the material is relatively inexpensive, plastics are often the only practical choice if large-volume solid scintillators are needed. In these cases the self-absorption of the scintillator light may no longer be negligible, and some attention should be given to the attenuation properties of the material. The distance in which the light intensity will be attenuated by a factor of 2 can be as much as several meters, although much smaller attenuation lengths are observed for some plastics.[6]

There is also a wide selection of plastic scintillators available as small-diameter fibers. Used either as single fibers or grouped together as bundles or ribbons, these scintillators lend themselves to applications in which the position of particle interactions must be sensed with good spatial resolution. A detailed discussion of the principles and properties of fiber scintillators is given beginning on p. 253 later in this chapter.

Because of the widespread application of plastic scintillators in particle physics measurements, where they may be exposed to sustained high levels of radiation, considerable attention[7–10] has been paid to the degradation in the scintillation output of plastics due to radiation damage. This process is a complicated one, and many variables such as the dose rate, the presence or absence of oxygen, and the nature of the radiation play important roles. There is also a tendency to observe some recovery or annealing of the damage over periods of time that may be hours or days following an exposure. In typical plastic scintillators, significant degradation in light yield is observed for cumulative gamma-ray exposures in the range of 10^3 or 10^4 Gy, whereas other radiation-resistant formulations[11] show little decrease in light output with doses as high as 10^5 Gy. The changes in measured light can consist either of a decreased light output caused by damage to the fluorescent component or a decrease in the light transmission caused by the creation of optical absorption centers.

4. THIN FILM SCINTILLATORS

Very thin films of plastic scintillator play a unique role in the field of radiation detectors. Because ultrathin films with a thickness as low as 20 μg/cm^2 can be fabricated, it is easy to provide a detector that is thin compared with the range of even weakly penetrating particles such as heavy ions. These films thus serve as transmission detectors, which respond to only the fraction of energy lost by the particle as it passes through the detector. The thickness can be as much as one or two orders of magnitude smaller than the minimum possible with other detector configurations, such as totally depleted silicon surface barriers. The films are available commercially[12] with thicknesses down to approximately 10 μm. Even thinner films can be produced by the user through techniques such as evaporation from a solution of plastic scintillator[13–16] or through the spin coating process.[17,18] The film can be deposited directly on the face of a photomultiplier tube,[14,19] or the light can be collected indirectly through a transparent light pipe in contact with the edges of the film.[20,21] Alternatively, the film can be placed within a reflecting cavity.[20,22–25] The response of these films does not follow directly from the expected energy loss of ions in the detector and is a more complex function of the ion velocity and atomic number.[16,19,26–29] The light yield per unit energy loss increases with decreasing atomic number of the ion, so that thin films can be useful transmission detectors for protons or alpha particles[15,22] even when the energy deposited is relatively small. In common with other organic scintillators, thin film detectors show scintillation decay times of only several ns, and they have proved very useful in fast timing measurements.[30]

5. LOADED ORGANIC SCINTILLATORS

Organic scintillators as a category are generally useful for the direct detection of beta particles (fast electrons) or alpha particles (positive ions). They also are readily adaptable to the detection of fast neutrons through the proton recoil process (see Chapter 15). Because of the low Z-value of their constituents (hydrogen, carbon, and oxygen), however, there is virtually no photoelectric cross section for gamma rays of typical energies. As a result, typical organic scintillators show no photopeak and will give rise only to a Compton continuum in their gamma-ray pulse height spectrum.

To provide some degree of photoelectric conversion of gamma rays, attempts have been made to add high-Z elements to organic scintillators. The most common form is the addition of lead or tin to common plastic scintillators up to a concentration of 10% by weight. It has also been demonstrated[31] that tin can be added to liquid organic scintillator solutions in concentrations of up to 54% by weight while retaining a weak scintillation light output. At low gamma-ray energies, the photopeak efficiency of these materials can be made relatively high,[32] and they have the additional advantages of fast response and low cost compared with more conventional gamma-ray scintillators.[33,34] Unfortunately, the addition of these high-Z elements inevitably leads to a decreased light output, and the energy resolution that can be achieved is therefore considerably inferior to that of inorganic scintillators.

Other examples of loading organic scintillators arise in connection with neutron detection. Liquid or plastic scintillators can be seeded with one of the elements with a high cross section for neutrons such as boron, lithium, or gadolinium. The secondary charged particles and/or gamma rays produced by netron-induced reactions may then be detected directly in the scintillator to provide an output signal. Scintillators of this type are discussed in further detail in Chapter 14.

C. Response of Organic Scintillators

An overall compilation of the properties of organic scintillators is given in Table 8.1.

1. LIGHT OUTPUT

A small fraction of the kinetic energy lost by a charged particle in a scintillator is converted into fluorescent energy. The remainder is dissipated nonradiatively, primarily in the form of lattice vibrations or heat. The fraction of the particle energy that is converted (the scintillation efficiency) depends on both the particle type and its energy. In some cases, the scintillation efficiency may be independent of energy, leading to a linear dependence of light yield on initial energy.

For organic scintillators such as anthracene, stilbene, and many of the commercially available liquid and plastic scintillators, the response to electrons is linear for particle energies above about 125 keV.[35] The response to heavy charged particles such as protons or alpha particles is always less for equivalent energies and is nonlinear to much higher initial energies. As an example, Fig. 8.3 shows the scintillation response of a typical plastic

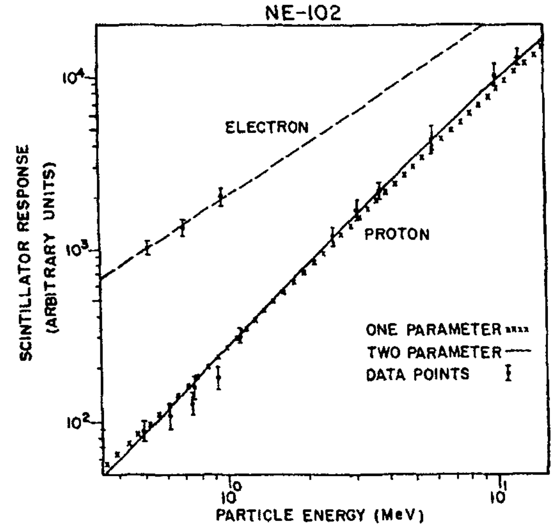

Figure 8.3 The scintillation light yield for a common plastic scintillator (NE 102) when excited by electrons and protons. The data are fit by curves from Eq. (8.3) (one parameter) and Eq. (8.9) (two parameter). (From Craun and Smith.[36])

Table 8.1 Properties of Some Commercially Available Organic Scintillators

Eljen	Bicron	Light Output %Anthracene*	Wavelength of Max Emission (nm)	Decay Constant (ns)	Attenuation Length (cm)	Refractive Index	H/C Ratio	Density	Loading Element % by weight or dist. feature	Softening or Flash Point (°C)	Uses
Crystal											
Anthracene		100	447	30		1.62	0.715	1.25		217	
Stilbene		50	410	4.5		1.626	0.858	1.16		125	
Plastic											
EJ-212	BC-400	65	423	2.4	250	1.581	1.103	1.032		70	General purpose
EJ-204	BC-404	68	408	1.8	160	1.58	1.107	1.032	1.8 ns time constant	70	Fast counting
EJ-200	BC-408	64	425	2.1	380	1.58	1.104	1.032		70	TOF counters, large area
EJ-208	BC-412	60	434	3.3	400	1.58	1.104	1.032	Longest attn. length	70	General purpose, large area, long strips
	BC-420	64	391	1.5	110	1.58	1.100	1.032	1.5 ns time constant	70	Ultrafast timing, sheet areas
EJ-232	BC-422	55	370	1.4	8	1.58	1.102	1.032	1.4 ns time constant	70	Very fast timing, small sizes
	BC-422Q	11	370	0.7	< 8	1.58	1.102	1.032	Benzephenone, 1%	70	Ultrafast timing, ultrafast counting
	BC-428	36	480	12.5	150	1.58	1.103	1.032	Green emitter	70	Photodiodes and CCDs; phoswich detectors
	BC-430	45	580	16.8	NA	1.58	1.108	1.032	Red emitter	70	Silicon photodiodes and red-enhanced PMTs
EJ-248	BC-434	60	425	2.2	350	1.59	0.995	1.049	High temp	100	General purpose
	BC-436	52	425	2.2	NA	1.61	0.960 D:C	1.130	Deuterium, 13.8%	90	Thin disks
EJ-240	BC-444	41	428	285	180	1.58	1.109	1.032		70	Phoswich detectors for dE/dx studies
EJ-256	BC-452	32	424	2.1	150	1.58	1.134	1.080	Lead, 5%	60	X-ray dosimetry (< 100 keV)
	BC-454	48	425	2.2	120	1.58	1.169	1.026	Boron, 5%	60	Neutron spectrometry, thermal neutrons
EJ-252	BC-470	46	423	2.4	200	1.58	1.098	1.037	Air equivalent	65	Dosimetry
	BC-490	55	425	2.3		1.58	1.107	1.030	Casting resin	70	General purpose
	BC-498	65	423	2.4		1.58	1.103	1.032	Applied like paint	70	β, γ detection
Liquid											
EJ-301	BC-501A	78	425	3.2			1.212	0.874	Pulse shape discrim.	26	γ > 100 keV, fast n spectroscopy
EJ-305	BC-505	80	425	2.5			1.331	0.877	High light output	47	γ, fast n, large volume
EJ-313	BC-509	20	425	3.1			0.0035	1.61	F	10	γ, fast n
EJ-321H	BC-517H	52	425	2.0			1.89	0.86	Mineral oil-based	81	γ fast n, cosmic, charged particles
	BC-517P	28	425	2.2			2.05	0.85	Mineral oil-based	115	γ, fast n, cosmic, charged particles
EJ-325	BC-519	60	425	4.0			1.73	0.875	Pulse shape discrim.	74	γ, fast n, n-γ discrimination
EJ-331	BC-521	60	425	4.0			1.31	0.89	Gd (to 1%)	44	Neutron spectroscopy, neutrino research
EJ-339	BC-523A	65	425	3.7			1.67	0.93	Enriched ^{10}B	1	Total absorption neutron spectrometry
EJ-335	BC-525	56	425	3.8			1.57	0.88	Gd (to 1%)	64	Neutron spectrometry, neutrino research
	BC-533	51	425	3.0			1.96	0.8	Low temp operation	65	γ, fast n, cosmic
	BC-537	61	425	2.8			.99 (D:C)	0.954	^{2}H	−11	Fast n, pulse shape discrimination
	BC-551	40	425	2.2			1.31	0.902	Pb (5% w/w)	44	γ, X-rays < 200 keV
	BC-553	34	425	3.8			1.47	0.951	Sn (10% w/w)	42	γ, X-rays

*NaI(Tl) is 230% on this scale

scintillator. At energies of a few hundred keV, the response to protons is smaller by a factor of 10 compared with the light yield of equivalent energy electrons. At higher energies the discrepancy is less, but the proton response is always below the electron response.

Because of the dependence of the light yield of organics on the type of particle, a special nomenclature is sometimes used to describe the absolute light yield. The term *MeV electron equivalent* (*MeVee*) is introduced to place the light yield on an absolute basis. The particle energy required to generate 1 MeVee of light by definition is 1 MeV for fast electrons but is several MeV for heavy charged particles because of their reduced light yield per unit energy.

The response of organic scintillators to charged particles can best be described by a relation between dL/dx, the fluorescent energy emitted per unit path length, and dE/dx, the specific energy loss for the charged particle. A widely used relation first suggested by Birks[1] is based on the assumption that a high ionization density along the track of the particle leads to quenching from damaged molecules and a lowering of the scintillation efficiency. If we assume that the density of damaged molecules along the wake of the particle is directly proportional to the ionization density, we can represent their density by $B(dE/dx)$, where B is a proportionality constant. Birks assumes that some fraction k of these will lead to quenching. A further assumption is that, in the absence of quenching, the light yield is proportional to energy loss:

$$\frac{dL}{dx} = S\frac{dE}{dx} \tag{8.2}$$

where S is the normal scintillation efficiency. To account for the probability of quenching, Birks then writes

$$\frac{dL}{dx} = \frac{S\dfrac{dE}{dx}}{1 + kB\dfrac{dE}{dx}} \tag{8.3}$$

Equation (8.3) is commonly referred to as *Birks' formula*. As a practical matter the product kB is treated as an adjustable parameter to fit experimental data for a specific scintillator.[37] In many cases, this single adjustable parameter can give very good fits to the shape of experimental data, with the value of S providing the absolute normalization.

When excited by fast electrons (either directly or from gamma-ray irradiation), dE/dx is small for sufficiently large values of E and Birks' formula then predicts

$$\left.\frac{dL}{dx}\right|_e = S\frac{dE}{dx} \tag{8.4}$$

or the incremental light output per unit energy loss is a constant

$$\left.\frac{dL}{dE}\right|_e = S \tag{8.5}$$

This is the regime in which the light output

$$L \equiv \int_0^E \frac{dL}{dE}\,dE = SE \tag{8.6}$$

is linearly related to the initial particle energy E.

On the other hand, for an alpha particle, dE/dx is very large so that saturation occurs along the track and Birks' formula becomes

$$\left.\frac{dL}{dx}\right|_\alpha = \frac{S}{kB} \tag{8.7}$$

The appropriate value of kB can therefore be determined by taking the ratio of these two responses:

$$kB = \left.\frac{dL}{dE}\right|_e \Bigg/ \left.\frac{dL}{dx}\right|_\alpha \tag{8.8}$$

In order to match experimental data more closely, other formulas for dL/dx have been proposed by a number of authors. These are in effect semiempirical formulas that introduce one or more additional fitting parameters. An extensive analysis of the response of a number of organic scintillators has been carried out by Craun and Smith.[36] Their analysis is based largely on the data of Smith et al.[38] and uses an extended version of Birks' formula

$$\frac{dL}{dx} = \frac{S\dfrac{dE}{dx}}{1 + kB\dfrac{dE}{dx} + C\left(\dfrac{dE}{dx}\right)^2} \tag{8.9}$$

where C is again treated as an empirically fitted parameter. This expression approaches the simple Birks' formula Eq. (8.3) for small values of dE/dx. Parameters for Eq. (8.9) are derived and listed in Ref. 36 for a variety of organic scintillators and exciting particles. Also given is a useful table of dE/dx values for organic scintillators of different composition for protons and deuterons.

The *alpha-to-beta ratio* is a widely used parameter to describe the difference of light output for an organic scintillator for electrons and charged particles of the same energy. The light yield for electrons is always higher than that for a charged particle of the same kinetic energy, and therefore the alpha-to-beta ratio is always less than 1. This ratio will depend on the energy at which the comparison is made, and no fixed value is applicable over the entire energy range. Measurements have been reported by Czirr[39] for a variety of organic scintillators.

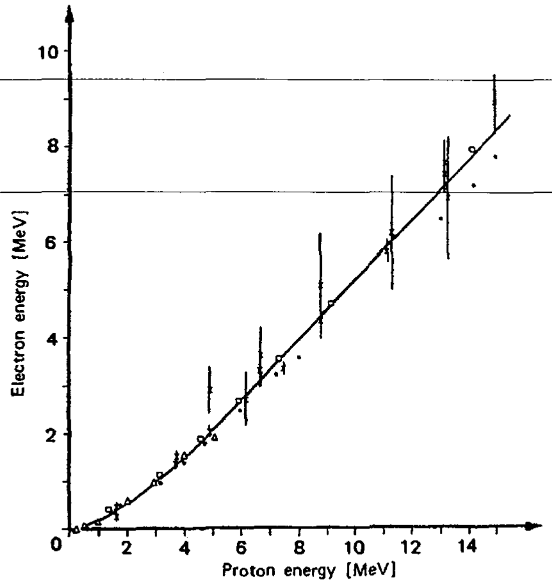

Figure 8.4 The light output (expressed in equivalent electron energy deposition) versus proton energy for liquid scintillator NE 213. (From Maier and Nitschke.[40])

The light output of NE 213 liquid scintillator as measured by Maier and Nitschke[40] is shown in Fig. 8.4. Typical of many organic scintillators, the light output can be represented as proportional to $E^{3/2}$, for energies below about 5 MeV, and becomes approximately linear for higher energies.

Clark[41] has compiled a set of data on the absolute scintillation efficiency [S in Eq. (8.5)] of plastic scintillators for gamma-ray excitation. These data are a useful supplement to older tabulations which can be found in Ref. 1. Clark points out the variability of different measurements attempting to determine absolute efficiencies, which in some cases can be as much as a factor of 2 discrepant. This variability can be traced in part to differences in the purity and past history of the scintillation material, and absolute values should always be used with caution. In some organics, the partial overlap of the emission and absorption spectra leads to a size dependence of the apparent efficiency for scintillation. Also, the anisotropic response of anthracene and stilbene further complicates efficiency measurements.

Prolonged exposure to ionizing radiation leads to a general deterioration of the properties of most organic scintillators (for example, see p. 224). Plastic scintillators exposed to light and oxygen have also been shown to undergo a long-term deterioration due to polymer degradation.[42] In addition to internal effects, the surface of plastics can often become crazed on exposure to extreme environments. The surface crazing leads to a substantial drop in observed light output from large scintillators because of the decreased efficiency of internal light reflection.

2. *TIME RESPONSE*

If it can be assumed that the luminescent states in an organic molecule are formed instantaneously and only prompt fluorescence is observed, then the time profile of the light pulse should be a very fast leading edge followed by a simple exponential decay [Eq. (8.1)]. Much of the published literature quotes a *decay time* that characterizes the prompt scintillation yield from various organic materials. Although this simple representation is often adequate for many descriptions of the scintillator behavior, a more detailed model of the time dependence of the scintillation yield must take into account two other effects: the finite time required to populate the luminescent states, and the slower components of the scintillation corresponding to delayed fluorescence and phosphorescence.

Times of approximately half a nanosecond are required to populate the levels from which the prompt fluorescence light arises. For the very fast scintillators, the decay time from these levels is only three or four times greater, and a full description of the expected pulse shape must take into account the finite rise time as well. One approach[43, 44] assumes that the population of the optical levels is also exponential and that the overall shape of the light pulse is given by

$$I = I_0(e^{-t/\tau} - e^{-t/\tau_1}) \tag{8.10}$$

where τ_1 is the time constant describing the population of the optical levels and τ is the time constant describing their decay. Values for these parameters for several plastic scintillators are given in Table 8.2. Other observations[45] have concluded that the population step is better represented by a Gaussian function $f(t)$ characterized by a standard deviation σ_{ET}. The overall light versus time profile is then described by

$$\frac{I}{I_0} = f(t)e^{-t/\tau} \tag{8.11}$$

Best fit values for σ_{ET} are also shown in Table 8.2. Experimentally, the rise and fall of the light output can be characterized by the full width at half maximum (FWHM) of the resulting light versus time profile, which can be measured using very fast timing procedures. It

Table 8.2 Some Timing Properties of Fast Plastic Scintillators

	Parameters for Eq. (8.10)		Parameters for Eq. (8.11)		Measured
	τ_1 (rise)	τ(decay)	σ_{ET}	τ	FWHM
NE 111	0.2 ns	1.7 ns	0.2 ns	1.7 ns	1.54 ns
Naton 136	0.4 ns	1.6 ns	0.5 ns	1.87 ns	2.3 ns
NE 102A	0.6 ns	2.4 ns	0.7 ns	2.4 ns	3.3 ns

Data from Bengtson and Moszynski.[45]

has become common to specify the performance of ultrafast organic scintillators by their FWHM time rather than the decay time alone.

Studies of the time response of organic scintillators have been reported in Refs. 46–49. In these measurements the emphasis is on conventional plastic scintillators, with the smallest FWHM reported to be 1.3 ns for NE 111. Lynch[44] has also reported results on light output and time response of a variety of liquid scintillators. Some attention[50–52] has focused on plastics to which a quenching agent has been deliberately added. Although the light output is reduced by an order of magnitude or more, the FWHM can be as small as a few hundred picoseconds. For these very fast scintillators, effects other than the scintillation mechanism can sometimes affect the observed time response. Among these is the finite flight time of the photons from the point of scintillation to the photomultiplier tube. Particularly in large scintillators, transit time fluctuation due to multiple light reflections at scintillator surfaces can amount to a sizable spread in the arrival time of the light at the photomultiplier tube photocathode.[53–55] Also, there is evidence[56,57] that self-absorption and reemission of the fluorescence plays an important role in causing an apparent worsening of the time resolution as the dimensions of a scintillator are increased.

Although fast decay time is an advantage in nearly all applications of scintillators, there is at least one application in which a slow decay is needed. In the phoswich detector (see p. 344) two different scintillation materials are employed, one of which must have an appreciably slower decay time than the other. For such applications, a plastic scintillator has been developed[58] with an unusually long decay of 225 ns, more typical of slower inorganic materials.

3. PULSE SHAPE DISCRIMINATION

For the vast majority of organic scintillators, the prompt fluorescence represents most of the observed scintillation light. A longer-lived component is also observed in many cases, however, corresponding to delayed fluorescence. The composite yield curve can often be represented adequately by the sum of two exponential decays—called the fast and slow components of the scintillation. Compared with the prompt decay time of a few nanoseconds, the slow component will typically have a characteristic decay time of several hundred nanoseconds. Because the majority of the light yield occurs in the prompt component, the long-lived tail would not be of great consequence except for one very useful property: *The fraction of light that appears in the slow component often depends on the nature of the exciting particle.* One can therefore make use of this dependence to differentiate between particles of different kinds that deposit the same energy in the detector. This process is often called *pulse shape discrimination* and is widely applied to eliminate gamma-ray-induced events when organic scintillators are used as neutron detectors.

There is strong evidence that the slow scintillation component originates with the excitation of long-lived triplet states (labeled T_1 in Fig. 8.1) along the track of the ionizing

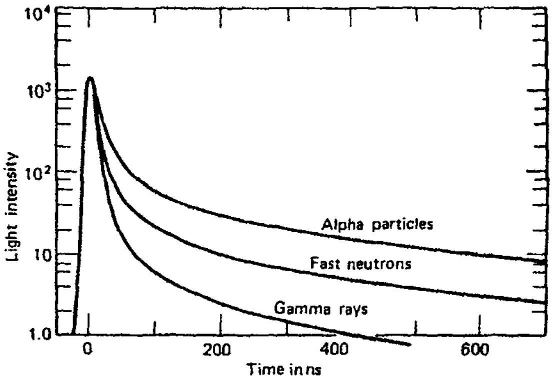

Figure 8.5 The time dependence of scintillation pulses in stilbene (equal intensity at time zero) when excited by radiations of different types. (From Bollinger and Thomas.[60])

particle. Bimolecular interactions between two such excited molecules can lead to product molecules, one in the lowest singlet state (S_1) and the other in the ground state. The singlet state molecule can then de-excite in the normal way, leading to delayed fluorescence. The variation in the yield of the slow component can then be partially explained by the differences expected in the density of triplet states along the track of the particle, because the bimolecular reaction yield should depend on the square of the triplet concentration. Therefore, the slow component fraction should depend primarily on the rate of energy loss dE/dx of the exciting particle and should be greatest for particles with large dE/dx. These predictions are generally confirmed by measurements of the scintillation pulse shape from a wide variety of organics.

Certain organic scintillators, including stilbene crystals[59] and a number of commercial liquid scintillators, are particularly favored for pulse shape discrimination because of the large differences in the relative slow component induced by different radiations. Figure 8.5 shows the differences observed in stilbene for alpha particles, fast neutrons (recoil protons), and gamma rays (fast electrons). In such scintillators, it is not only possible to differentiate radiations with large dE/dx differences (such as neutrons and gamma rays) but also to separate events arising from various species of heavy charged particles as well. Reviews of the pulse shape discrimination properties of different types of organic scintillators and examples of applications are given in Refs. 61–69. Electronic circuits designed to carry out this pulse shape discrimination are described in Chapter 17.

II. INORGANIC SCINTILLATORS

A. Scintillation Mechanism in Inorganic Crystals with Activators

The scintillation mechanism in inorganic materials depends on the energy states determined by the crystal lattice of the material. As shown in Fig. 8.6, electrons have available only discrete bands of energy in materials classified as insulators or semiconductors. The lower band, called the *valence band*, represents those electrons that are essentially bound at lattice sites, whereas the *conduction band* represents those electrons that have sufficient energy to be free to migrate throughout the crystal. There exists an intermediate band of energies, called the *forbidden band*, in which electrons can never be found in the pure

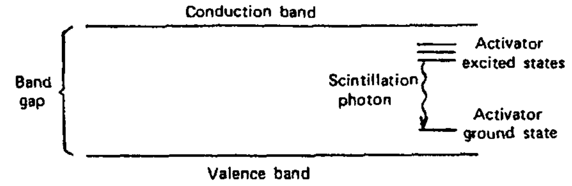

Figure 8.6 Energy band structure of an activated crystalline scintillator.

crystal. Absorption of energy can result in the elevation of an electron from its normal position in the valence band across the gap into the conduction band, leaving a hole in the normally filled valence band. In the pure crystal, the return of the electron to the valence band with the emission of a photon is an inefficient process. Furthermore, typical gap widths are such that the resulting photon would be of too high an energy to lie in the visible range.

To enhance the probability of visible photon emission during the de-excitation process, small amounts of an impurity are commonly added to inorganic scintillators. Such deliberately added impurities, called *activators*, create special sites in the lattice at which the normal energy band structure is modified from that of the pure crystal. As a result, there will be energy states created within the forbidden gap through which the electron can de-excite back to the valence band. Because the energy is less than that of the full forbidden gap, this transition can now give rise to a visible photon and therefore serve as the basis of the scintillation process. These de-excitation sites are called *luminescence centers* or *recombination centers*. Their energy structure in the host crystalline lattice determines the emission spectrum of the scintillator.

A charged particle passing through the detection medium will form a large number of electron–hole pairs created by the elevation of electrons from the valence to the conduction band. The positive hole will quickly drift to the location of an activator site and ionize it, because the ionization energy of the impurity will be less than that of a typical lattice site. Meanwhile, the electron is free to migrate through the crystal and will do so until it encounters such an ionized activator. At this point the electron can drop into the activator site, creating a neutral configuration that can have its own set of excited energy states. These states are illustrated in Fig. 8.6 as horizontal lines within the forbidden gap. If the activator state that is formed is an excited configuration with an allowed transition to the ground state, its de-excitation will occur very quickly and with high probability for the emission of a corresponding photon. If the activator is properly chosen, this transition can be in the visible energy range. Typical half-lives for such excited states are on the order of 50–500 ns. Because the migration time for the electron is much shorter, all the excited impurity configurations are formed essentially at once and will subsequently de-excite with the half-life characteristic of the excited state. It is the decay time of these states that therefore determines the time characteristics of the emitted scintillation light. Some inorganic scintillators can adequately be characterized by a single decay time or a simple exponential, although more complex time behavior is often observed.

There are processes that compete with the one just described. For example, the electron upon arriving at the impurity site can create an excited configuration whose transition to the ground state is forbidden. Such states then require an additional increment of energy to raise them to a higher-lying state from which de-excitation to the ground state is possible. One source of this energy is thermal excitation and the resulting slow component of light is called *phosphorescence*. It can often be a significant source of background light or "afterglow" in scintillators.

A third possibility exists when an electron is captured at an activator site. Certain radiationless transitions are possible between some excited states formed by electron capture and the ground state, in which case no visible photon results. Such processes are called *quenching* and represent loss mechanisms in the conversion of the particle energy to scintillation light.

As an alternative to the independent migration of the electron and hole described above, the pair may instead migrate together in a loosely associated configuration known as an *exciton*. In this case the electron and hole remain associated with each other but are free to drift through the crystal until reaching the site of an activator atom. Similar excited activator configurations can again be formed and give rise to scintillation light in their de-excitation to the ground configuration.

A measure of the efficiency of the scintillation process follows from a simple energy calculation. For a wide category of materials, it takes on the average about three times the bandgap energy to create one electron-hole pair. In sodium iodide, this means about 20 eV of charged particle energy must be lost to create one electron–hole pair. For 1 MeV of particle energy deposited in the scintillator, about 5×10^4 electron–hole pairs are thus created. Various experimental determinations have shown that the absolute scintillation efficiency of thallium-activated sodium iodide is about 12%. Absorption of 1 MeV of energy should therefore yield about 1.2×10^5 eV in total light energy, or 4×10^4 photons with an average energy of 3 eV. The yield is thus very close to 1 photon per electron-hole pair originally formed, and the energy transfer to activator sites must be extremely efficient. The processes of energy transfer in alkali halide scintillators have been reviewed by Murray[70] and by Kaufman et al.[71]

One important consequence of luminescence through activator sites is the fact that the crystal can be transparent to the scintillation light. In the pure crystal, roughly the same energy would be required to excite an electron–hole pair as that liberated when that pair recombines. As a result the emission and absorption spectra will overlap and there will be substantial self-absorption. As we have seen, however, the emission from an activated crystal occurs at an activator site where the energy transition is less than that represented by the creation of the electron–hole pair. As a result the emission spectrum is shifted to longer wavelengths and will not be influenced by the optical absorption band of the bulk of the crystal.

The emission spectrum of the light produced by a number of inorganic scintillators is shown in Fig. 8.7. To make full use of the scintillation light, the spectrum should fall near

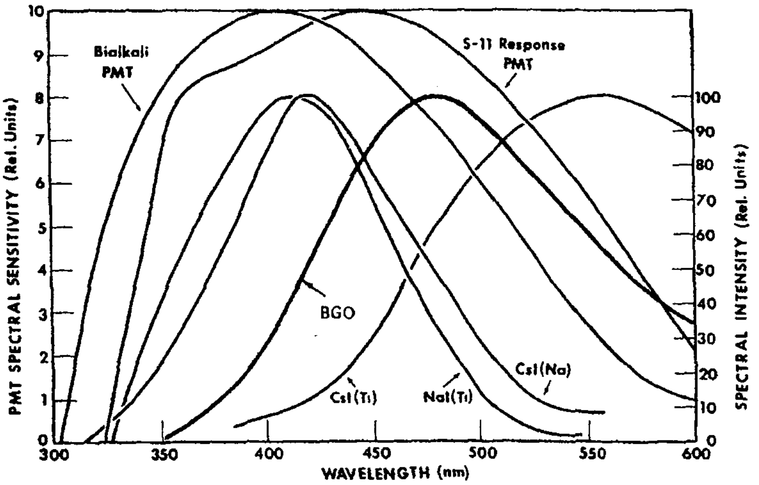

Figure 8.7 The emission spectra of several common inorganic scintillators. Also shown are the response curves for two widely used photocathodes. (Primarily from *Scintillation Phosphor Catalog*, The Harshaw Chemical Company. The emission spectrum for BGO is from Ref. 72.)

the wavelength region of maximum sensitivity for the device used to detect the light. For reference, the responses of several common photocathodes are also plotted in Fig. 8.7 (other photocathode responses are plotted in Fig. 9.2, and that for a typical silicon photodiode in Fig. 9.15).

The scintillation properties at room temperature of a collection of inorganic scintillators are compiled in Table 8.3. The decay times shown in the fourth column are only approximate in that in most cases they represent the dominant decay component only. Many (if not most) inorganic scintillators show more than one decay component, and examples in which a second component is important are also indicated. Where percentages are listed, they represent the relative yields of the components shown. The fifth column is an estimate of the total number of scintillation photons produced over the entire emission spectrum from the deposition of 1 MeV of energy by fast electrons. These values are generally obtained from measurements in which the quantum efficiency of the photomultiplier tube or photodiode used to measure the light (see Chapter 9) is known as a function of wavelength. There is considerable variability in published values for a given material, most likely because of differences in impurity levels or variations in the optical quality of the samples. The sixth column compares the relative pulse amplitude when the scintillator is excited by fast electrons (or gamma rays) and coupled to a glass end-window photomultiplier tube (UV insensitive) with a bialkali photocathode. The variability of photocathode spectral response may also introduce additional variations in these values.

For common inorganic scintillators, the light yield is more nearly proportional to deposited radiation energy than is typically observed in organic scintillators. Quenching processes that are present still lead to some nonlinearity, but often to a much lesser extent than in organics. Variance in the light yield for different types of particles of equal energy is also observed. As in organic scintillators, heavy charged particles produce less light per unit energy. The *alpha-to-beta ratio* (see p. 228) can be much closer to unity than in typical organics (for example, it is in the range of 0.66 to 0.67 for both NaI(Tl) and CsI(Tl) scintillators), but is as low as 0.20 for oxide-based materials such as BGO and GSO described later in this chapter.[73]

B. Characteristics of Alkali Halide Scintillators

1. *NaI(Tl)*

In 1948, Robert Hofstadter[79] first demonstrated that crystalline sodium iodide, in which a trace of thallium iodide had been added in the melt, produced an exceptionally large scintillation light output compared with the organic materials that had previously received primary attention. This discovery, more than any other single event, ushered in the era of modern scintillation spectrometry of gamma radiation. It is remarkable that the same material remains preeminent in the field despite decades of subsequent research into other scintillation materials. Large ingots can be grown from high-purity sodium iodide to which about 10^{-3} mole fraction of thallium has been added as an activator. Scintillators of unusual size or shape can also be fabricated by pressing small crystallites together. NaI(Tl) is hygroscopic and will deteriorate due to water absorption if exposed to the atmosphere for any length of time. Crystals must therefore be "canned" in an air-tight container for normal use.

The most notable property of NaI(Tl) is its excellent light yield. In common with other typical inorganic scintillators, NaI(Tl) shows a small but measurable nonproportionality of its scintillation response with deposited electron energy (see Fig. 8.8). The departure from proportionality is most pronounced at low energies, and some of the practical effects on scintillator performance are discussed later in Chapter 10. It has come to be accepted as the standard scintillation material for routine gamma-ray spectroscopy and can be

Table 8.3 Properties of Common Inorganic Scintillators

	Specific Gravity	Wavelength of Max. Emission	Refractive Index	Decay Time (μs)	Abs. Light Yield in Photons/MeV	Relative Pulse Height Using Bialk. PM tube	References
Alkali Halides							
NaI(Tl)	3.67	415	1.85	0.23	38 000	1.00	
CsI(Tl)	4.51	540	1.80	0.68 (64%), 3.34 (36%)	65 000	0.49	78, 90, 91
CsI(Na)	4.51	420	1.84	0.46, 4.18	39 000	1.10	92
Li(Eu)	4.08	470	1.96	1.4	11 000	0.23	
Other Slow Inorganics							
BGO	7.13	480	2.15	0.30	8200	0.13	
$CdWO_4$	7.90	470	2.3	1.1 (40%), 14.5 (60%)	15 000	0.4	98–100
ZnS(Ag) (polycrystalline)	4.09	450	2.36	0.2		1.3[a]	
CaF_2 (Eu)	3.19	435	1.47	0.9	24 000	0.5	
Unactivated Fast Inorganics							
BaF_2 (fast component)	4.89	220		0.0006	1400	na	107–109
BaF_2 (slow component)	4.89	310	1.56	0.63	9500	0.2	107–109
CsI (fast component)	4.51	305		0.002 (35%), 0.02 (65%)	2000	0.05	113–115
CsI (slow component)	4.51	450	1.80	multiple, up to several μs	varies	varies	114, 115
CeF_3	6.16	310, 340	1.68	0.005, 0.027	4400	0.04 to 0.05	76, 116, 117
Cerium-Activated Fast Inorganics							
GSO	6.71	440	1.85	0.056 (90%), 0.4 (10%)	9000	0.2	119–121
YAP	5.37	370	1.95	0.027	18 000	0.45	78, 125
YAG	4.56	550	1.82	0.088 (72%), 0.302 (28%)	17 000	0.5	78, 127
LSO	7.4	420	1.82	0.047	25 000	0.75	130, 131
LuAP	8.4	365	1.94	0.017	17 000	0.3	134, 136, 138
Glass Scintillators							
Ce activated Li glass[b]	2.64	400	1.59	0.05 to 0.1	3500	0.09	77, 145
Tb activated glass[b]	3.03	550	1.5	~3000 to 5000	~50 000	na	145
For comparison, a typical organic (plastic) scintillator:							
NE102A	1.03	423	1.58	0.002	10 000	0.25	

[a] for alpha particles

[b] Properties vary with exact formulation. Also see Table 15.1.

Source: Data primarily from Refs. 74 and 75, except where noted.

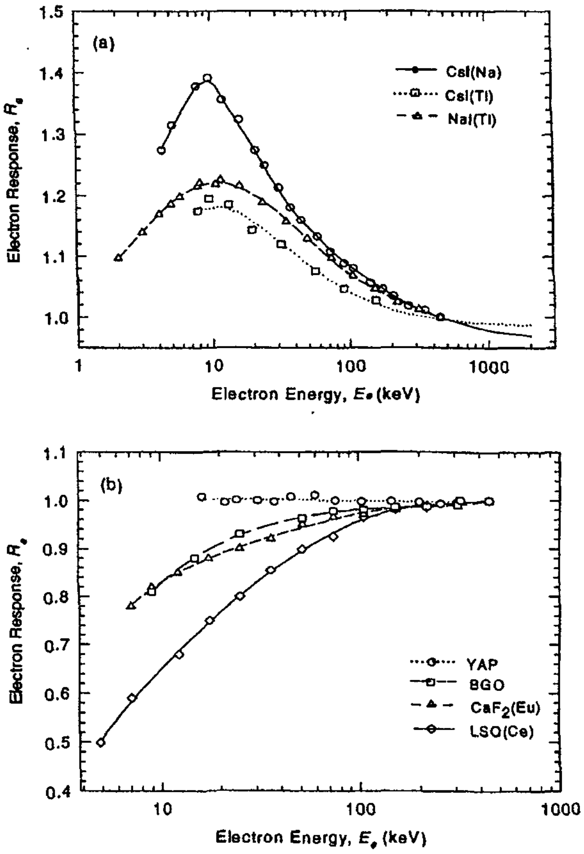

Figure 8.8 The relative scintillation response per unit energy deposited for fast electrons plotted as a function of energy for the scintillation materials shown. The curves are normalized to unity at 445 keV. Perfectly linear response would correspond to a horizontal line on this plot. (From Mengesha et al.[80])

machined into a wide assortment of sizes and shapes. The crystal is somewhat fragile and can easily be damaged by mechanical or thermal shock.

The dominant decay time of the scintillation pulse is 230 ns, uncomfortably long for some fast timing or high counting rate applications. In addition to this prompt yield, a phosphorescence with characteristic 0.15 s decay time has also been measured,[81] which contributes about 9% to the overall light yield. Other longer-lived phosphorescence components have also been measured.[82] Because the anode time constant of photomultiplier tubes is usually set much shorter than these decay times, each photoelectron associated with the phosphorescence is normally resolved individually. At low counting rates, the result is then a series of single-electron pulses that follow the main scintillation pulse and usually are well below the amplitude of interest in the measurement. There are applications, however, in which single-electron sensitivity is needed and the influence of these phosphorescence pulses can be significant. At high counting rates, the phosphorescence will tend to build up due to the multiple overlap from many preceding pulses. This afterglow is often an undesirable characteristic of sodium iodide used in high-rate applications.

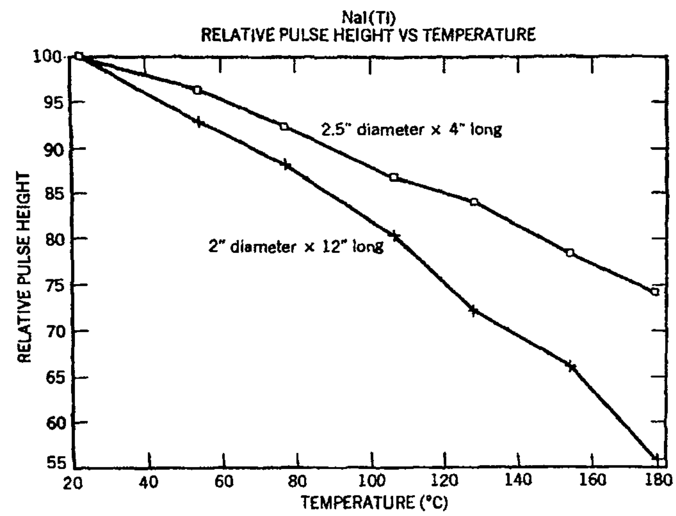

Figure 8.9 The temperature dependence of the light yield measured from two NaI(Tl) crystals. The measurements were made using an oven equipped with a light pipe, and the temperature of the photomultiplier tube was held constant. The difference in behavior between the two crystals is probably due to changes in surface reflectivity. (Data courtesy R. Dayton, Bicron Corporation, Newbury, Ohio.)

The properties summarized above are for thallium-activated sodium iodide operated at room temperature. In some applications, the scintillator must be operated at either lower or higher ambient temperatures. Figure 8.9 shows the dependence of the total light yield in thallium-activated sodium iodide as a function of temperature. The dropoff in scintillation yield with increasing temperature, typical of most scintillation materials, results in generally poorer energy resolution when the scintillator must be used at elevated temperatures. The scintillation decay time in NaI(Tl) is also a function of temperature (see Fig. 8.10), with somewhat faster response at higher temperatures.

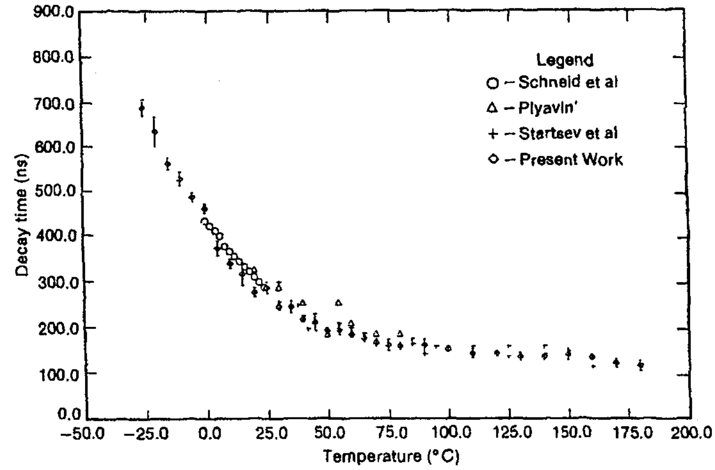

Figure 8.10 Temperature dependence of the scintillation decay time in NaI(Tl). (From Schweitzer and Ziehl.[83])

2. *CsI(Tl) and CsI(Na)*

Cesium iodide is another alkali halide that has gained substantial popularity as a scintillation material. It is commercially available with either thallium or sodium as the activator element, and very different scintillator properties are produced in the two cases. Cesium iodide has a somewhat larger gamma-ray absorption coefficient per unit size compared to sodium iodide. This advantage is of primary importance for applications such as space instrumentation where size and weight are at a premium. Because it is less brittle than sodium iodide, it can be subjected to more severe conditions of shock and vibration. When cut into thin sheets, cesium iodide may be bent into various shapes without fracturing, and it is reasonably soft and malleable. An extensive bibliography of the properties of cesium iodide (both sodium and thallium activated) can be found in Ref. 84.

A most useful property of CsI(Tl) is its variable decay time for various exciting particles. Pulse shape discrimination techniques can therefore be used to differentiate among various types of radiation.[85–87] Particularly clean separations can be achieved between charged particles such as protons or alpha particles on one hand and electron events on the other hand. The material is less hygroscopic than NaI(Tl) but will deteriorate if exposed to water or high humidity.

CsI(Tl) also has a useful property when grown in thin layers on specially prepared patterned substrates. The material can be produced with a microstructure[88] consisting of columns oriented perpendicular to the surface of the layer. Each column may have a diameter as small as 5 μm, and to some extent behaves as an optically isolated scintillator. Layers with thickness of hundreds of microns are often needed for good detection efficiency in the imaging of X-rays. The columnar microstructure inhibits the lateral spread of the scintillation light that would take place if the layer were grown as a single crystal, and better spatial resolution can be achieved for equivalent thickness.[89]

The emission spectrum of CsI(Tl) is peaked at a much longer wavelength than that for NaI(Tl) (see Fig. 8.7) and is poorly matched to the response of PM tubes with S-11 or bialkali photocathodes. For that reason, the light output is often quoted as being substantially lower in CsI(Tl). However, when measurements are made using photodiodes with extended response into the red region of the spectrum, the scintillation yield is actually higher[75] than that of any other scintillator. The absolute light yield at room temperature is measured[90] to be about 65,000 photons/MeV, with a maximum value about 6% higher at −35°C. The yield falls off with temperature change on either side of this maximum, to 64% of the room temperature value at −100°C and to 95% at +50°C.

The luminescent states in CsI(Tl) are populated through an exponential process that results in an unusually long rise time of 20 ns for the initial appearance of the light. The subsequent decay of these states is among the slowest for the commonly used scintillation materials. The light emission for gamma-ray excitation shows two primary components[91] with decay times and relative intensities at room temperature of 0.68 μs (64%) and 3.34 μs (36%).

CsI(Na) has an emission spectrum that is similar to that of NaI(Tl) with a light yield that is comparable, but its relatively slow decay is a disadvantage. The decay is reported to consist of two components with mean lives of 0.46 and 4.18 μs, and a dependence of the slow to fast component ratio has been shown for various exciting particles.[92] Long-lived phosphorescence components in cesium iodide have also been reported.[93] CsI(Na) is hygroscopic and must be sealed against exposure to ambient atmospheres.

3. *LiI(Eu)*

Lithium iodide (europium activated) is an alkali halide of special interest in neutron detection. As discussed in Chapter 14, crystals prepared using lithium enriched in ^{6}Li provide for the efficient detection of low-energy neutrons through the ^{6}Li(n, α) reaction. Scintillation properties of this material are included in Table 8.3.

C. Other Slow (> 200 ns) Inorganic Crystals

1. Bismuth Germanate (or BGO)

An alternative scintillation material, $Bi_4Ge_3O_{12}$ (commonly abbreviated as BGO) is commercially available as crystals of reasonable size. A major advantage over many other scintillators is its high density (7.13 g/cm^3) and the large atomic number (83) of the bismuth component. These properties result in the largest probability per unit volume of any commonly available scintillation material for the photoelectric absorption of gamma rays. Its mechanical and chemical properties make it easy to handle and use, and detectors using BGO can be made more rugged than those employing the more fragile and hygroscopic sodium iodide. Unfortunately, the light yield from BGO is relatively low, being variously reported at 10–20% of that of NaI(Tl). Furthermore, its relatively high refractive index (2.15) makes efficient collection of the light more difficult than for scintillators with lower index values. It is therefore of primary interest when the need for high gamma-ray counting efficiency outweighs considerations of energy resolution. Some comparative gamma-ray spectra for BGO and NaI(Tl) are shown in Chapter 10.

Figure 8.11 shows the time profile of the light emitted in a scintillation event in both BGO and NaI(Tl). In BGO, the principal decay time of 300 ns is preceded by a faster component of the light with 60 ns decay time that represents about 10% of the total light yield. On the other hand, the initial decay of the NaI(Tl) light pulse is slightly slower than the

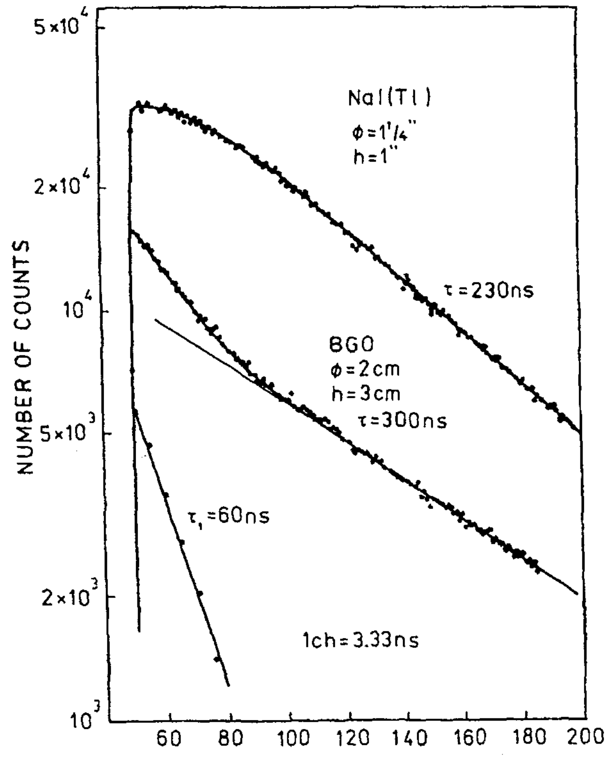

Figure 8.11 Measurements of the light pulse shapes from BGO and NaI(Tl). The abscissa represents time, the ordinate the relative light output. The BGO yield is represented as the sum of separate decay components with 60 and 300 ns decay times. (From Moszynski et al.[94])

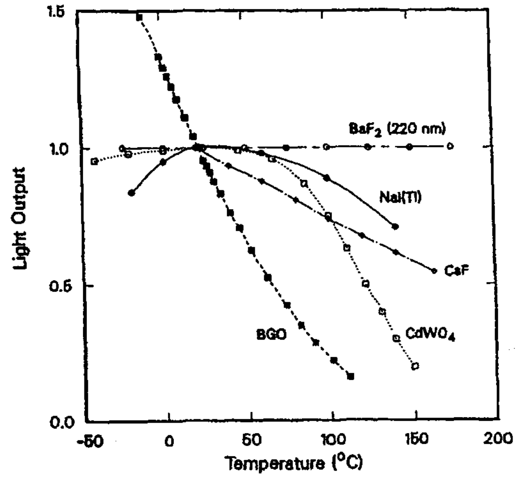

Figure 8.12 The dependence of the light output of some common scintillators as a function of temperature. Only the fast (220 nm) component from BaF_2 is included (From Melcher.[97])

230 ns principal decay. These differences, coupled with the much lower light yield from BGO, result in an overall timing resolution for BGO that is about a factor of 2 worse than that for NaI(Tl).[94] In BGO there are almost none of the long decay components that lead to afterglow in sodium iodide and some other scintillators. BGO has therefore found widespread application in X-ray computed tomography scanners where scintillators operated in current mode must accurately follow rapid changes in X-ray intensity.

BGO is an example of a "pure" inorganic scintillator that does not require the presence of a trace activator element to promote the scintillation process. Instead, the luminescence is associated[95] with an optical transition of the Bi^{3+} ion that is a major constituent of the crystal. There is a relatively large shift between the optical absorption and emission spectra of the Bi^{3+} states. Therefore, relatively little self-absorption of the scintillation light occurs, and the crystal remains transparent to its own emission over dimensions of many centimeters. The scintillation efficiency depends strongly on the purity of the crystal, and some of the variability in the light yield reported from BGO in the past can be attributed to using crystals with different residual levels of impurities.[96] The crystals are typically grown by the Czochralski method in which a crystal boule is pulled from a molten mixture of bismuth oxide and germanium oxide at a rate of a few millimeters per hour. The boule can then be cut and polished using conventional methods. BGO remains two to three times more costly than NaI(Tl) and is currently available only in limited sizes.

In common with many other scintillators, the light output from BGO decreases with increasing temperature. Figure 8.12 shows its relative light output together with that of several other scintillators as a function of temperature. Since the light yield is already low at room temperature, its rapid dropoff severely limits the usefulness of BGO in high-temperature applications.

2. *Cadmium Tungstate $CdWO_4$*

Cadmium tungstate has been known as a scintillator since about 1950, but it has only been in the 1990s that crystals of interesting size and good optical quality have been widely investigated. The light yield is about 40% of that of NaI(Tl),[98,99] with an emission spectrum peaked in the visible near 470 nm. It has a high density and effective atomic number so that it is an excellent candidate for gamma-ray measurements. Its major drawback is its relatively long decay time, a mixture of two components for gamma ray excitation with 1.1 μs

(40%) and 14.5 μs (60%).[99] The relative intensity of these components changes for different types of particles[100] allowing their separate identification using pulse shape discrimination techniques.

Because of the relatively long decay times, pulse mode applications are limited to those in which the counting rate is not high. Excellent gamma-ray energy resolution of 6.8% at 662 keV has been demonstrated for a small (1 cm^3) crystal.[99] Resolutions closer to 10–12% are more typical of larger size crystals.[101] The light collection is somewhat hindered by the high index of refraction (2.3) that makes efficient coupling to photomultiplier tubes or photodiodes more difficult.

The principal application of this material has been as an X-ray detector operated in current mode where the long decay time is not an issue. It is remarkably free of long-lived phosphorescence, making it especially suitable for X-ray computed tomography applications where "afterglow" is highly undesirable in rapidly changing X-ray fluxes.

3. ZnS(Ag)

Silver-activated zinc sulfide is one of the older inorganic scintillators. It has a very high scintillation efficiency comparable to that of NaI(Tl) but is available only as a polycrystalline powder. As a result, its use is limited to thin screens used primarily for alpha particle or other heavy ion detection. Thicknesses greater than about 25 mg/cm^2 become unusable because of the opacity of the multicrystalline layer to its own luminescence. These scintillation screens played a key role in the early experiments of Rutherford, in which alpha particle interactions were visually observed through a low-power microscope.

4. CaF_2(Eu)

Europium-activated calcium fluoride is notable as a nonhygroscopic and inert inorganic scintillator that can often be used where severe environmental conditions preclude other choices. It is relatively fracture resistant and nonreactive, with a vapor pressure low enough to be usable under vacuum conditions. Its scintillation properties are included in Table 8.3. Even though the light yield is 50% of that of NaI(Tl), the relatively long decay time of 900 ns has inhibited its widespread use as a general scintillator.

D. Unactivated Fast Inorganics with Low Light Yield

1. Barium Fluoride BaF_2

Barium fluoride has the distinction of being the first inorganic crystal discovered to have a very fast component in its scintillation decay.[102-105] It is the only presently known scintillator with high atomic number components that has a decay time of less than 1 ns. This combination of properties therefore makes the material attractive for scintillation detectors in which both high detection efficiency per unit volume and a fast response are required.

Unactivated BaF_2 has been known[106] as a scintillation material since the early 1970s. However, it was not until 1983 that it was shown[102] that the scintillation light actually consists of two components: a fast component with decay time of 0.6 ns emitted in the short wavelength region of the spectrum, and a slower component with 630 ns decay time at somewhat longer wavelengths. The two components are identified in the emission spectrum shown in Fig. 8.13. The fast component went unobserved for many years because most photomultiplier tubes are not sensitive to this short wavelength region of the spectrum. However, if quartz end-window tubes or other light sensors are used that are sensitive in the ultraviolet, about 20% of the total scintillation yield at room temperature is measured in the fast component. It results from the creation of a hole in the outer core band of the ionic crystal, followed by the filling of this hole by an electron from the valence band. This process is characterized by very short transition times and the resulting emission is usually

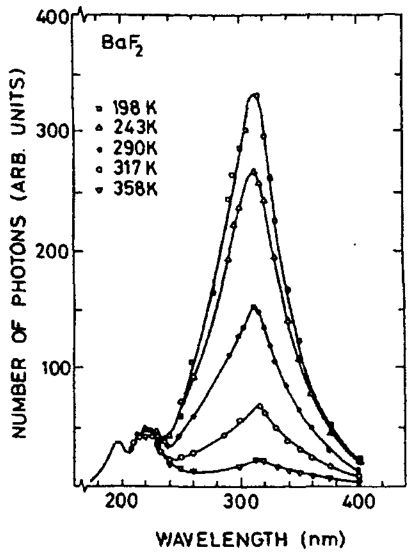

Figure 8.13 The scintillation emission spectra from BaF_2 measured at various temperatures. The fast component (corresponding to the two small peaks at the left) does not display the strong temperature dependence of the slow component. (From Schotanus et al.[107,108])

in the ultraviolet region of the spectrum. If the principal band gap of the crystal is larger than the energy of the UV photon, then the scintillation light can escape reabsorption and be collected by the photomultiplier tube.

The total light yield in BaF_2 is only about 20% of that observed in NaI(Tl), so the attainable energy resolution is considerably poorer. The light yield in the fast component is quite small, only about 1400 photons per MeV.[109] However, a number of applications have been demonstrated[110-112] in which the fast timing capability coupled with the high density and atomic number of the material have made it the scintillation material of choice.

2. *Pure Cesium Iodide CsI*

When activated with thallium, cesium iodide has the highest scintillation yield of any known material. In its pure state, it is also a much weaker scintillator (with output between 5 and 8% of that of NaI(Tl) when measured with a photomultiplier tube). However, much of this light shows a mixture of fast components with an effective decay time of about 10 ns that appears in a peak around 305 nm in the ultraviolet region of the spectrum. A broader emission band in the visible range of 350 to 600 nm that has a much longer decay time of up to several microseconds is also often observed. The relative intensities of these components tends to vary among the measurements reported in the literature[113,114] for different samples of the material, but they are roughly comparable in yield in one study of commercially supplied crystals.[115] The slow component is absent in other measurements of highly purified material,[114] indicating that its origin may be related to residual impurities in some crystals.

3. *Cerium Fluoride* CeF_3

Because of the widespread use of the element cerium as an activator in other crystal matrices, where it acts as a luminescence center, it is not surprising that there has been substantial interest in examining the scintillation potential of compounds of cerium as well. The most widely examined of these is cerium fluoride (CeF_3) that displays weak scintillation light equivalent to about 5% of that of NaI(Tl). The main interest in this material comes about because of its relatively fast decay time. When measured in the visible band, the decay appears to be a single exponential with a decay time of about 27 ns. When the observations are extended in the ultraviolet range,[116] a second component with decay time of about 5 ns is also observable. The total light yield from small volume crystals is reported[117] to be 2100 photons per MeV.

E. Cerium-Activated "Fast" Inorganics

Beginning in the late 1980s, it was realized that the cerium activator could be incorporated into new categories of crystals, resulting in scintillators with reasonably good light yield. The principal decay time of the cerium luminescence ranges from about 20 to 80 ns, depending on the host crystal.[118] Thus the timing characteristics of these scintillators occupy an intermediate position between the organics with a few nanosecond decay time and the older inorganics in which it is several hundred nanoseconds.

1. Gadolinium Silicate Gd_2SiO_5 (or GSO)

This material can be grown in reasonably large sizes as single crystals[119] and the atomic number of 64 for gadolinium offers attractive properties in gamma-ray spectroscopy. Maximum light yield is observed at a cerium doping concentration of about 0.5 mole percent. The scintillation decay time also depends on the cerium doping level, but is dominated by a fast component of about 56 ns at this cerium doping concentration. A longer decay time component of 400 ns is present to 10% intensity ratio as well.[120] The light output also shows an unusually long *rise* time of 10 to 20 ns, depending on the cerium concentration, caused by a slow population process for the fluorescent states. The total light yield is about 20% of that of NaI(Tl). An energy resolution of about 9% for 662 keV gamma rays has been reported as typical performance.[121] Additional properties are given in Table 8.3. It also appears[122] that GSO shows excellent radiation stability, with no appreciable radiation damage observed for gamma-ray exposures up to 10^7 Gy.

2. Yttrium Aluminum Perovskite $YAlO_3$ (or YAP)

This crystal has been known for some time in its role as a laser material when doped with Nd. When doped with cerium, however, it displays some attractive properties as a scintillator. It has a total light output variously reported as 40 to 50% of that of NaI(Tl) and an unusually fast principal decay time of 27 ns. It displays excellent physical properties of hardness, strength, and inertness that readily allow easy fabrication and handling. Its scintillation properties[123–125] show the best performance for small-size crystals, and there is evidence[126] that the light yield and energy resolution suffer for crystals that are larger than a few centimeters in dimension. Small-size crystals show excellent energy resolution, for example, 5.7% at 662 keV,[125] while at the same time offering outstanding timing resolution as low as 160 ps. A slower component of the decay with about 10 μs time constant constitutes less than 10% of the total intensity. YAP demonstrates excellent proportionality of its light output versus energy (see Fig. 8.8), allowing preservation of good energy resolution even when gamma rays undergo multiple interactions in the detector.[124] (See Chapter 10.)

3. Yttrium Aluminum Garnet $Y_3Al_5O_{12}$ (or YAG)

This material when doped with Nd also has a long history as a laser material, but it also has interesting scintillation properties when doped with cerium. The light yield per unit energy is about half that of NaI(Tl), but its spectrum is somewhat unusual in that it is shifted toward longer wavelengths relative to many other scintillators. The peak in the emission spectrum occurs at 550 nm, and it is no longer a good match to many photomultiplier tube spectral responses. Instead, these longer wavelengths are better suited for readout using semiconductor photodiodes. The decay shows several components[127, 128] with principal decay times of 88 ns and 302 ns. For gamma-ray excitation, the relative intensities of these two components are 72% and 28%, respectively. When irradiated with alpha particles, the ratio reverses to 34% and 66%, allowing applications in which pulse shape discrimination can be used to separate different particle types.[127]

4. *Lutetium Oxyorthosilicate $Lu_2(SiO_4)O$ (or LSO)*

This material was first described as a scintillator in 1991.[129] It has some very interesting properties including a light yield approximately 75% of that of NaI(Tl), a fast decay time of 47 ns,[130] and an emission spectrum conveniently peaked at 420 nm. Lutetium is a rare earth whose high atomic number of 71 makes it an attractive component in scintillators intended for gamma-ray spectroscopy. However, its cost and availability for fabrication into large-volume crystals are still open to some question. The natural element contains the isotope ^{176}Lu which is radioactive and adds an inherent background of about 300 counts/s per cm^3 of LSO. The best energy resolution reported for 662 keV gamma rays of 7.5% is obtainable only in small crystals, and more typical energy resolutions of 10% or more are observed in larger crystals. The scintillation response is known[131] to be rather nonlinear (see Fig. 8.8), so some of the degradation in energy resolution may be due to this influence. The light emission appears to consist strictly of a single 47-ns component and is free of the slower components that sometimes plague other inorganic scintillators.[132] An unusual degree of variability in the light output has been observed from various samples of LSO crystals,[133] possibly caused by different levels of trace impurities that can serve as traps for either electrons or holes before they diffuse to a cerium fluorescence site.

5. *Lutetium Orthoaluminate $LuAlO_3$ (or LuAP)*

Motivated by the favorable properties of YAP, described above, there has been interest in exploring its chemical analogue LuAP as a host for the cerium activator. YAP is limited somewhat in its application to gamma ray spectroscopy because of the relatively low atomic number ($Z = 39$) of yttrium. Substituting lutetium with $Z = 71$ provides a much more attractive possibility. In fact LuAP has the highest linear attenuation coefficient for common gamma rays of any scintillator, even exceeding that of BGO. Furthermore, most of the scintillation light appears with a very short decay constant of 17 ns[134] and a relatively high light output that may be more than 50% of that of NaI(Tl). This combination of properties would make the material unparalleled for many gamma-ray applications. Thus there has been a great deal of interest[134–139] in developing practical scintillators from this material. Measurements show that there is very little departure from proportionality in its light yield as a function of deposited energy,[140] minimizing the potential loss of energy resolution due to nonproportionality discussed in Chapter 10. An excellent gamma-ray energy resolution of 4.38% at 662 keV was obtained in the same study for a 3 mm thick crystal coupled to a photomultiplier tube. At the present stage of development, however, useful crystals are limited to thicknesses of less than a centimeter because of strong self-absorption[133] of the scintillation light. This limitation offsets some of the inherent advantages of the high atomic number and density of the material in gamma-ray applications. LuAP also shares with LSO the potentially troublesome natural background caused by the radioactivity of the ^{176}Lu component.

F. Glass Scintillators

Silicate glasses containing lithium and activated with cerium are widely used as neutron detectors, and a collection of their physical and scintillation properties may be found in Table 15.1. Bollinger et al.[141] investigated the properties of a variety of lithium and boron glasses as scintillation materials. The light output observed for the lithium formulations averaged over a factor of 10 larger than that for the boron-containing glasses. The lithium formulations have therefore predominated. In silicate glasses, cerium is the only activator that produces fast scintillation light useful for pulse mode operation. The emission is peaked in the blue region of the spectrum and is associated with the Ce^{3+} sites within the glass. Modern scintillation glasses[142] are made from various mixtures of SiO_2, LiO_2, Al_2O_3, MgO, and Ce_2O_3, with BaO sometimes added to increase the glass density.

The absolute scintillation efficiency for converting fast electron energy to light has been measured[143] in the range from 1 to 2%, generally varying inversely with lithium concentration of the glass formulation. The response to charged particles is nonlinear and always considerably below that to electrons of the same energy. For example, the light output for 1 MeV protons, deuterons, and alpha particles is lower than that for 1 MeV electrons by factors of 2.1, 2.8, and 9.5, respectively.[144]

Despite the fact that their relative light output is quite low (typically a maximum of 3500 photons/MeV), glass scintillators are sometimes applied in beta or gamma-ray counting when severe environmental conditions prevent the use of more conventional scintillators. Examples include conditions in which the scintillator must be exposed to corrosive chemical environments or operated at high temperatures. The decay time of glass scintillators (typically 50–75 ns) is intermediate between faster organics and slower crystalline inorganics. Because the material can be fabricated in much the same manner as other glasses, it is widely available in physical forms other than the more common cylindrical shapes. For example, glass scintillators are commercially available as small-diameter fibers whose properties are described later in this chapter. The material is also available as a powder or small-diameter spheres for use in flow cells in which the radioactive material is allowed to pass through a chamber filled with the porous scintillator.

Because glasses may contain naturally radioactive thorium or potassium, precautions must be taken if scintillators are to be applied in low-level counting systems where a minimum background is required. Ordinary glass scintillators will show a spontaneous background rate of about 100–200 disintegrations per minute for every 100 g of material. Glasses are commercially available that are manufactured from low-thorium materials and that are processed to minimize contamination by any other alpha-active materials. These low-background glasses will have a background activity of less than 20 disintegrations per minute per 100 g.

When used as a neutron counter, the lithium content of the glasses is normally enriched to 95% or more in ^6Li. If applied as a beta or gamma counter, this enrichment is not required and can actually be a hindrance if the detector is operated with any appreciable neutron background. Therefore, one of the commercially available forms fabricated using either natural lithium or lithium depleted in ^6Li is normally chosen for these applications.

Another form of glass scintillator, activated with terbium rather than cerium, has found some use in imaging applications. The scintillation decay time is now very much longer (3–5 ms) so that these formulations are no longer useful in pulse mode applications. However, the total light yield is many times larger than from the cerium-activated glass, reaching as high as 50,000 photons per MeV.[145] The light emission is in the green part of the spectrum, peaking at about 550 nm. The specific gravity of these glasses can also be made as high as 3.5, enhancing the interaction probability for X- or gamma rays. These terbium-activated glasses offer some attraction for the imaging of X-rays, where the emitted light is recorded using a position sensitive detector that integrates the light yield over the exposure period.

Some ceramic formulations[146] can also show good light yield, but most have decay times of hundreds of microseconds that are too long to be of interest in pulse mode spectroscopy. They have found current mode application in X-ray computed tomography where their brightness and lack of afterglow on the millisecond time scale are valuable properties.

G. Scintillator Gases

Certain high-purity gases can serve as useful scintillation detection media. Considerable experience has been gained for the noble gases, with xenon and helium receiving the most attention. The mechanism giving rise to the scintillation photons is relatively simple: The incident radiation or charged particle leaves a population of excited gas molecules in its wake as it passes through the scintillator. As these excited molecules return to their ground state, through a variety of different mechanisms, photons will be emitted. The emission spectra correspond to the *second continuum* spectra observed in rare gas discharges. The photons are emitted during the transition from the two lowest molecular excited states to the ground state and much of the scintillation emission lies in the ultraviolet region of the spectrum rather than in the visible.[†] As a result, photomultiplier tubes or photodiodes that are sensitive in the near-ultraviolet must be employed if the scintillations are to be detected directly. Alternatively, a small concentration of a second gas such as nitrogen may be added to shift the emission spectrum by absorbing the ultraviolet and reradiating the energy at a longer wavelength. Because of a variety of competing parallel modes of de-excitation, such as intermolecular collisions or internal quenching, the overall scintillation efficiency of gases is characteristically quite low. However, the transitions take place in a very short time, typically a few nanoseconds or less, and gas scintillators can be among the fastest of all radiation detectors.

In addition to their fast response, gas scintillators have the relative advantage of easily variable size, shape, and stopping power for incident radiations. They also tend to be unusually linear over wide ranges of particle energy and dE/dx. Their major disadvantage is the low light yield, which is, at best, over an order of magnitude below that of NaI(Tl) for equivalent particle energy loss. They have been widely applied in the spectroscopy of heavy ions, often with a pressurized active volume. Some scintillation properties of several noble gases are given in Table 8.4. Extensive reviews of gas scintillators can be found in Refs. 1 and 149, and some measurements of specific properties in Refs. 150–153.

Some noble gases when condensed as a cryogenic liquid or solid have also been observed to be quite efficient scintillators. Results have been reported[154–159] on liquid and solid argon, krypton, and xenon and also on liquid helium.[160] The emission spectra are peaked in the UV region around 150 nm. Experimental measurements of the absolute light yield in both liquid argon or liquid xenon show considerable variance, but it is evident that both liquids have relatively high scintillation efficiency. Typical results[161] show a yield of about 40,000 photons/MeV, comparable to that of NaI(Tl) at room temperature. Attenuation lengths for the scintillation light are observed[162] to be between 0.5 and 1.0 m in both liquids. There are obvious difficulties in efficiently collecting the scintillation light while the condensed gas is maintained at cryogenic temperature, and the collection efficiency can be inhibited by optical scattering from density variations in the liquid caused by temperature gradients near the light sensor or walls of the chamber.[163] Xenon in liquid or solid form has the most appeal as a potential gamma-ray detector because of its high atomic number of 54. Kubota et al.[158] present measurements of the decay time characteristics of these condensed gases, with all showing both fast and slow components with relative intensities that depend on the type of exciting particle. Values for the principal decay component range from 6 ns in condensed argon to about 30 ns in condensed xenon.

[†] There is some evidence[147] that Ne, Ar, Kr, and Xe also emit a significant scintillation component in the near-infrared region of the spectrum. By using a PM tube with extended long-wavelength response, this component in argon can be converted into pulses that are large enough to carry out alpha particle spectroscopy with a 5.1% energy resolution.[148]

Table 8.4 Properties of Gas Scintillators at Atmospheric Pressure

Gas	Mean Wavelength of Emission	Number of Photons with $\lambda > 200$ nm per 4.7 MeV Alpha Particle
Xenon	325 nm	3,700
Krypton	318 nm	2,100
Argon	250 nm	1,100
Helium	390 nm	1,100
Nitrogen (for comparison)	390 nm	800
NaI(Tl)	415 nm	41,000

Source: J. B. Birks, *The Theory and Practice of Scintillation Counting.* Copyright 1964 by Pergamon Press, Ltd. Used with permission.

H. Radiation Damage Effects in Inorganic Scintillators

All scintillation materials are subject to radiation damage effects when exposed over prolonged periods to high fluxes of radiation. The damage is most likely evidenced as a reduction in the transparency of the scintillator caused by the creation of color centers that absorb the scintillation light. In addition, there may also be interference with the processes that give rise to the emission of the scintillation light itself. Radiation exposures can also induce long-lived light emission in the form of phosphorescence that can be troublesome in some measurements. The damage effects are often observed to be rate dependent and will vary greatly with the type of radiation involved in the exposure. The effects are often at least partially reversible, with annealing taking place even at room temperature over hours or days following the exposure.

A comprehensive review has been published[164] of the effects of radiation damage in a number of common inorganic scintillators. It was found that the creation of color centers dominates over the damage to the scintillation mechanism in all of the scintillators studied (NaI(Tl), CsI(Tl), CsI, BaF_2, BGO, and $PbWO_4$). The damage in the alkali halides was observed to be closely coupled with the presence of oxygen contamination leading to the formation of hydroxyl species. On the other hand, in the oxide scintillators, the damage was found to be related to structural defects, such as oxygen vacancies in the crystalline lattice.

Because of the many variables such as dose rate, types of particle, energy of particle, and the presence or absence of oxygen or other impurities, it is difficult to quantify the exact radiation dose expected to produce measurable damage in specific circumstances. However, some rough numbers and relative sensitivities have been quoted.[165] Of the scintillation materials discussed in this chapter, the most sensitive appear to be the thallium-activated alkali halides for which exposures of 10 Gy can be significant. At the other extreme, evidence exists that GSO begins to show effects only at doses as high as 10^6 Gy. Between these extremes, roughly in order of increasing radiation resistance, are CsF, BGO, YAP, CeF_3, and BaF_2. Radiation damage in plastic scintillators was discussed earlier in this chapter.

III. LIGHT COLLECTION AND SCINTILLATOR MOUNTING

A. Uniformity of Light Collection

In any scintillation detector, one would like to collect the largest possible fraction of the light emitted isotropically from the track of the ionizing particle. Two effects arise in practical cases that lead to less than perfect light collection: optical self-absorption within the scintillator and losses at the scintillator surfaces. With the exception of very large scintillators (many centimeters in dimension) or rarely used scintillation materials (e.g., ZnS), self-absorption is usually not a significant loss mechanism. Therefore, the uniformity of light collection normally depends primarily on the conditions that exist at the interface between the scintillator and the container in which it is mounted.

The light collection conditions affect the energy resolution of a scintillator in two distinct ways. First, the statistical broadening of the response function discussed in Chapter 10 will worsen as the number of scintillation photons that contribute to the measured pulse is reduced. The best resolution can therefore be achieved only by collecting the maximum possible fraction of all photons emitted in the scintillation event. Second, the *uniformity* of the light collection will determine the variation in signal pulse amplitude as the position of the radiation interaction is varied throughout the scintillator. Perfect uniformity would ensure that all events depositing the same energy, regardless of where they occur in the scintillator, would give rise to the same mean pulse amplitude. With ordinary scintillators of a few centimeters in dimension, uniformity of light collection is seldom a significant contributor to the overall energy resolution. In larger scintillators, particularly those that are viewed along a thin edge, variations in light collection efficiency can often dominate the energy resolution.

Because the scintillation light is emitted in all directions, only a limited fraction can travel directly to the surface at which the photomultiplier tube or other sensor is located. The remainder, if it is to be collected, must be reflected one or more times at the scintillator surfaces. Two situations may prevail when the light photon reaches the surface, as illustrated in Fig. 8.14. If the angle of incidence θ is greater than the critical angle θ_c, total internal reflection will occur. If θ is less than θ_c, partial reflection (called *Fresnel* reflection) and partial transmission through the surface will occur. The fraction of reflected light drops to only a few percent when the angle of incidence is near zero. The critical angle θ_c is determined by the indices of refraction for the scintillation medium n_0 and the surrounding medium (often air) n_1:

$$\theta_c = \sin^{-1}\frac{n_1}{n_0} \tag{8.12}$$

To recapture the light that does escape from the surface, the scintillator is normally surrounded by a reflector at all surfaces except that at which the photomultiplier tube is mounted. Reflectors can be either *specular* or *diffuse*. A polished metallic surface will act as a specular reflector for which the angle of reflection equals the angle of incidence. Better results are usually obtained, however, with a diffuse reflector such as magnesium oxide or aluminum oxide. Here the angle of reflection is approximately independent of the angle of incidence and follows a distribution given by Lambert's law:

$$\frac{dI(\psi)}{dI_0} = \cos\psi \tag{8.13}$$

where ψ is the reflection angle with respect to the direction perpendicular to the surface. Commercially prepared sodium iodide crystals are normally reflected with dry MgO

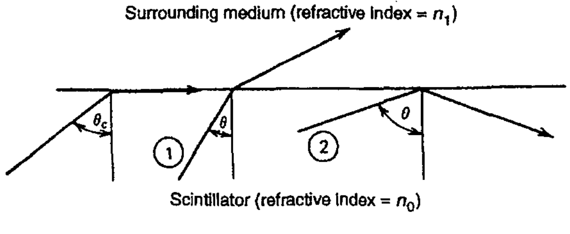

Figure 8.14 Conditions at the interface of dissimilar optical media ($n_0 > n_1$). Ray ① may escape, but ray ② will be internally reflected at the surface.

powder packed around surfaces of the crystal which have been slightly roughened with an abrasive. Plastic scintillators are usually left with a polished surface, especially when the light must be collected over large dimensions involving multiple reflections. White reflecting paint is easy to apply to scintillators but is an inferior reflector to dry powder. In custom-made scintillators, better results are usually obtained by spraying the surface with a slurry of magnesium oxide in water and allowing the layer to dry. In other circumstances, wrapping with white teflon tape and/or millipore filter paper[166] can also be effective.

Although total internal reflection is desirable at reflecting surfaces, it must be minimized at the surface from which the scintillator is viewed to prevent internal trapping of the light. Ideally, one would like to optically couple the scintillator to the photocathode of the PM tube through a transparent medium of the same index of refraction as the scintillator. Then Eq. (8.12) would predict no internal reflection and all light incident on the surface would be conducted into the glass end window of the PM tube on which the photocathode is deposited. The refractive indices of plastic, liquid, and glass scintillators are fairly close to that of the glass end window (about 1.5). In those cases, near-perfect coupling will be achieved if the interface between the scintillator and PM tube is filled with an optical coupling fluid of the same refractive index. Some internal reflection will inevitably occur for scintillators with a higher index (such as NaI or BGO), and a light photon will be reflected back into the scintillator if its angle of incidence is too large. The usefulness of scintillators with a very high refractive index is seriously hampered because of excessive internal trapping of the scintillation light. High-viscosity silicone oil is commonly used as the coupling agent between the scintillator and PM tube. Design of the scintillation detector must provide a means to prevent the long-term flow of the fluid away from the interface. If the detector will be subjected to severe temperature cycling or vibration, it is sometimes preferable to couple the scintillator with a transparent epoxy cement.

A simple test can be made of light-collecting uniformity by allowing a narrowly collimated gamma-ray beam to strike selected portions of a scintillation crystal. With a uniform surface treatment it is often found that those areas closest to the photocathode give rise to a larger pulse height because of more favorable light collection. In order to compensate for this natural tendency, the surface is often preferentially treated to enhance light collection from the points in the crystal farthest from the photocathode.

It is also possible to model the optical behavior and light collection efficiency in scintillators using Monte Carlo calculations.[167–170] These codes are based on computer modeling of the geometry and optical characteristics of the scintillator under study. Simulations are based on the generation of individual scintillation photons within the scintillator and tracking their fate as they propagate through the scintillator and interact with surfaces. Assumptions must be made about the optical absorption and scattering properties of the scintillator, the reflection and/or absorption characteristics of the surfaces, and the indices of refraction of all optical media through which the scintillation photons pass. These codes prove to be quite accurate in the prediction not only of the total fraction of light collected but also in studying the uniformity and time characteristics of the collected light.

Good light collection in the scintillator also requires that either a single crystal or single piece of plastic be used for the scintillating medium, or that special precautionary techniques be used in the event that separate pieces are cemented together. If separate pieces are used, the additional surfaces will often introduce added reflection and can seriously affect the overall uniformity of light collection. For materials that are difficult to grow in large single crystals, an alternative approach is to suspend granules of the material in a transparent matrix. Examples include the mixture of zinc sulfide powder in clear epoxy[171] or the suspension of barium fluoride powder in liquids.[172] In the ideal case, the indices of refraction of the two materials would be perfectly matched so that the mixture would remain optically clear to allow the propagation of the scintillation light over large distances. As a practical matter, it is very difficult to obtain a perfect match and the mixtures are normally limited to relatively thin layers. The index of refraction for any material is a function of the wavelength of the light, and even if a good match is made at a specific wavelength, it is unlikely that it will remain perfect over the entire emission spectrum of the scintillation material. Care must also be taken to avoid the inclusion of microscopic air bubbles that represent large local changes in refractive index.

Any scintillation counter must be shielded from ambient room light. For temporary arrangements not involving hygroscopic crystals, a simple wrapping of the reflected scintillator and photomultiplier tube with black paper, followed by a layer of the ubiquitous black tape, will often suffice. Commercial sodium iodide scintillation crystals are usually canned in a metallic container and must be hermetically sealed. The surface through which the light is to be collected is provided with a glass or quartz window. The opposite surface is covered with an opaque but thin metallic sheet to provide an entrance window for soft radiations. In cases in which the scintillation counter must be used in low background counting, special care must be given to the proper choice of materials used in contact with the crystal. Some types of glass, for example, are very high in potassium and as a result will generate a large background contribution from the natural ^{40}K activity.

Light collection in large scintillators can often be enhanced by the use of more than one photomultiplier tube. Although this is not usually an attractive option for routine use because of the added complexity, the gains that can be achieved are, in some cases, substantial. The average number of reflections required for a typical event to reach a photomultiplier tube will obviously be less if more than one escape surface is provided. The fewer the reflections, the greater the light collection efficiency, and consequently the greater uniformity of pulse height response. Because of the importance of self-absorption in large scintillators, there often is no substitute for multiple PM tubes in these cases.

More complete discussions of scintillator mounting and reflection are given by Birks[1] and Bell.[173] A useful review of light collection methods and surface properties has also been published by Keil.[174]

B. Light Pipes

It is often unadvisable or even impossible to couple a photomultiplier tube directly to one face of a scintillator. For example, the size or shape of the scintillator may not conveniently match the circular photocathode area of commercially available PM tubes. One solution is to place the unreflected scintillator near the center of a large box, whose interior surfaces are coated with a diffuse reflector. One or more PM tubes can then view the interior of the box to record some fraction of the light that eventually escapes from the scintillator. If the fraction of the box surface replaced by PM tubes is small and the reflectivity of the coating is high,[175] the light is thoroughly randomized before being detected. Very uniform light collection can therefore be achieved even for scintillators with complex or unusual shape. Because of inevitable light losses, however, the total fraction of light collected is typically small. Better light collection efficiency usually can be achieved by using a transparent solid, known as a *light pipe*, to physically couple the scintillator to the PM tube and to act as a guide for the scintillation light.

Light pipes also serve a useful purpose in other situations. If scintillation measurements are to be made in a strong magnetic field, the PM tube must be shielded from the field and this often implies its removal to a location some distance away from the scintillator. Very thin scintillators should not be mounted directly on the PM tube end window to avoid the pulse height variations that can arise due to photocathode nonuniformities. A light pipe between the thin scintillator and the PM tube will spread the light from each scintillation event over the entire photocathode to average out these nonuniformities and improve the pulse height resolution.

Light pipes operate on the principle of total internal reflection outlined in the previous section. They are generally optically transparent solids with a relatively high index of

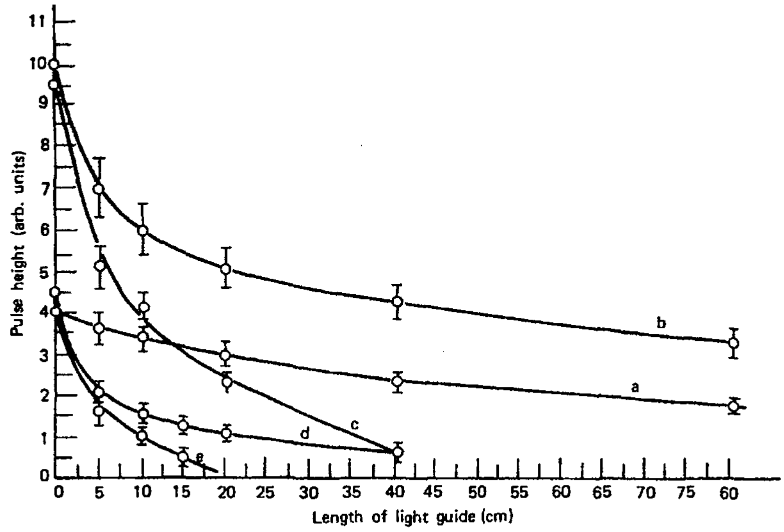

Figure 8.15 Variation of pulse height with length of light guide for various reflective wrappings. (*a*) Total internal reflection only, (*b*) total internal reflection with reflective covering, (*c*) surface of light guide painted with NE 560 reflector paint, (*d*) specular reflector without light guide, (*e*) diffuse reflector without light guide. (From Kilvington et al.[176])

refraction to minimize the critical angle for total internal reflection. Surfaces are highly polished and are often surrounded by a reflective wrapping to direct back some of the light that escapes at angles less than the critical angle. Lucite, with an index of refraction of 1.49–1.51, is the most widely used material and can easily be formed into complex shapes. A study of the effects of various surface and outer reflector arrangements with Lucite light pipes has been reported by Kilvington et al.,[176] and the data are summarized in Fig. 8.15.

For an isotropic light source located near the axis of a transparent cylindrical rod, the following approach can be used to estimate the fraction of light that will be conducted in one direction along the length of the rod by successive internal reflections. Each reflected ray will also pass near the cylinder axis, and these are called *meridional rays* in the discussion of scintillation fibers later in this chapter. In the sketch below, only the light emitted within the cone angle ϕ_c will be incident on the rod surface at the critical angle θ_c or greater and therefore undergoes total internal reflection. Because the angle of reflection equals the angle of incidence, subsequent arrivals of the reflected light at the rod surface will also be above the critical angle, and this light is therefore "piped" along the rod length as in an optical fiber. The fractional solid angle subtended by this angle ϕ_c is calculated as

$$F = \frac{\Omega}{4\pi} = \frac{1}{4\pi}\int_{\phi=0}^{\phi=\phi_c} d\Omega = \frac{1}{4\pi}\int_0^{\phi_c} 2\pi \sin\phi \, d\phi$$

$$= \tfrac{1}{2}(1 - \cos\phi_c) = \tfrac{1}{2}(1 - \sin\theta_c)$$

$$= \tfrac{1}{2}(1 - n_1/n_0) \qquad (8.14)$$

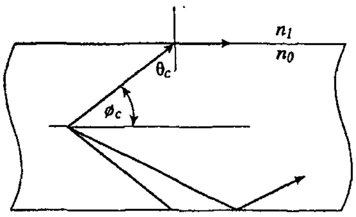

In a cylindrical rod of refractive index $n_0 = 1.5$ surrounded by air ($n_1 \cong 1$), Eq. (8.14) predicts that 16.7% of the isotropically generated light is piped in one direction. Another 16.7% is piped in the opposite direction and may be reflected back depending on the surface conditions at the end of the cylinder.

In slab geometry, the light that reaches a surface with incident angle θ greater than the critical angle θ_c will be trapped and conducted to the slab edges by total internal reflection. For rays with $\theta < \theta_c$, there is some possibility that Fresnel reflection will prevent escape at the first surface. However, then the ray is reflected back into the slab at an angle equal to its angle of incidence, and it arrives at the opposite surface again with $\theta < \theta_c$. Even if several Fresnel reflections happen to occur, eventually the ray will escape. Thus all rays that escape the slab are confined to a double ended cone with apex at the point of origin of the light, axis perpendicular to the slab surfaces, and a vertex angle of θ_c. The total escaping fraction of light is thus given by

$$E = 2\cdot\frac{\Omega}{4\pi} = \frac{1}{2\pi}\int_{\theta=0}^{\theta=\theta_c} d\Omega = \frac{1}{2\pi}\int_{0}^{\theta_c} 2\pi \sin\theta \, d\theta$$

$$= 1 - \cos\theta_c = 1 - \sqrt{1-\left(\frac{n_1}{n_0}\right)^2}$$

The fraction of light trapped in the slab is therefore

$$F = 1 - E = \sqrt{1-\left(\frac{n_1}{n_0}\right)^2} \tag{8.15}$$

For a slab with refractive index of 1.5 surrounded by air, this result predicts that 75% of the light is piped to the edges.

To maximize the fraction of light that is piped in either geometry, one wants the refractive index of the light pipe n_0 to be as large as possible. In reality, however, the light is generated inside the scintillator, not the light pipe, and it is usually the scintillator refractive index that determines the fraction of light collected. This is particularly true when the scintillator is long in the direction perpendicular to the viewing surface, and a typical scintillation photon is multiply reflected before collection. The scintillator then acts as its own light pipe between the point of scintillation and the exit surface.

For the simple case of a cylindrical scintillation crystal and tube of equal diameter, the light pipe can be a simple cylinder of the same diameter. More often, however, the light pipe cross section shape must vary along its length in order to serve as a smooth transition between the scintillator exit surface and the PM tube end window. No matter how complex the shape of a conventional light pipe may be, the flux of light photons per unit area per unit solid angle can never be greater at any point inside the pipe than at its input. Any light pipe whose cross-sectional area decreases from scintillator to PM tube will therefore result in some light loss. If the cross-sectional area is maintained constant and sharp bends are avoided, however, the pipe can theoretically transmit all the light that enters within the acceptance angle at the input end. Light pipes with this property are called *adiabatic*[177] and obviously require the use of a PM tube with a photocathode area at least as large as the scintillator exit surface.

In cases in which the edge of a thin but large-area scintillator is to be viewed, a unique arrangement known as the strip light guide has found widespread application. As shown in Fig. 8.16, the coupling is accomplished through a number of twisted strips that are aligned at the scintillator edge but converge to a more compact pattern at the photomultiplier end. The unit can easily be made from flat plastic strips, which are then bent following heating and formed to the required shape. Practical guides for these procedures are given by Dougan et al.[178] and Piroue.[179]

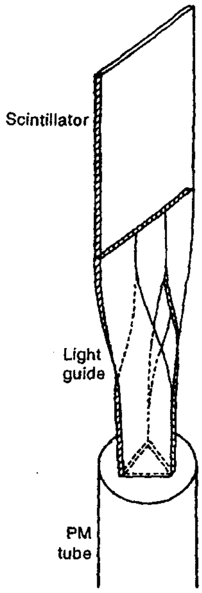

Figure 8.16 A strip light guide can be used to couple the edge of a large, flat scintillator to a PM tube.

C. Fiber Scintillators

1. GENERAL PROPERTIES

Some scintillation materials can also be fabricated as small diameter fibers in which a fraction of the scintillation light is conducted over substantial distance by total internal reflection. General reviews of scintillating fibers of this type are given in Refs. 180–182. As shown in Fig. 8.17, a common configuration consists of a core, in which the scintillation light is generated through interaction of the incident radiation, surrounded by a thin layer of cladding material. Both the core and the cladding are transparent materials, and the index of refraction of the core is higher than that of the cladding. Light rays that arrive at the core–cladding interface with an angle of incidence that is greater than the critical angle for total internal reflection are "piped" down the length of the fiber. In some cases, a light absorbing "extramural absorber" may be applied to the outer surface of the cladding to provide optical isolation.

For a typical core material with index of refraction of 1.58 surrounded by air, the index change would be large enough to pipe over a third of the light toward one end or the other. However, when a cladding material is added to protect the core surface from abrasion or accumulation of foreign material that would inhibit the light piping effect, then the index of refraction change is less pronounced and only 5 to 10% of the light is trapped. Some of

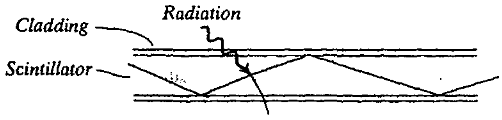

Figure 8.17 Cross section of a typical fiber scintillator. Some fraction of the emitted light is trapped by total internal reflection at the core-cladding interface.

the light escaping into the cladding can be trapped at the cladding–air interface, but this component generally represents a minor contribution because of the inferior optical quality of the outer surface due to inevitable scratching or contamination picked up during handling. Multiclad fibers consist of a core and two layers of cladding, with refractive indices that are sequentially lower for the inner and outer cladding materials. They provide two protected reflection surfaces, and tend to trap about 40% more light than comparable single-clad fibers.[183] Photomultiplier tubes can be used at both ends of the fiber to produce nearly coincident pulses from an interaction of a particle or photon. Alternatively, the light can be measured only at one end of the fiber while the opposite end is mirrored to reflect back as much as possible of the light that initially was trapped in the opposite direction.

2. *PLASTIC AND LIQUID CORE FIBERS*

Plastic scintillators are readily fabricated (e.g., Ref. 184) into fibers with round, square, or other cross-sectional shapes. The most common formulations are based on a core of polystyrene (refractive index $n = 1.58$) with a few percent of organic fluor. Common cladding materials are polymethylmethyacrylate ($n = 1.49$) or fluorinated polymethacrylate ($n = 1.42$).

The typical diameters of common plastic fibers range from a few tenths of a millimeter to several millimeters. For plastic fibers that are smaller in diameter, there is a decrease in the observed light yield due to inhibition of the energy transfer that must occur from the plastic matrix to the organic fluor molecules that are the actual source of the scintillation light. Typical of other plastic scintillators, the emission spectrum is generally peaked in the blue region, with decay times of 2 to 4 ns.

Many plastic fibers are fabricated from this type of two-component solution in which the organic fluor is distributed in a solid matrix. In order to achieve maximum light yield in small dimensions, a relatively high fluor concentration of several percent is normally used. Other plastic fibers consist of three-component systems in which a wavelength shifter is provided as an additional constituent. The wavelength shifter, typically another organic molecule, has the function of absorbing the primary scintillation fluorescence and re-emitting it at a longer wavelength. This spectral shift can reduce the amount of self-absorption that occurs as the light propagates along the length of the fiber.

A glass capillary tube filled with liquid organic scintillator can also function in much the same way as a fiber scintillator if there is a significant reduction in index of refraction from the liquid to the glass.[185–187] This approach exploits the good light yield[188] and fast decay time of liquid scintillators (similar to that of plastic scintillators), while also offering less susceptibility to radiation damage effects compared with plastics.[189] The excellent optical quality of the liquid–glass interface can result in a light loss that is as low as 10^{-6} per reflection,[190] and capillaries with inner diameter as small as 20 μm can have attenuation length (defined below) of up to 3 meters.[191]

Scintillating fibers are sometimes grouped together to form ribbons or bundles to suit various applications. Figure 8.18 shows a ribbon array in which two staggered layers of fibers are arranged so that an incident charged particle will nearly always pass through a substantial chord length in one of the fibers. Glass capillaries can also be easily fused together into bundles as illustrated in Fig. 8.19.

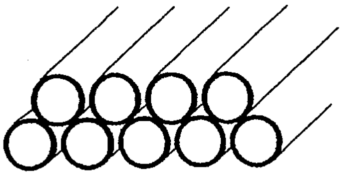

Figure 8.18 A double-layer ribbon made up of fiber scintillators. (From Baumbaugh et al.[192])

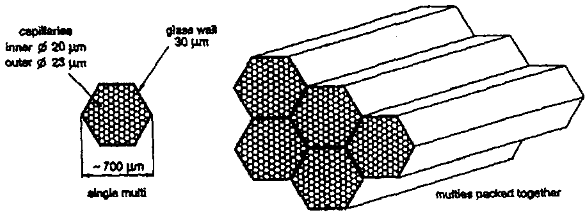

Figure 8.19 Glass capillaries fused into bundles (or "multies") and operated filled with liquid scintillator. (From Ferroni and Martellotti.[193])

3. GLASS FIBERS

The glass materials commonly used as scintillators can be easily drawn into small diameter fibers. A typical cerium activated glass scintillator will have an index of refraction of about 1.59. A cladding glass is then chosen with a lower index of refraction, normally around 1.51. If an extramural absorber is required by the application, it can be a coating of black glass or polymer material.

Glasses can be drawn down to fiber diameters as small as 10 μm without appreciable loss in the scintillation efficiency. The energy transfer required from the glass matrix to the activator sites occurs over much smaller distances than in plastics, so that the drop in scintillation efficiency for small diameter plastic fibers is not observed in glass. Compared with plastics, the absolute scintillation efficiency is lower in glasses, so the light yield is less, and the decay time of 50–80 ns is substantially longer. Glass fibers incorporating ^{6}Li as a constituent have proved to be useful in some specialized neutron detection applications.

Glass fibers can also be fused into bundles or large-diameter plates that have very different optical properties than bulk scintillators of the same outer dimension. Because the scintillation light is confined to the individual fiber in which it originated, the loss of spatial resolution caused by the spread of the light in a bulk scintillator is avoided. This property has been exploited in glass fiber plates for X-ray imaging,[194–196] particle tracking,[197] and neutron[198] imaging.

4. LIGHT CAPTURE FRACTION

For the most common type of fiber with a round cross section, the sketch in Fig. 8.20 shows two extremes of the geometric conditions that can hold for the emitted light. At one extreme, if the light is emitted at the exact axis of the fiber, the light consists of "meridional rays" that always pass through the fiber center axis even after many reflections. From

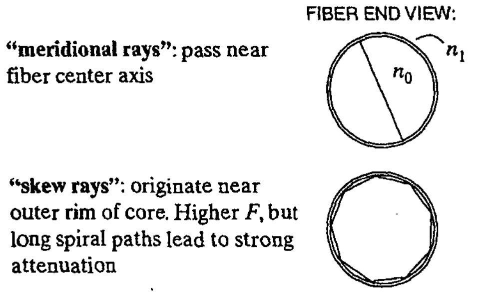

Figure 8.20 Sketch showing the distinction between "meridional rays" that originate near the axis of the fiber, and "skew rays" that represent a much longer transmission path through the fiber.

simple laws of optics [see Eq. (8.14)] one can then write an exact expression for the fraction of these rays that are captured in one direction by total internal reflection as

$$F = \frac{1}{2}\left(1 - \frac{n_1}{n_0}\right)$$

where n_1 and n_0 are the refractive indices of the cladding and core, respectively. For isotropic light emission, equal amounts are captured in both directions, so the total light capture fraction is double that given by the above expression. At the other extreme, light emitted near the outer diameter of the core will often travel a spiral path as it is propagated along the length of the fiber. These "skew rays" theoretically have a higher capture fraction, but in practice must undergo many more reflections at the core–cladding interface that tends to highly attenuate their propagation. The net result is that the actual capture fraction for uniformly distributed points of origin within a circular cross-section fiber is higher by perhaps 10 to 30% than that given by the expression above for meridional rays.

The limited trapping angle within the fiber also influences the timing properties of the signal derived from the light detected at the fiber end. In general, the spread in path lengths will be smaller than that observed for a bulk scintillator of the same length, by as much as a factor of 1.8 over a 2 m distance.[199] Because the variation of optical path lengths can be the limiting factor in the timing resolution of large scintillators, fibers can show superior timing properties under some conditions.

5. LIGHT YIELD AND PROPAGATION

The factors affecting scintillation light yield from plastic, liquid, and glass scintillators are discussed elsewhere in this chapter. Table 8.5 lists some typical values for the type of scintillation materials commonly used for fiber fabrication. These quoted yields are for low dE/dx particles such as fast electrons and will be lower for heavily ionizing particles such as recoil nuclei. As in normal scintillators, this light is emitted in all directions and only the fraction discussed earlier will be captured through total internal reflection.

The intensity of the scintillation light propagated along the length of the fiber is attenuated due to several effects:

1. Any imperfections at the core–cladding interface may disturb the total internal reflection.
2. Some of the scintillation light may be reabsorbed in the fiber due to overlap of the emission and absorption bands of the fluorescent species.
3. Rayleigh scattering from small density fluctuations in the core can deflect an optical ray so that it is no longer totally internally reflected.

The cumulative effect of these attenuation processes is often expressed as a quoted *attenuation length* for the fiber. If the attenuation probability per path length is constant,

Table 8.5 Typical Light Yield for Fiber Scintillators (for low dE/dx particles, in all directions, will be reduced by light capture fraction)

Core material	photons/keV	λ_{peak} (nm)
Glass scintillator	3–5	400
Plastic scintillator	8–10	420
Liquid scintillator	11–13	420
For comparison:		
NaI(Tl)	38	415

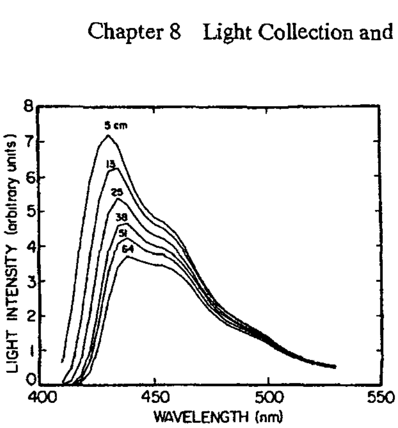

Figure 8.21 The spectrum of scintillation light after transmission through various lengths of fiber scintillator, showing the preferential absorption of the shorter wavelengths. (From Davis et al.[200])

one would expect the intensity of light I at a distance x from the original scintillation site to fall off exponentially as

$$\frac{I}{I_0} = e^{-x/L}$$

where I_0 is the intensity close to the site and L is the attenuation length. Typical values of L for fibers range from a few tens of centimeters to several meters.

The behavior actually observed in fibers often departs from this simple exponential behavior. One of the important causes of this deviation is the fact that the short wavelengths in the emission spectrum tend to be more readily reabsorbed than the long wavelengths. This effect is illustrated in Fig. 8.21 where the measured optical spectrum of the transmitted light is shown as a function of distance along the fiber. The average of the spectrum at large distances is shifted substantially toward the longer wavelengths due to the preferential absorption that occurs for the short wavelength components. The measured intensity of the light therefore is more likely to behave as shown in Fig. 8.22. Over short distances, the stronger absorption of the short wavelengths results in a smaller attenuation length, whereas the light that persists over longer distances is attenuated less and is characterized by a larger attenuation length.

Because of the limited energy loss of charged particles in small diameter fibers and the relatively low scintillation efficiency of organic and glass scintillators, the scintillation light generated under typical conditions in fibers is rather small. Furthermore, only a small fraction of this light is captured and piped successfully to the end of the fiber. Therefore, typical conditions may involve scintillation pulses consisting of no more than tens of photons or less. Thus, the pulses are often near the noise level of the measurement system and show relatively large event-to-event fluctuations because of the fundamental statistical fluctuations in the number of detected photons. Therefore, many applications involve using these pulses as simple indicators of the passage of a charged particle rather than in an attempt to

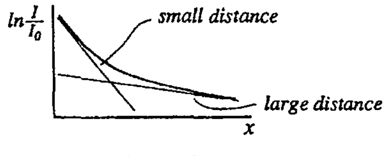

Figure 8.22 The total light transmitted by a fiber as a function of its length. The attenuation length is related to the slope of this plot, and the preferential absorption of the short wavelengths leads to smaller attenuation length for short fibers compared with longer ones.

accurately measure the deposited energy. Light sensors with the lowest possible noise level are important to be able to clearly distinguish the signal pulses under these demanding circumstances. Examples of successful fiber readout sensors include photomultiplier tubes (often the position-sensitive type[201]), avalanche photodiodes (see Chapter 9), and image intensifier tubes viewed by CCDs (see Chapter 11).

6. RADIATION DAMAGE

Fiber scintillators are subject to damage by high doses of radiation because of several effects. The material damage caused by radiation can lower the scintillation light yield and also affect the light absorption along the length of the fiber. Radiation-induced absorption centers tend to attenuate the blue end of the spectrum most severely. It has been observed[202,203] that exposures to gamma rays of about 10^3–10^4 Gy or fast neutron fluences of 10^{12} n/cm^2 can result in a significant lowering of the attenuation length of plastic fibers. There is some indication that liquid core glass capillaries may tolerate an order of magnitude or higher dose before the same effects are observed.[204]

As with the damage in conventional plastic scintillators discussed earlier, the magnitude of the effects in plastic fibers is strongly influenced by the nature of the radiation, the irradiation rate,[202] and the presence or absence of oxygen during the exposure.[205] A partial recovery of the scintillation yield following the exposure is usally observed that results from a slow annealing of the damage over times that may be a month or more at room temperature.

D. Wavelength Shifters

Light collection from large scintillators or complex geometries can sometimes be aided through the use of optical elements that employ *wavelength shifting* techniques. Many liquid or plastic scintillators routinely incorporate an organic additive whose function is to absorb the primary scintillation light and reradiate the energy at a longer wavelength. In that case, the objective is to better match the emission spectrum to the response peak of a photomultiplier tube. The same process can be used to help light collection by exploiting the fact that the reradiated light is emitted isotropically so that its direction bears no relation to the direction of the absorbed light. This feature allows the light to "turn corners" that would otherwise be impossible.

To illustrate, suppose that the primary scintillation light is generated within a large slab scintillator shown in Fig. 8.23. Rather than collect light from the edges of the slab, there are circumstances in which it may be preferable instead to couple the light to one or more cylindrical rods or optical fibers that run perpendicular to the slab surface. (Such could be the case, for example, if a large number of slabs were involved, and a few PM tubes were

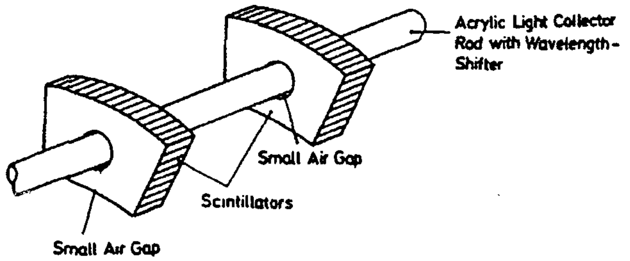

Figure 8.23 Sections of two slab scintillators are shown coupled to a common light pipe loaded with wavelength shifter. Light passing across the air gap and entering the pipe can be absorbed, reradiated, and guided to the ends of the rod. (From Eckardt et al.[206])

used at the ends of the rods to record light from all the slabs.) The rods would then be made of optically transparent material to act as light pipes. If the scintillator and rods have similar indices of refraction, it is very difficult to couple light efficiently from the slab to a perpendicular rod in optical contact. Light that is conducted by total internal reflection along the slab arrives at the rod at angles that are not favorable for subsequent internal reflection within the rod. Also, if other slabs are in optical contact with the rod, the light piping properties of the rod are no longer preserved.

A solution to both difficulties follows if the rod is doped with a wavelength shifter[207–210] and passed through the slab in an air-filled hole of slightly larger diameter (see Fig. 8.23). Now the index change is preserved over the entire surface of the rod, and it will therefore act as a near-ideal light pipe. Some fraction of the light from the slab that arrives at a hole may pass across the air gap and enter the rod. The doping level of the wavelength shifter is adjusted so that there is a good probability of absorption of the primary light within the rod. The reradiated light is now isotropic, and one-third or more will typically be piped along the length of the rod. The shifted wavelength is now away from the strong absorption bands of the dopant, so that further loss along the rod length can largely be avoided.

Since there are several inefficient steps in this example, the overall light collection efficiency of such a scheme cannot compare with that obtainable with a more direct coupling of the photomultiplier tube to the scintillator. In some applications, however, the scintillation light yield per event may be large enough to allow one to tolerate considerable loss in the collection process. In such cases, the added flexibility afforded by wavelength shifting techniques has led to successful applications in complex detector geometries[211] or in the compact readout of large-area scintillators.[212]

The same light collection principle can be applied using plastic fibers whose core contains a wavelength-shifting fluor. These can be single- or double-clad fibers that are very similar in structure to the scintillating fibers discussed earlier. For best light propagation along the fiber, one wants a large shift between the optical absorption and emission bands for the fluor so that minimal self-absorption takes place. The most common circumstance is for the fluor to absorb strongly in the blue portion of the spectrum (where most scintillation materials have prominent emission) and to re-emit green or yellow light. Under good conditions, the shifted light can be conducted over a meter or more of the fiber without excessive loss. For circumstances in which the light must be transmitted larger distances from the detector to the light sensor, a clear fiber with better light conduction can be matched to the primary fiber.[213] In some designs,[214,215] the wavelength-shifting fibers are positioned in grooves machined into the surface of the primary scintillation detector. Wavelength-shifting fibers can also be useful to collect the light emitted in other types of detectors, for example, for high-pressure gas proportional scintillation chambers[216,217] where direct viewing with a light sensor may not be convenient.

One of the important properties is the quantum efficiency of the wavelength shifter, or the probability that a wavelength-shifted photon will be emitted per absorbed photon. This efficiency can be as high as 90% for some organic fluors, but it is more typically[218–220] in the range of 70–80%. High quantum efficiencies are obviously needed to preserve the statistical information carried by the number of original photons.

Another important property is the decay time of the wavelength-shifting molecules. The absorption and re-radiation of the primary scintillation light can substantially slow the light emission if the lifetime of the wavelength shifting excited states is comparable with or longer than that of the primary fluor. For example, in the wavelength shifter known as *K27* (a green-emitting fluor), the decay time is 12 ns. Because this time is much longer than the 2–4 ns decay time of typical organic fluors, the time characteristics of the collected light are now dominated by the wavelength shifter rather than the primary scintillator. For critical timing situations, faster wavelength shifters can be chosen.

PROBLEMS

8.1 Calculate the scintillation efficiency of anthracene if 1 MeV of particle energy loss creates 20,300 photons with average wavelength of 447 nm.

8.2 Assuming a decay constant of 230 ns, how much time is required for a NaI(Tl) scintillation event to emit 99% of the total light yield?

8.3 Assuming that the scintillation light pulse in each case is a pure exponential, find the ratio of the maximum brightness (rate of photon emission) of pulses generated by equal electron energy deposition in NaI(Tl) and anthracene.

8.4 Make a selection between a typical inorganic scintillator [say, NaI(Tl)] and a typical organic (say, a plastic scintillator) on the basis of the following properties:

- **(a)** Speed of response.
- **(b)** Light output.
- **(c)** Linearity of light with deposited energy.
- **(d)** Detection efficiency for high-energy gamma rays.
- **(e)** Cost.

8.5 Explain the function of the activator added in trace quantities to many inorganic scintillators. Why are they not needed in organic scintillators?

8.6 Which scintillation material is most efficient at converting the energy of a 2 MeV electron into light?

8.7 Explain the following statement: Organic crystalline scintillators remain good energy-to-light converters when dissolved in a solvent, while inorganics no longer function as scintillators if dissolved.

8.8 Scintillation light is emitted isotropically within a slab of plastic scintillator (see Table 8.1). If the other dimensions of the slab are assumed to be infinite, calculate the fraction of the light that escapes from either slab surface.

8.9 The dark-adapted human eye may be able to detect as few as 10 visible photons as a single flash. Will an observer with pupil diameter of 3 mm be able to see individual scintillation events caused by a 1 MeV beta particle in NaI(Tl) while viewing the surface of the scintillator at a distance of 10 cm?

8.10 **(a)** A 1 MeV fast electron passes across the 0.3 mm diameter of a plastic fiber scintillator. From the data given in Chapter 2, estimate the deposited energy.

(b) Assuming a reasonable scintillation efficiency, calculate the corresponding number of scintillation photons created along the track.

(c) The refractive index for the core and the cladding are 1.58 and 1.49, respectively, and the fiber has an attenuation length of 2 m. Estimate the number of scintillation photons arriving at one end of the fiber that is 1 m from the point of interaction.

REFERENCES

1. J. B. Birks, *The Theory and Practice of Scintillation Counting*, Pergamon Press, Oxford, 1964.
2. *Selected Papers on Phosphors, LEDs, and Scintillators*, M. J. Weber, ed., SPIE Optical Engineering Press, Bellingham, Washington, 1998.
3. J. B. Birks and R. W. Pringle, *Proc. R. Soc. Edinburgh Sect. A* **70**, 233 (1972).
4. D. B. Oliver and G. F. Knoll, *IEEE Trans. Nucl. Sci.* **NS-15**(3), 122 (1968).
5. C. Zorn et al., *IEEE Trans. Nucl. Sci.* **37**(2), 487 (1990).
6. J. K. Walker, *Nucl. Instrum. Meth.* **68**, 131 (1969).
7. A. D. Bross and A. Pla-Dalmau, *IEEE Trans. Nucl. Sci.* **39**(5), 1199 (1992).
8. E. Biagtan, E. Goldberg, J. Harmon, and R. Stephens, *Nucl. Instrum. Meth.* **B93**, 296 (1994).
9. V. G. Vasil'chanko et al., *Nucl. Instrum. Meth.* **A369**, 55 (1996).
10. E. Biagtan et al., *Nucl. Instrum. Meth.* **B108**, 125 (1996).
11. V. G. Senchishin et al., *Nucl. Instrum. Meth.* **A364**, 253 (1995).
12. G. Bendiscioli et al., *Nucl. Instrum. Meth.* **206**, 471 (1983).
13. M. L. Muga, D. J. Burnsed, and W. E. Steeger, *Nucl. Instrum. Meth.* **104**, 605 (1972).
14. N. N. Ajitanand and K. N. Iyengar, *Nucl. Instrum. Meth.* **133**, 71 (1976).
15. H. Geissel et al., *Nucl. Instrum. Meth.* **144**, 465 (1977).
16. C. Manduchi, M. T. Russo-Manduchi, and G. F. Segato, *Nucl. Instrum. Meth.* **A243**, 453 (1986).
17. E. Norbeck, T. P. Dubbs, and L. G. Sobotka, *Nucl. Instrum. Meth.* **A262**, 546 (1987).
18. L. W. Weathers and M. B. Tsang, *Nucl. Instrum. Meth.* **A381**, 567 (1996).
19. F. D. Brooks, W. A. Cilliers, and M. S. Allie, *Nucl. Instrum. Meth.* **A240**, 338 (1985).
20. T. Batsch and M. Moszynski, *Nucl. Instrum. Meth.* **125**, 231 (1975).
21. J. W. Kohl, *Nucl. Instrum. Meth.* **125**, 413 (1975).
22. K. Ettling and W. Von Witsch, *Nucl. Instrum. Meth.* **148**, 299 (1978).
23. G. Bendiscioli, V. Filippini, C. Marciano, A. Rotondi, and A. Zenoni, *Nucl. Instrum. Meth.* **227**, 478 (1984).
24. A. Galindo-Uribarri et al., *Nucl. Instrum. Meth.* **A301**, 457 (1991).
25. Z. Youxiong et al., *Nucl. Instrum. Meth.* **A355**, 464 (1995).
26. L. Muga, *Nucl. Instrum. Meth.* **124**, 541 (1975).
27. M. L. Muga and J. D. Bridges, *Nucl. Instrum. Meth.* **134**, 143 (1976).
28. I. Kanno and T. Nakagome, *Nucl. Instrum. Meth.* **A251**, 108 (1986).

29. I. Kanno and T. Nakagome, *Nucl. Instrum. Meth.* **A244**, 551 (1986).
30. T. Batsch and M. Moszynski, *Nucl. Instrum. Meth.* **123**, 341 (1975).
31. C. B. Ashford, I. B. Berlman, J. M. Flournoy, L. A. Franks, S. G. Iversen, and S. S. Lutz, *Nucl. Instrum. Meth. Phys. Res.* **A243**, 131 (1986).
32. Z. H. Cho, I. Ahn, and C. M. Tsai, *IEEE Trans. Nucl. Sci.* **NS-21**(1), 218 (1974).
33. L. A. Eriksson, C. M. Tsai, Z. H. Cho, and C. R. Hurlbut, *Nucl. Instrum. Meth.* **122**, 373 (1974).
34. Z. H. Cho, C. M. Tsai, and L. A. Eriksson, *IEEE Trans. Nucl. Sci.* **NS-22**(1), 72 (1975).
35. E. Brannon and G. L. Olde, *Radiat. Res.* **16**, 1 (1962).
36. R. L. Craun and D. L. Smith, *Nucl. Instrum. Meth.* **80**, 239 (1970).
37. M. Hirschberg et al., *IEEE Trans. Nucl. Sci.* **39(4)**, 511 (1992).
38. D. L. Smith, R. G. Polk, and T. G. Miller, *Nucl. Instrum. Meth.* **64**, 157 (1968).
39. J. B. Czirr, *Nucl. Instrum. Meth.* **25**, 106 (1963).
40. K. H. Maier and J. Nitschke, *Nucl. Instrum. Meth.* **59**, 227 (1968).
41. D. Clark, *Nucl. Instrum. Meth.* **117**, 295 (1974).
42. N. A. Weir, *Int. J. Appl. Radiat. Isotopes* **23**, 371 (1972).
43. A. Raviart and V. Koechlin, *Nucl. Instrum. Meth.* **29**, 45 (1964).
44. F. J. Lynch, *IEEE Trans. Nucl. Sci.* **NS-15**(3), 102 (1968).
45. B. Bengtson and M. Moszynski, *Nucl. Instrum. Meth.* **117**, 227 (1974).
46. T. M. Kelly, J. A. Merrigan, and R. M. Lambrecht, *Nucl. Instrum. Meth.* **109**, 233 (1973).
47. P. B. Lyons and J. Stevens, *Nucl. Instrum. Meth.* **114**, 313 (1974).
48. F. J. Lynch, *IEEE Trans. Nucl. Sci.* **NS-22**(1), 58 (1975).
49. S. Sanyal, S. C. Pancholi, and S. L. Gupta, *Nucl. Instrum. Meth.* **136**, 157 (1976).
50. P. B. Lyons, C. R. Hurlbut, and L. P. Hocker, *Nucl. Instrum. Meth.* **133**, 175 (1976).
51. P. B. Lyons et al., *IEEE Trans. Nucl. Sci.* **NS-24**(1), 177 (1977).
52. K. G. Tirsell et al., *IEEE Trans. Nucl. Sci.* **NS-24**(1), 250 (1977).
53. M. Kurata et al., *Nucl. Instrum. Meth.* **A349**, 447 (1994).
54. S. Albergo et al., *Nucl. Instrum. Meth.* **A362**, 423 (1995).
55. X. H. Yang et al., *Nucl. Instrum. Meth.* **A354**, 270 (1995).
56. M. Moszynski and B. Bengtson, *Nucl. Instrum. Meth.* **142**, 417 (1977).
57. B. Sipp and J. A. Miehe, *Nucl. Instrum. Meth.* **114**, 255 (1974).
58. M. Bantel et al., *Nucl. Instrum. Meth.* **226**, 394 (1984).
59. P. Harihar et al., *Nucl. Instrum. Meth.* **A336**, 176 (1993).
60. L. M. Bollinger and G. E. Thomas, *Rev. Sci. Instrum.* **32**, 1044 (1961).
61. T. G. Miller, *Nucl. Instrum. Meth.* **63**, 121 (1968).
62. J. B. Czirr, *Nucl. Instrum. Meth.* **88**, 321 (1970).
63. R. A. Winyard and G. W. McBeth, *Nucl. Instrum. Meth.* **98**, 525 (1972).
64. D. B. C. B. Syme and G. I. Crawford, *Nucl. Instrum. Meth.* **104**, 245 (1972).
65. I. B. Berlman and O. J. Steingraber, *Nucl. Instrum. Meth.* **108**, 587 (1973).
66. M. Ahmed, *Nucl. Instrum. Meth.* **143**, 255 (1977).
67. M. Moszynski et al., *Nucl. Instrum. Meth.* **A317**, 262 (1992).
68. M. Moszynski et al., *Nucl. Instrum. Meth.* **A350**, 226 (1994).
69. G. Ranucci, A. Goretti, and P. Lombardi, *Nucl. Instrum. Meth.* **A412**, 374 (1998).
70. R. B. Murray, *IEEE Trans. Nucl. Sci.* **NS-22**(1), 54 (1975).
71. R. G. Kaufman, W. B. Hadley, and H. N. Hersh, *IEEE Trans. Nucl. Sci.* **NS-17** (3), 82 (1970).
72. C. L. Melcher et al., *IEEE Trans. Nucl. Sci.* **NS-32**(1), 529 (1985).
73. E. V. Sysoeva, V. A. Tarasov, O. V. Zelenskaya, and V. A. Sulga, *Nucl. Instrum. Meth.* **A414**, 274 (1998).
74. E. Sakai, *IEEE Trans. Nucl. Sci.* **NS-34**(1), 418 (1987).
75. I. Holl, E. Lorenz, and G. Mageras, *IEEE Trans. Nucl. Sci.* **35**(1), 105 (1988).
76. W. W. Moses and S. E. Derenzo, *IEEE Trans. Nucl. Sci.* **36(1)**, 173 (1989).
77. S. Brollo, G. Zanella, and R. Zannoni, *Nucl. Instrum. Meth.* **A293**, 601 (1990).
78. M. Moszynski et al., *IEEE Trans. Nucl. Sci.* **44(3)**, 1052 (1997).
79. R. Hofstadter, *Phys. Rev.* **74**, 100 (1948).
80. W. Mengesha, T. D. Taulbee, B. D. Rooney, and J. D. Valentine, *IEEE Trans. Nucl. Sci.* **45(3)**, 456 (1998).
81. S. Koicki, A. Koicki, and V. Ajdacic, *Nucl. Instrum. Meth.* **108**, 297 (1973).
82. C. F. G. Delaney and A. M. Lamki, *Int. J. Appl. Radiat. Isotopes* **19**, 169 (1968).
83. J. S. Schweitzer and W. Ziehl, *IEEE Trans. Nucl. Sci.* **NS-30**(1), 380 (1983).
84. C. J. Crannell, R. J. Kurz, and W. Viehmann, *Nucl. Instrum. Meth.* **115**, 253 (1974).
85. S. Usuda, A. Mihara, and H. Abe, *Nucl. Instrum. Meth.* **A321**, 247 (1992).
86. M. Moszynski et al., *Nucl. Instrum. Meth.* **A336**, 587 (1993).
87. B. Ye et al., *Nucl. Instrum. Meth.* **A345**, 115 (1994).
88. V. V. Nagarkar et al., *IEEE Trans. Nucl. Sci.* **45(3)**, 492 (1998).
89. T. Jing et al., *IEEE Trans. Nucl. Sci.* **39(5)**, 1195 (1992).
90. J. D. Valentine, D. K. Wehe, G. F. Knoll, and C. E. Moss, *IEEE Trans. Nucl. Sci.* **40(4)**, 1267 (1993).
91. J. D. Valentine et al., *Nucl. Instrum. Meth.* **A325**, 147 (1993).
92. S. Keszthelyi-Landori and G. Hrehuss, *Nucl. Instrum. Meth.* **68**, 9 (1969).
93. P. E. Francois and D. T. Martin, *Int. J. Appl. Radiat. Isotopes* **21**, 687 (1970).
94. M. Moszynski et al., *Nucl. Instrum. Meth.* **188**, 403 (1981).
95. M. J. Weber and R. R. Monchamp, *J. Appl. Phys.* **44**, 5495 (1973).
96. R. G. L. Barnes et al., *IEEE Trans. Nucl. Sci.* **NS-31**(1), 249 (1984).
97. C. L. Melcher, *Nucl. Instrum. Meth.* **B40/41**, 1214 (1989).
98. M. Kobayashi, M. Ishii, Y. Usuki, and H. Yahagi, *Nucl. Instrum. Meth.* **A349**, 407 (1994).
99. D. R. Kinloch, W. Novak, P. Raby, and I. Toepke, *IEEE Trans. Nucl. Sci.* **41(4)**, 752 (1994).
100. T. Fazzini et al., *Nucl. Instrum. Meth.* **A410**, 213 (1998).
101. S. Ph. Burachas et al., *Nucl. Instrum. Meth.* **A369**, 164 (1996).
102. M. Laval et al., *Nucl. Instrum. Meth.* **206**, 169 (1983).
103. K. Wisshak and F. Kaeppeler, *Nucl. Instrum. Meth.* **227**, 91 (1984).
104. Y. C. Zhu et al., *Nucl. Instrum. Meth.* **A244**, 577 (1986).
105. H. J. Karwowski et al., *Nucl. Instrum. Meth.* **A245**, 207 (1986).
106. M. R. Farukhi and C. F. Swinehart, *IEEE Trans. Nucl. Sci.* **NS-18**(1), 200 (1971).
107. P. Schotanus et al., *Nucl. Instrum. Meth.* **A238**, 564 (1985).
108. P. Schotanus et al., *Nucl. Instrum. Meth.* **A259**, 586 (1987).
109. P. Dorenbos et al., *IEEE Trans. Nucl. Sci.* **40(4)**, 424 (1993).
110. M. Moszynski et al., *Nucl. Instrum. Meth.* **226**, 534 (1984).

111. H. Mach, R. L. Gill and M. Moszynski, *Nucl. Instrum. Meth.* **A280**, 49 (1989).
112. R. Novotny, *IEEE Trans. Nucl. Sci.* **38(2)**, 379 (1991).
113. S. Kubota, S. Sakuragi, S. Hashimoto, and J. Ruan (Gen), *Nucl. Instrum. Meth.* **A268**, 275 (1988).
114. S. Keszthelyi-Landori et al., *Nucl. Instrum. Meth.* **A303**, 374 (1991).
115. P. Schotanus, R. Kamermans, and P. Dorenbos, *IEEE Trans. Nucl. Sci.* **37(2)**, 177 (1990).
116. D. F. Anderson, *Nucl. Instrum. Meth.* **A287**, 606 (1990).
117. E. Auffray et al., *Nucl. Instrum. Meth.* **A383**, 367 (1996).
118. C. W. E. van Eijk, *Nucl. Instrum. Meth.* **A392**, 285 (1997).
119. H. Ishibashi et al., *IEEE Trans. Nucl. Sci.* **45(3)**, 518 (1998).
120. M. Tanaka et al., *Nucl. Instrum. Meth.* **A404**, 283 (1998).
121. S. Nakayama et al., *Nucl. Instrum. Meth.* **A404**, 34 (1998).
122. M. Kobayashi and M. Ishii, *Nucl. Instrum. Meth.* **B61**, 491 (1991).
123. S. Baccaro et al., *Nucl. Instrum. Meth.* **A361**, 209 (1995).
124. M. Kapusta, J. Pawelke, and M. Moszynski, *Nucl. Instrum. Meth.* **A404**, 413 (1998).
125. M. Moszynski et al., *Nucl. Instrum. Meth.* **A404**, 157 (1998).
126. A. Del Guerra, G. Di Domenico, R. Pani, and G. Zavattini, *IEEE Trans. Nucl. Sci.* **44(6)**, 2415 (1997).
127. M. Moszynski et al., *Nucl. Instrum. Meth.* **A345**, 461 (1994).
128. T. Ludziejewski et al., *Nucl. Instrum. Meth.* **A398**, 287 (1997).
129. C. L. Melcher and J. S. Schweitzer, *Nucl. Instrum. Meth.* **A314**, 212 (1992).
130. T. Ludziejewski et al., *IEEE Trans. Nucl. Sci.* **42(4)**, 328 (1995).
131. P. Dorenbos et al., *IEEE Trans. Nucl. Sci.* **41(4)**, 735 (1994).
132. H. Suzuki, T. A. Tombrello, C. L. Melcher, and J. S. Schweitzer, *IEEE Trans. Nucl. Sci.* **40(4)**, 380 (1993).
133. A. Lempicki and J. Glodo, *Nucl. Instrum. Meth.* **A416**, 333 (1998).
134. M. Moszynski et al., *Nucl. Instrum. Meth.* **A385**, 123 (1997).
135. W. W. Moses et al., *IEEE Trans. Nucl. Sci.* **42(4)**, 275 (1995).
136. A. Lempicki et al., *IEEE Trans. Nucl. Sci.* **42(4)**, 280 (1995).
137. A. Lampicki et al., *IEEE Trans. Nucl. Sci.* **43(3)**, 1316 (1996).
138. K. S. Shah, P. Bennett, and M. R. Squillante, *IEEE Trans. Nucl. Sci.* **43(3)**, 1267 (1996).
139. C. Dujardin et al., *IEEE Trans. Nucl. Sci.* **45(3)**, 467 (1998).
140. M. Kapusta, M. Balcerzyk, M. Moszynski, and J. Pawelke, *Nucl. Instrum. Meth.* **A421**, 610 (1999).
141. L. M. Bollinger, G. E. Thomas, and R. J. Ginther, *Nucl. Instrum. Meth.* **17**, 97 (1962).
142. A. D. Bross, *Nucl. Instrum. Meth.* **A247**, 319 (1986).
143. A. W. Dalton, *Nucl. Instrum. Meth.* **A259**, 545 (1987).
144. A. W. Dalton, *Nucl. Instrum. Meth.* **A254**, 361 (1987).
145. P. Pavan, G. Zanella, R. Zannoni, and P. Polato, *Nucl. Instrum. Meth.* **B61**, 487 (1991).
146. C. Greskhovich and S. Duclos, *Annu. Rev. Mater. Sci.* **27**, 69 (1997).
147. P. Lindblom and O. Solin, *Nucl. Instrum. Meth.* **A268**, 204 (1988).
148. P. Lindblom and O. Solin, *Nucl. Instrum. Meth.* **A268**, 212 (1988).
149. M. Mutterer, *Nucl. Instrum. Meth.* **196**, 73 (1982).
150. M. Mutterer, J. Pannicke, K. Scheele, W. Spreng, J. P. Theobald, and P. Wastyn, *IEEE Trans. Nucl. Sci.* **NS-27**(1), 184 (1980).
151. M. Suzuki, J. Ruangen, and S. Kubota, *Nucl. Instrum. Meth.* **192**, 565 (1982).
152. M. Suzuki, *Nucl. Instrum. Meth.* **215**, 345 (1983).
153. P. Grimm, F.-J. Hambsch, M. Mutterer, J. P. Theobald, and S. Kubota, *Nucl. Instrum. Meth.* **A262**, 394 (1987).
154. P. Belli et al., *Nucl. Instrum. Meth.* **A310**, 150 (1991).
155. M. Miyajima, S. Sasaki, H. Tawara, and E. Shibamura, *IEEE Trans. Nucl. Sci.* **39(4)**, 536 (1992).
156. R. van Sonsbeck, C. W. E. van Eijk, and R. W. Hollander, *Nucl. Instrum. Meth.* **A367**, 362 (1995).
157. J. Seguinot, J. Tischhauser, and T. Ypsilantis, *Nucl. Instrum. Meth.* **A354**, 280 (1995).
158. S. Kubota et al., *Nucl. Instrum. Meth.* **196**, 101 (1982).
159. W. Baum, S. Götz, H. Heckwolf, P. Heeg, M. Mutterer, and J. P. Theobald, *IEEE Trans. Nucl. Sci.* **35**(1), 102 (1988).
160. A. Helaly et al., *Nucl. Instrum. Meth.* **A241**, 169 (1985).
161. T. Doke, K. Masuda, and E. Shibamura, *Nucl. Instrum. Meth.* **A291**, 617 (1990).
162. N. Ishida et al., *Nucl. Instrum. Meth.* **A384**, 380 (1997).
163. N. Ishida et al., *Nucl. Instrum. Meth.* **A327**, 152 (1993).
164. R. Zhu, *Nucl. Instrum. Meth.* **A413**, 297 (1998).
165. M. Ishii and M. Kobayashi, *Prog. in Crystal Growth and Char. of Mat.* **23(1-4)**, 245 (1992).
166. F. Tonetto el al., *Nucl. Instrum. Meth.* **A420**, 181 (1999).
167. J. Bea et al., *Nucl. Instrum. Meth.* **A350**, 184 (1994).
168. V. A. Baranov, V. V. Filchenkov, A. D. Konin, and V. V. Zhuk, *Nucl. Instrum. Meth.* **A374**, 335 (1996).
169. C. E. Ordonez, W. Chang, J. Liu, and D. Gunter, *IEEE Trans. Nucl. Sci.* **44(3)**, 1237 (1997).
170. D. Vozza, C. Moisan, and S. Paquet, *IEEE Trans. Nucl. Sci.* **44(2)**, 179 (1997).
171. S. A. McElhaney, J. A. Ramsey, M. L. Bauer, and M. M. Chiles, *Nucl. Instrum. Meth.* **A299**, 111 (1990).
172. D. R. Winn and M. Whitmore, *IEEE Trans. Nucl. Sci.* **36(1)**, 256 (1989).
173. P. R. Bell, "The Scintillation Method," in *Beta- and Gamma-Ray Spectroscopy* (K. Siegbahn, ed.), Elsevier-North Holland, Amsterdam, 1955.
174. G. Keil, *Nucl. Instrum. Meth.* **87**, 111 (1970).
175. S. P. Ahlen, B. G. Cartwright, and G. Tarle, *Nucl. Instrum. Meth.* **143**, 513 (1977).
176. A. I. Kilvington, C. A. Baker, and P. Illinesi, *Nucl. Instrum. Meth.* **80**, 177 (1970).
177. R. L. Garwin, *Rev. Sci. Instrum.* **23**, 755 (1952).
178. P. Dougan, T. Kivikas, K. Lugner, W. Ramsay, and W. Stiefler, *Nucl. Instrum. Meth.* **78**, 317 (1970).
179. P. A. Piroue, Conference on Instrumentation Techniques in Nuclear Pulse Analysis, National Academy of Sciences, National Research Council Publication 1184 (Nuclear Science Series Report #40) 1964.
180. T. O. White, *Nucl. Instrum. Meth.* **A273**, 820 (1988).
181. R. Ruchti, Nuclear Physics B (Proc. Suppl.) **44**, 308 (1995).
182. H. Leutz, *Nucl. Instrum. Meth.* **A364**, 422 (1995).
183. A. P. Ivashkin, Yu. G. Kudenko, O. V. Mineev, and J. Imazato, *Nucl. Instrum. Meth.* **A394**, 321 (1997).
184. Ph. Rebourgeard et al., *Nucl. Instrum. Meth.* **A427**, 543 (1999).
185. S. V. Golovkin et al., *Nucl. Instrum. Meth.* **A305**, 385 (1991).
186. M. Adinolfi et al., *Nucl. Instrum. Meth.* **A315**, 177 (1992).
187. P. Annis et al., *Nucl. Instrum. Meth.* **A367**, 377 (1995).
188. A. Cardini et al., *Nucl. Instrum. Meth.* **A361**, 129 (1995).
189. S. V. Golovkin et al., *Nucl. Instrum. Meth.* **A362**, 283 (1995).
190. P. Annis et al., *Nucl. Instrum. Meth.* **A386**, 72 (1997).
191. S. Buontempo et al., *Nucl. Instrum. Meth.* **A360**, 7 (1995).
192. B. Baumbaugh et al., *Nucl. Instrum. Meth.* **A345**, 271 (1994).

193. F. Ferroni and G. Martellotti, *Nucl. Instrum. Meth.* **A368**, 224 (1995).
194. H. Shao, D. W. Miller and C. R. Pearsall, *IEEE Trans. Nucl. Sci.* **38(2)**, 845 (1991).
195. P. Ottonello, G. A. Rottigni, G. Zanella, and R. Zannoni, *Nucl. Instrum. Meth.* **A323**, 485 (1992).
196. G. Gennaro, M. Malvestio, G. Zanella, and R. Zannoni, *Nucl. Instrum. Meth.* **A382**, 567 (1996).
197. C. D'Ambrosio, H. Leutz, T. Shimizu, and O. Shinji, *Nucl. Instrum. Meth.* **A325**, 161 (1993).
198. P. L. Reeder et al., *Nucl. Instrum. Meth.* **A402**, 155 (1998).
199. M. Kuhlen et al., *Nucl. Instrum. Meth.* **A301**, 223 (1991).
200. A. J. Davis et al., *Nucl. Instrum. Meth.* **A276**, 347 (1989).
201. V. Agoritsas et al., *Nucl. Instrum. Meth.* **A357**, 78 (1995).
202. K. Wick et al., *Nucl. Instrum. Meth.* **B61**, 472 (1991).
203. A. Murakami, H. Yoshinaka, and M. Goto, *IEEE Trans. Nucl. Sci.* **40(4)**, 495 (1993).
204. A. Cardini et al., *Nucl. Instrum. Meth.* **A346**, 163 (1994).
205. K. G. Young et al., *IEEE Trans. Nucl. Sci.* **40(4)**, 461 (1993).
206. V. Eckardt et al., *Nucl. Instrum. Meth.* **155**, 389 (1978).
207. W. Selove, W. Kononenko, and B. Wilsker, *Nucl. Instrum. Meth.* **161**, 233 (1979).
208. W. Viehmann and R. L. Frost, *Nucl. Instrum. Meth.* **167**, 405 (1979).
209. W. Kononenko, W. Selove, and G. E. Theodosiou, *Nucl. Instrum. Meth.* **206**, 91 (1983).
210. C. Aurouet et al., *Nucl. Instrum. Meth.* **211**, 309 (1983).
211. V. I. Kryshkin and A. T. Ronzhin, *Nucl. Instrum. Meth.* **A247**, 583 (1986).
212. G. Keil, *Nucl. Instrum. Meth.* **83**, 145 (1970).
213. T. Asakawa et al., *Nucl. Instrum. Meth.* **A340**, 458 (1994).
214. K. Hara et al., *Nucl. Instrum. Meth.* **A365**, 370 (1995).
215. D. V. H. Bengis and R. M. Sealock, *IEEE Trans. Nucl. Sci.* **42(4)**, 374 (1995).
216. A. Parsons et al., *IEEE Trans. Nucl. Sci.* **36(1)**, 931 (1989).
217. T. K. Edberg et al., *Nucl. Instrum. Meth.* **A316**, 38 (1992).
218. P. L. Hink et al., SPIE Proceedings **1549**, 193 (1991).
219. A. Pla-Dalmau, G. W. Foster, and G. Zhang, *Nucl. Instrum. Meth.* **A361**, 192 (1995).
220. C. H. Lally, G. J. Davies, W. G. Jones, and N. J. T. Smith, *Nucl. Instrum. Meth.* **B117**, 421 (1996).

Chapter 9

Photomultiplier Tubes and Photodiodes

I. INTRODUCTION

The widespread use of scintillation counting in radiation detection and spectroscopy would be impossible without the availability of devices to convert the extremely weak light output of a scintillation pulse into a corresponding electrical signal. The photomultiplier (PM) tube accomplishes this task remarkably well, converting light signals that typically consist of no more than a few hundred photons into a usable current pulse without adding a large amount of random noise to the signal. Although there has been some progress (described later in this chapter) in the development of semiconductor photodiodes for use with scintillators, the PM tube remains the most widely used device for this purpose. A great variety of commercially available PM tubes are sensitive to radiant energy in the ultraviolet, visible, and near-infrared regions of the electromagnetic spectrum. They have many applications in optical spectroscopy, laser measurements, and astronomy. Useful reviews of PM tube properties and design characteristics can be found in Ref. 1. In this chapter the discussion is limited to those designs of primary interest for scintillation counting. Morton has published[2] a very readable historical account of the development of tubes for this purpose. Useful guides and standards for the testing of PM tubes for scintillation counting have been developed as part of a series of such standards published[3] by the IEEE.

The simplified structure of a typical photomultiplier tube is illustrated in Fig. 9.1. An outer (usually glass) envelope serves as a pressure boundary to sustain vacuum conditions inside the tube that are required so that low-energy electrons can be accelerated efficiently by internal electric fields. The two major components inside the tube are a photosensitive layer, called the *photocathode*, coupled to an electron multiplier structure. The photocathode serves to convert as many of the incident light photons as possible into low-energy electrons. If the light consists of a pulse from a scintillation crystal, the photoelectrons produced will also be a pulse of similar time duration. Because only a few hundred photoelectrons may be involved in a typical pulse, their charge is too small at this point to serve as a convenient electrical signal. The electron multiplier section in a PM tube provides an efficient collection geometry for the photoelectrons as well as serving as a near-ideal amplifier to greatly increase their number. After amplification through the multiplier structure, a typical scintillation pulse will give rise to 10^7-10^{10} electrons, sufficient to serve as the charge signal for the original scintillation event. This charge is conventionally collected at the anode or output stage of the multiplier structure.

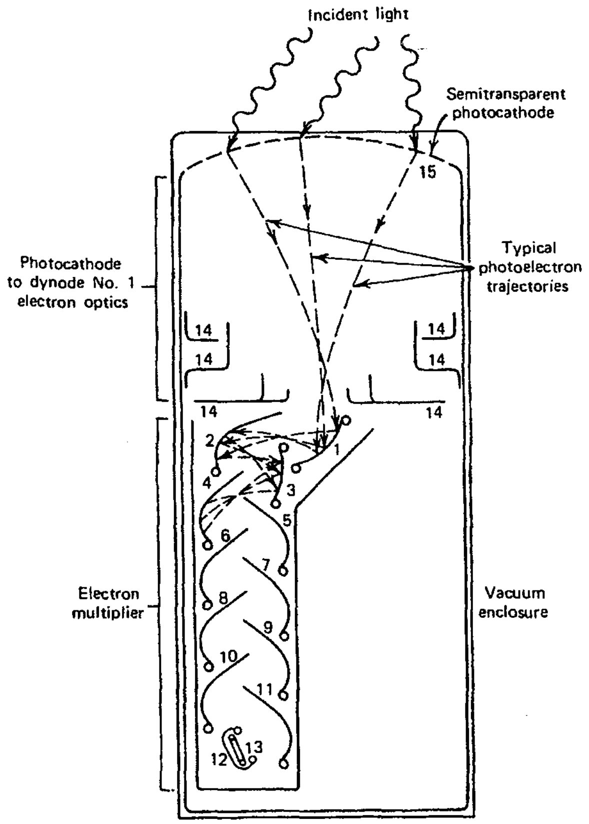

Figure 9.1 Basic elements of a PM tube. (From Ref. 1.)

Most photomultipliers perform this charge amplification in a very linear manner, producing an output pulse at the anode that remains proportional to the number of original photoelectrons over a wide range of amplitude. Much of the timing information of the original light pulse is also retained. Typical tubes, when illuminated by a very short duration light pulse, will produce an electron pulse with a time width of a few nanoseconds after a delay time of 20–50 ns.

PM tubes are commercially available in a wide variety of sizes and properties. We begin our discussion with the important elements of PM tube design and their influence on overall performance.

II. THE PHOTOCATHODE

A. The Photoemission Process

The first step to be performed by the PM tube is the conversion of incident light photons into electrons. This process of photoemission can be thought of as occurring in three sequential stages: (1) the absorption of the incident photon and transfer of energy to an electron within the photoemissive material, (2) the migration of that electron to the surface, and (3) the escape of the electron from the surface of the photocathode.

The energy that can be transferred from the photon to an electron in the first step is given by the quantum energy of the photon $h\nu$. For blue light typical of that emitted by many scintillators, the quantum energy is about 3 eV. In step 2, some of that energy will be lost through electron–electron collisions in the migration process. Finally, in step 3, there must be sufficient energy left for the electron to overcome the inherent potential barrier that always exists at any interface between material and vacuum. This potential barrier (often called the *work function*) is normally greater than 3 or 4 eV for most metals but can be as low as 1.5–2 eV for suitably prepared semiconductors.

From these energy considerations, some general comments can be made regarding photocathodes. First, the finite potential barrier in step 3 imposes a minimum energy on the incoming light photon even if all other energy losses are zero. All photocathodes therefore have a long-wavelength (small ν) cutoff that is usually in the red or near-infrared portion of the spectrum.[†] Even for higher-energy light photons, the surface barrier should be as low as possible to maximize the number of escaping electrons. The rate of energy loss as the electron migrates to the surface should be kept small in order to maximize the depth in the material (called the *escape depth*) at which electrons may originate and still reach the surface with sufficient energy to overcome the potential barrier. The rate of energy loss in metals is relatively high, and an electron can travel no more than a few nanometers before its energy drops below the potential barrier. Therefore, only the very thin layer of material lying within a few nanometers of the surface will contribute any photoelectrons from common metals. In semiconductors, the rate of energy loss is much lower and the escape depth can extend to about 25 nm. This, however, is still a very small thickness even with respect to stopping visible light. Photocathodes of this thickness are semitransparent and will cause less than half the visible light to interact within the photosensitive layer. Therefore, such photocathodes cannot come close to converting all the visible light photons into electrons, no matter how low the potential barrier may be.

In order for an incident light photon to be absorbed in a semiconductor, its energy must exceed the bandgap energy E_g. (For a discussion of the band structure in semiconductors, see Chapter 11.) The absorption process consists simply of elevating an electron from the normally populated valence band to the conduction band. Within about a picosecond, these electrons rapidly lose energy through phonon interactions with the crystal until their energy is at the bottom of the conduction band. In normal semiconductors, the electron potential outside the surface is higher than the bottom of the conduction band by an amount called the *electron affinity*. If an electron is to escape, it must reach the surface in the short time before phonon interactions have reduced its energy to the bottom of the conduction band. The electron, however, will remain at the bottom of the conduction band for perhaps another 100 ps before recombining with a hole and dropping to the valence band. The use of *negative electron affinity* materials, discussed more fully later in this chapter, leads to a much greater escape depth by allowing electrons that have dropped to the bottom of the conduction band to also escape if they reach the surface (see Fig. 9.4).

B. Spontaneous Electron Emission

The surface potential barrier influences another important property of photocathodes: *thermionic noise*. Normal conduction electrons within the photocathode material will always have some thermal kinetic energy that, at room temperature, will average about 0.025 eV. There is a spread in this distribution, however, and those electrons at the extreme upper end of the distribution can occasionally have an energy that exceeds the potential barrier. If that electron is close enough to the surface, it may escape and give rise to a spontaneous thermally induced signal. In metals, the thermal emission rate is low ($\sim 100/\text{m}^2 \cdot \text{s}$)

[†] The presence of low concentrations of impurity states in some photocathode materials can result in a small but measurable sensitivity beyond the normal cutoff wavelength into the infrared region of the spectrum.

because of the relatively high potential barrier. In semiconductors, the lower potential barrier leads to thermal emission rates as high as 10^6–$10^8/\mathrm{m}^2 \cdot \mathrm{s}$. Their superior photosensitivity is therefore achieved only at the price of a higher noise rate from thermally stimulated electron emission.

On theoretical grounds, the rate of thermionic emission should rise exponentially with photocathode temperature. The observed rate of spontaneous electron emission does increase with temperature, but the dependence is generally much milder than this prediction, indicating the influence of nonthermal effects in determining the overall emission rate.

C. Fabrication of Photocathodes

Photocathodes can be constructed as either opaque or semitransparent layers. Each type is used in a somewhat different geometric arrangement. An opaque photocathode is normally fabricated with a thickness somewhat greater than the maximum escape depth and is supported by a thick backing material. Photoelectrons are collected from the same surface on which the light is incident. Semitransparent photocathodes generally are no thicker than the escape depth and are deposited on a transparent backing (often the glass end window of the PM tube). Light first passes through the transparent backing and subsequently into the photocathode layer, and photoelectrons are collected from the opposite surface. Because they are more readily adaptable to tube designs that use a flat end window, semitransparent photocathodes are more common in PM tubes designed for scintillation counters.

An important practical property of photocathodes is the uniformity to which their thickness can be held over the entire area of the photocathode. Variations in thickness give rise to corresponding changes in the sensitivity of the photocathode and can be one source of resolution loss in scintillation counters. This problem is especially serious for large-diameter PM tubes.

D. Quantum Efficiency and Spectral Response

The sensitivity of photocathodes can be quoted in several ways. When applied to dc light measurements, it is traditional to quote an overall photocathode efficiency in terms of current produced per unit light flux on its surface (amperes per lumen). A unit of greater significance in scintillation counting is the *quantum efficiency* (*QE*) of the photocathode. The quantum efficiency is simply defined as

$$\mathrm{QE} = \frac{\text{number of photoelectrons emitted}}{\text{number of incident photons}} \tag{9.1}$$

The quantum efficiency would be 100% for an ideal photocathode. Because of the limitations mentioned earlier, practical photocathodes show maximum quantum efficiencies of 20–30%.

The quantum efficiency of any photocathode will be a strong function of wavelength or quantum energy of the incident light, as shown in Fig. 9.2. To estimate the effective quantum efficiency when used with a particular scintillator, these curves must be averaged over the emission spectrum of the scintillator. One consideration in selecting a photocathode is to seek a high quantum efficiency over the wavelength range in which the emission spectrum of the scintillator is concentrated.

The sensitivity at the long-wavelength or low photon energy end of the scale is largely limited by the reduced absorption of light in the photocathode and the low energy imparted to the photoelectron. At a sufficiently high λ this electron no longer has sufficient energy to escape the surface of the photocathode and the response drops to zero. The response at the opposite end of the scale is normally not a function of the photocathode

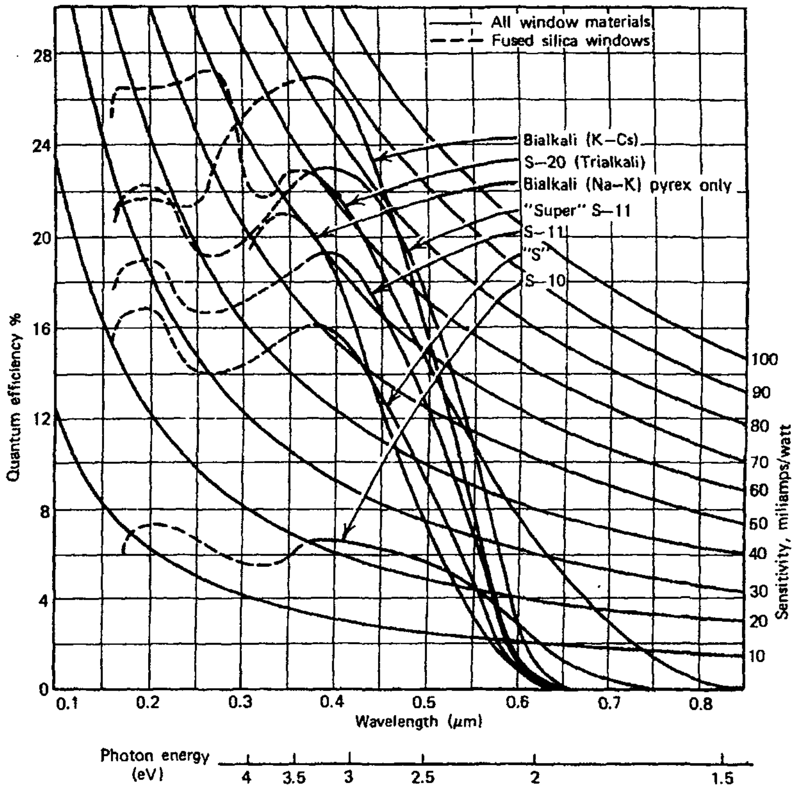

Figure 9.2 The spectral sensitivity of a number of photocathode materials of interest in PM tubes. The use of silica or quartz windows is necessary to extend the response into the ultraviolet region. (Courtesy of EMI GENCOM Inc., Plainview, NY.)

itself but rather of the window through which the light must enter to reach the photoemissive layer. For normal glass, the cutoff will be at a wavelength in the region of 350 nm, which is usually adequate for most scintillation materials. For some scintillators (e.g., noble gases), however, a significant part of the emission spectrum can be in the ultraviolet region with shorter wavelength. For such applications, special PM tubes with entrance windows made from fused silica or quartz can be used to extend the sensitivity to wavelengths as short as about 160 nm.

An alternative measure of quantum efficiency is sometimes quoted for PM tubes used in scintillation counting. The number of photoelectrons produced per unit energy lost in a scintillator mounted with close optical coupling to the photocathode is proportional to the quantum efficiency averaged over the emission spectrum of the scintillator. Because of the widespread use of thallium-activated sodium iodide as a scintillation crystal, the standard for quotation is the number of photoelectrons produced from a given photocathode per keV of energy loss by fast electrons in a NaI(Tl) crystal from which nearly all the light is collected. For photocathodes with peak quantum efficiency of 25–30%, measurements give about 8–10 photoelectrons per keV energy loss.[4,5] The reciprocal of this value, or the average energy loss required to create one photoelectron, is therefore approximately 100–120 eV. As emphasized elsewhere in this text, this value for the energy loss required to produce one basic information carrier in a typical scintillation detector is much larger than the equivalent value in gas-filled or semiconductor detectors.

Presently available materials for photocathodes include a *multialkali* material based on the compound Na_2KSb. Prepared by activation with a small amount of cesium, this material was the first to show a relatively high quantum efficiency of up to 30% in the blue region of the spectrum. A later formulation based on K_2CsSb activated with oxygen and cesium is given the name *bialkali* and can show an even higher efficiency in the blue. Furthermore, thermionic emission from bialkali photocathodes tends to be significantly lower than that from the multialkali materials, leading to lower spontaneous noise rates from tubes with this photocathode.

III. ELECTRON MULTIPLICATION

A. Secondary Electron Emission

The multiplier portion of a PM tube is based on the phenomenon of secondary electron emission (see p. 42). Electrons from the photocathode are accelerated and caused to strike the surface of an electrode, called a *dynode.* If the dynode material is properly chosen, the energy deposited by the incident electron can result in the reemission of more than one electron from the same surface. The process of secondary electron emission is similar to that of photoemission discussed in the previous section. In this case, however, electrons within the dynode material are excited by the passage of the energetic electron originally incident on the surface rather than by an optical photon.

Electrons leaving the photocathode have a kinetic energy on the order of 1 eV or less. Therefore, if the first dynode is held at a positive potential of several hundred volts, the kinetic energy of electrons on arrival at the dynode is determined almost entirely by the magnitude of the accelerating voltage. The creation of an excited electron within the dynode material requires an energy at least equal to the bandgap, which typically may be of the order of 2–3 eV. Therefore, it is theoretically possible for one incident electron to create on the order of 30 excited electrons per 100 V of accelerating voltage. Because the direction of motion of these electrons is essentially random, many will not reach the surface before their de-excitation. Others that do arrive at the surface will have lost sufficient energy so that they cannot overcome the potential barrier at the surface and are therefore incapable of escaping. Therefore, only a small fraction of the excited electrons ultimately contribute to the secondary electron yield from the dynode surface.

The secondary electron yield is a sensitive function of incident electron energy. If a relatively low-energy electron strikes the dynode surface, little energy is available for transfer to electrons in the dynode material, and relatively few electrons will be excited across the gap between the valence and conduction bands. At the same time, because the distance of penetration is not large, most of these excited electrons will be formed near the surface. For incident electrons of higher energy, more excited electrons will be created within the dynode but at greater average depth. Because the probability of escape will diminish with

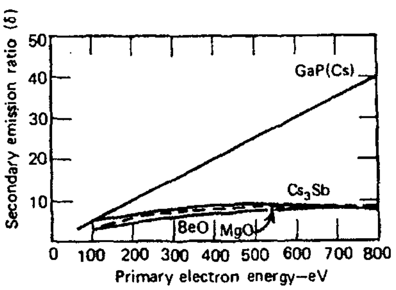

Figure 9.3 Variation of the secondary emission yield with primary electron energy for standard dynode materials (lower three curves) and an NEA material [GaP(Cs)]. (From Krall et al.[6])

increasing depth, the observed electron yield will be maximized at an optimum incident electron energy.

The overall multiplication factor for a single dynode is given by

$$\delta = \frac{\text{number of secondary electrons emitted}}{\text{primary incident electron}} \tag{9.2}$$

and should be as large as possible for maximum amplification per stage in the photomultiplier tube. A plot of δ versus incident electron energy is given in Fig. 9.3 for several dynode materials. For the conventional dynode materials of BeO, MgO, and Cs_3Sb, the maximum multiplication factor reaches about 10 for an optimum incident energy near 1 keV, although values of 4–6 are more typical at conventional interdynode voltages of a few hundred volts.

B. Negative Electron Affinity Materials

The secondary emission yield of dynodes can be increased significantly through the use of *negative electron affinity* (NEA) materials.[6–10] The most successful of these materials has been gallium phosphide (GaP), heavily doped to a concentration of about 10^{19} atoms/cm^3 with a *p*-type material such as zinc. The zinc creates acceptor sites within the bulk of the gallium phosphide. A thin, nearly monatomic layer of an electropositive material such as cesium is then applied to one surface. The acceptors at the surface attract an electron from the electropositive cesium, and each cesium atom becomes ionized and is held to the surface by electrostatic forces.

The effect of this surface treatment can best be illustrated through the band structure diagram shown in Fig. 9.4. At the left is shown a conventional band diagram for undoped gallium phosphide, which is also representative of conventional dynode materials. The series of arrows on the left shows a typical history of an electron that does not escape. The original excitation causes a number of electrons to be elevated from the valence band to some point well up into the conduction band. As these electrons diffuse, they lose energy primarily through phonon interactions, such that within about a picosecond, these "hot" electrons have come into thermal equilibrium with their local environment and their energy has relaxed to near the bottom of the conduction band. If this electron is to escape, it must reach the surface with an energy greater than the potential that exists on the vacuum side of the surface. Once the electron drops to the bottom of the conduction band, its energy is normally below the vacuum potential and is too low to permit escape. In this case only a short time is available for the electron to escape and it cannot travel large distances from its point of origin. Therefore, relatively small escape depths of only a few nanometers are possible. However, the electron will tend to diffuse for a substantially longer time (typically 100 ps) before dropping across the gap to rejoin the valence band.

On the right is shown the band bending created by the filling of acceptor sites at the surface by the thin cesium layer. The effect of the bending is to bring the vacuum potential below that of the bottom of the conduction band in the interior of the material. Therefore, electrons

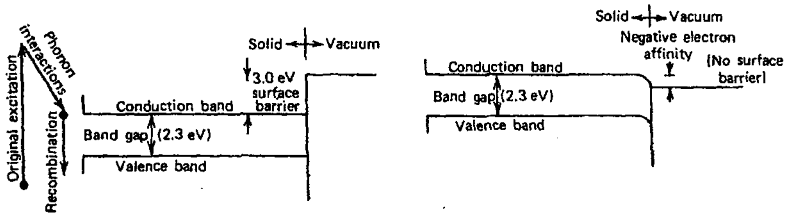

Figure 9.4 Band structure near the surface for conventional semiconductors (left) and NEA materials (right). (Adapted from Krall et al.[6])

that have already dropped to the bottom of the conduction band still have sufficient energy to escape if they happen to diffuse to the surface. Because the thickness of the bent-band region is very small, it can be less than a mean free path and the electron may escape without further energy loss in the surface region. The net effect is that the electrons that have already reached the bottom of the conduction band are still candidates for escape and remain so for a period of time that is about 100 times greater than in the previous case. The average escape depth will therefore tend to be much greater and can reach tens or hundreds of nanometers.

The effect of this change on the secondary electron yield is profound. The increased time over which electrons may escape enhances the escape probability for any typical electron. Furthermore, excited electrons created deep within the dynode material remain candidates for escape. Therefore, the secondary electron yield will continue to increase with increasing primary electron energy until the distance of penetration of the primary is very large. These effects are reflected in the yield curve for a GaP(Cs) dynode shown in Fig. 9.3. Secondary electron yields of 50 or 60 are readily achieved with an interstage voltage of 1000 V, and much higher values are possible in principle if even larger voltages are permitted by the PM tube design.

A secondary advantage of NEA materials is evident in PM tubes used for ultrafast timing applications. Because almost all escaping electrons have previously dropped to the bottom of the conduction band, their average energy is lower and much more uniform than secondary electron energies from conventional materials. Because variations in initial energy contribute to the time spread in the multiplier section, a narrower distribution leads to less time broadening. Furthermore, the higher gain per stage permits a reduction in the number of stages required for a given total gain, also reducing the overall time spread.

C. Multiple Stage Multiplication

To achieve electron gains on the order of 10^6, all PM tubes employ multiple stages. Electrons leaving the photocathode are attracted to the first dynode and produce δ electrons for each incident photoelectron. The secondaries that are produced at the surface of the first dynode again have very low energies, typically a few eV. Thus, they are quite easily guided by another electrostatic field established between the first dynode and a second similar dynode. This process can be repeated many times, with low-energy secondary electrons from each dynode accelerated toward the following dynode. If N stages are provided in the multiplier section, the overall gain for the PM tube should be given simply by

$$\text{overall gain} = \alpha\delta^N \tag{9.3}$$

where α is the fraction of all photoelectrons collected by the multiplier structure. Conventional dynode materials are characterized by a typical value of $\delta = 5$, and α is near unity for well-designed tubes. Ten stages will therefore result in an overall tube gain of 5^{10}, or about 10^7. If high-yield NEA dynodes are used with $\delta = 55$, the same gain can be achieved with only four stages.

The overall gain of a PM tube is a sensitive function of applied voltage V. If δ were a linear function of interdynode voltage, then the overall gain of a 10-stage tube would vary as V^{10}. As shown in Fig. 9.3, however, δ for conventional dynodes varies as some fractional power of interdynode voltage so that the overall gain is more typically proportional to $V^6 - V^9$.

D. Statistics of Electron Multiplication

If δ were strictly a constant, each photoelectron would be subject to exactly the same multiplication factor. Under fixed operating conditions, all output pulses that originate from a single photoelectron would then have the same amplitude. In practice, the emission of secondary electrons is a statistical process, and therefore the specific value of δ at a given dynode will fluctuate from event to event about its mean value. The shape of the single photoelectron pulse height spectrum observed from a real PM tube is an indirect measure of the degree of fluctuation in δ and has thus been the subject of extensive investigation.

In the most simple model, the production of secondary electrons at a dynode can be assumed to follow a Poisson distribution about the average yield. For a single photoelectron incident on the first dynode, the number of secondaries produced has a mean value of δ and standard deviation σ of $\sqrt{\delta}$ (see Chapter 3). The relative variance, defined as $(\sigma/\delta)^2$, is thus equal to $1/\delta$. When this process is now compounded over N identical stages of the PM tube, the mean number of electrons collected at the anode (and hence the pulse amplitude) is given by δ^N. It can be demonstrated from the properties of Poisson statistics that the relative variance in this number is now

$$\frac{1}{\delta} + \frac{1}{\delta^2} + \frac{1}{\delta^3} + \ldots + \frac{1}{\delta^N} \cong \frac{1}{\delta - 1} \tag{9.4}$$

Thus, if $\delta \gg 1$, the relative variance or spread in the output pulse amplitude is dominated by fluctuations in the yield from the first dynode where the absolute number of electrons is smallest.

In many applications of scintillators, hundreds or thousands of photoelectrons contribute to each pulse, and they are therefore much larger than single photoelectron pulses. When poor light collection or low-energy radiations are involved, however, signal pulses corresponding to only a few photoelectrons may be involved. Then the fluctuations in electron multiplication may interfere with the ability to discriminate against noise events, many of which correspond to single photoelectrons. Figure 9.5 shows the expected distribution in the number of secondaries produced by the first dynode when struck by different numbers of photoelectrons. If the value of δ is small, it is impossible to separate cleanly the events caused by one photoelectron from those in which more photoelectrons are involved. If the dynodes are characterized by a larger value of δ, however, the separation is much more distinct and it is possible to distinguish peaks in the distribution corresponding to discrete numbers of photoelectrons up to about 4 or 5. This behavior is demonstrated in Fig. 9.6 in the pulse height spectrum observed from a PM tube with a high-δ first dynode made from a NEA material.

Experimental measurements of the single photoelectron pulse height spectra from PM tubes generally show a peaked distribution,[12,13] but with a larger relative variance than that predicted by the Poisson model. In fact, observations made under some conditions show no

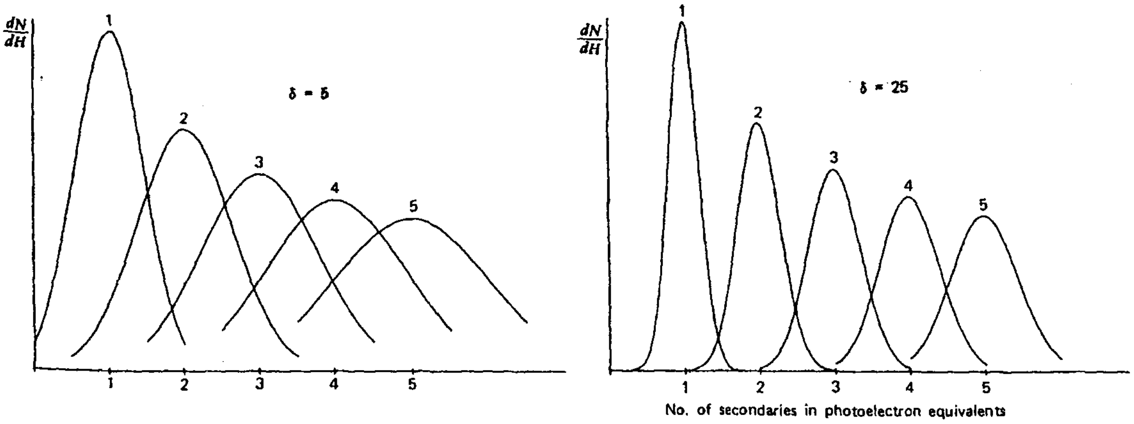

Figure 9.5 Statistical broadening of the secondary electron yield from the first dynode of a PM tube. Numbers identify the number of incident photoelectrons. Two cases are shown representing conventional dynodes (δ = 5) and NEA materials (δ = 25).

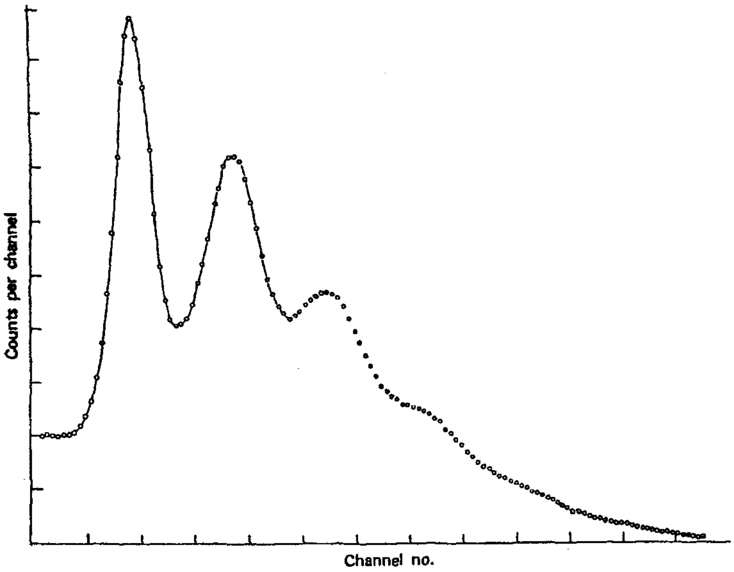

Figure 9.6 The measured pulse height spectrum for weak scintillation events obtained from a RCA 8850 photomultiplier tube. The high-gain first dynode results in distinguishable peaks in the spectrum corresponding to 1, 2, and 3 photoelectrons per pulse. (From Houtermans.[11])

peak at all, but rather an exponential-like distribution.[14] These discrepancies have led to alternate models of the multiplication statistics in which a Polya distribution[15] or compound Poisson[16,17] is substituted for the simple Poisson description of electron multiplication. No universal descriptions have as yet emerged that can accommodate all experimental measurements, and it is possible that differences in specific electron trajectories and dynode properties may preclude a general model applicable to all PM tubes.

IV. PHOTOMULTIPLIER TUBE CHARACTERISTICS

A. Structural Differences

Figure 9.7 shows some representative construction details of PM tubes of various designs. All consist of a semitransparent photocathode, a photoelectron collection region between the photocathode and the first dynode, a multistage electron multiplier section, and an anode for collection of the amplified charge. These structures are enclosed in a glass vacuum envelope, through which electrical leads are conducted at the base. Tubes with flat end plate windows are the only type in general use for scintillation counting, so cylindrical scintillation crystals can easily be mounted directly on the end window adjacent to the photocathode. Tubes are available commercially with circular photocathodes ranging in diameter from a few millimeters to over 20 cm. A nominal 2-in. (5 cm) diameter is one of the common choices in many scintillation applications, and the widest selection is generally available in this size. PM tubes with square and hexagonal photocathodes have also been introduced for specialized applications in which an array of tubes must be closely packed.

The "venetian blind" type of construction is one of the oldest used for photomultiplier tubes and is now virtually obsolete. It is readily adaptable to tubes of varying numbers of stages but suffers from a relatively slow response time due to low electric fields at the surface of the dynodes. The "box and grid" structure is also fairly old and slow, but it is still

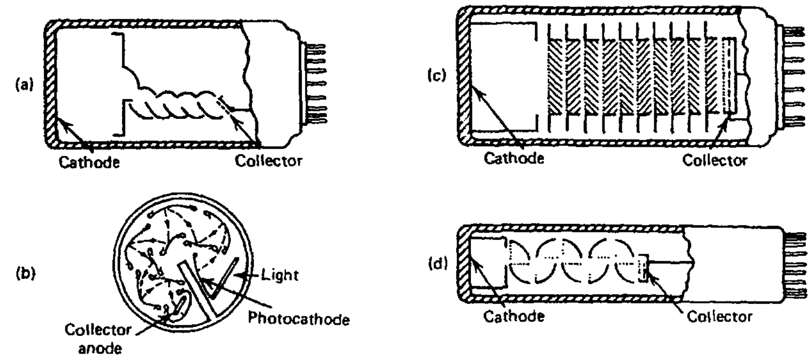

Figure 9.7 Configurations of some common types of PM tubes. (*a*) Focused linear structure. (*b*) Circular grid. (*c*) Venetian blind. (*d*) Box-and-grid. (Courtesy of EMI GENCOM Inc., Plainview, NY.)

standard in many tubes of large diameter. The circular grid and linear multiplier structures were introduced to speed up the electron transit time through the multiplier structure and are used in those PM tubes with the fastest response time.

Photomultiplier tubes should be protected from excessive mechanical shock or vibration to avoid physical damage to internal components. Also, some modulation of the output signal can be induced by vibration of the multiplier structures. Most tube manufacturers offer a rugged version of some of their photomultiplier tubes (often originally designed for space applications). These are provided with electron multiplier structures and other internal components mechanically arranged to resist vibration and shock. Standard tubes are quite adequate in this respect for most scintillation counting applications, but rugged versions can be helpful in counters designed for field use where they may be subjected to rough handling.

Another type of specialized electron multiplier is the continuous channel, illustrated in Fig. 9.8. This device is extremely simple, consisting of a hollow glass tube whose inner surface acts as a secondary electron emitter. A potential difference is applied across the length of the tube, thereby attracting electrons from the entrance end to the exit end. Electrons entering the tube will eventually strike the wall giving rise to a pulse of secondary electrons. These will be further accelerated along the length of the tube until they in turn also strike the wall, giving rise to further secondaries. The device acts much like a photomultiplier tube with continuous dynodes available along its entire length. The number of times an entering electron and its subsequent secondaries strike the wall is an accident of past orientation and individual trajectories and will vary considerably for different entering electrons. When operated at high voltages, the electron gain may be large enough so that

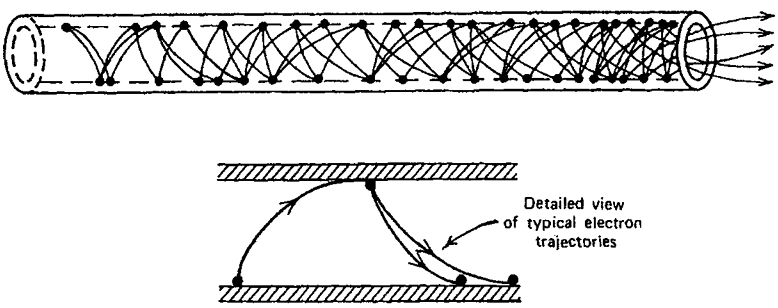

Figure 9.8 Continuous channel electron multiplier.

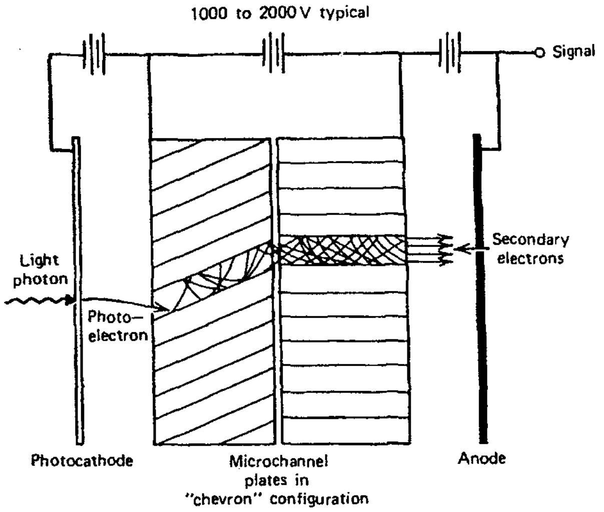

Figure 9.9 Elements of a PM tube based on microchannel plate electron multiplication.

the resulting space charge near the exit of the channel limits the total charge per pulse to about 10^6 or 10^7 electrons at saturation for channels of small diameter.

Channel multipliers must be shaped to prevent feedback problems that can arise when positive ions occasionally formed within the channel are accelerated in the reverse direction from the electrons. By forming the channel as a curve or chevron, these ions can be made to strike a wall before their energy is high enough to create secondary electrons.

Clusters of many thousands of tubes can be fabricated to form a *microchannel plate.* Each channel is of very small diameter (typically 15–50 μm) and acts as an independent electron multiplier. Their application as the multiplier element in PM tubes is reviewed in Refs. 18–21. In the configuration shown in Fig. 9.9, each photoelectron generally enters a separate channel. If all channels are operated in charge saturation and are identical, then the total collected charge is proportional to the number of original photoelectrons.

The primary advantage of PM tubes based on microchannel plates lies in their excellent timing properties.[22–27] The total electron transit time through a channel is a few nanoseconds, compared with 20–50 ns for conventional multiplier structures (see the following section). The spread in transit time, which determines timing performance, is about 100 ps, a factor of 2 or 3 better than the fastest conventional PM tube currently available.

B. Pulse Timing Properties

Because the time required for photoemission in the photocathode or secondary emission from dynodes is very short (0.1 ns or less), the time characteristics of the PM tube are determined exclusively by the electron trajectories. The *electron transit time* of a PM tube is defined as the average time difference between the arrival of a photon at the photocathode and the collection of the subsequent electron burst at the anode. In PM tubes of various designs, electron transit times range from 20–80 ns. In most timing applications, however, the transit time itself is not of primary importance because if it were always a constant, it would introduce only a fixed delay in the derived signal. Instead, the *spread in transit time* is a more important quantity because it determines the time width of the pulse of electrons arriving at the anode of the tube. The timing response of a typical PM tube is illustrated in Fig. 9.10.

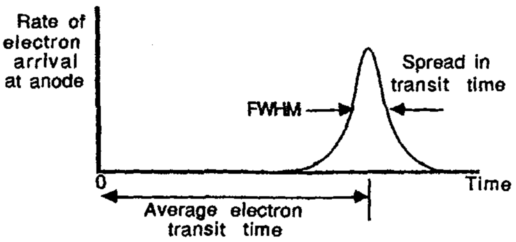

Figure 9.10 The response of a PM tube to a short pulse of light on the photocathode.

The region between the photocathode and first dynode is critical in determining the timing properties. To allow uniform collection over large photocathodes, this distance is kept fairly large compared with interdynode distances (see Fig. 9.11). The difference in paths between a photoelectron leaving the center of the photocathode and one at the edge is often a dominant factor in the observed spread in transit time. The photocathode is often curved to minimize the transit time spread across its diameter. It is convenient to have a flat outer surface for scintillator mounting, so an end window with a plano-concave shape is frequently used with the photocathode deposited on the inner curved surface. A second source of transit time spread arises from the distribution in initial velocities of photoelectrons leaving the photocathode. This effect can be minimized by using a large voltage difference between the photocathode and first dynode.

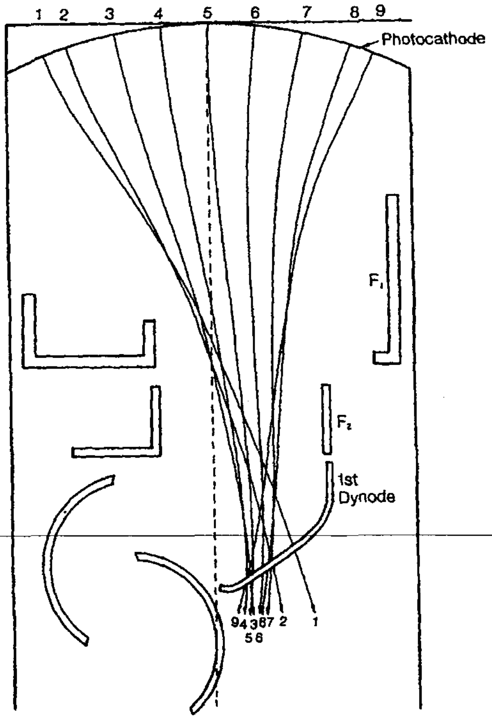

Figure 9.11 Computer-generated trajectories of electrons accelerated from the photocathode to the first dynode in a PM tube. In this design, the photocathode is curved to minimize the spread in transit time. Structures labeled F_1 and F_2 are electrodes carrying adjustable voltage that electrostatically focus the electrons for optimum performance. (From Kume et al.[28])

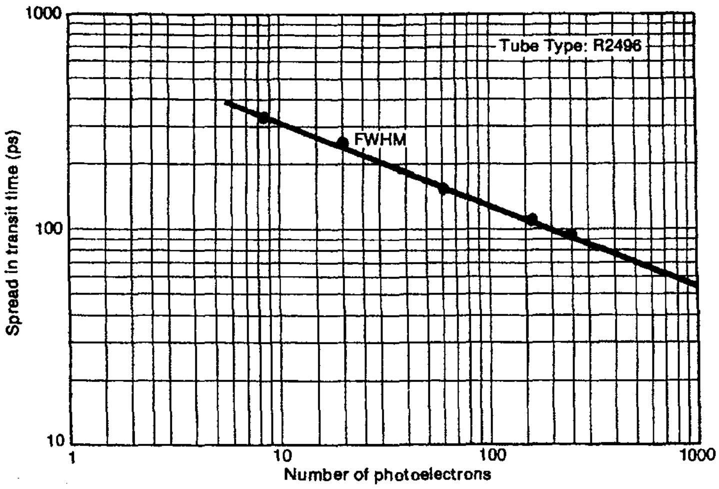

Figure 9.12 Measurements of the transit time spread observed from the PM tube shown in Fig. 9.11 as a function of the average number of photoelectrons generated per pulse. (From Kume et al. [28])

The amount of transit time spread observed for a specific pulse also depends on the number of initial photoelectrons per pulse. To simplify the analysis and comparison of different photomultipliers, many of the measurements reported in the literature concentrate on the transit time spread due to a *single* photoelectron. This parameter does not include the important contribution of the cathode to first dynode space,[29,30] and is only a measure of the time spreads introduced subsequent to the first dynode. As the number of photoelectrons increases, a larger number of samplings of various possible electron trajectories through the tube are made. If the distribution in the various possible transit times is assumed to be Gaussian, then statistical theory predicts that the relative spread in transit times should vary inversely with the square root of the number of photoelectrons. In Fig. 9.12, this behavior is verified for a typical PM tube. Thus, high light yield from a scintillator is important in timing applications as well as in pulse height measurements. The time spread attributable to the multiplier section also decreases with increasing interdynode voltage, and the best timing performance is normally obtained by operating the tube at maximum voltage permitted by the ratings.

The timing performance of PM tubes is a continuing area of development, and some trends are reviewed in Ref. 31. Table 9.1 lists data for a number of representative tubes on the electron transit time and anode rise time (related to the spread in transit time). When used with slow inorganic scintillators, PM tubes are fast enough so that their contribution to the overall time response usually is not an important factor. It is only when scintillators with shorter decay times are employed to derive a fast timing signal that the PM tube can become a significant element in determining the resultant timing properties.

C. Maximum Ratings

All commercial photomultipliers are supplied with a set of maximum voltage and current ratings that are not to be exceeded during routine use. Detailed specifications will often give individual values for maximum photocathode to first dynode, dynode to dynode, last dynode to anode, and cathode to anode maximum voltages as well. These limits are set by a variety of conditions including ohmic leakage and dark current considerations. The user is often more interested in a single figure for the maximum applied voltage when using the

Table 9.1 Properties of Some Commercially Available Photomultiplier Tubes

A	B	C	D	E	F	G	H	I	J	K	L	M	N
Ham	1635	10	8	L8	BA	1250	1500	1.1	95	76	1	0.8	8.5
Ham	1450	19	15	L10	BA	1500	1800	1.7	115	88	3	1.8	19
Ham	380	38	34	L10	BA	1250	1750	1.1	95	88	3	2.7	37
Ham	1306	51	46	B8	BA	1000	1500	0.27	110	95	2	7.0	60
Ham	3318	51 sq	45	BM10	BA	1000	1500	0.27	110	95	2	4.8	45
Ham	3336	60 h	55	BM10	BA	1000	1500	0.27	110	95	2	6.0	47
Burle	4516	19	13	L10	BA	1500	1800	0.52	66	—	0.2	1.8	20
Burle	S83010E	38	32	C10	RbCsSb	1000	1000	2.4	100	92	1	2.8	32
Burle	S83054F	51	47	B8	BA	800	1200	0.10	10.5[a]	103	3	11	63
Burle	S83020F	60 h	56	L10	BA	1100	1700	0.10	71	100	1	10	69
Burle	S83079F	76 sq	—	B8	BA	800	1200	0.21	11.3[a]	100	3	14	73
Burle	S83006F	130	111	T10	BA	1100	1650	0.07	92	105	1	22	105
ADIT	B29B02H	29	24	B11	BA	1100	1500	1.0	70	80	10	11	35
ADIT	B51B01	51	46	B10	BA	1100	1500	1.0	70	80	10	17	45
ADIT	B76B01	76	70	B10	BA	1100	1500	1.0	70	80	10	17	50
ADIT	B133D01	127	119	B10	BA	1100	1500	1.0	120	97	10	17	50
ETL	9078	19	15	L10	BA	900	1200	0.71	70	90	0.1	1.8	20
ETL	9924	30	23	B11	RbCs	870	1050	2.1	95	100	0.1	15	80
ETL	9266	52	45	L10	BA	900	1100	0.6	80	100	0.2	4	37
ETL	9350	200	190	L14	BA	1550	2300	67	75	100	15	5	80

A = manufacturer: Ham = Hamamatsu, ETL = Electron Tubes Limited.
B = model number.
C = diameter or dimension of tube outline (sq = square, h = hex) in mm.
D = minimum usable photocathode dimension.
E = dynode structure: L = linear focused, B = box and grid, BM = box and mesh, C = circular.
F = photocathode material: BA = bialkali.
G = recommended operating voltage.
H = maximum tube voltage.
I = gain × 10^6 at voltage in G.
J = cathode luminous sensitivity (μA/lm) measured with 2854 K tungsten source.
K = cathode radiant sensitivity (mA/W) measured at or near the wavelength of photocathode peak sensitivity.
L = dark current (an approximate number due to large variations in the method of measurement between different manufacturers) (nA).
M = anode rise time at voltage in G (ns).
N = transit time at voltage in G (ns).

[a] cathode luminous sensitivity is measured using a blue Corning C.S. No. 5-58 filter.

manufacturer's recommended voltage divider string. Because virtually every PM tube will show an increase in gain as the voltage is increased, the maximum value for applied voltage practically determines the maximum gain obtainable from the tube.

Maximum values are also often given for photocathode current and anode current. The first limit is usually set by consideration of photocathode resistivity, which can give rise to distorted electrostatic fields at high currents, whereas the anode limit is set by heat dissipation considerations. In normal pulse-mode scintillation counting, current limits seldom are of concern because the maximum counting rate permitted by pile up and pulse resolution considerations nearly always corresponds to an average current far less than the maximum ratings.

D. Photomultiplier Tube Specifications

Manufacturers will conventionally quote performance of PM tubes in terms of certain characteristics, which are defined here.

1. *Overall Luminous Sensitivity.* Defined as the ratio of the measured anode current at operating voltage to the luminous flux from a tungsten light source of specified temperature incident on the photocathode. This quantity is an overall measure of the expected current from the PM tube per unit incident light from a broad-band source. The units are amperes per lumen (A/lm).
2. *Cathode Luminous Sensitivity.* Defined as above, except that the current of photoelectrons leaving the photocathode is substituted in the numerator for the anode current. This quantity is again measured in amperes per lumen, is a characteristic only of the photocathode, and is independent of the electron multiplier structure.
3. *Overall Radiant Sensitivity.* This parameter is defined as the ratio of anode current to radiant power at a given wavelength incident on the photocathode. Units are amperes per watt (A/W).
4. *Cathode Radiant Sensitivity.* Defined as above, except that the photocathode current is substituted for the anode current.
5. *Dark Current.* Normally specified in terms of anode current measured without photocathode illumination when the tube is operated to provide a given overall luminous sensitivity.
6. *Anode Pulse Rise Time.* Quoted as the time taken for the output pulse to rise from 10 to 90% of the peak when the photocathode is illuminated by a flash of light of very short duration.
7. *Anode Pulse Width.* Normally quoted as the time width of the output pulse measured at half maximum amplitude, again for short-duration illumination of the photocathode.

Table 9.1 lists specifications for a number of commercial photomultiplier tubes of significant current interest in scintillation counting. Because PM tube design remains a rapidly developing area, potential users should always seek up-to-date information directly from the tube manufacturers.

E. Linearity

The electron multiplication factor in nearly all PM tubes remains constant for pulses that range in size from a single photoelectron to many thousands. Under these conditions the amplitude of the pulse collected at the anode is linearly related to the number of photoelectrons, and consequently to the intensity of the scintillation light flash. Nonlinearities can arise for very large pulses caused by space charge effects between the last dynode and anode where the number of electrons is greatest. The buildup of space charge affects the trajectories of electrons in this region and causes some to be lost that would otherwise be collected. Another factor that can cause nonlinearities at high pulse amplitudes is any deviation of dynode voltages from their equilibrium value during the course of the pulse. Under normal circumstances in scintillation pulse counting, these effects are seldom important with an adequately designed tube base (see later discussion) and the photomultiplier tube remains in the linear range.

F. Noise and Spurious Pulses

Usually the most significant source of random noise from a photomultiplier tube results from thermionic electrons that are spontaneously emitted by the photocathode. The pulses that result from this process correspond to a single photoelectron, so their amplitude is limited to the lowest end of the scale. Because most scintillation counting is done under conditions in which a scintillation pulse corresponds to many photoelectrons, amplitude discrimination is usually sufficient to eliminate all contributions of this thermal noise. In applications in which very-low-energy radiation is measured or in which single photons are detected, valid signal events may also correspond to a single photoelectron and therefore may be indistinguishable from thermionic noise. In that event there is no alternative but to try to reduce the noise contribution as much as possible. The rate at which these pulses are observed is proportional to the area of the photocathode, and therefore one should select a tube of the smallest diameter required for a specific application in order to minimize these dark pulses. The rate at which thermionic electrons are emitted per unit area varies greatly between photocathode materials, and bialkali photocathodes are among the most quiet. Typical spontaneous emission rates at room temperature are in the range of 10^2–10^4 electrons/$\text{cm}^2 \cdot \text{s}$. The dark current specifications given in Table 9.1 largely reflect the contribution of thermionic electrons, and the tubes with lowest noise rates are those with the lowest dark currents for equivalent luminous sensitivity.

The significance of this spontaneous electron emission from the photocathode can be quite different depending on whether the scintillator–PM tube combination is operated in pulse or current mode. Choosing for illustration a value of 10^3 electrons/s randomly emitted from the entire photocathode, a tube operated in pulse mode will produce small noise pulses with amplitude that corresponds to a single photoelectron with an average time spacing of 1 ms. Typical shaping times used for scintillation detectors are in the microsecond range, so the probability is very small that even one such photoelectron will contribute to a given scintillation pulse. If the single photoelectron pulses are much smaller than the signal pulses so that they can be amplitude discriminated, then there is no appreciable contribution to the noise characteristics of the measurement. In current mode, however, all the dark current adds to the signal current, and the fluctuation in its value can be a significant contributor to the uncertainty in measuring the signal. To estimate the steady-state dark current associated with the same example as above for the spontaneous emission rate, we assume a gain of 10^6 in the electron multiplier section of the PM tube:

$$I_{\text{dark}} = (10^3 \text{ elec/s})(10^6)(1.6 \times 10^{-19} \text{ C/elec}) = 160 \text{ pA}$$

The measurement of currents of this order of magnitude or less from the PM tube anode will be subject to noise introduced by the dark current fluctuations.

For some photocathodes the rate at which thermionic electrons are emitted can be drastically reduced by cooling the tube. Reductions by a factor of 100 or more may be observed with proper temperature reduction. Dry ice or liquid nitrogen are often used for cooling, but self-contained refrigerators are also commercially available for this purpose. Problems that can arise in connection with PM tube cooling include water vapor condensation on exposed cold surfaces and increased photocathode electrical resistance at lower temperatures. Large photocathode resistance can distort the electrostatic field between the photocathode and first dynode and may lead to a loss in photoelectron collection efficiency.

Photomultiplier tubes should be stored in the dark when not in use. Exposure to room light is disastrous while voltage is supplied to the tube because very high illumination levels lead to anode currents that greatly exceed the maximum ratings and that can quickly damage the multiplier structures. Incident light, especially from fluorescent tubes, is to be avoided even when no voltage is applied to the tube because of the temporary increase in dark pulses that will result. It is not unusual to observe an increase of 100 or more in the rate of dark pulses immediately after exposure to intense room light, and a measurable increase can persist for several hours. It appears that the major cause of this increased noise rate is the emission of light from phosphorescence states in the glass envelope of the PM tube.

Another source of dark pulses originates with natural radioactivity in the structure of the tube itself. The most important components are usually ^{40}K and thorium contained in the glass envelope. A beta particle produced in radioactive decay will give rise to a flash of Cherenkov radiation, which can liberate photoelectrons from the photocathode in much the same way as normal scintillation events. For applications in which the ultimate in low background is a necessity, special tubes with low-activity glass to minimize these events are available. Scintillation or Cherenkov light produced in the glass by external radiation can also be a significant source of dark pulses.[32,33] One such source is cosmic radiation (see p. 761), which generally results in dark pulses of small amplitude from Cherenkov light produced in the thin end window of the tube. Because of the low specific energy loss of the secondary cosmic radiations and the low light yield from the Cherenkov process, the corresponding dark pulses correspond to only a few photoelectrons and are therefore usually discarded by amplitude discrimination in typical scintillation applications. However, if very weak scintillation events must be recorded, these dark pulses can be of the same size as the signal. In such cases, the rate from cosmic radiation can be minimized by operating the tube with its major axis oriented horizontally so that the end window presents minimum cross section to the cosmic secondaries that are directed preferentially in a downward vertical direction.

Afterpulses are another type of noise sometimes observed in PM tubes.[34] These are satellite pulses that will sometimes follow a true signal pulse after a short delay period. One mechanism that can give rise to afterpulsing is the emission of light from the latter stages of the multiplier structure, which finds its way back to the photocathode. Such afterpulses will be delayed by a time characteristic of the electron transit time through the tube, or roughly 20–50 ns. Because these pulses often correspond to a single photon, their amplitude is usually quite small. Another cause of afterpulsing can be an imperfect vacuum within the tube. Traces of residual gas can be ionized by the passage of electrons through the multiplier structure. The positive ions that are formed will drift in the reverse direction and some may find a path back to the photocathode. Typical ions will liberate tens or hundreds of photoelectrons when they strike the photocathode, and the resulting pulse will be of rather large size. Because the velocity of the positive ion is relatively low, the time it takes to drift back to the photocathode can range from hundreds of nanoseconds to a microsecond or more. The time spacing between the primary pulse and the afterpulse from this mechanism is therefore relatively large. Because the amount of residual gas can vary considerably between tubes of identical design, problems caused by afterpulsing in some applications may often be eliminated by simple substitution of another tube. The probability of production of an afterpulse increases linearly with primary pulse amplitude in at least one tube design but is usually no more than a few percent. Afterpulsing is therefore of little consequence in ordinary scintillation spectroscopy but can become a serious perturbing effect in timing measurements where the pulses of interest follow a preceding high-intensity burst of radiation. Discussions of the afterpulsing characteristics of some PM tubes, together with electronic means of afterpulse suppression, may be found in Refs. 35–39.

G. Photocathode Nonuniformities

Direct measurement (e.g., see Ref. 9, 40, or 41) has shown that the sensitivity of photocathodes, especially those with large diameters, is far from uniform across the entire photocathode area. This problem is further compounded by the difficulties of achieving uniform photoelectron collection to the first dynode from the entire photocathode area. The combination of these two effects can lead to situations in which the anode pulse observed for a given flash of light may vary by as much as 30–40% as the position of the illumination is moved across the photocathode area. This nonuniformity is a potentially serious problem in scintillation counting because response variations will tend to spoil the energy resolution of the system. One means of reducing the problem is to place a light pipe between the scintillator and end window of the PM tube. This is especially important for thin scintillators and tends to spread light from any scintillation event over the entire photocathode, thereby averaging out much of the nonuniformity.

H. Gain Variations with Counting Rate

Another nonideality of PM tubes of which the user should be aware is the possibility of gain changes during the course of a measurement. The most common situation is one in which the counting rate changes by a large factor. If the divider string current is too low (see p. 284), changes in count rate can lead to gain changes due to resulting variations in the dynode potentials.[42] Even if this effect is totally eliminated, the tube may require several hours to stabilize at a constant count rate as thermal and space charge effects created by the electron current through the multiplier structure of the tube reach equilibrium.[43] The gain changes may not be fully reversible, and hysteresis effects have been observed experimentally.[44] Photomultiplier structures can be designed to minimize these drifts, and a good tube will not change its gain by more than 1% as the counting rate is varied from 10^3 to 10^4 per second.[3] Specifications of this type can often be found for many PM tube designs. The gradual drift in tube gain that often follows a large change in tube current or counting rate is called *fatigue*[45, 46] and can be a serious problem if the tube current changes by orders of magnitude during the course of the measurement.

V. ANCILLARY EQUIPMENT REQUIRED WITH PHOTOMULTIPLIER TUBES

A. High-Voltage Supply and Voltage Divider

An external voltage source must be connected to the PM tubes in such a way that the photocathode and each succeeding multiplier stage are correctly biased with respect to one another. Because electrons must be attracted, the first dynode must be held at a voltage that is positive with respect to the photocathode, and each succeeding dynode must be held at a positive voltage with respect to the preceding dynode. For efficient photoelectron collection, the voltage between photocathode and first dynode is often several times as great as the dynode-to-dynode voltage differences.

The interstage voltage requirements of a PM tube may, in principle, be supplied by individual voltage sources, such as a multicell battery. Battery supplies are practical in some applications where counting rates are low, but often are unattractive because of the rapid discharge rates due to the current demands of the latter stages of the PM tube. The internal current in the PM tube is at a maximum between the last dynode and the anode, so the battery cell that supplies the voltage to the last dynode must be capable of a current drain equal to the average dc current leaving this dynode.

In the vast majority of cases, the voltage differences are provided instead by a resistive voltage divider and a single source of high voltage. Figure 9.13*a* shows a typical wiring diagram for the base of a PM tube in which a positive polarity high voltage is used. In this case

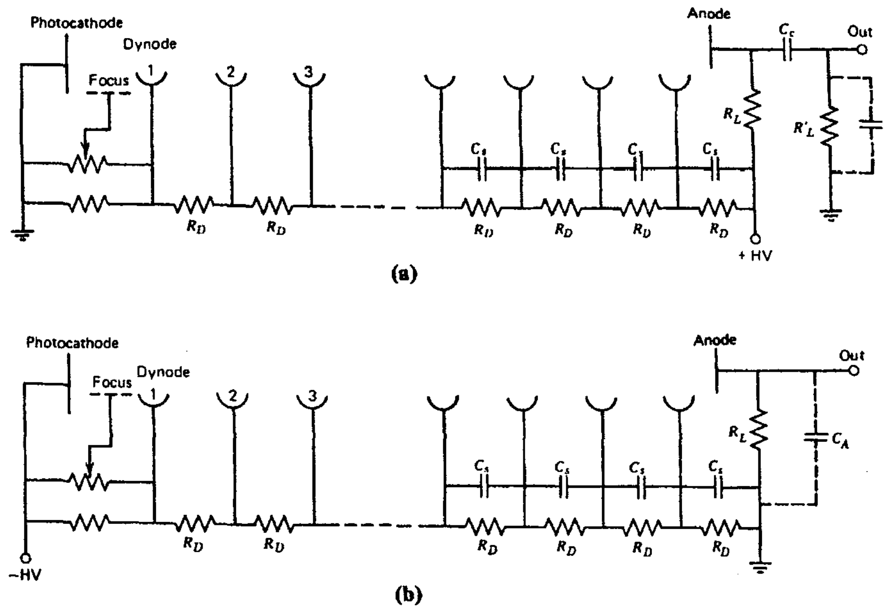

Figure 9.13 Typical wiring diagrams for the base of a PM tube. Scheme (*a*) utilizes positive high voltage and a grounded photocathode. Scheme (*b*) uses negative high voltage, and the photocathode must be isolated from ground. Values of the divider string resistors R_D are chosen using criteria given in the text. The equivalent anode load resistance is R_L in (*b*), and the parallel combination of R_L and R'_L in (*a*). Other identifications are given in the text.

the cathode of the PM tube is grounded, and the divider string supplies successively increasing positive voltages to each dynode down the multiplying string. The anode is at a dc potential equal to the supply voltage, and signal pulses must therefore be capacitively coupled from the anode to allow the pulse component to be passed on at ground potential to succeeding electronic devices. The load resistor R_L can be chosen by the experimenter so that the resulting anode circuit time constant is of proper magnitude. The anode capacitance C_A usually is not a physical capacitor, but only the stray capacitance associated with the anode structure and connecting cables. An analysis of the pulse shape expected from this anode circuit is given later in this chapter.

The direct current through the divider string is determined simply by the ratio of the applied high voltage and the summed resistance of all the resistors in the divider string. In order to use the simplest and least expensive voltage supply, one would like to keep this current at a minimum. Small currents also minimize problems caused by heat dissipation in the divider resistors. However, the divider string current should in principle be kept large compared with the internal PM tube current represented by the pulse of electrons flowing from dynode to dynode. If the internal current at the peak of a pulse becomes comparable with the divider current, the voltages of the dynodes normally will begin to deviate from their equilibrium values, leading to drift of the PM tube gain. This problem is especially serious for the last few stages of the PM tube where peak currents are at a maximum. To suppress this effect, it is commonplace to provide *stabilizing capacitors* (labeled as C_s in Fig. 9.13) to the stages of the divider string near the anode to help hold these latter dynode voltages at a constant value throughout the pulse. The stabilizing capacitor momentarily supplies the current lost from the dynode during the pulse and is recharged by the divider string current during the period between pulses. To prevent a more than 1% interdynode voltage change, the charge stored on the stabilizing capacitor (given by the product of capacitance value and the interdynode voltage) must be 100 times greater than the charge emitted by that dynode during the pulse.

A numerical example is instructive at this point. Assume we start with a scintillation event that liberates 1000 photoelectrons from the photocathode of the PM tube. Further assume that the PM tube provides an overall gain of 10^6, so that 10^9 electrons per pulse leave the last dynode and are collected by the anode. If these scintillation pulses are occurring at a rate of 10^5 per second, then the average dc anode current can easily be calculated as

$$\begin{aligned} I_{\text{avg}} &= 10^9 \frac{\text{electrons}}{\text{pulse}} \times 1.6 \times 10^{-19} \frac{\text{coulomb}}{\text{electron}} \times 10^5 \frac{\text{pulses}}{\text{second}} \\ &= 1.6 \times 10^{-5}\ \text{A} = 0.016\ \text{mA} \end{aligned} \tag{9.5}$$

Because this current appears in discrete pulses, however, the peak current during a pulse is substantially higher. As an extreme case, assume we have a very fast organic scintillator whose decay time combined with the transit time spread in the PM tube produces a narrow electron pulse of 5-ns width. The peak pulse current is then approximately

$$\begin{aligned} I_{\text{peak}} &= 10^9\ \text{electrons} \times 1.6 \times 10^{-19} \frac{\text{coulomb}}{\text{electron}} \times \frac{1}{5 \times 10^{-9}\ \text{s}} \\ &= 0.032\ \text{A} = 32\ \text{mA} \end{aligned} \tag{9.6}$$

For photomultipliers operated in either current or pulse mode, the current through the voltage divider string should be kept large compared with the average dc signal current. In the example shown, this criterion can easily be met with a voltage supply capable of a few tenths of a milliampere. In pulse mode, however, the instantaneous demands in the last few stages of the PM tube can be many times greater. In the case of the example above, it would be impractical to attempt to design the divider string with a dc current much larger than the maximum pulse current as well. In that case, a divider string current of 10 or 20 mA might be used and stabilizing capacitors provided for the last few stages in which the peak pulse current is greater than 1–2 mA. Alternate schemes which employ zener diodes or transistors to stabilize the dynode voltages are described in Refs. 47 and 48.

The polarity (+ or −) of the high voltage used with PM tubes is in some sense an arbitrary choice. In the example given previously, the photocathode end of the divider string was grounded, which then required the application of positive high voltage to the anode end of the string. Exactly the same interdynode voltages can be achieved by grounding the opposite (or anode) end of the divider string and applying negative high voltage to the photocathode end. This latter arrangement is shown in Fig. 9.13*b*. The designer of the tube base circuit must choose one of these alternatives, and both are in common use. It is therefore important that users be aware of which convention has been chosen by the manufacturer of their own tube base before initial use of the equipment with a PM tube. Mistakenly applying the wrong polarity to a PM tube is not usually fatal to the tube, but electrons will refuse to swim uphill and the PM tube will not work. Designing the tube base for positive high voltage is in some ways simpler because it allows the photocathode of the PM tube to be grounded. Because this end is often in contact with a scintillation crystal whose cover must be exposed, it is convenient to keep the crystal at ground potential as well. Operating the tube with negative high voltage means that the photocathode will be at the full high voltage supplied to the tube, and care must be taken to prevent spurious pulses due to high-voltage leakage through the glass tube envelope to nearby grounded structures. A high electric field across the tube end window can also induce spurious pulses in some tubes due to electroluminescence in the glass. An advantage that stems from use of negative high voltage is the elimination of the coupling capacitor (C_c in Fig. 9.13*a*) required if positive polarity is used. The anode is now at ground potential, and signal pulses can be direct-coupled into subsequent measuring circuits. This advantage is particularly important for fast pulse applications in which it is often desirable to couple the anode directly into a 50-ohm transmission line structure. It is also the necessary choice when the tube is to be dc-coupled to allow its operation in current mode.

Because the gain of a PM tube is extremely sensitive to changes in voltage, it is very important that sources of high voltage be well regulated and free of ripple. Drifts in the high voltage will show up as corresponding changes in tube gain and can, if sufficiently large, deteriorate the energy resolution of a scintillation counter. Any ripple is likely to be superimposed on the output signal, especially if the tube is operated with the photocathode grounded. In that case, any fluctuations in the supply voltage can be capacitively coupled directly onto the signal output. If the tube is operated with negative high voltage, the anode end of the tube is at ground potential, and ripples in the high voltage supply are important only to the extent that they modulate the overall gain of the tube.

The very large changes in gain that accompany changes in voltage with a PM tube are often a great convenience in setting up a counting system. Although the timing properties of the tube are optimized only when operated near the recommended voltage, other general properties such as linearity and relative signal-to-noise are not seriously changed over wide ranges of voltage. Therefore, it is often possible to operate a PM tube well below its recommended voltage without appreciably hurting its performance. The experimenter can therefore conveniently change the gain of the PM tube by orders of magnitude to suit the needs of the remainder of the signal chain simply by changing the applied voltage. This procedure is often followed in simple scintillation counters to determine counting plateaus and optimum operating conditions.

In those cases in which the tube voltage is likely to be varied over wide regions, the performance sometimes can suffer at the lower voltages due to reduced gain at the critical first dynode. It is here that the statistical properties of the PM tube are largely determined. In these cases a zener diode is sometimes used in conjunction with the divider string to hold the voltage between the photocathode and first dynode at a constant value, whereas the remainder of the divider string is varied.

In the usual case, the electrical signal from a PM tube is derived from the anode. The burst of electrons in the last stage of the PM tube is simply collected, resulting in a charge Q of negative polarity. As shown in Section VII of this chapter, a corresponding voltage pulse is then developed across the load resistance in the anode circuit. In some specialized applications, there may be some advantage in deriving an alternative signal from a preceding dynode. At each dynode stage, a net positive charge is induced during a pulse since more electrons leave the stage than were originally collected. This positive charge becomes progressively larger for each succeeding dynode stage due to the electron multiplication produced by each dynode. If a load resistor is placed between a given dynode and the voltage divider chain shown in Fig. 9.13, then a positive voltage pulse of smaller amplitude than the negative anode pulse can be observed. There has been some demonstration[22,49,50] that a dynode signal taken several stages before the anode has some advantage in fast timing measurements. However, the vast majority of scintillation pulses are taken from the PM tube anode, and the analysis of pulse shape beginning on p. 292 applies equally well to dynode or anode pulses. For simplicity, the analysis assumes that the anode pulse also corresponds to a positive charge Q, even though in practice the polarity of the anode pulse will be negative.

B. Magnetic Shielding

The electron optics within a PM tube are particularly sensitive to stray magnetic fields because of the low average energy (on the order of 100 eV) of the electrons traveling from stage to stage. Even the influence of the earth's magnetic field is sufficient to have an appreciable effect on the trajectories of these electrons. In situations in which the tube is likely to be physically moved or brought near equipment with stray magnetic fields, it is essential that a magnetic shield be provided to prevent gain shifts of the PM tube. The most common form consists of a thin cylinder of mu-metal that fits closely around the outside glass envelope of the PM tube. For most tube designs, this shield must be held at photocathode potential in order to avoid noise due to electroluminescence in the glass envelope.

VI. PHOTODIODES AS SUBSTITUTES FOR PHOTOMULTIPLIER TUBES

A. Potential Advantages

Photomultiplier tubes are the most common light amplifiers used with scintillators, both in pulse and current mode operation. However, advances in the development of semiconductor photodiodes have led to the substitution of solid-state devices for PM tubes in some applications. In general, photodiodes offer the advantages of higher quantum efficiency (and therefore the potential for better energy resolution), lower power consumption, more compact size, and improved ruggedness compared with PM tubes used in scintillation counting. Photodiodes are also virtually insensitive to magnetic fields and therefore can sometimes be substituted in experiments where magnetic fields prevent the use of PM tubes. Because of the relatively small dimensions over which charges must move in these devices, their time response is comparable to that of conventional PM tubes, and they can be used to good advantage in coincidence and other timing applications.

There are two general designs that have received attention as possible substitutes for PM tubes. *Conventional photodiodes* have no internal gain and operate by directly converting the optical photons from the scintillation detector to electron–hole pairs that are simply collected. *Avalanche photodiodes* incorporate internal gain through the use of higher electric fields that increase the number of charge carriers that are collected.

B. Conventional Photodiodes

Reference 51 presents a useful review of the application of conventional photodiodes for scintillator readout. When light is incident on a semiconductor, electron–hole pairs are generated in a manner similar to that detailed in Chapter 11 for incident ionizing radiation. Photons corresponding to typical scintillation light carry about 3–4 eV of energy, sufficient to create electron–hole pairs in a semiconductor with a bandgap of approximately 1–2 eV. (This process of conversion of visible light to electrical carriers is the basis of the common solar cell.) The conversion is not limited by the need for charge carriers to escape from a surface as in a conventional photocathode, so the maximum quantum efficiency of the process can be as high as 60–80%, several times larger than in a PM tube. This high quantum efficiency also spans a much wider wavelength range than is typical for photocathodes in PM tubes, so a much higher primary charge usually is created by the light from the scintillator. However, there is no subsequent amplification of this charge as in a PM tube, so the output signal is smaller by orders of magnitude.

A common configuration for a silicon photodiode is shown in Fig. 9.14. Light is incident on a p-layer entrance window that is kept as thin as possible to enhance transmission

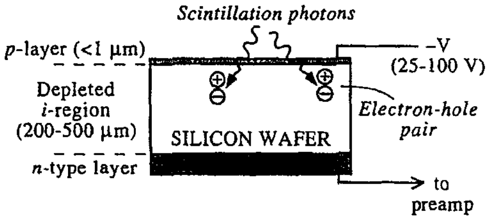

Figure 9.14 Basic configuration of a conventional photodiode.

of the light to the active volume of the silicon. Electrons and holes (see Chapter 11) produced by the light are collected at the boundaries of the central *i*-region driven by the electric field resulting from the applied voltage. The corresponding induced charge is processed in an attached preamplifier to produce the output signal pulse.

In a typical scintillation event, only a few thousand visible photons are produced, so the size of the charge pulse that can be developed is limited at best to no more than the same number of electronic charges. Because of the small signal amplitude, electronic noise is a major problem in pulse mode operation, especially for large-area detectors and low-energy radiations. In an extensive study of the performance of many different scintillators with a silicon photodiode, Sakai[5] measured energy resolution values at 662 keV that were always much poorer (often by a factor of 2) than in equivalent measurements with a PM tube. Differences were smaller for higher-energy gamma rays, but the PM tube performance was always superior. Successful applications to date have largely been limited to high-energy radiations[52–55] and/or small-diameter diodes[56–60] for which the associated dark current and capacitance are also small. In current mode, the cumulative effect of many scintillation events at high rates can override the inherent noise, resulting in excellent operational characteristics. For example, photodiodes have become the light detector of choice for current mode scintillators used in X-ray computed tomography (CT) scanners for medical imaging.[61,62]

Because photodiodes are similar to the silicon particle detectors discussed in Chapter 11, they share many of the same properties. Photodiodes are generally designed as fully depleted detectors, consisting of high purity *p*- or *n*-type silicon with highly doped *p*- and *n*-type contacts on opposite surfaces. This so-called PIN configuration is discussed in further detail in Chapter 11. The noise behavior also follows that of other semiconductor detectors and a detailed description is given in Chapter 17. Briefly, the noise arises largely from two separate sources. The first, generally called *series noise*, primarily originates from sources within the preamplifier input stage. Its relative importance increases with detector capacitance. For that reason, photodiodes with area beyond about 1 cm^2 show high noise levels and therefore are not used widely in the readout of scintillators. A second noise source, generally called *parallel noise*, is due largely to fluctuations in the leakage current in the photodiode. Since the leakage current will also tend to increase with the size of the photodiode, this second source of noise also inhibits the use of large areas. The capacitance of the photodiode will decrease as its thickness is increased, but the leakage current will tend to increase. Photodiodes common for scintillator applications are fabricated using silicon wafers of 300–500 μm thickness as something of a compromise between these conflicting trends. This thickness is much greater than would be required simply to be opaque to the incident light.

The relative contributions of series and parallel noise also depend on the shaping time constant chosen in the pulse processing electronics. Longer shaping times will tend to reduce the relative importance of series noise but will increase the importance of parallel noise (see Fig. 17.16). There will be an optimum in the choice of shaping time that will minimize the noise contribution. There are other considerations that enter this choice, however, such as the need to keep the shaping time longer than the scintillator decay time to avoid signal loss or the preference for short shaping times to minimize pulse pileup at high rates.

The spectral response of a typical silicon photodiode is plotted in Fig. 9.15. The quantum efficiency reaches higher values and extends much farther into the long wavelength region than that of typical photocathodes. This extended spectral response is particularly important for scintillators (such as CsI(Tl) or BGO) with emission spectra that have significant yield at longer wavelengths (see Fig. 8.7). The relative light yields for various scintillation materials given previously in Table 8.3 were measured using a typical PM tube photocathode response, and the values change significantly when measured with a photodiode. For example, the pulse amplitude from CsI(Tl) is smaller than the equivalent pulse from NaI(Tl) when measured with PM tubes but becomes over twice as large if the measurement is made with a silicon photodiode.[5]

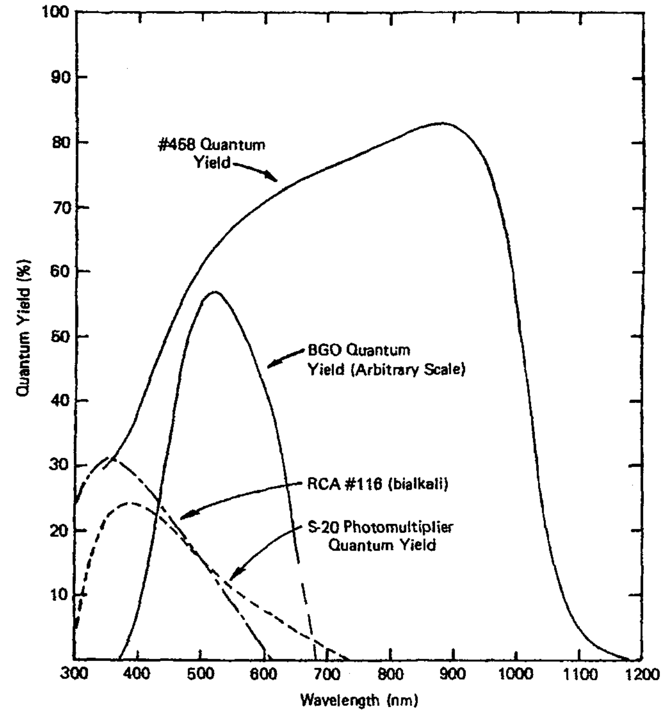

Figure 9.15 A comparison of the quantum efficiency of a silicon photodiode (labeled #458) with representative bialkali and S-20 photocathode quantum efficiencies. The emission spectrum from a BGO scintillator is shown for reference. (From Groom.[63])

For typical photodiodes fabricated from silicon, the noise levels are much larger than in an equivalent photomultiplier tube. Since the dark current is one of the contributors to the noise, its contribution and the overall noise figure can be reduced by cooling the photodiode (see Fig. 9.16). The rapid rise in dark current above room temperature has generally prevented the use of silicon photodiodes in applications requiring operation at elevated temperatures.

Another way to reduce dark current is to choose semiconductor materials with a wider band gap than silicon. For example, successful photodiodes have been fabricated using mercuric iodide crystals that have several orders of magnitude lower dark current. As a result, excellent energy resolution has been demonstrated[65–67] in scintillators coupled to small mercuric iodide photodiodes. The attainable energy resolution, because of the high quantum efficiency of the semiconductor material, is actually superior to that obtainable even with the best photomultiplier tubes. One example,[66] a 1.27-cm diameter mercuric iodide photodiode coupled to a CsI(Tl) scintillator, achieved an energy resolution of 4.58% at 662 keV.

An alternative approach to improve the noise figure in photodiodes is to reduce their capacitance. One interesting possibility[68, 69] is to choose the silicon drift configuration described in Chapter 13. These "drift photodiodes" have the combined property of relatively large area (up to 1 cm^2) and exceptionally low capacitance. To further reduce their noise, the leakage current can be suppressed by modest cooling to around 0°C. While still limited to small diameters, silicon drift photodiodes coupled to CsI(Tl) have shown the best energy resolution (4.34% at 662 keV) observed to date from any scintillation

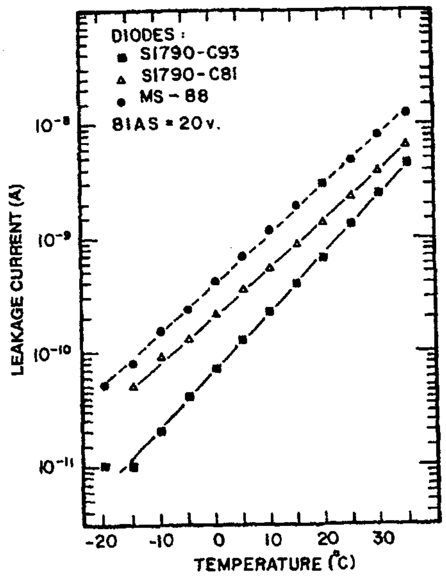

Figure 9.16 The temperature dependence of the leakage current for some typical silicon photodiodes. (From Bian et al.[64])

detector. Again, much of the improved energy resolution arises because of the improved statistics resulting from the high-quantum efficiency of the photodiode.

The rise time of the pulse from a conventional photodiode is ultimately limited by the charge collection time from the active volume, typically only a few nanoseconds. However, timing resolution is normally determined by the uncertainties introduced by the relatively high noise level. Because series noise tends to be dominant, best spectroscopic behavior is obtained by using long shaping times (see Chapter 17). Techniques for generating timing pulses generally dictate a somewhat shorter shaping time and hence introduce a larger degree of noise into the signal.

Because noise considerations limit the size of photodiodes to relatively small sizes (typically 1-cm diameter or less) it is difficult to obtain good light collection from larger size scintillators that are more typical of gamma-ray spectroscopy applications. It is tempting to think about the alternative of using multiple photodiodes to cover a greater fraction of the exit window of the scintillator, and to then add together the signals from all the photodiodes. It turns out that this approach is not very satisfactory, since not only the signal but also the noise will be additive from the multiple diodes. First stated as *Groom's theorem*,[63] the light collection and hence the signal will increase roughly in proportion to the total area of photodiodes, but the noise will also increase by the same factor. The net result is very little change in the signal-to-noise ratio.

Both conventional and avalanche photodiodes respond directly to ionizing radiation in a manner similar to that described in Chapter 11 for silicon junction detectors. When used to read out the light from scintillators, there is the possibility that, in addition to registering the pulses of light, the photodiode may also respond directly if the incident radiation can penetrate the scintillator and reach the photodiode active volume. This so-called *nuclear counter effect* can be particularly troublesome because the size of the pulse produced by these direct interactions in the silicon will always be many times greater than the pulses produced from the scintillator light. Direct interactions in the silicon produce an electron–hole pair for every 3.6 eV deposited, while 15 to 20 times that energy deposition is needed in a good scintillator to produce the same charge. The difference comes about because scintillators typically convert only about 5–10% of the particle energy into light, not all that light enters the photodiode, and there is less than 100% quantum efficiency in converting that light into electron–hole pairs. In order to minimize this nuclear counter effect, the photodiode should be kept thin. However, the capacitance of the diode increases as its thickness is decreased, adding to the noise level. Thus some compromise must be struck between avoidance of these direct interactions and the preservation of reasonable energy resolution.

C. Avalanche Photodiodes

The small amount of charge that is produced in a conventional photodiode by a typical scintillation event can be increased through an *avalanche* process that occurs in a semiconductor at high values of the applied voltage. The charge carriers are accelerated sufficiently between collisions to create additional electron–hole pairs along the collection path, in much the same way that gas multiplication occurs in a proportional counter. (This same process is described in Chapter 13 in connection with *avalanche diode* detectors for ionizing radiations.) The internal gain helps pull the signal up from the electronic noise level and permits good energy resolution in pulse mode at lower radiation energy than possible using conventional photodiodes. Because the gain factor is very sensitive to temperature and applied voltage, avalanche photodiodes require well-regulated high-voltage supplies for stable operation. For current mode applications, the inherent stability of conventional photodiodes (without gain) is usually preferred.

Avalanche photodiodes can be fabricated in a number of different ways, but a common choice known as the *reach-through configuration* is shown in Fig. 9.17. Light enters through the thin p^+ layer on the left of the diagram and interacts somewhere within the π region that constitutes most of the diode thickness. The results of interactions are electron–hole pairs, and the electron is drawn to the right through the drift portion and into the multiplying

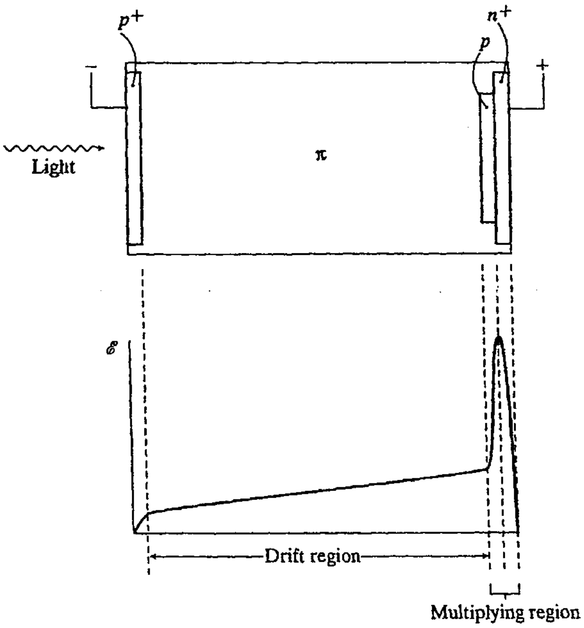

Figure 9.17 The reach-through configuration for an avalanche photodiode is sketched at the top of the figure. Below is a plot of the resulting electric field when a bias voltage is applied.

region where a high electric field exists. Here additional electron–hole pairs are created, increasing the measured signal. Gain factors of a few hundred are typical under normal circumstances. This enhancement of the signal is sufficient to allow much lower light levels to be sensed, or lower energies measured in their use with scintillators. Through the use of antireflective coatings on the external surface of the photodiode, quantum efficiencies as high as 80% are achievable at the peak wavelength of the response, typically in the 500–600 nm range. Enhanced shorter wavelength response is important for scintillators, many of which have their peak emission in the blue region of the spectrum. Measures can be taken[70] to enhance the blue sensitivity of photodiodes by proper choice of antireflective coating and the minimization of surface dead layer thickness.

In the multiplication process, electrons are drawn through the high field region and create additional electron–hole pairs. The electrons continue on in the same direction, but the holes will be attracted in the opposite direction. At sufficiently high field values, the holes can also multiply and, since hole multiplication also produces additional free electrons, this process leads to a runaway. That occurs at the breakdown voltage, and the applied voltage under normal circumstances is kept somewhat below this level. In this region, the overall gain will be an exponential function of applied voltage, accounting for the extreme sensitivity to applied voltage. The gain factor is also a strong function of temperature,[71] decreasing by a few percent per degree as the temperature is increased.

The timing properties of avalanche photodiodes can be quite favorable. In ideal cases, the limiting factor will be the variations in the electron drift time with position of interaction of the incident photon within the photodiode. These variations lead to a typical variability on the order of a nanosecond in the time at which the avalanche is triggered. In addition, the noise present with the signal also leads to timing uncertainty that often dominates the achievable timing performance. In favorable circumstances, a timing resolution of well under a nanosecond can be obtained,[72] but it is more typically a few nanoseconds or more.[73] Because of the higher signal/noise provided by the gain, shorter shaping times can be used with avalanche photodiodes than would be possible with an equivalent conventional photodiode, permitting higher rate operation and better timing resolution.

The multiplication process in an avalanche photodiode involves electrons undergoing collisions at random positions throughout the avalanche. When an ionizing collision occurs, one free electron is increased to two. The pulse-to-pulse fluctuations in gain are somewhat more significant than those observed from a typical PM tube. We have seen from Eq. (9.4) that the relative fluctuations in the gain of a PM tube decrease as the gain per dynode δ increases. Although the analogy is not exact, avalanche multiplication can be thought of as having a δ value of 2, much lower than the values typical for PM tube dynodes, and therefore the overall fluctuations might be expected to be larger. These fluctuations can be a significant contributor to the overall energy resolution observed when avalanche photodiodes are used with scintillators. The same categories of electronic noise previously mentioned for standard photodiodes are also still present, potentially degrading the energy resolution. On the other hand, the high quantum efficiency of avalanche photodiodes compared with PM tubes helps to offset these disadvantages, and excellent energy resolution has been demonstrated[74–76] in their use with small-volume scintillators.

VII. SCINTILLATION PULSE SHAPE ANALYSIS

The shape of the voltage pulse produced at the anode of a PM tube following a scintillation event depends on the time constant of the anode circuit. As discussed in Chapter 4, two extremes can be identified, both of which are commonly used in connection with scintillation counting. The first corresponds to those situations in which the time constant is chosen to be large compared with the decay time of the scintillator. This is the situation usually chosen if good pulse height resolution is a major objective and pulse rates are not excessively high. Then each pulse of electrons is integrated by the anode circuit to produce a voltage pulse whose amplitude is equal to Q/C, the ratio of the collected electron charge to the anode circuit capacitance. The second extreme is obtained by setting the anode circuit time constant to be much smaller than the scintillator decay time. As the following analysis will show, a much faster pulse results, which can often be an advantage in fast timing applications or when high pulse rates are encountered. At the same time, a sacrifice is then made in pulse amplitude and resolution.

The anode circuit can be idealized as shown in Fig. 9.18. C represents the capacitance of the anode itself, plus capacitance of the connecting cable and input capacitance of the circuit to which the anode is connected. The load resistance R may be a physical resistor wired into the tube base (see Fig. 9.13) or, if none is provided, the input impedance of the connected circuit. The current flowing into the anode $i(t)$ is simply the current of electrons from a single pulse, assumed to begin at $t = 0$. The shape of $i(t)$ will obviously influence the shape of the anode voltage pulse, and we choose for analysis a simplified representation of a typical electron pulse following a scintillation event. The principal component of emitted light from most scintillators can be adequately represented as a simple exponential decay. If the spread in transit time of the PM tube is small compared with this decay time, then a realistic model of the electron current arriving at the PM tube anode is simply

$$i(t) = i_0 e^{-\lambda t} \tag{9.7}$$

where λ is the scintillator decay constant. The initial current i_0 can be expressed in terms of the total charge Q collected over the entire pulse by noting

$$Q = \int_0^\infty i(t)\,dt = i_0 \int_0^\infty e^{-\lambda t}\,dt = \frac{i_0}{\lambda} \tag{9.8}$$

Therefore

$$i_0 = \lambda Q \tag{9.9}$$

and

$$i(t) = \lambda Q e^{-\lambda t} \tag{9.10}$$

To derive the voltage pulse $V(t)$ expected at the anode, we first note that the current flowing into the parallel RC circuit must be the sum of the current flowing into the capacitance i_C and the current through the resistance i_R

$$i(t) = i_C + i_R \tag{9.11}$$

$$i(t) = C\frac{dV(t)}{dt} + \frac{V(t)}{R} \tag{9.12}$$

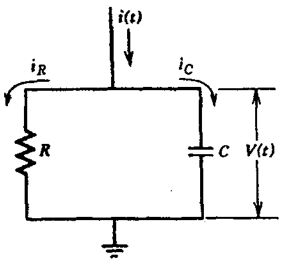

Figure 9.18 Simple parallel RC circuit representing a PM tube anode circuit.

Inserting Eq. (9.10) for $i(t)$ and dividing by C, we obtain

$$\frac{dV(t)}{dt} + \frac{1}{RC}V(t) = \frac{\lambda Q}{C}e^{-\lambda t} \tag{9.13}$$

The solution to this first-order inhomogeneous differential equation with initial condition $V(0) = 0$ can be shown to be

$$V(t) = \frac{1}{\lambda - \theta} \cdot \frac{\lambda Q}{C}(e^{-\theta t} - e^{-\lambda t}) \tag{9.14}$$

where $\theta \equiv \frac{1}{RC}$ is the reciprocal of the anode time constant.

Case 1. Large Time Constant

If the anode time constant is made large compared with the scintillator decay time, then $\theta \ll \lambda$ and Eq. (9.14) can be approximated by

$$V(t) \cong \frac{Q}{C}(e^{-\theta t} - e^{-\lambda t}) \tag{9.15}$$

A plot of this pulse form is shown in Fig. 9.19. Because $\theta \ll \lambda$, the first exponential in Eq. (9.15) decays slowly and the short time behavior is approximately

$$V(t) \cong \frac{Q}{C}(1 - e^{-\lambda t}) \qquad \left(t \ll \frac{1}{\theta}\right) \tag{9.16}$$

After a sufficiently long time, the second exponential decays to zero, and the long-time behavior is determined by the first exponential:

$$V(t) \cong \frac{Q}{C}e^{-\theta t} \qquad \left(t \gg \frac{1}{\lambda}\right) \tag{9.17}$$

The following important observations can now be made:

1. The leading edge of the pulse has the time behavior $(1 - e^{-\lambda t})$ and its rise time therefore is determined by the scintillator decay constant λ. Fast scintillators have large λ values that lead to fast-rising pulses.
2. The tail of the pulse has the time behavior $e^{-\theta t}$ and therefore decays away at a rate determined by the anode circuit time constant $RC \equiv 1/\theta$.
3. The amplitude of the pulse is given simply by Q/C, but this value is reached only if $\theta \ll \lambda$. Restated, the anode circuit time constant must be large compared with the scintillator decay time.

Most scintillation counting is carried out in this mode because the pulse height is maximized and subsequent sources of noise will have minimum degrading effect on pulse height resolution. Furthermore, the pulse amplitude achieved is not sensitive to changes in load resistance or to small changes in time characteristics of the electron pulse.

The experimenter must then choose a time constant that is at least 5–10 times greater than the scintillator decay time but that is not excessively long to prevent needless pulse pileup with the tail from a preceding pulse at high rates. The time constant is determined by the product RC, and either the anode capacitance or load resistance can be varied to change its value. In most applications, however, it is the resistance that must be tailored to achieve the desired time constant because the capacitance is intentionally held at its minimum value to maximize the pulse amplitude (Q/C).

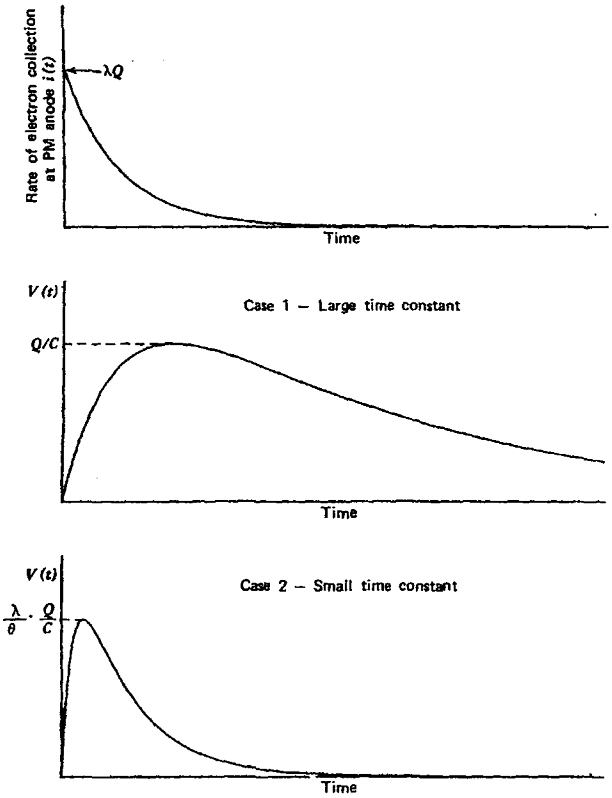

Figure 9.19 For the assumed exponential light pulse shown at the top, plots are given of the anode pulse $V(t)$ for the two extremes of large and small anode time constant. The duration of the pulse is shorter for Case 2, but the maximum amplitude is much smaller.

Case 2. Small Time Constant

In the opposite extreme, the anode time constant is set at a small value compared with the scintillator decay time, or $\theta \gg \lambda$. Now Eq. (9.14) becomes

$$V(t) = \frac{\lambda}{\theta}\cdot\frac{Q}{C}(e^{-\lambda t} - e^{-\theta t}) \tag{9.15a}$$

This pulse shape is also graphed in Fig. 9.19. The behavior at small values of t is now

$$V(t) = \frac{\lambda}{\theta}\cdot\frac{Q}{C}(1 - e^{-\theta t}) \qquad \left(t \ll \frac{1}{\lambda}\right) \tag{9.16a}$$

whereas for large t

$$V(t) = \frac{\lambda}{\theta}\cdot\frac{Q}{C}e^{-\lambda t} \qquad \left(t \gg \frac{1}{\theta}\right) \tag{9.17a}$$

The following general conclusions now apply:

1. The leading edge of the pulse has the time behavior $(1 - e^{-\theta t})$, which is determined by the anode time constant $RC \equiv 1/\theta$.
2. The tail of the pulse has the time behavior $e^{-\lambda t}$, which is identical to that of the scintillator light.
3. The maximum amplitude of the pulse is now $(\lambda Q/\theta C)$, a great deal smaller than the Case 1 maximum (Q/C) because, by definition of Case 2, $\lambda \ll \theta$.

The voltage pulse is now of much shorter duration than in Case 1, and its shape approaches that of the scintillator-produced PM tube current as the time constant is made smaller and smaller. This short duration comes at the price of a much reduced pulse amplitude, which varies linearly with the time constant and inversely with the scintillator decay time. Under fixed conditions, however, the pulse amplitude still is a linear measure of the charge Q collected by the anode, although it is more likely to be subject to fluctuations due to noise and component instabilities.

The simplified model we have used assumes a continuous and smooth current $i(t)$, which does not fully represent the discreteness or "clumped" nature of the anode current that ultimately arises from discrete photoelectrons. In Case 1, effects of the discreteness are largely smoothed out by the current integration process that takes place. In Case 2, however, no integration is carried out and the pulse form is much more sensitive to fluctuations that originate from the statistical nature of the photoelectron production. These fluctuations in pulse shape and amplitude are most serious for weak scintillation events, which produce only a small number of photoelectrons. The effect is illustrated in Fig. 9.20. When the anode time constant is very small, no significant integration of the current occurs, and the anode voltage signal reproduces the time dependence of the current shown at the middle of the figure. Only those photoelectrons contribute to the amplitude of the output pulse that, when broadened by the transit time spread of the PM tube, pile up during the early part of the scintillation event. Thus the light generated later in the decay of the scintillator does not contribute to the pulse amplitude. In contrast, the pulse shown at the bottom of the figure is taken with a large enough anode time constant to fully integrate all the light from the scintillator, and the statistical fluctuations in its amplitude will be minimized.

Even if a long anode time constant is chosen, the effective number of photoelectrons contributing to a typical pulse may be reduced in the pulse shaping step carried out in the subsequent pulse processing electronics. To avoid compromising the measured energy reso-

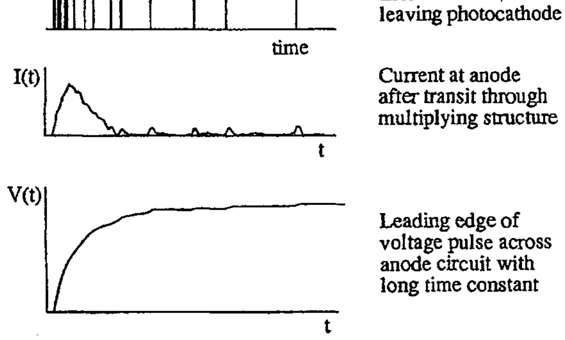

Figure 9.20 The sketch at the top represents the emission of electrons from the photocathode as a function of time following a scintillation event. The resulting current arriving at the anode is shown in the middle plot, and the bottom curve is the leading edge of the voltage pulse produced by integrating this current on an anode circuit with a long time constant.

lution, shaping times must be chosen that are several times longer than the scintillator decay time to ensure that most of the amplitude information survives through the shaping process. In order to have 95% of the scintillation light contribute to the pulse amplitude, an effective integration time that is three times the decay constant is required. Even using pulse shaping methods such as delay line clipping or gated integration (see Chapter 16) that lead to integrated pulses of minimum width, this requirement sets a lower limit on the pulse width, which in turn determines the maximum counting rate that can be tolerated. At a fundamental level, it is the overlap of the light itself from successive events within the scintillator that sets this limit. As an example, NaI(Tl) with a decay time of 230 ns thus requires a minimum pulse width of 690 ns for near-complete integration of the light. In order to avoid losing more than 10% of these pulses to pile-up (see Chapter 17), the counting rate must be held to below 74,000/s. To extend scintillation spectroscopy to higher rates, either complex pulse shape analysis schemes[77] must be employed to separate the pulses that fall near each other (not yet a common practice), or a scintillation material with faster decay time must be substituted.

VIII. HYBRID PHOTOMULTIPLIER TUBES

An interesting variant of the traditional photomultiplier tube (PMT) design is most frequently called the *hybrid photomultiplier tube* (*HPMT*) or, alternatively, the *hybrid photodiode* (*HPD*). As shown in Fig. 9.21, the basic principle involves a fundamentally different way of multiplying the charges created in a photocathode by incident light. As in a conventional PMT, the light is converted to electrons with a wavelength-dependent quantum efficiency in a photocathode. The conventional electron multiplier structure is now replaced by a silicon detector (of the type described in Chapter 11) placed in the same vacuum housing. A large voltage difference, typically between 10 and 15 kV, is applied between the photocathode and the silicon detector to accelerate electrons through the vacuum between the two elements of the tube. Photoelectrons emerge from the photocathode with very little energy—typically 1 eV or less. However, as they are drawn toward the silicon detector, they undergo continuous acceleration through the vacuum and strike the silicon detector front surface as high energy electrons. For example, if a voltage of 10 kV is applied, then the electrons arrive with a kinetic energy of 10 keV. As detailed in Chapter 11, an energetic electron of this type will lose its energy in the silicon detector through the creation of multiple electron–hole pairs. A 10-keV electron will create about 2800 such pairs if its entire energy is deposited in the active volume of the detector. Since each pair carries an electronic charge, the process just described effectively results in the multiplication of the unit charge of each photoelectron by a factor of 2800. Although this level of amplification is far less than that typical of PMTs (10^6–10^7), it nonetheless can produce signals of sufficient size to be successfully amplified in the succeeding electronic components.

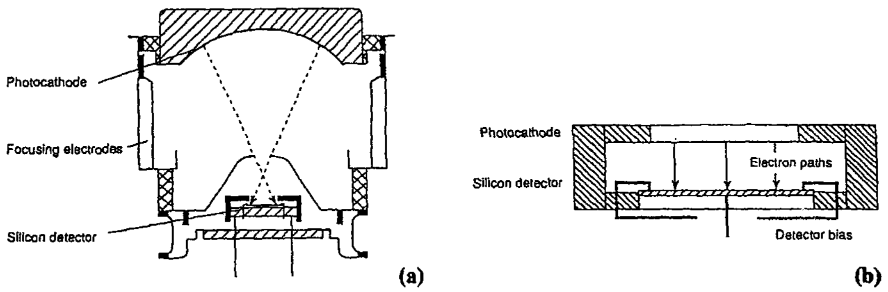

Figure 9.21 Elements of hybrid photomultiplier tubes. Part (*a*) shows the electrostatic focusing arrangement, while part (*b*) shows a proximity-focused configuration. (From Basa, et al.[78])

A. HPMT Designs

The fabrication of HPMTs involves overcoming potential difficulties of compatibility of the components in the same high vacuum environment. The photocathode is easily "poisoned" or made inefficient by trace residual gas impurities, and the silicon detector can develop high noise levels if surface contaminants produce excess leakage current. Overcoming these difficulties has led to the commercial availability of HPMT beginning in the 1990s.

As shown in Fig. 9.21, there are two general types of HPMTs: those that employ electrostatic focusing, and those that are proximity-focused. The first type uses focusing electrodes to create electron optics that guide the electrons from the large-area photocathode to a small-area silicon detector. This design has the advantage that the small silicon diode has a low capacitance and leakage current, and therefore operates at a relatively low noise level. The second type (proximity-focused) uses a larger silicon detector of about the same diameter as the photocathode and provides a much smaller gap between the two. In this case, the electrons are drawn from the photocathode to the detector along electric field lines that are essentially parallel to the tube axis. Proximity-focused tubes may incorporate a gap of only a few millimeters and therefore can be very compact with overall length of 3 cm or less. This type, with its short and parallel electron paths, is perturbed by external magnetic fields much less than electrostatically focused designs, particularly when they are oriented with the magnetic field parallel to the tube axis.

B. Operational Characteristics

HPMTs have been successfully demonstrated to read out the light from typical scintillation gamma spectrometers[79] and are often applied in situations in which the detected light levels are very low. The most striking advantage of the HPMT over conventional tubes is the much lower statistical spread in the amplitude of the output pulse. As previously illustrated in Fig. 9.5, this statistical spread is determined almost exclusively by the number of charge carriers produced per incident electron in the first stage of amplification. The larger this number, the smaller will be the relative statistical broadening. In ordinary PMTs, a typical number for the first stage multiplication might be 5, while in high gain NEA dynode materials it could be as large as 25. The corresponding number in the HPMT is typically 2500–3500. Thus if repeated events occur in which exactly a fixed number of photoelectrons are released from the photocathode, the pulse height spectrum recorded from these events will be much broader from a PMT than from a HPMT. One way of illustrating the statistical effects is to record the pulse height spectrum while the tube is illuminated with a weak light source that creates a series of pulses whose average number of photoelectrons is relatively small. One example of this type of spectrum was given previously for a NEA dynode PM tube in Fig. 9.6. With a perfect light sensor, the recorded spectrum would consist of a series of separately resolved peaks corresponding to 1, 2, 3, ... photoelectrons per pulse. Because of statistical spreading, the spectrum resolves only the first three of these peaks. Contrast that circumstance with the spectrum shown in Fig. 9.22, taken from a HPMT. Here the peaks are separately resolvable all the way to a value of 14 photoelectrons. These peaks are seen to be superimposed on a broad continuum that arises largely because some of the incident electrons are backscattered from the silicon detector before they deposit all their energy. For incident 13 keV electrons, about 18% of the electrons are backscattered.[80]

One of the major benefits of the superior statistical behavior of the amplification is the ability to better separate those events that correspond to a single photoelectron from those that arise from multiple photoelectrons. For example, thermionic noise arises from single photoelectrons emitted randomly in time from the photocathode, and therefore such noise pulses will appear in the single photoelectron peak. If that peak is cleanly separated from those corresponding to multiple photoelectrons, then a simple pulse height discrimination

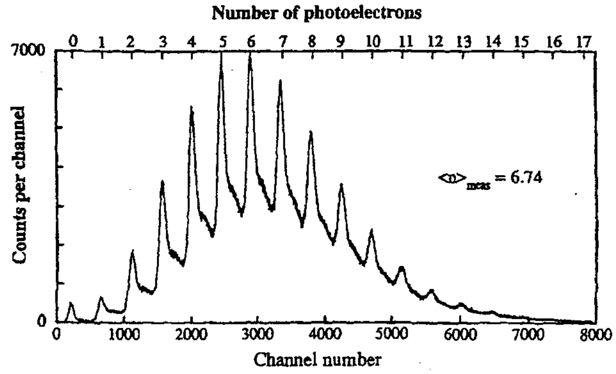

Figure 9.22 Pulse height spectrum taken from a hybrid photomultiplier tube when illuminated by light pulses of low intensity. Separate peaks can be distinguished for events that originate from the discrete number of photoelectrons shown along the top of the plot. (From D'Ambrosio et al.[80])

can eliminate the thermionic noise without sacrificing more than absolutely necessary of the signal events. The clean resolution of single photon events from electronic noise has also been exploited in many applications in which the signal itself consists of only single photoelectrons released from the photocathode. If the only broadening effects were statistical, the individual photoelectron peaks shown in Fig. 9.22 should have a predicted pulse height resolution of under 1% (see discussion of energy resolution in Chapter 11). The widths actually observed are much broader than this because of the added contribution of electronic noise in the amplifying elements necessary to process these low-level signals.

HPMTs also have a number of other operational advantages. Because the gain factor depends only on the energy deposited in the silicon detector, it should vary linearly with the value of the applied high voltage. This behavior is observed experimentally if allowance is made for the energy loss of the electrons in the entrance window of the detector (typically a few hundred to a thousand eV). In contrast, for a conventional PMT the gain typically varies as the voltage raised to the seventh or eighth power [see Eq. (9.3)]. Thus there is much less sensitivity to instability or drift in the voltage supply. Furthermore, the only current drawn from the high voltage supply is the internal current represented by the flow of photoelectrons. This current is many orders of magnitude smaller than the current typically required in the resistive divider string of a PMT to stabilize the interdynode voltages. For these reasons, much simpler and more compact high voltage supplies can be used with HPMTs, despite the somewhat higher values of the voltages required. The simplicity of the single-stage multiplication also generally results in much less temperature sensitivity of the gain than in a conventional tube.

The timing properties of HPMTs are also quite favorable. In either the electrostatic-focused or proximity-focused tubes, there is very little spread in the transit time compared with that observed from conventional PMTs. The accelerated photoelectrons are stopped near the entrance of the silicon detector, forming electron–hole pairs. The silicon detector, which typically might be 300 μm thick, is normally biased to collect positive charges (holes) at the front surface and negative charges (electrons) at the rear. Thus the holes are quickly collected, and it is the flow of electrons through most of the thickness of the depletion region that gives rise to the observed signal current (see discussions in Chapter 11). The corresponding current pulse from small-diameter (low capacitance) silicon detectors has a duration of a few nanoseconds with rise and fall times of less than 1 ns. Timing precision of 100 ps has been demonstrated,[81] but best performance is only achieved in applications for which large light pulses are produced because of the influence of the electronic noise in the external electronics on the timing precision.

C. Variants of the HPMT

Several other versions of the HPMT have been investigated that employ different types of silicon detectors. Because the gain achievable using a conventional silicon detector is only a few thousand, designs have been produced that substitute an avalanche silicon detector that provides an additional internal gain factor. Small diameter avalanche photodiodes are capable of providing an internal gain of several hundred, thereby boosting the overall gain of the tube to over 10^5. This type of amplification is now much more typical of conventional PMTs, and overcomes many of the problems of low amplitude pulses. However, the statistics of the gain multiplication caused by avalanching adds a large broadening to the output pulses, and the individual photoelectron peaks illustrated in Fig. 9.22 can no longer be observed. Another variation is to substitute a position-sensitive silicon detector. This implementation converts the HPMT into a position-sensitive PMT of the type discussed in the next section. In one such design,[82] 1024 separate pixels were provided on the silicon detector, each bonded to its own read-out electronics. Further developments of this type should be expected in this rapidly developing area of technology.

IX. POSITION-SENSING PHOTOMULTIPLIER TUBES

In ordinary scintillation counting, the light from a typical scintillation event is spread over the entire PM tube photocathode, and therefore the point of interaction within the photocathode is of no particular interest. However, there are some specialized applications, for example, in particle physics or in nuclear medicine, in which the position of the arriving photon on the photocathode carries some information. For these applications, there has been interest in developing PM tubes that can provide some position information regarding the incident light.

A first requirement in any such design is to use an electron-multiplying structure that maintains spatial separation between the multiplied electron clouds originating from photoelectrons generated at separate locations on the photocathode. This requirement rules out the common multiplier structures such as those illustrated in Fig. 9.7 in which electrons from all areas of the photocathode are focused onto a common dynode. However, several of the electron multiplier structures we have already discussed meet this requirement of confining the multiplied electrons to a localized position. These include the microchannel plate multiplier in which each multiplied electron cloud is confined to a single small channel, and the hybrid photomultiplier tube in which electrons from the photocathode are accelerated onto a corresponding position on a silicon detector. PMTs based on these multiplier configurations are commercially available and can be used in position sensing or imaging applications.

Other specialized dynode multiplier structures have also been developed specifically to produce position-sensitive photomultiplier tubes. The first of these consists of a fine mesh structure in which as many as 16–20 stages of multiplication are produced by layering metal dynodes that are perforated with many holes, as illustrated in Fig. 9.23. When an appropriate surface treatment is given to the dynode structures and they are operated at optimum potential between layers, secondary electron yields of about three per stage are achievable. Thus an overall gain of 10^6–10^9 can be realized,[83] using up to 20 stages. With this configuration, there is a natural tendency for the charge to spread as the multiplication takes place from stage to stage. This spreading is clearly undesirable if the ultimate in spatial resolution is needed. Thus other dynode designs have evolved using fine meshes[84,85] or a metal channel dynode structure (see Fig. 9.24) that do a better job of confining the multiplied charge to a narrow spot. A concern in the design of this type of position-sensitive PMT is the uniformity of response to light across the entrance area of the photocathode. Factors of two deviation in the gain of the tube can be observed[87] in some types of tubes.

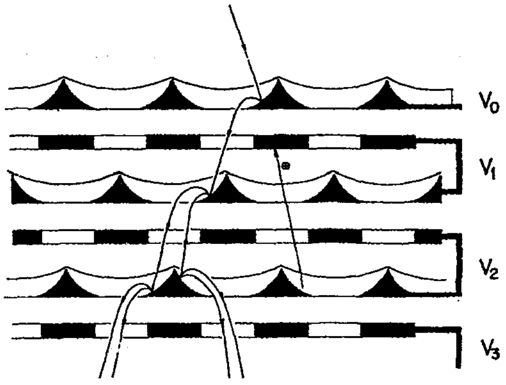

Figure 9.23 Cross section of a focused mesh electron multiplier. Each cusp-shaped dynode layer has an associated guard plate with its holes aligned over the points of the cusps. The guard plate helps focus the emitted secondary electrons onto the next dynode layer and also stops any secondary ions (the upward arrow shown) from causing ion feedback. (From Vallerga et al.[83])

These variations involve not only the nonuniformity of the photocathode but also variations in the probability of collecting a photoelectron depending on its emission position.

At the anode end or output of the tube, several schemes can be used to retain the position information. The most direct method is to simply divide the anode into separate discrete anodes or pixels, each with its own individual readout connection. As long as the cross-talk caused by electron spreading is kept small, an array of 8 × 8 anodes is equivalent to packaging 64 separate photomultiplier tubes in a common vacuum enclosure. Such tubes have been made available commercially that have sufficient pulse height resolution to distinguish the peak in the spectrum from the detection of single photons. An alternative method is to provide two layers of anode wires, each layer consisting of multiple parallel wires. The two layers are oriented with their wires perpendicular to those in the other layer to produce separate x and y position coding. This "crossed anode wire" readout is widely used for position-sensitive PM tubes because the charge division scheme illustrated in Fig. 9.25 can be used to reduce the number of readout channels to four. Alternatively, each separate anode wire can be read out with its own preamplifier[87] to allow greater flexibility for correction of inevitable nonlinearities in the spatial signals using the charge-sharing technique.

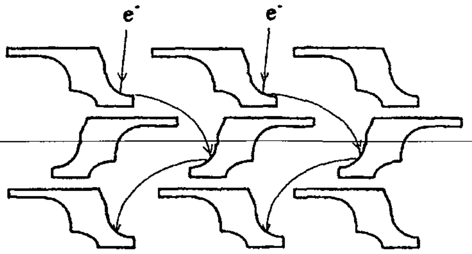

Figure 9.24 Cross section of a metal channel dynode structure. (From Yoshizawa and Takeuchi.[86])

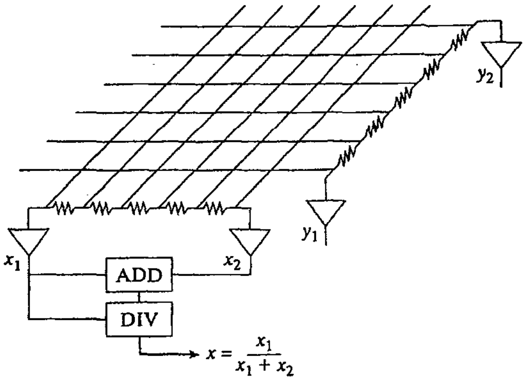

Figure 9.25 Illustration of the crossed-wire scheme for readout of a position-sensing photomultiplier tube. A resistor chain interconnecting all the wires running in one dimension is provided with preamplifiers on each end. Carrying out the operations shown produces a pulse that ideally is proportional only to the event coordinate in that dimension.

X. PHOTOIONIZATION DETECTORS

There is another alternative to PM tubes that has been exploited for applications in which the light to be detected is in the ultraviolet portion of the spectrum. Certain organic compounds in the gaseous phase can be ionized by UV photons to form ion pairs. If the organic vapor is incorporated as a component of the fill gas of a conventional detector that is sensitive to ionization (such as a proportional counter), then the signal pulse amplitude will reflect the number of incoming photons that have undergone conversion to ions. Furthermore, if position-sensitive detectors such as multiwire proportional counters are used, the spatial position of the conversion point can also be determined.

Some organic compounds that are of interest as photoionization agents are listed in Table 9.2. Of these, TMAE and TEA have received the most attention. It has been shown that each can be successfully incorporated into standard proportional gases with typical concentration of up to 3%. In the case of TMAE, its vapor pressure of 0.35 torr at 20°C (Ref. 89) is a limit on its room temperature absolute concentration in the gas phase. At that partial pressure, its quantum efficiency is approximately 2% per mm of path length for the fast component of the emission spectrum (see Fig. 8.13) from BaF_2 (Ref. 90). The vapor reacts with oxygen and organic materials such as vacuum grease and O-rings, so that some care is needed in chamber design and gas handling procedures. TEA is somewhat easier to handle and has a higher vapor pressure, but its higher photoionization potential limits its response to shorter wavelengths.

Table 9.2 Some Organics Potentially Useful in Photoionization Detectors

Acronym	Chemical Name	Vapor Phase Ionization Potential (eV)	Long-Wavelength Cutoff (nm)
TMAE	Tetrakis(dimethylamino)ethylene	5.36	231
TMBI	1,1′,3,3′-Tetramethyl-2,2′-biimidazolidinylidene	5.41	229
TMAB	1,1,4,4-Tetrakis(dimethylamino)butadiene	5.60	221
TMPD	*N,N,N′,N′*-tetramethyl-*p*-phenylenediamine	6.20	200
TEA	Triethylamine	7.5	165

Data as tabulated by Policarpo.[88]

Photoionization detectors are not commercially available, but they can offer interesting properties for specialized applications. They can be made in almost unlimited size with excellent uniformity of response over the large area entrance window. Good spatial resolution can also be achieved (of interest in imaging applications) by incorporating the position-sensing techniques discussed in Chapter 5 for large-area proportional detectors. They have found useful application in the detection of UV emissions from scintillators,[90–92] Cherenkov detectors,[93–95] and gas proportional scintillation counters.[88, 93]

PROBLEMS

9.1. Calculate the long-wavelength limit of the sensitivity of a photocathode layer with work function of 1.5 eV.

9.2. Find the transit time for an electron between typical dynodes in a PM tube if the interdynode spacing is 12 mm and the potential difference is 150 V per stage. For simplicity, assume a uniform electric field.

9.3. Using the data plotted in Fig. 9.3, find the total applied voltage necessary for a PM tube with a six-stage multiplier using GaP(Cs) dynodes to achieve an electron gain factor of 10^6.

9.4. The dark current from a PM tube with electron gain of 10^6 is measured to be 2 nA. What is the corresponding electron emission rate from the photocathode?

9.5. The gain per dynode δ of a 10-stage PM tube varies as $V^{0.6}$ where V is the interdynode voltage. If the tube is operated at an overall voltage of 1000 V, how much voltage fluctuation can be tolerated if the gain is not to change by more han 1%?

9.6. The decay time (inverse of the decay constant) for scintillations in NaI(Tl) is 230 ns. Neglecting any time spread introduced by the PM tube, find the maximum value of the voltage pulse amplitude for anode circuit time constants of 10, 100, and 1000 ns. Express your answer as a ratio to the amplitude that would be observed for an infinite time contant. What is the minimum value of the time constant if this ratio is to be at least 0.9?

9.7. A current pulse of the following shape flows into a parallel RC circuit:

$$
\begin{aligned}
i(t) &= I \qquad 0 \le t < T \\
i(t) &= 0 \qquad T \le t
\end{aligned}
$$

Find the general solution $V(t)$ for the voltage appearing across the circuit, assuming $V(0) = 0$. Sketch the solution in he two limits:

(a) $RC >> T$.

(b) $RC << T$.

9.8. Calculate the amplitude of the signal pulse expected from a NaI(Tl)–PM tube combination under the following circumstances:

Radiation energy loss: 1.2 MeV.

Light collection efficiency: 70%.

Photocathode quantum efficiency: 20%.

PM tube electron gain: 100,000.

Anode capacitance: 100 pF.

Anode load resistance: 10^5 ohms.

Any other physical parameters you may need can be found in the text.

9.9. What is the principal advantage of microchannel plate PM tubes compared with more conventional designs?

9.10. The bandgap energy in silicon at room temperature is 1.11 eV. Calculate the longest wavelength of light that is energetically capable of exciting an electron across this gap to create an electron–hole pair in a photodiode.

9.11. A scintillator absorbs an incident flux of 5 MeV alpha particles that totals 10^6 particles/s. The scintillation efficiency for these particles is 3%, and the average wavelength of the emitted light is 420 nm. If the scintillator is coupled to a photodiode with an average quantum efficiency of 75% for the scintillation light and the light collection efficiency is 80%, estimate the expected signal from the photodiode when operated in current mode.

9.12. Estimate the acceleration voltage required for a hybrid photomultiplier tube using a silicon diode to have a charge gain of 5000.

REFERENCES

1. *RCA Photomultiplier Manual.* Technical Series PT-61, RCA Solid State Division, Electro Optics and Devices, Lancaster, PA, 1970. (See also other manufacturer's publications such as *Photomultiplier Tubes, Principles and Applications*, Philips Photonics, Philips Export B. V., 1994; *Photomultiplier Tube, Principle to Application*, Hamamatsu Photonics K. K., 1994.)
2. G. A. Morton, *IEEE Trans. Nucl. Sci.* **NS-22** (1), 26 (1975).
3. "Test Procedures for Photomultipliers for Scintillation Counting and Glossary for Scintillation Counting Field," IEEE Standard 398-1990, (1990).
4. M. Miyajima, S. Sasaki, and E. Shibamura, *Nucl. Instrum. Meth.* **224**, 331 (1984).
5. E. Sakai, *IEEE Trans. Nucl. Sci.* **NS-34** (1), 418 (1987).
6. H. R. Krall, F. A. Helvy, and D. E. Persyk, *IEEE Trans. Nucl. Sci.* **NS-17**(3), 71 (1970).
7. R. E. Simon and B. F. Williams, *IEEE Trans. Nucl. Sci.* **NS-15**(3), 167 (1968).
8. G. A. Morton, H. M. Smith, Jr., and H. R. Krall, *IEEE Trans. Nucl. Sci.* **NS-16** (1), 92 (1969).
9. B. Leskovar and C. C. Lo, *IEEE Trans. Nucl. Sci.* **NS-19**(3), 50 (1972).
10. H. R. Krall and D. E. Persyk, *IEEE Trans. Nucl. Sci.* **NS-19**(3), 45 (1972).
11. H. Houtermans, *Nucl. Instrum. Meth.* **112**, 121 (1973).
12. T. Sandor, *Nucl. Instrum. Meth.* **78**, 8 (1970).
13. R. Bosshard et al., *IEEE Trans. Nucl. Sci.* **NS-19**(3), 107 (1972).
14. F. W. Inman and J. J. Muray, *IEEE Trans. Nucl. Sci.* **NS-16**(2), 62 (1969).
15. J. R. Prescott, *Nucl. Instrum. Meth.* **39**, 173 (1966).
16. J. P. Ballini, *Nucl. Instrum. Meth.* **116**, 109 (1974).
17. J. Ballini, P. Cazes, and P. Turpin, *Nucl. Instrum. Meth.* **134**, 319 (1976).
18. B. Leskovar, *Phys. Today* **30**(11), 42 (1977).
19. G. Pietri, *IEEE Trans. Nucl. Sci.* **NS-22**(5), 2084 (1975).
20. S. Dhawan and R. Majka, *IEEE Trans. Nucl. Sci.* **NS-24**(1), 270 (1977).
21. C. C. Lo, P. Lecomte, and B. Leskovar, *IEEE Trans. Nucl. Sci.* **NS-24**(1), 302 (1977).
22. B. Leskovar and C. C. Lo, *IEEE Trans. Nucl. Sci.* **NS-25**(1), 582 (1978).
23. M. Moszynski, J. Vacher, and R. Odru, *Nucl. Instrum. Meth.* **204**, 141 (1982).
24. M. Moszynski, J. Vacher, and R. Odru, *Nucl. Instrum. Meth.* **204**, 471 (1983).
25. J. De Vries and C. W. E. Van Eijk, *Nucl. Instrum. Meth.* **A239**, 243 (1985).
26. B. Leskovar and T. T. Shimizu, *IEEE Trans. Nucl. Sci.* **NS-34**, 427 (1987).
27. V. V. Anashin et al., *Nucl. Instrum. Meth.* **A357**, 103 (1995).
28. H. Kume et al., *IEEE Trans. Nucl. Sci.* **NS-33**(1), 364 (1986).
29. F. de la Barre, *Nucl. Instrum. Meth.* **102**, 77 (1972).
30. B. Sipp and J. A. Miehe, *Nucl. Instrum. Meth.* **114**, 249 (1974).
31. M. Moszynski, *Nucl. Instrum. Meth.* **A337**, 154 (1993).
32. F. A. Johnson, *Nucl. Instrum. Meth.* **87**, 215 (1970).
33. G. Gangopadhyay, D. Banerjee, and R. Bhattacharya, *Nucl. Instrum. Meth.* **A336**, 186 (1993).
34. G. A. Morton, H. M. Smith, and R. Wasserman, *IEEE Trans. Nucl. Sci.* **NS-14**(1), 443 (1967).
35. S. J. Hall and J. McKeown, *Nucl. Instrum. Meth.* **112**, 545 (1973).
36. R. Staubert et al., *Nucl. Instrum. Meth.* **84**, 297 (1970).
37. S. S. Stevens and J. W. Longworth, *IEEE Trans. Nucl. Sci.* **NS-19**(1), 356 (1972).
38. G. P. Lamaze, J. K. Whittaker, R. A. Schrack, and O. A. Wasson, *Nucl. Instrum. Meth.* **123**, 403 (1975).
39. R. Mirzoyan, E. Lorenz, D. Petry, and C. Prosch, *Nucl. Instrum. Meth.* **A387**, 74 (1997).
40. J. M. Paul, *Nucl. Instrum. Meth.* **89**, 285 (1970).
41. H. J. Kellermann et al., *Nucl. Instrum. Meth.* **115**, 301 (1974).
42. A. K. Gupta and N. Nath, *Nucl. Instrum. Meth.* **53**, 352 (1967).
43. C. Weitkamp, G. G. Slaughter, W. Michaelis, and H. Schmidt, *Nucl. Instrum. Meth.* **61**, 122 (1968).
44. M. Yamashita, *Nucl. Instrum. Meth.* **142**, 435 (1977).
45. L. Cathy, "Control of Fatigue in Photomultipliers," DP-642 (1961).
46. R. D. Conner and M. K. Husain, *Nucl. Instrum. Meth.* **6**, 337 (1960).
47. R. D. Hiebert, H. A. Thiessen, and A. W. Obst, *Nucl. Instrum. Meth.* **142**, 467 (1977).
48. C. R. Kerns, *IEEE Trans. Nucl. Sci.* **NS-24**(1), 353 (1977).
49. J. De Vries and F. E. T. Kelling, *Nucl. Instrum. Meth.* **A262**, 385 (1987).
50. B. Bengtson and M. Moszynski, *Nucl. Instrum. Meth.* **204**, 129 (1982).
51. M. Suffert, *Nucl. Instrum. Meth.* **A322**, 523 (1992).
52. R. Glasow et al., *Nucl. Instrum. Meth.* **228**, 354 (1985).
53. G. Hall et al., *IEEE Trans. Nucl. Sci.* **NS-33**(1), 310 (1986).
54. W. G. Gong et al., *Nucl. Instrum. Meth.* **A268**, 190 (1988).
55. V. Prat et al., *Nucl. Instrum. Meth.* **A380**, 209 (1996).
56. S. E. Derenzo, *Nucl. Instrum. Meth.* **219**, 117 (1984).
57. H. Grassmann et al., *Nucl. Instrum. Meth.* **A234**, 122 (1985).
58. E. Gramsch et al., *Nucl. Instrum. Meth.* **A311**, 529 (1992).
59. A. J. Bird et al., *IEEE Trans. Nucl. Sci.* **40(4)**, 395 (1993).
60. V. Prat, H. Simon, and A. Kazandjian, *Nucl. Instrum. Meth.* **A369**, 617 (1996).
61. D. P. Boyd, *IEEE Trans. Nucl. Sci.* **NS-26**(2), 2836 (1979).
62. T. Takahashi, H. Itoh, T. Shimada, and H. Takeuchi, *IEEE Trans. Nucl. Sci.* **37(3)**, 1478 (1990).
63. D. E. Groom, *Nucl. Instrum. Meth.* **219**, 141 (1984).
64. Z. Bian, J. Dobbins, and N. Mistry, *Nucl. Instrum. Meth.* **A239**, 518 (1985).
65. J. Markakis, *IEEE Trans. Nucl. Sci.* **NS-35**(1), 356 (1988).
66. Y. J. Wang et al., *IEEE Trans. Nucl. Sci.* **43(3)**, 1277 (1996).
67. M. P. Tornai et al., *IEEE Trans. Nucl. Sci.* **44(3)**, 1127 (1997).
68. C. Fiorini et al., *Nucl. Instrum. Meth.* **A409**, 395 (1998).
69. C. Fiorini, F. Perotti, and C. Labanti, *IEEE Trans. Nucl. Sci.* **45(3)**, 483 (1998).
70. E. Gramsch and R. E. Avila, *Nucl. Instrum. Meth.* **A414**, 299 (1998).
71. S. Kobayashi, K. Yamaoka, M. Amami, and M. Kobayashi, *Nucl. Instrum. Meth.* **A364**, 95 (1995).
72. M. Moszynski et al., *IEEE Trans. Nucl. Sci.* **43(3)**, 1298 (1996).
73. C. Carrier and R. Lecomte, *Nucl. Instrum. Meth.* **A299**, 115 (1990).
74. K. M. James and M. J. Masterson, *Nucl. Instrum. Meth.* **A313**, 196 (1992).
75. A. Ochi, Y. Nishi, and T. Tanimori, *Nucl. Instrum. Meth.* **A378**, 267 (1996).
76. M. Moszynski et al., *IEEE Trans. Nucl. Sci.* **45(3)**, 472 (1998).
77. W. -H. Wong and H. Li, *IEEE Trans. Nucl. Sci.* **45(3)**, 838 (1998).

78. S. Basa et al., *Nucl. Instrum. Meth.* **A330**, 93 (1993).

79. G. Bellia, L. Cosentino, P. Finocchiaro, and K. Loukachine, *Nucl. Instrum. Meth.* **A385**, 116 (1997).

80. C. D'Ambrosio et al., *Nucl. Instrum. Meth.* **A345**, 279 (1994).

81. P. Benetti et al., *Nucl. Instrum. Meth.* **A367**, 384 (1995).

82. T. Gys et al., *Nucl. Instrum. Meth.* **A387**, 131 (1997).

83. J. Vallerga, J. Hull, and M. Lampton, *IEEE Trans. Nucl. Sci.* **35(1)**, 539 (1988).

84. S. Suzuki et al., *IEEE Trans. Nucl. Sci.* **40(4)**, 431 (1993).

85. D. Grigoriev, O. Johnson, W. Worstell, and V. Zavarzin, *IEEE Trans. Nucl. Sci.* **44(3)**, 990 (1997).

86. Y. Yoshizawa and J. Takeuchi, *Nucl. Instrum. Meth.* **A387**, 33 (1997).

87. R. A. Kroeger et al., *IEEE Trans. Nucl. Sci.* **44(3)**, 881 (1997).

88. A. J. P. L. Policarpo, *Nucl. Instrum. Meth.* **196**, 53 (1982).

89. D. F. Anderson, *IEEE Trans. Nucl. Sci.* **NS-28**(1), 842 (1981).

90. C. L. Woody, C. I. Petridou, and G. C. Smith, *IEEE Trans. Nucl. Sci.* **NS-33**(1), 136 (1986).

91. D. F. Anderson et al., *Nucl. Instrum. Meth.* **225**, 8 (1984).

92. D. Visvikis et al., *Nucl. Instrum. Meth.* **A392**, 414 (1997).

93. D. F. Anderson, *IEEE Trans. Nucl. Sci.* **NS-32** (1), 495 (1985).

94. P. Krizan et al., *Nucl. Instrum. Meth.* **A367**, 257 (1995).

95. J. Va'vra, J. Kadyk, J. Wise, and P. Coyle, *Nucl. Instrum. Meth.* **A370**, 352 (1996).

Chapter 10

Radiation Spectroscopy with Scintillators

The widespread availability in the early 1950s of thallium-activated sodium iodide scintillation detectors allowed the spectroscopy of gamma rays to be carried out for the first time with small, portable instruments. With this development, a practical detector was available that could provide a high efficiency for the detection of gamma rays and, at the same time, was capable of sufficiently good energy resolution to be useful in separating the contributions of polyenergetic gamma-ray sources. Gamma-ray spectroscopy using scintillators has since developed into a mature science with applications in an impressive array of technical fields.

Despite the fact that it was virtually the first practical solid detection medium used for gamma-ray spectroscopy, NaI(Tl) remains the most popular scintillation material for this application. This extraordinary success stems from its extremely good light yield, excellent linearity, and the high atomic number of its iodine constituent. Other scintillators mentioned in Chapter 8, notably cesium iodide and some of the newer inorganic scintillators, have also achieved some success in gamma-ray spectroscopy, but the combined use of all other materials extends to only a small fraction of the cases in which sodium iodide is found. In the sections that follow, we concentrate on NaI(Tl), with the understanding that most of the discussion and general conclusions can be extended to other scintillation materials by taking into account the differences in their gamma-ray interaction probabilities and scintillation properties.

Useful textbook reviews of scintillation spectroscopy of gamma radiation have been published by Birks,[1] Shafroth,[2] and Siegbahn.[3]

GENERAL CONSIDERATIONS IN GAMMA-RAY SPECTROSCOPY

An X-ray or gamma-ray photon is uncharged and creates no direct ionization or excitation of the material through which it passes. The detection of gamma rays is therefore critically dependent on causing the gamma-ray photon to undergo an interaction that transfers all or part of the photon energy to an electron in the absorbing material. These interaction processes are detailed in Chapter 2 and represent sudden and major alterations of the photon properties, as opposed to the continuous slowing down of heavy charged particles or electrons through many simultaneous interactions.

Because the primary gamma-ray photons are "invisible" to the detector, it is only the fast electrons created in gamma-ray interactions that provide any clue to the nature of the incident gamma rays. These electrons have a maximum energy equal to the energy of the incident gamma-ray photon and will slow down and lose their energy in the same man as any other fast electron, such as a beta particle. Energy loss is therefore through ion tion and excitation of atoms within the absorber material and through bremsstrahl emission (see Chapter 2).

In order for a detector to serve as a gamma-ray spectrometer, it must carry out two d tinct functions. First, it must act as a conversion medium in which incident gamma rays ha a reasonable probability of interacting to yield one or more fast electrons; second, it mu function as a conventional detector for these secondary electrons. In the discussion that fo lows, we first assume that the detector is sufficiently large so that the escape of second electrons (and any bremsstrahlung created along their track) is not significant. For incide gamma rays of a few MeV, the most penetrating secondary electrons will also be created wi a few MeV kinetic energy. The corresponding range in typical solid detector media is a fe millimeters (most bremsstrahlung photons generated along the electron track will be co siderably less penetrating). The assumption of complete electron absorption therefo implies a detector whose minimum dimension is at least about a centimeter. Then only small fraction of the secondary electrons, which are created more or less randomly throug out the volume of the detector, lie within one range value of the surface and could possib escape. Later in this chapter we discuss the complicating effects of electron a bremsstrahlung escape in small detectors as a perturbation on the simpler model that follow

The following discussions are kept relatively general so that they apply not only other scintillation materials but also to other solid or liquid detection media used gamma-ray spectroscopy. Chapters 12 and 13 discuss semiconductor detectors, which al have been widely applied to gamma-ray spectroscopy. The following section serves as general introduction to these chapters as well, because the basic modes of gamma-r interactions are identical for all detector types.

Because of the low stopping power of gases, the requirement of full energy absorpti for the secondary electrons generally rules out gas-filled detectors for the spectroscopy gamma rays. Exceptions to this statement are possible only if the gas is at very high pre sure (see the discussion of high pressure xenon chambers in Chapter 19) or if the incide photon has very low energy. The penetration distance of a 1 MeV electron in STP gases several meters, so normal gas-filled detectors of practical size can never come close absorbing all the secondary electron energy. To complicate the situation further, m gamma-ray-induced pulses from a gas-filled counter arise from gamma-ray interactio taking place in the solid counter wall, following which the secondary electron finds its w to the gas. Under these conditions, the electron loses a variable and indeterminate amou of energy in the wall, which does not contribute to the detector output pulse, and virtual all hope of relating the electron to incident gamma-ray energy is lost.

II. GAMMA-RAY INTERACTIONS

Of the various ways gamma rays can interact in matter, only three interaction mechanis have any real significance in gamma-ray spectroscopy: photoelectric absorption, Compt scattering, and pair production. As detailed in Chapter 2, photoelectric absorption p dominates for low-energy gamma rays (up to several hundred keV), pair production p dominates for high-energy gamma rays (above 5–10 MeV), and Compton scattering is t most probable process over the range of energies between these extremes. The ato number of the interaction medium has a strong influence on the relative probabilities these three interactions, as can be seen from the formulas and plots given in Chapter 2. T most striking of these variations involves the cross section for photoelectric absorptio which varies approximately as $Z^{4.5}$. As we shall see from the following discussion, becau photoelectric absorption is the preferred mode of interaction, there is a premium on cho ing detectors for gamma-ray spectroscopy from materials that incorporate elements with high atomic number.

. Photoelectric Absorption

Photoelectric absorption is an interaction in which the incident gamma-ray photon disappears. In its place, a photoelectron is produced from one of the electron shells of the absorber atom with a kinetic energy given by the incident photon energy $h\nu$ minus the binding energy of the electron in its original shell (E_b). This process is shown in the diagram below. For typical gamma-ray energies, the photoelectron is most likely to emerge from the K shell, for which typical binding energies range from a few keV for low-Z materials to tens of keV for materials with higher atomic number. Conservation of momentum requires that the atom recoils in this process, but its recoil energy is very small and usually can be neglected..

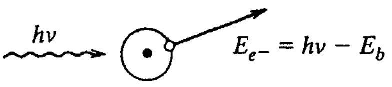

The vacancy that is created in the electron shell as a result of the photoelectron emission is quickly filled by electron rearrangement. In the process, the binding energy is liberated either in the form of a characteristic X-ray or Auger electron. In iodine, a characteristic X-ray is emitted in about 88% of the cases.[4] The Auger electrons have extremely short range because of their low energy. The characteristic X-rays may travel some distance (typically a millimeter or less) before being reabsorbed through photoelectric interactions with less tightly bound electron shells of the absorber atoms. Although escape of these X-rays can at times be significant, for now we assume that they are also fully absorbed in keeping with our simplified model.

Thus, the effect of photoelectric absorption is the liberation of a photoelectron, which carries off most of the gamma-ray energy, together with one or more low-energy electrons corresponding to absorption of the original binding energy of the photoelectron. If nothing escapes from the detector, then the sum of the kinetic energies of the electrons that are created must equal the original energy of the gamma-ray photon.

Photoelectric absorption is therefore an ideal process if one is interested in measuring the energy of the original gamma ray. The total electron kinetic energy equals the incident gamma-ray energy and will always be the same if monoenergetic gamma rays are involved. Under these conditions, the differential distribution of electron kinetic energy for a series of photoelectric absorption events would be a simple delta function as shown below. The single peak appears at a total electron energy corresponding to the energy of the incident gamma rays.

B. Compton Scattering

The result of a Compton scattering interaction is the creation of a recoil electron and tered gamma-ray photon, with the division of energy between the two dependent on scattering angle. A sketch of the interaction is given below.

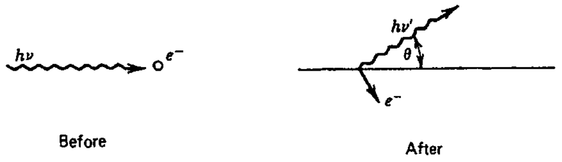

The energy of the scattered gamma ray $h\nu'$ in terms of its scattering angle θ is given by

$$h\nu' = \frac{h\nu}{1 + (h\nu/m_0c^2)(1 - \cos\theta)} \qquad (10.1$$

where m_0c^2 is the rest mass energy of the electron (0.511 MeV). The kinetic energy of th recoil electron is therefore

$$E_{e^-} = h\nu - h\nu' = h\nu\left(\frac{(h\nu/m_0c^2)(1 - \cos\theta)}{1 + (h\nu/m_0c^2)(1 - \cos\theta)}\right) \qquad (10.2$$

Two extreme cases can be identified:

1. A grazing angle scattering, or one in which $\theta \cong 0$. In this case, Eqs. (10.1) and (10.2 predict that $h\nu' \cong h\nu$ and $E_{e^-} \cong 0$. In this extreme, the recoil Compton electron ha very little energy and the scattered gamma ray has nearly the same energy as th incident gamma ray.
2. A head-on collision in which $\theta = \pi$. In this extreme, the incident gamma ray i backscattered toward its direction of origin, whereas the electron recoils along th direction of incidence. This extreme represents the maximum energy that can b transferred to an electron in a single Compton interaction. Equations (10.1) an (10.2) yield for this case

$$h\nu'\Big|_{\theta=\pi} = \frac{h\nu}{1 + 2h\nu/m_0c^2} \qquad (10.3$$

$$E_{e^-}\Big|_{\theta=\pi} = h\nu\left(\frac{2h\nu/m_0c^2}{1 + 2h\nu/m_0c^2}\right) \qquad (10.4$$

In normal circumstances, all scattering angles will occur in the detector. Therefore, continuum of energies can be transferred to the electron, ranging from zero up to the maximum predicted by Eq. (10.4). Figure 10.1 shows the shape of the distribution of Compto recoil electrons predicted by the Klein–Nishina cross section (Chapter 2) for several different values of the incident gamma-ray energy. For any one specific gamma-ray energ the electron energy distribution has the general shape shown in the sketch below.

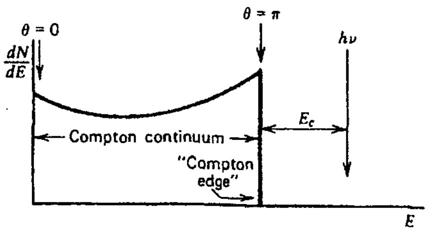

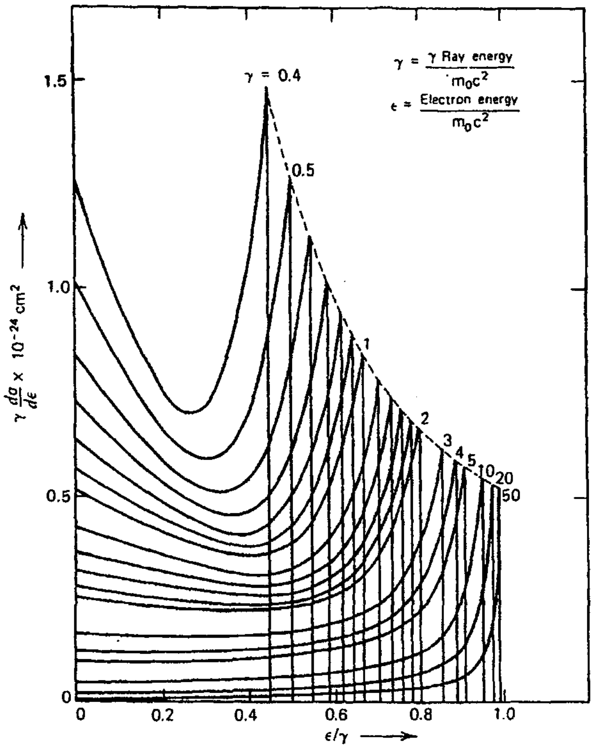

Figure 10.1 Shape of the Compton continuum for various gamma-ray energies. (From S. M. Shafroth (ed.), *Scintillation Spectroscopy of Gamma Radiation.* Copyright 1964 by Gordon & Breach, Inc. By permission of the publisher.)

The gap between the maximum Compton recoil electron energy and the incident gamma-ray energy is given by

$$E_C \equiv h\nu - E_{e^-}\Big|_{\theta = \pi} = \frac{h\nu}{1 + 2h\nu/m_0c^2} \qquad (10.5)$$

In the limit that the incident gamma-ray energy is large, or $h\nu \gg m_0c^2/2$, this energy difference tends toward a constant value given by

$$E_C \cong \frac{m_0c^2}{2} \ (= 0.256\,\mathrm{MeV}) \qquad (10.6)$$

The preceding analysis is based on the assumption that Compton scattering involves electrons that are initially free or unbound. In actual detector materials, the binding energy of the electron prior to the scattering process can have a measurable effect on the shape of the Compton continuum. These effects will be particularly noticeable for low incident gamma-ray energy. They involve a rounding-off of the rise in the continuum near its upper extreme and the introduction of a finite slope to the abrupt drop of the Compton edge. These effects are often masked by the finite energy resolution of the detector but can be evident in the spectra from detectors with high inherent resolution (see Fig. 13.9). The finite momentum of orbital electrons also causes gamma-ray photons that are scattered at a fixed angle from a monoenergetic source to have a narrow distribution in their energy (the "Doppler spread"), as contrasted with a single energy predicted by Eq. (10.1).

C. Pair Production

The third significant gamma-ray interaction is pair production. The process occurs in the intense electric field near the protons in the nuclei of the absorbing material and corresponds to the creation of an electron–positron pair at the point of complete disappearance of the incident gamma-ray photon. Because an energy of $2m_0c^2$ is required to create the electron–positron pair, a minimum gamma-ray energy of 1.02 MeV is required to make the process energetically possible. If the incident gamma-ray energy exceeds this value, the excess energy appears in the form of kinetic energy shared by the electron–positron pair. Therefore, the process consists of converting the incident gamma-ray photon into electron and positron kinetic energies, which total

$$E_{e^-} + E_{e^+} = h\nu - 2m_0c^2 \tag{10.7}$$

For typical energies, both the electron and positron travel a few millimeters at most before losing all their kinetic energy to the absorbing medium. A plot of the total (electron + positron) charged particle kinetic energy created by the incident gamma ray is again a simple delta function, but it is now located $2m_0c^2$ below the incident gamma-ray energy, as illustrated in the sketch below. In our simple model, this amount of energy will be deposited each time a pair production interaction occurs within the detector. As introduced in the next section, this energy corresponds to the position of the *double escape peak* in actual gamma-ray pulse height spectra.

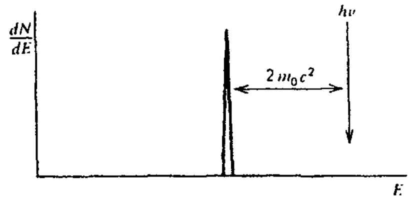

The pair production process is complicated by the fact that the positron is not a stable particle. Once its kinetic energy becomes very low (comparable to the thermal energy of normal electrons in the absorbing material), the positron will annihilate or combine with a normal electron in the absorbing medium. At this point both disappear, and they are replaced by two annihilation photons of energy m_0c^2 (0.511 MeV) each. The time required for the positron to slow down and annihilate is small, so that the annihilation radiation appears in virtual coincidence with the original pair production interaction.

III. PREDICTED RESPONSE FUNCTIONS

A. "Small" Detectors

As an example of one extreme in gamma-ray detector behavior, we first examine the expected response of detectors whose size is small compared with the mean free path of the *secondary gamma radiations* produced in interactions of the original gamma rays. These secondary radiations consist of Compton scattered gamma rays, together with annihilation photons formed at the end of the tracks of positrons created in pair production. Because the mean free path of the secondary gamma rays is typically of the order of several centimeters, the condition of "smallness" is met if the detector dimensions do not exceed 1 or 2 cm. At the same time, we retain our original simplifying assumption that all charged particle energy (photoelectron, Compton electron, pair electron, and positron) is completely absorbed within the detector volume.

The predicted electron energy deposition spectra under these conditions are illustrated in Fig. 10.2. If the incident gamma-ray energy is below the value at which pair production is significant, the spectrum results only from the combined effect of Compton scattering

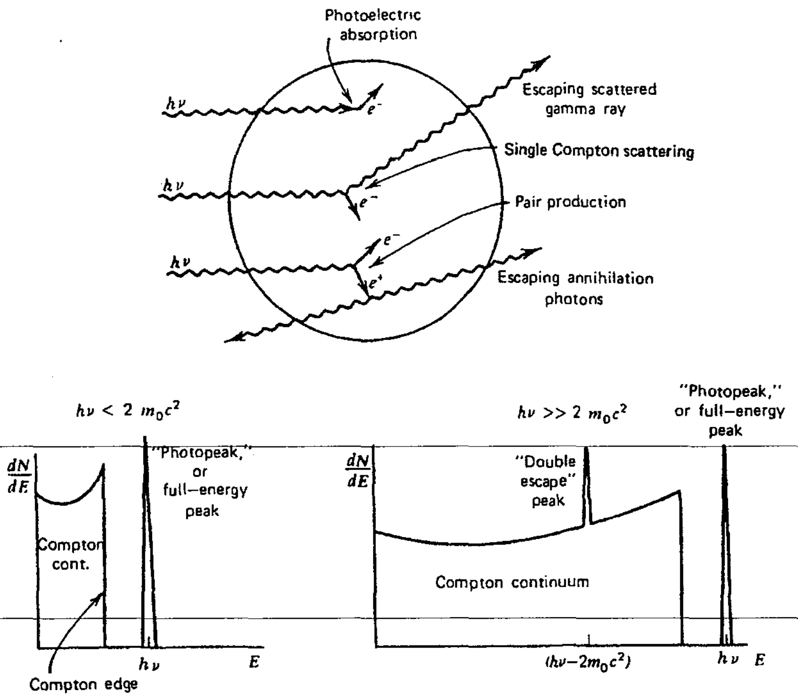

Figure 10.2 The "small detector" extreme in gamma-ray spectroscopy. The processes of photoelectric absorption and single Compton scattering give rise to the low-energy spectrum at the left. At higher energies, the pair production process adds a double escape peak shown in the spectrum at the right.

and photoelectric absorption. The continuum of energies corresponding to Compton scattered electrons is called the *Compton continuum*, whereas the narrow peak corresponding to photoelectrons is designated as the *photopeak.* For the "small" detector, only single interactions take place, and the ratio of the area under the photopeak to the area under the Compton continuum is the same as the ratio of the photoelectric cross section to the Compton cross section in the detector material.

If the incident gamma-ray energy is sufficiently high (several MeV), the results of pair production are also evident in the electron energy spectrum. For a small detector, only the electron and positron kinetic energies are deposited, and the annihilation radiation escapes. The net effect is to add a *double escape peak* to the spectrum located at an energy of $2m_0c^2$ (~1.02 MeV) below the photopeak. The term *double escape* refers to the fact that both annihilation photons escape from the detector without further interaction.

Very Large Detectors

As an opposite extreme case, imagine that gamma rays could be introduced near the center of a very large detector, perhaps in an arrangement resembling that of Fig. 10.3. The detector dimensions are now assumed to be sufficiently large so that all secondary radiations, including Compton scattered gamma rays and annihilation photons, also interact within the detector active volume and none escape from the surface. For typical gamma-ray energies, this condition would translate into requiring detector dimensions on the order of many tens of centimeters, unrealistically large for most practical cases.

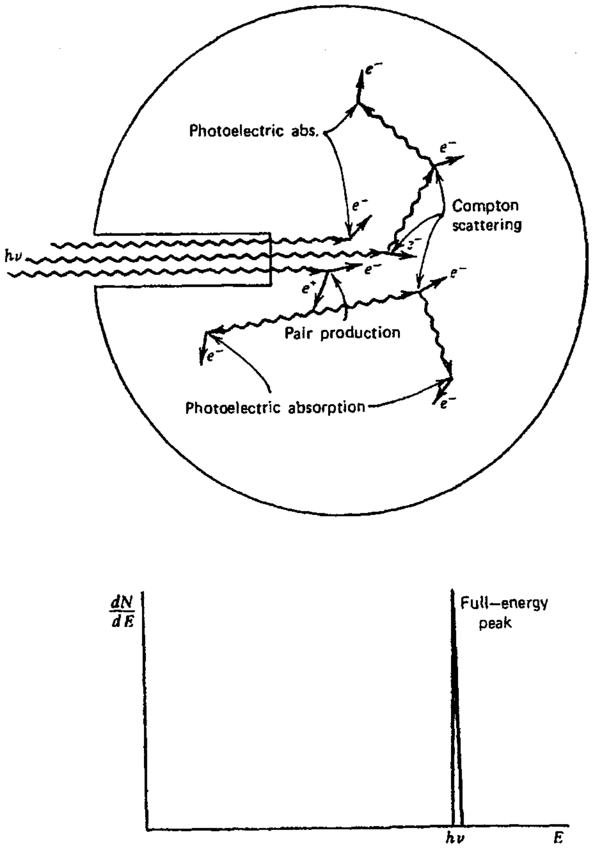

Figure 10.3 The "large detector" extreme in gamma-ray spectroscopy. All gamma-ray photons, no matter how complex their mode of interaction, ultimately deposit all their energy in the detector. Some representative histories are shown at the top.

Nonetheless, it is helpful to see how increasing the detector size greatly simplifies i response function. Some typical histories, obtained by following a particular source gamm ray and all subsequent secondary radiation, are sketched in Fig. 10.3. If the initial interactio is a Compton scattering event, the scattered gamma ray will subsequently interact at som other location within the detector. This second interaction may also be a Compton scatte ing event, in which case a scattered photon of still lower energy is produced. Eventually, photoelectric absorption will occur and the history is terminated at that point.

It is important to appreciate the small amount of time required for the entire history t take place. The primary and secondary gamma rays travel at the speed of light. If the averag migration distance of the secondary gamma rays is of the order of 10 cm, the total elapse time from start to finish of the history will be less than a nanosecond. This time is substan tially less than the inherent response time of virtually all practical detectors used in gamma ray spectroscopy. Therefore, the net effect is to create the Compton electrons at each scat tering point and the final photoelectron in time coincidence. The pulse produced by th detector will therefore be the sum of the responses due to each individual electron. If th detector responds linearly to electron energy, then a pulse is produced which is proportiona to the *total* energy of all the electrons produced along the history. Because nothing escape from the detector, this total electron energy must simply be the original energy of the gamma-ray photon, no matter how complex any specific history may be. *The detector response is the same as if the original gamma-ray photon had undergone a simple photoelectric absorption in a single step.*

The same type of argument can be used if the history involves a pair production event. The annihilation photons formed when the positron is stopped are now assumed to interact through Compton scattering or photoelectric absorption elsewhere in the detector. Again, if the detector is large enough to prevent any secondary radiation from escaping, the sum of the kinetic energies of the electron–positron pair and subsequent Compton and photoelectrons produced by interaction of the annihilation radiation must equal the original gamma-ray photon energy. Therefore, the detector response is again simply proportional to the original gamma-ray energy.

The conclusion to be reached is therefore very simple: If the detector is sufficiently large and its response linearly dependent on electron kinetic energy, then the signal pulse is identical for all gamma-ray photons of the same energy, regardless of the details of each individual history. This circumstance is very fortunate because the detector response function now consists of the single peak shown in Fig. 10.3 rather than the more complex function shown in Fig. 10.2. The ability to interpret complex gamma-ray spectra involving many different energies is obviously enhanced when the response function consists of a single peak.

By common usage, the corresponding peak in the response function is often called the *photopeak*, just as in the case of the small detector. It should be realized, however, that in addition to simple photoelectric events, much more complex histories involving multiple Compton scattering or pair production also contribute pulses that fall within this peak. A better name is the *full-energy peak* because it represents all histories in which all of the original gamma-ray energy is fully converted to electron kinetic energy.

Intermediate Size Detectors

Real detectors of the sizes in common use for gamma-ray spectroscopy are neither small nor large by the standards given above. For usual geometries in which the gamma rays are incident externally on the surface of the detector, even large-volume detectors appear finite because some interactions will take place near the entrance surface. Normal detector response functions therefore combine some of the properties discussed for the two previous cases, as well as additional features related to *partial* recovery of the secondary gamma-ray energy. Some representative histories that illustrate these added possibilities are shown in Fig. 10.4, together with corresponding features in the response function.

The spectrum for low to medium gamma-ray energies (where pair production is not significant) again consists of a Compton continuum and photopeak. Now, however, the ratio of the area under the photopeak to that under the Compton continuum is significantly enhanced over that for the very small detector due to the added contribution of multiple events to the photopeak. The lower the incident gamma-ray energy, the lower will be the average energy of a Compton scattered photon and the corresponding average distance of migration. Thus, even detectors of moderate size will appear to be large, and the relative area under the photopeak increases with decreasing incident photon energy. At very low energies (say, < 100 keV) the Compton continuum may effectively disappear.

At medium energies, the possibility of multiple Compton scattering followed by escape of the final scattered photon can lead to a total energy deposition that is greater than the maximum predicted by Eq. (10.4) for single scattering. These multiple events can thus partially fill in the gap between the Compton edge and the photopeak, as well as distort the shape of the continuum predicted for single scattering.

If the gamma-ray energy is high enough to make pair production significant, a more complicated situation prevails. The annihilation photons now may either escape or under-

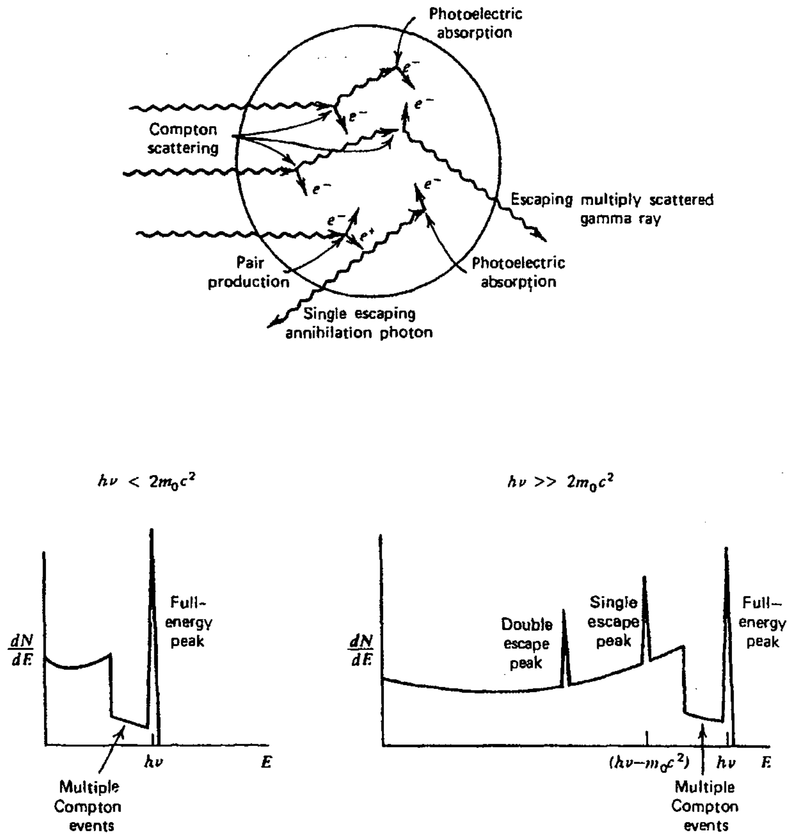

Figure 10.4 The case of intermediate detector size in gamma-ray spectroscopy. In addition to the continuum from single Compton scattering and the full-energy peak, the spectrum at the left shows the influence of multiple Compton events followed by photon escape. The full-energy peak also contains some histories that began with Compton scattering. At the right, the single escape peak corresponds to initial pair production interactions in which only one annihilation photon leaves the detector without further interaction. A double escape peak as illustrated in Fig. 10.2 will also be present due to those pair production events in which both annihilation photons escape.

go further interaction within the detector. These additional interactions may lead to eith partial or full-energy absorption of either one or both of the annihilation photons.

If both annihilation photons escape without interaction, events occur that contribute the double escape peak discussed previously. Another relatively frequent occurrence is history in which one annihilation photon escapes but the other is totally absorbed. The events contribute to a *single escape peak*, which now appears in the spectrum at an ener of m_0c^2 (0.511 MeV) below the photopeak. A continuous range of other possibilities exis in which one or both of the annihilation photons are partially converted to electron ener through Compton scattering and subsequent escape of the scattered photon. Such even accumulate in a broad continuum in the pulse height spectrum lying between the doub escape peak and the photopeak.

The response function to be expected for a real gamma-ray detector will depend on the size, shape, and composition of the detector, and also the geometric details of the irradiation conditions. For example, the response function will change somewhat if a point gamma-ray source is moved from a position close to the detector to one that is far away. The variation is related to the differences in the spatial distribution of the primary interactions that occur within the detector as the source geometry is changed. In general, the response function is too complicated to predict in detail other than through the use of Monte Carlo calculations, which simulate the histories actually taking place in a detector of the same size and composition.

Some properties of the response function are of general interest in gamma-ray spectroscopy. The *photofraction* is defined as the ratio of the area under the photopeak (or full-energy peak) to that under the entire response function. It is a direct measure of the probability that a gamma ray that undergoes interaction of any kind within the detector ultimately deposits its full energy. Large values of the photofraction are obviously desirable to minimize the complicating effects of Compton continua and escape peaks in the spectrum.

At high gamma-ray energies, the single and double escape peaks are quite prominent parts of the response function and can, under some circumstances, become larger than the photopeak. The ratio of the area under the single or double escape peak to the area under the photopeak is also a widely quoted property of the response function that can help in the interpretation of complex spectra.

Complications in the Response Function

1. SECONDARY ELECTRON ESCAPE

If the detector is not large compared with typical secondary electron ranges, a significant fraction of the electrons may leak from the detector surface and their energy will not be fully collected. This effect is enhanced for high gamma-ray energies for which the average secondary electron energy is also high. Electron leakage will tend to distort the response function by moving some events to a lower amplitude from that which would be observed if the entire electron energy were collected. The shape of the Compton continuum will therefore be altered somewhat to favor lower amplitudes. Because some events will be lost from the photopeak, the photofraction will be reduced as compared with the situation in which electron leakage is not important.

2. BREMSSTRAHLUNG ESCAPE

One of the mechanisms by which secondary electrons lose energy is by the radiation of bremsstrahlung photons. [The fraction lost by this process increases sharply with electron energy and becomes the dominant process for electrons with energy over a few MeV. Bremsstrahlung production scales approximately as Z^2 of the absorber [see Eq. (2.11)] so its importance is greatest in detectors with high atomic number. Even though the electron itself may be fully stopped within the detector, there is a possibility that some fraction of the bremsstrahlung photons may escape without being reabsorbed. The effects on the response function are similar to those described in the previous paragraph for electron escape and are again most important when the incident gamma-ray energy is large. For both secondary electron or bremsstrahlung escape, the effects are to change the shape of the response function somewhat, but additional peaks or sharp features are not introduced.]

3. CHARACTERISTIC X-RAY ESCAPE

In the photoelectric absorption process, a characteristic X-ray often is emitted by the absorber atom. In the majority of cases this X-ray energy is reabsorbed near the original interaction site. If the photoelectric absorption occurs near a surface of the detector, however, the X-ray photon may escape as shown in the sketch below.

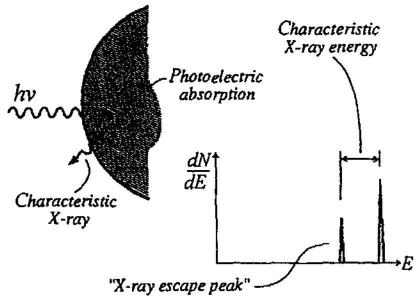

In this event, the energy deposited in the detector is decreased by an amount equal to the X-ray photon energy. Without the X-ray escape, the original gamma ray would have been fully absorbed and the resulting pulse would have contributed to the photopeak. With escape, a new category of events is created in which an amount of energy equal to the original gamma-ray energy minus the characteristic X-ray energy is repeatedly deposited in the detector. Therefore, a new peak will appear in the response function and will be located at a distance equal to the energy of the characteristic X-ray below the photopeak. These peaks are generally labeled "X-ray escape peaks" and tend to be most prominent at low incident gamma-ray energies and for detectors whose surface-to-volume ratio is large. Examples are shown in the spectra of Figs. 10.10 and 13.7.

For gamma rays whose energies are above the *K*-shell binding energy of the absorber, most photoelectric absorptions involve these most tightly-bound electrons in the atom. The main characteristic X-ray escape peak is therefore located below the full-energy peak by an amount given by the *K*-shell binding energy. More subtle effects are also present in principle because of interactions in and transitions to the more weakly-bound electron shells, but corresponding escape peaks are usually difficult to resolve from the full-energy peak because of the much lower X-ray energies that are involved.

4. SECONDARY RADIATIONS CREATED NEAR THE SOURCE

a. Annihilation Radiation

If the gamma-ray source consists of an isotope that decays by positron emission, an additional peak in the spectrum at 0.511 MeV is to be expected from the annihilation photons created when the positron is stopped. Most standard gamma-ray sources are encapsulated in a covering sufficiently thick to fully stop all the positrons, and thus they undergo annihilation in the region immediately surrounding the source. This region therefore acts as a source of 0.511 MeV annihilation radiation, which is superimposed on the gamma-ray spectrum expected from decay of the source itself. For detector geometries in which it is possible to detect both annihilation photons from a single decay simultaneously (as in a well counter), then a peak at 1.022 MeV may also be observed in the recorded spectrum.

b. Bremsstrahlung

Most commonly-available gamma-ray sources decay by beta-minus emission, and the source encapsulation is usually also thick enough to stop these beta particles. In other cases, an external absorber may be used to prevent the beta particles from reaching the detector where their energy deposition would needlessly complicate the gamma-ray spectrum. In the absorption process, however, some secondary radiation in the form of bremsstrahlung will be generated and may reach the detector and contribute to the measured spectrum. In principle, the bremsstrahlung spectrum may extend to an energy equal to the maximum beta particle energy, but significant yields are confined to energies that are

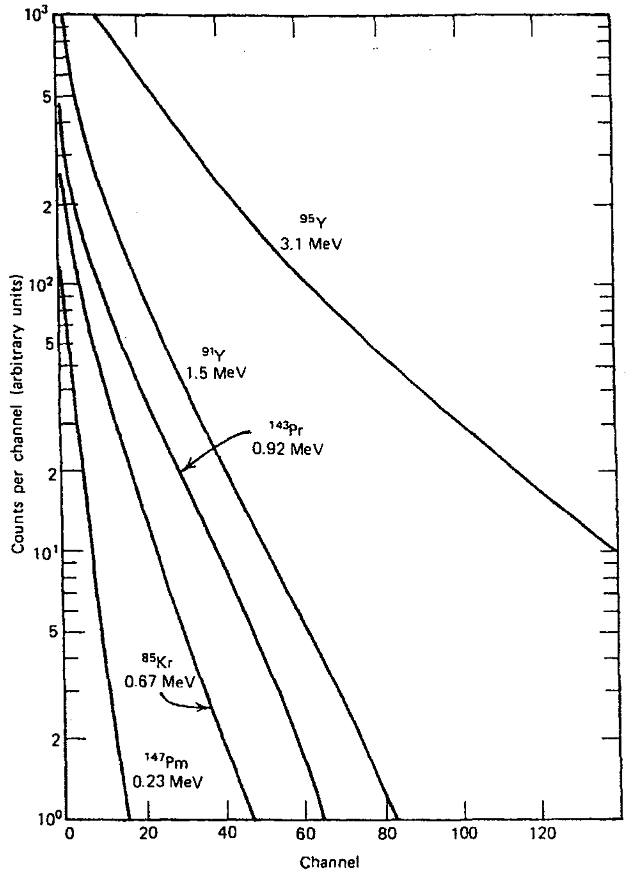

Figure 10.5 Shape of the bremsstrahlung spectra produced by beta particles with the indicated endpoint energies. (From Heath.[5])

much lower than this value. Some examples of bremsstrahlung energy spectra are given in Fig. 10.5, which illustrates the shape of the spectrum favoring low-energy bremsstrahlung photon emission. Because these spectra are continua, they do not lead to peaks in the recorded spectra but rather can add a significant continuum on which all other features of the gamma-ray spectra are superimposed. Because the bremsstrahlung contribution cannot simply be subtracted as a background, its inclusion can lead to errors in quantitative measurements of areas under peaks in the gamma-ray spectrum. To minimize the generation of bremsstrahlung, the use of beta absorbers made from low atomic number materials, such as beryllium, is often preferred.

5. EFFECTS OF SURROUNDING MATERIALS

In any practical application, a detector used for gamma-ray spectroscopy is surrounded by other materials that can have a measurable influence on its response. At a very minimum, the detector is encapsulated to provide a barrier against moisture and light or is mounted within a vacuum enclosure. To reduce natural background, most gamma-ray detectors are also operated within a shielded enclosure. The gamma-ray source itself is often part of a larger sample of material or is contained within some type of encapsulation. All these

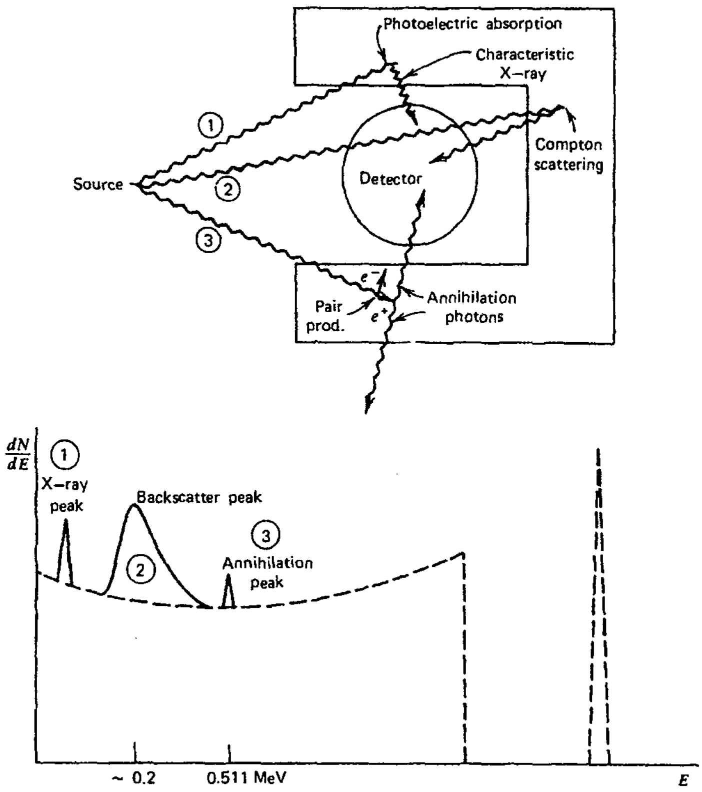

Figure 10.6 Influence of surrounding materials on detector response. In addition to the expected spectrum (shown as a dashed line), the representative histories shown at the top lead to the indicated corresponding features in the response function.

materials are potential sources of secondary radiations that can be produced by interac tions of the primary gamma rays emitted by the source. If the secondary radiations reac the detector, they can influence the shape of the recorded spectrum to a noticeable exten Some possibilities are illustrated in Fig. 10.6.

a. Backscattered Gamma Rays

Pulse height spectra from gamma-ray detectors often show a peak in the vicinity c 0.2–0.25 MeV, called the *backscatter peak*. The peak is caused by gamma rays from th source that have first interacted by Compton scattering in one of the materials surround ing the detector. Figure 10.7 shows the energy dependence of these scattered gamma ray as a function of the scattering angle. From the shape of these curves, it can be seen that an scattering angle greater than about 110–120° results in scattered photons of nearly identi cal energy. Therefore, a monoenergetic source will give rise to many scattered gamma ray whose energy is near this minimum value, and a peak will appear in the recorded spectrum The energy of the backscatter peak will correspond to Eq. (10.3):

$$hv'\big|_{\theta=\pi} = \frac{hv}{1 + 2hv/m_0c^2}$$

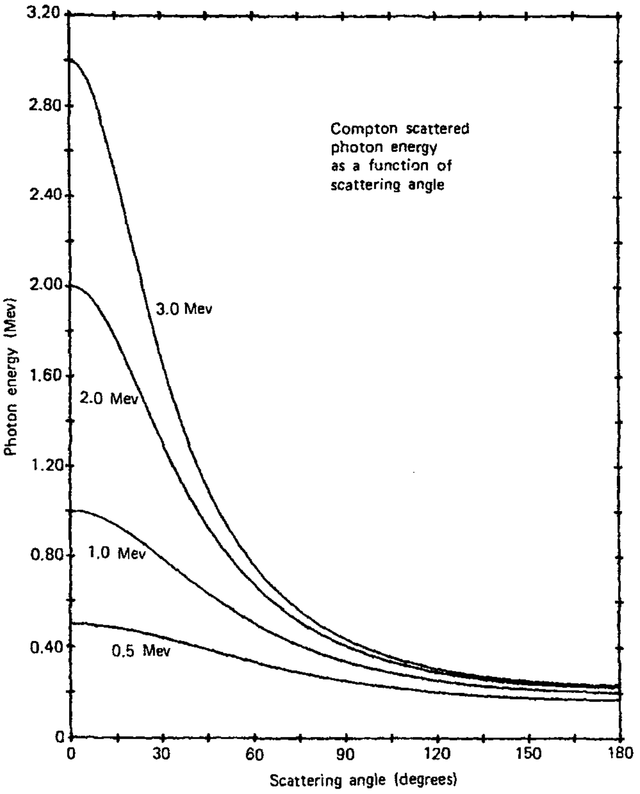

Figure 10.7 Variation of scattered gamma-ray energy with scattering angle.

In the limit that the primary gamma-ray energy is large ($h\nu \gg m_0c^2/2$), this expression reduces to

$$h\nu'\Big|_{\theta=\pi} \cong \frac{m_0c^2}{2} \tag{10.8}$$

Thus, the backscatter peak always occurs at an energy of 0.25 MeV or less.

b. Other Secondary Radiations

In addition to Compton scattering, other interactions of the primary gamma rays in the surrounding materials can give noticeable peaks in the recorded spectrum. For example, photoelectric absorption in the materials immediately surrounding the detector can lead to generation of a characteristic X-ray that may reach the detector. If the atomic number of the material is high, the X-ray photon will be relatively energetic and can penetrate significant thicknesses of intervening material. Therefore, high-Z materials should be avoided in the immediate vicinity of the detector. On the other hand, the most effective shielding materials are those with high atomic numbers such as lead. A *graded shield* is one in which the bulk of the shield is made from high-Z materials, but the inner surface is lined with a material with lower atomic number. This inner lining serves to absorb the characteristic X-ray emitted by the bulk of the shield, at the same time emitting only low-energy or weakly penetrating X-rays of its own.

If the energy of the primary gamma rays is high, pair production within high-Z surrounding materials can give a significant yield of annihilation radiation. A peak can therefore appear at 0.511 MeV in the spectrum from the detection of these secondary photons. There is a danger of confusing this peak with that expected from annihilation radiation produced by radioactive sources that are positron emitters, and care must therefore be exercised in identifying the source of these annihilation photons.

E. Summation Effects

Additional peaks caused by the coincident detection of two (or more) gamma-ray photons may also appear in the recorded pulse height spectrum. The most common situation occurs in applications involving an isotope that emits multiple cascade gamma rays in its decay, as illustrated in Fig. 10.8. If we assume that no isomeric states are involved, the lifetime of the intermediate state is generally so short that the two gamma rays are, in effect, emitted in coincidence. It is then quite possible for both gamma-ray photons from a single decay to interact and deposit all their energy within a time that is short compared with the response time of the detector or the resolving time of the following electronics. If enough of these events occur, a *sum coincidence peak* will be observable in the spectrum that occurs at a pulse height that corresponds to the sum of the two individual gamma-ray energies. A continuum of sum events will also occur at lower amplitudes due to the summation of partial energy loss interactions.

The relative number of events expected in the sum peak depends on the branching ratio of the two gamma rays, the angular correlation that may exist between them, and the solid angle subtended by the detector. A complete analysis is often quite complex, but the following simplified derivation illustrates the general approach that can be applied.

Let ϵ_1 be the intrinsic peak efficiency of the detector for gamma ray ①, and let Ω be the fractional solid angle (steradians/4π) subtended by the detector. Then the full-energy peak area for gamma ray ① in the absence of summing effects is

$$N_1 = \epsilon_1 \Omega S y_1 \tag{10.9}$$

where S is the number of source decays over the observation period and y_1 is the yield of gamma ray ① per disintegration. Applying the same definitions to gamma ray ②, we obtain

$$N_2 = \epsilon_2 \Omega S y_2 \tag{10.10}$$

The probability of simultaneous detection of both gamma rays is the product of both individual detection probabilities, multiplied by a factor $W(0°)$ to account for any angular correlation between the gamma-ray photons. $W(0°)$ is defined as the relative yield of γ_2 per

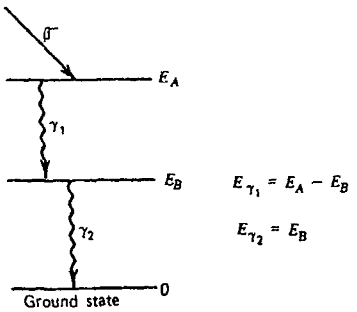

Figure 10.8 Simplified nuclear decay scheme which can lead to summation effects in gamma spectra. Provided the intermediate state (at E_B) is short-lived, γ_1 and γ_2 are emitted in virtual coincidence.

unit solid angle about the 0° direction defined by the detector position, given that γ_1 is emitted in the same direction. Then the sum peak area should be

$$\begin{aligned} N_{12} &= S\,(\epsilon_1 \Omega y_1)(\epsilon_2 \Omega y_2) W(0^\circ) \\ &= S \epsilon_1 \epsilon_2 y_1 y_2 \Omega^2 W(0^\circ) \end{aligned} \tag{10.11}$$

The summation process not only creates the sum peak but also removes events that would otherwise fall within individual gamma-ray full-energy peaks. The remaining number of full-energy events for γ_1 is [from Eqs. (10.9) and (10.11)]

$$\begin{aligned} N_1\Big|_{\substack{\text{with} \\ \text{summation}}} &= N_1 - N_{12} \\ &= \epsilon_1 \Omega S y_1 [1 - \epsilon_2 \Omega y_2 W(0^\circ)] \end{aligned} \tag{10.12}$$

Because a coincident event of any kind from γ_2 (not just a photopeak event) will remove a count from N_1, the detection efficiency ϵ_2 should now be interpreted as the intrinsic *total* efficiency. For these losses to remain small, the fractional solid angle Ω is often restricted to small values to keep the second term in the above equation much smaller than the first. If the solid angle is too large, quantitative measurements based on determination of the area under full-energy peaks can be in error unless an accounting of the second term is provided.[6]

The summation process described above involves multiple radiations from the same nuclear decay event and therefore is classified as a *true coincidence* by the definitions given in Chapter 17. Another process can also lead to summed pulses due to the accidental combination of two separate events from independent decays that occur closely spaced in time. Because the time intervals separating adjacent events are randomly distributed, some will be less than the inherent resolving time of the detector or pulse-processing system. These *chance coincidences* increase rapidly with increasing counting rate and will occur even in the absence of true coincidences. A corresponding sum peak can therefore appear in spectra from isotopes that emit only a single radiation per decay. For both true coincidence and chance summing, there will also be many cases in which a second interaction involves partial rather than full energy absorption in the detector. For this category of events, the first event (assumed here to be a full-energy absorption) still is lost from the peak where it normally would be expected in the absence of summing. Now, however, the summed pulse is stored into a continuum that lies above the expected peak and it does not contribute to a sum peak in the spectrum.

Chance coincidences will occur if a second pulse arrives within the resolving time t_r following a typical signal pulse. For a random pulse rate of r_s and $r_s t_r \ll 1$, the rate at which coincidences occur should be the fraction of all time that lies within t_r of a preceding pulse (given by $r_s t_r$) multiplied by the rate of pulse arrival (r_s), or

$$r_{ch} = r_s^2 t_r \tag{10.13}$$

Therefore, the accidental sum peak will have an intensity that is proportional to the square of the counting rate, whereas both the true sum peak or normal photopeaks will be linearly related to the counting rate. When multiple radiations are involved, accidental sum peaks may potentially occur at all possible combinations of any two single energies. At normal rates and typical detector solid angles, however, sum peaks are usually lost in fluctuations in the continua and background present from other energies, except at the upper energy extremes of the spectrum where such backgrounds are low.

As a practical matter, the resolving time t_r is normally set by the shaping time constants of the linear amplifier used in the pulse-processing chain from the detector. The chance coincidences therefore take the form of *pulse pile-up* in the amplifier, which is further detailed in the discussions of Chapter 17.

F. Coincidence Methods in Gamma-Ray Spectrometers

1. CONTINUUM REDUCTION

For an ideal gamma-ray detector, the response function would simply be a single w resolved peak with no associated continuum. Then the pulse height spectrum from a co plex gamma-ray source could be most easily interpreted, and the presence of high-en gamma rays would not hinder the detection of weak radiations at lower energies.

At the price of added complexity, some steps can be taken to approach this ideal mo closely, even for gamma-ray detectors with response functions that are inherently mo complicated. These methods involve placing other detectors around the primary detect and employ coincidence or anticoincidence techniques to select preferentially those even that are most likely to correspond to full-energy absorption. For the case of sodium iodi spectrometers, the most common methods involve the use of an annular detector su rounding the primary crystal for Compton suppression by anticoincidence, or the use two or more adjacent crystals in the *sum-coincidence* mode. Representative descriptions sodium iodide spectrometers in which one or both of these methods of continuum su pression have been applied are given in Refs. 7–11.

An explanation of these techniques is postponed until Chapter 12, where their use wi germanium detectors is detailed. Although significant improvements in peak-to-continuu ratios can be achieved by applying these methods to NaI(Tl) spectrometers, current atte tion has focused on their application to germanium systems where continua are much mo prominent and greater gains can be achieved through their suppression.

2. THE COMPTON SPECTROMETER

The combination of two separated gamma-ray detectors operated in coincidence, as show in Fig. 10.9, is another configuration that can simplify the response function at the expens of detection efficiency. A collimated beam of gamma rays is allowed to strike the fir

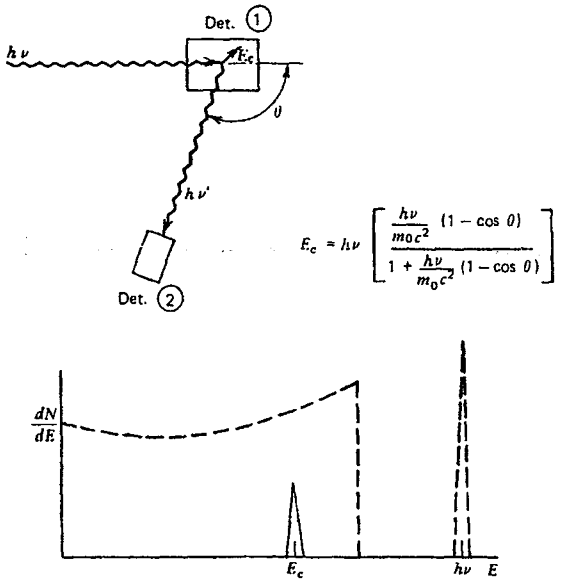

Figure 10.9 The geometry of the Compton spectrometer is shown at the top. The spectrum of those events from detector ① that are in coincidence with pulses from detector ② is shown as the solid peak at the bottom. The normal spectrum from detector ① is shown as the dashed curve.

detector in which the desired mode of interaction is now Compton scattering. Some fraction of the scattered gamma rays will travel to the second detector where they may also interact to give a second pulse. Because the separation distance is normally no greater than a few tens of centimeters, the pulses are essentially in time coincidence. By selectively recording only those pulses from the first crystal that are in coincidence with a pulse from the second crystal, the recorded spectrum largely reflects only single Compton scattering events. Because the angle of scattering is fixed, a constant amount of energy is deposited for each scattering interaction involving monoenergetic incident gamma rays. Photoelectric absorption and all other events that do not lead to coincidence between the two detectors are excluded. The response function is thus reduced to a single peak, which appears at a position within the original Compton continuum determined by the scattering angle. For typical gamma ray energies, the Doppler spread in the scattered photon energy (see p. 311) is usually small compared with the broadening effects of the variation in scattering angles introduced by the finite sizes of the detectors.

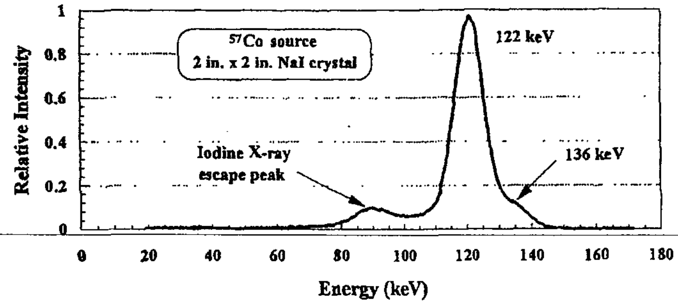

Figure 10.10 Pulse height spectrum from a NaI(Tl) scintillator for gamma rays emitted by ^{57}Co at 122 and 136 keV. The iodine X-ray escape peak lies 28 keV below the corresponding full energy peak and is evident only for the more intense 122 keV gamma ray.

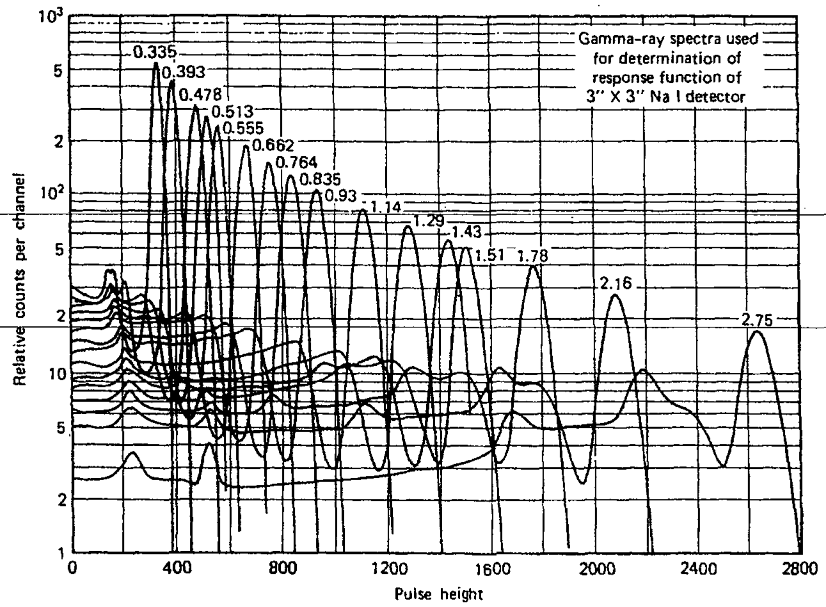

Figure 10.11 Response functions for a 7.62 cm × 7.62 cm cylindrical NaI(Tl) scintillator for gamma rays from 0.335 to 2.75 MeV. (From Heath.[5])

IV. PROPERTIES OF SCINTILLATION GAMMA-RAY SPECTROMETERS

A. Response Function

Sodium iodide gained much of its early popularity because the relatively high atomic number ($Z = 53$) of its iodine constituent ensures that photoelectric absorption will be a relatively important process. The corresponding high intrinsic detection efficiency and large photofraction have contributed to the success of sodium iodide scintillation spectrometers. Other materials, such as cesium iodide or BGO, have even higher density or effective atomic number, and therefore the response function for these materials shows an even greater detection efficiency and photofraction. However, the relatively high light output and smaller decay time have led to the dominance of NaI(Tl) in spectroscopy with scintillators.

The importance of many of the factors that influence the shape of the response function for NaI(Tl) scintillators is detailed by Mueller and Maeder.[12] An extensive catalog of experimentally measured gamma-ray spectra for nearly 300 radionuclides as recorded by a 3 in. × 3 in. NaI(Tl) spectrometer has been published by Heath.[5] A later compilation by Adams and Dams[6] contains spectra for both 3 in. × 3 in. and 4 in. × 4 in. cylindrical sodium iodide crystals. These published data can be of considerable help in predicting the response function to be expected from a scintillation spectrometer when applied to gamma-ray-emitting isotopes. Examples of gamma-ray spectra are given in Figs. 10.10 through 10.13. Many of the features described in the previous discussion can be observed in these spectra.

A direct comparison of gamma-ray spectra observed under similar conditions from equal size crystals of sodium iodide and BGO is shown in Fig. 10.14. The considerably better energy resolution of sodium iodide is evidenced by the smaller widths of the peaks in the bottom spectrum. The higher efficiency of BGO is apparent, especially at the higher energy, from the larger area under the photopeaks in the upper spectrum. The larger photofraction of BGO also results in less prominent Compton continua and annihilation quanta escape peaks. A collection of spectra from gamma rays covering the range from 124 keV to 11.67 MeV taken with 2.54 × 2.54 and 7.62 × 7.62 cm BGO detectors can be found in Ref. 14.

Because of the lack of suitable sources, it is often difficult experimentally to measure the response function for all gamma-ray energies of potential interest. It is then necessary

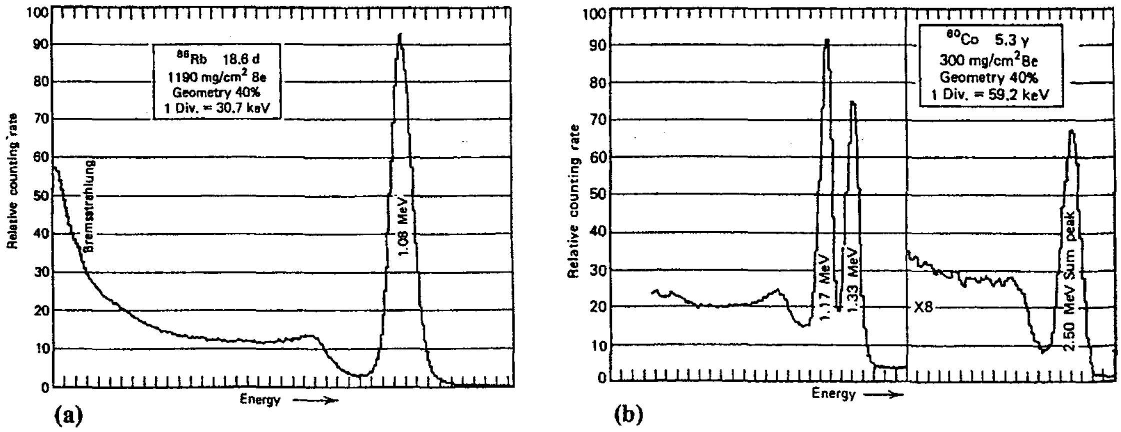

Figure 10.12 Pulse height spectra recorded from NaI(Tl) scintillation detectors. (*a*) A spectrum for a ^{86}Rb source (1.08 MeV gamma rays) showing the contribution at the lower end of the scale from bremsstrahlung generated in stopping the beta particles emitted by the source. (*b*) Spectrum from a ^{60}Co source (1.17 and 1.33 MeV gamma rays emitted in coincidence) taken under conditions in which the solid angle subtended by the detector is relatively large, enhancing the intensity of the sum peak at 2.50 MeV. (From F. Adams and R. Dams, *Applied Gamma-Ray Spectrometry*, 2nd ed. Copyright 1970 by Pergamon Press, Ltd. Used with permission.)

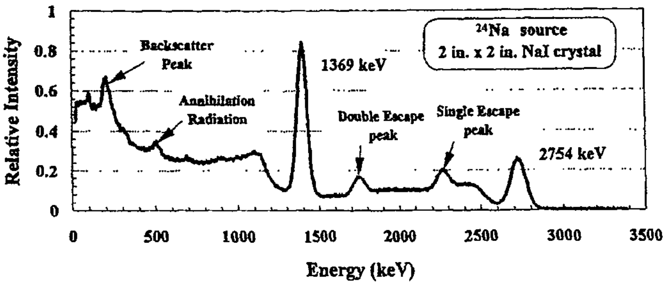

Figure 10.13 Pulse height spectrum from a NaI(Tl) scintillator for gamma rays emitted by ^{24}Na at 1369 and 2754 keV. The single and double escape peaks corresponding to pair production interactions of the higher energy gamma rays are very apparent, as is the annihilation radiation peak at 511 keV due to pair production interactions in surrounding materials.

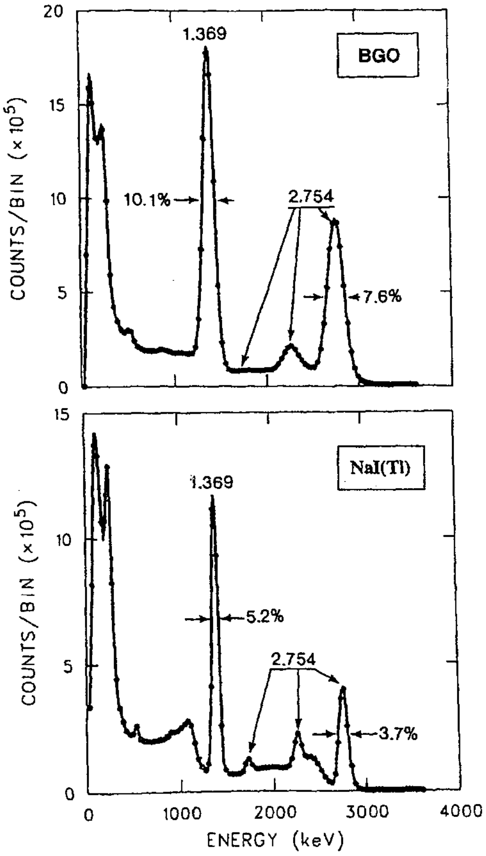

Figure 10.14 Comparative pulse height spectra measured for BGO (top) and NaI(Tl) (bottom) scintillators of equal 7.62 cm × 7.62 cm size for gamma rays from ^{24}Na. (From Moss et al.[13])

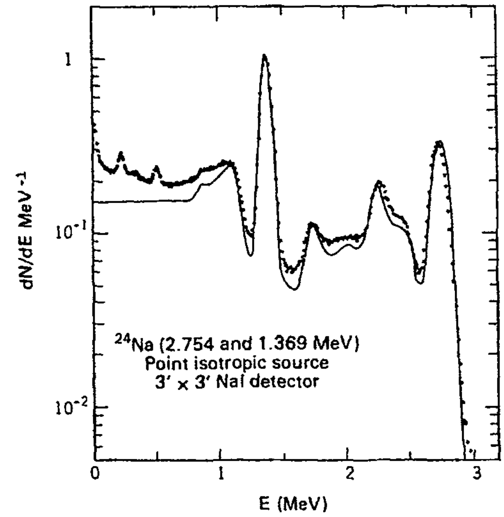

Figure 10.15 A comparison of a measured pulse height spectrum (points) with a theoretical spectrum calculated by Monte Carlo methods. (From Berger and Seltzer.[15])

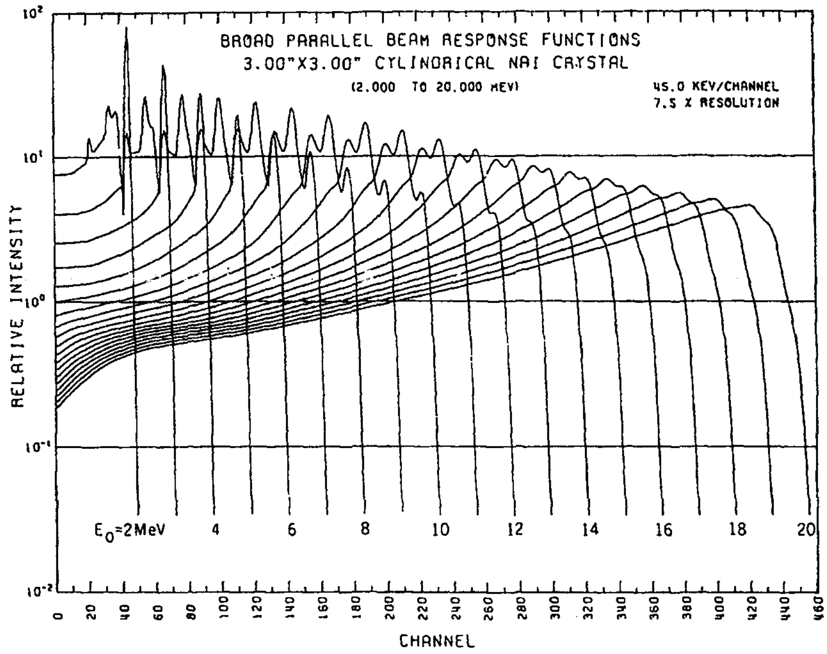

Figure 10.16 Calculated response functions for a NaI(Tl) scintillation detector extending to 20 MeV. (From Berger and Seltzer.[15])

to resort to calculations to derive the response function. Because of the complexity of the situation in which multiple interactions play an important role, virtually all practical calculations are done using the Monte Carlo method. The work of Berger and Seltzer[15] is a good example of such a calculation for sodium iodide cylindrical detectors. This publication also contains an extensive list of references to prior experimental and calculational efforts. Figure 10.15 shows the good match to experimental data that can be obtained when the computational model contains sufficient detail to provide adequate representation of all important interactions taking place within the detector. Figure 10.16 illustrates a set of calculated response functions for a sodium iodide scintillator extending to relatively high gamma-ray energies. The gradual disappearance of the photopeak and the broadening of the escape peaks as the gamma-ray energy increases is clearly illustrated by this series of plots. The photopeak disappears because pair production becomes the dominant mode of interaction, and the high-energy pair that is produced is difficult to absorb fully because of losses from bremsstrahlung emission and leakage from the surface of the crystal. The broadening of the escape peak is due to the additional statistical fluctuations in the number of photoelectrons produced as their number increases (see Section B.2 below).

Energy Resolution

In contrast to the theoretical energy deposition spectra shown in Figs. 10.2 to 10.4, the measured response functions shown above contain the "blurring" effects due to the finite energy resolution of the detector. The most striking difference is the fact that all peaks now have some finite width rather than appearing as narrow, sharp lines.

As introduced in Chapter 4, the *energy resolution* R is defined as

$$R = \frac{\text{FWHM}}{H_0} \tag{10.14}$$

where FWHM = full width at half maximum of the full-energy peak
H_0 = mean pulse height corresponding to the same peak

~~The energy resolution of scintillators is the poorest of any commonly used detector, and~~ therefore the spectra have relatively broad peaks.

1. ORIGINS OF RESOLUTION LOSS

From the arguments of Chapter 4, the finite energy resolution of any detector may contain contributions resulting from the separate effects of charge collection statistics, electronic noise, variations in the detector response over its active volume, and drifts in operating parameters over the course of the measurement. For scintillation detectors, the fluctuations in PM tube gain from event to event (see p. 273) can also add to the measured resolution. Also in some scintillators, the departure from exact proportionality between absorbed particle energy and light yield can be a significant contributor to the energy resolution for measurements on gamma rays (see p. 332). For the majority of applications of scintillators to gamma-ray spectroscopy, the first of these sources is normally the most significant. Contributions of electronic noise are usually negligible, so that preamplifiers and other electronic components used with scintillators need not include elaborate schemes for noise reduction. Variations in the light collected from scintillation events over the volume of the crystal can be a significant problem, so the techniques discussed in Chapter 8 for promoting uniform light collection are quite important. In commercially prepared crystals of typical sizes, these nonuniformities normally are a small part of the total peak width. Drifts in the operating parameters are usually associated with the PM tube and can be severe if the detector is subject to large changes in counting rate or temperature. Some methods of spectrum stabilization discussed in Chapter 18 can be applied in these cases but usually are necessary only under extreme conditions.

2. *PHOTOELECTRON STATISTICS*

Statistical spreads are therefore left as the single most important cause of peak broadening in scintillators. The statistical fluctuations will be most significant at the point in the signal chain at which the numbers of information carriers are at a minimum. For scintillation counters, this point is reached after conversion of the scintillation light to electrons by the photocathode of the PM tube.

A representative numerical example is helpful in illustrating this point. In the signal chain illustrated below, it is assumed that exactly 0.5 MeV of electron energy is deposited by the gamma-ray photon in the scintillation crystal. In thallium-activated sodium iodide the scintillation efficiency is about 12%. In the example, 60 keV is thus converted by the scintillator into visible light with an average photon energy of about 3 eV. Therefore, about 20,000 scintillation photons are produced per pulse. With allowance for some light loss at the crystal surface and at the crystal–phototube interface, perhaps 15,000 of these light photons ultimately reach the photocathode. If we assume that the average quantum efficiency of the photocathode over the scintillation spectrum is 20%, then 3000 photoelectrons are produced. This number is now the minimum in the signal chain because subsequent stages in the PM tube multiply the number of electrons.

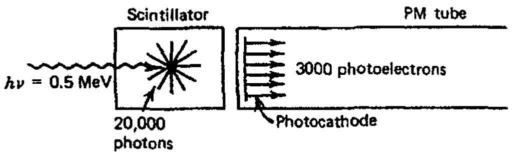

The amplitude of the signal produced by the PM tube is proportional to this number of photoelectrons. For repeated events in which exactly the same energy is deposited in the crystal, the pulse amplitude will fluctuate as a result of the inherent statistical variation in the number of photoelectrons collected for each event. If we assume that Poisson statistics hold, then the standard deviation of the number of photoelectrons should be the square root of the mean number produced. Therefore, in our example we would expect a standard deviation of $\sqrt{3000}$, or about 1.8% of the mean value. Energy resolution is formally defined in terms of the full width at half maximum of the peak rather than its standard deviation. For an assumed Gaussian shape, the FWHM is 2.35 values of the standard deviation, and therefore the statistical contribution to the energy resolution for the example should be 4.3%.

In many practical cases, the statistical broadening of the peak predominates over other potential sources of resolution loss. In that event, the variation of the resolution with gamma-ray energy can be predicted simply by noting that the FWHM of the peak is proportional to the square root of the gamma-ray photon energy. The average pulse height produced is directly proportional to the gamma-ray energy. Therefore, from the definition of energy resolution,

$$R \equiv \frac{\text{FWHM}}{H_0} = K\frac{\sqrt{E}}{E} = \frac{K}{\sqrt{E}} \tag{10.15}$$

where K is a constant of proportionality. The energy resolution should thus be inversely proportional to the square root of the gamma-ray energy. If we take the logarithm of both sides of Eq. (10.15), we derive

$$\ln R = \ln K - \tfrac{1}{2}\ln E \tag{10.16}$$

Therefore, a plot of ln R versus ln E should be a straight line with slope of $-\frac{1}{2}$.

Figure 10.17 shows a plot of experimentally determined resolution values for a sodium iodide scintillator as a function of the gamma-ray energy at which they were measured. The data adhere fairly closely to a straight line, but the slope is not as steep as predicted.

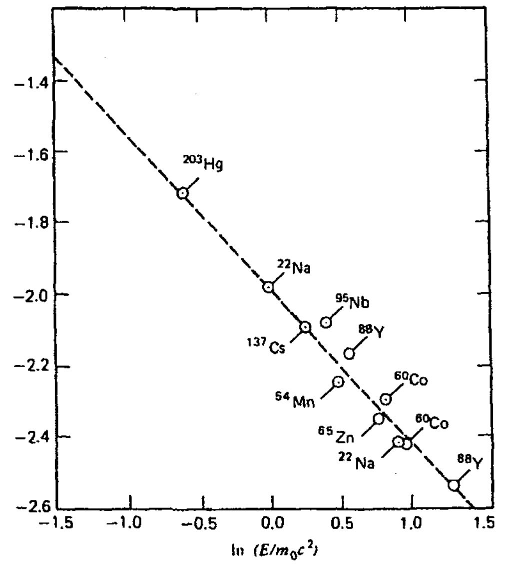

Figure 10.17 Experimentally measured resolution R from a NaI(Tl) scintillation detector for various gamma-ray energies E. (From Beattie and Byrne.[16])

indicating the influence of nonstatistical sources of the peak broadening. A more adequate representation of measured data can take the form

$$R = \frac{(\alpha + \beta E)^{1/2}}{E} \qquad (10.17)$$

where α and β are constants particular to any specific scintillator–PM combination.

3. OTHER FACTORS IN ENERGY RESOLUTION

Other sources of resolution loss in scintillation spectrometers are conveniently categorized into three groups: those that are characteristic of the crystal itself (the *intrinsic crystal resolution*), those effects that are characteristic of the PM tube, and the variable probability that a visible photon generated by a scintillation event in the crystal produces a photoelectron that is collected by the first dynode of the PM tube (the *transfer variance*).

The intrinsic crystal resolution includes any variation caused by local fluctuations in the scintillation efficiency of the crystal. With modern fabrication techniques, the uniformity of sodium iodide crystals is generally sufficiently good so that the line broadening caused by this effect alone would be very small (less than 2%). More significant fluctuations arise because of the less-than-perfect reflection conditions that exist at the surface of the crystal. The consequent nonuniform light collection efficiency can introduce significant line broadening, especially in crystals of large size.

The variance introduced by the photomultiplier tube can be a significant contribution. Uniformity of photoelectron collection from the photocathode is an important factor, as is the statistical fluctuation in the electron multiplication. There is considerable variation in the performance of different photomultipliers in this regard, even among different samples of the same design. For example, in a study of several hundred PM tubes sampled from a few standard types, Persyk and Moi[17] observed an average NaI scintillator energy resolution of 10–11% for ^{57}Co radiation (122 keV). The best PM tube included in the sample, however, gave a corresponding value of 8.5%.

A more subtle component of the intrinsic crystal resolution arises from the nonlinearity in the response of most scintillation materials (see Fig. 8.8). If all incident gamma rays underwent an interaction in which their entire energy were converted to a single electron, this nonlinearity would not be a source of resolution loss. However, the incident gamma-ray energy may be subdivided among two or more secondary electrons through single or multiple Compton scattering followed by photoelectric absorption. Furthermore, even if simple photoelectric absorption occurs, the excited atom that remains may convert its excitation energy in a number of ways which lead to varying electron energy spectra, primarily in the form of Auger electrons. Consequently, even a monoenergetic flux of incident gamma rays will lead to a wide distribution of electron energies within the crystal. If the response of the crystal is not linear with electron energy, the total light yield will be different from event to event, depending on details of the energy subdivision between the various electrons that are produced. A number of studies[18, 19] conclude that the effects of nonlinearity can have a significant impact on the observed energy resolution from scintillators. As one example, Fig. 10.18 shows that the calculated effect of nonproportionality in sodium iodide can be as large a contributor to the overall energy resolution as the contribution of photoelectron statistics at energies above about 300 keV. This source of peak broadening would clearly be more serious in scintillators with a larger degree of nonlinearity than seen in NaI(Tl). In discussing the effects of nonlinearity of scintillators, it is important to distinguish between the response to fast electrons as opposed to the response to X-rays or gamma rays. The first is expected to be an intrinsic property of the scintillator, whereas the second depends on the particular mix of secondary electrons produced by photon interactions. Since this mix can change with the size of the crystal because of the increased importance of multiple scattering, the two behaviors will not be expected to be identical.[20] One should also be careful to distinguish between the terms *nonlinearity* and *nonproportionality*.[20] A linear behavior between light output and energy deposited merely requires that a straight-line fit can be made to the data, whereas the term *proportionality* requires that, in addition, the best-fit line pass through the origin. The response of a given scintillator may be perfectly linear over a range of energies, but there can still be some contribution to gamma-ray peak broadening unless the response is also proportional to energy.

Because the energy resolution varies with energy, values are usually specified at a fixed gamma-ray energy for comparison purposes. It is conventional to quote the energy resolution for gamma-rays from ^{137}Cs (0.662 MeV) as a standard. The energy resolution for other gamma-ray energies can then be estimated through the use of Eq. (10.15).

Good quality solid sodium iodide scintillators coupled to modern PM tubes can achieve an energy resolution of about 6–7% at 0.662 MeV. If the shape of the crystal is more complicated than a simple right cylinder, the added difficulty of attaining uniformity in light collec-

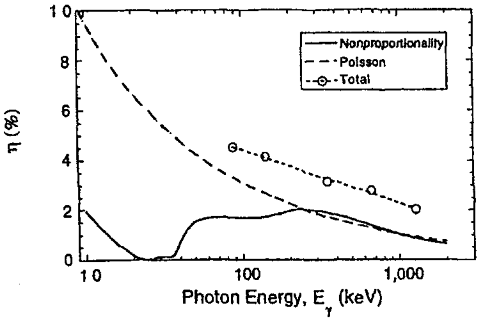

Figure 10.18 A comparison of the predicted contributions of scintillator nonproportionality and Poisson photoelectron statistics to the energy resolution of a 2.54 cm × 2.54 cm NaI(Tl) scintillator. The points labeled "Total" are measured resolution values. (From Valentine et al.[19])

tion will often make the resolution somewhat worse. For example, the energy resolution for crystals with a center well is generally 1–3% larger than the equivalent solid cylinder.

4. PREVENTION OF RESOLUTION LOSS CAUSED BY LONG-TERM DRIFT

In scintillator measurements that must extend over many hours or days, some resolution loss can be experienced as a result of drifts in the gain of the PM tube and other circuit components. Some electronic methods that can be used to minimize or completely eliminate these effects are outlined in Chapter 18. These techniques work best when there is a single isolated peak in the spectrum from which an error signal can be derived to adjust a variable gain component in the signal chain. If a strong isolated peak does not exist in the measured spectrum, or if the counting rates are low, these methods may be impractical.

For scintillation counters, an alternative method can be used, which is based on providing a reference light source within the scintillation package to produce an artificial peak in the spectrum. If the light pulses are of constant intensity, a feedback signal can be generated to adjust the system gain to hold the resulting peak at a constant position in the measured spectrum. Light sources used for this purpose fall into two general categories: those that consist of a combination of a radioactive isotope with a suitable phosphor, and those that are basically electronic in design. A common requirement is that their yield be extremely stable over long periods of time because any change in light output will be interpreted as a drift in the gain of the counting system. Discussions of the design of light sources used for this purpose are given in Refs. 21–25.

. Linearity

For all scintillators, the *scintillation efficiency* or amount of light generated per unit energy loss (dL/dE) depends both on the particle type and its kinetic energy. For an ideal spectrometer, dL/dE would be a constant independent of particle energy. The total light yield would then be directly proportional to the incident particle energy, and the response of the scintillator would be perfectly linear.

For electrons in NaI(Tl), the scintillation efficiency does vary mildly with electron energy (see Fig. 8.8). For direct electron spectroscopy, some significant nonlinearity should thus be expected. In gamma-ray measurements, monoenergetic gamma rays create varied combinations of secondary electrons with widely different energies. Figure 8.8 is therefore sampled at many points over the energy scale even for a single photon energy, and some of the nonlinearity is averaged out. The average pulse height observed for gamma rays is therefore closer to being linear with photon energy, but measurable nonlinearities remain.

Figure 10.19 shows some experimental results for linearity measurements with gamma rays on NaI(Tl). This nonlinearity must be taken into account when relating the pulse

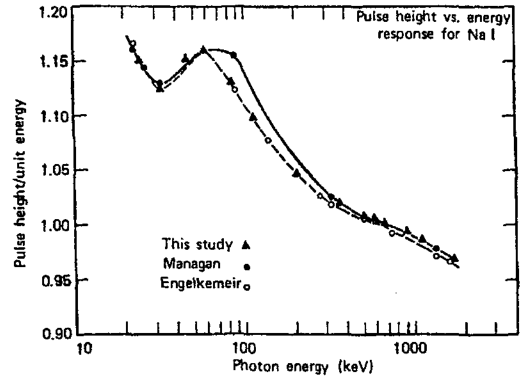

Figure 10.19 The differential linearity measured for a NaI(Tl) scintillator. (From Heath.[5])

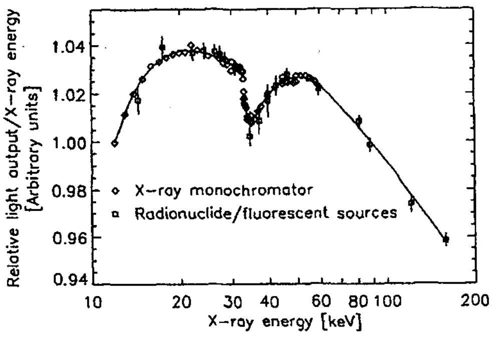

Figure 10.20 Measured light output per unit deposited energy for NaI(Tl), normalized to unity at 88 keV. (From Wayne et al.[26])

height scale to gamma-ray energy. In practice, a calibration is usually carried out in which peak positions are plotted versus known gamma-ray energies. Because Fig. 10.19 represents the slope of this calibration line, a small degree of curvature or nonlinearity should be expected. For interpolation between narrowly spaced peaks of known energy, however, the assumption of linearity normally leads to a negligible error.

Figure 10.20 shows the measured relative light output from sodium iodide over the low-energy range. The dip that is evident in this plot occurs near the K-shell absorption edge of iodine. The response of the scintillator really depends on the energy that is deposited by secondary electrons produced by the incident photon, and a complex mix of photoelectrons and/or Auger electrons will result from various types of photon interactions as illustrated in Fig. 10.21. The detailed yields of these secondary electrons will change abruptly at the

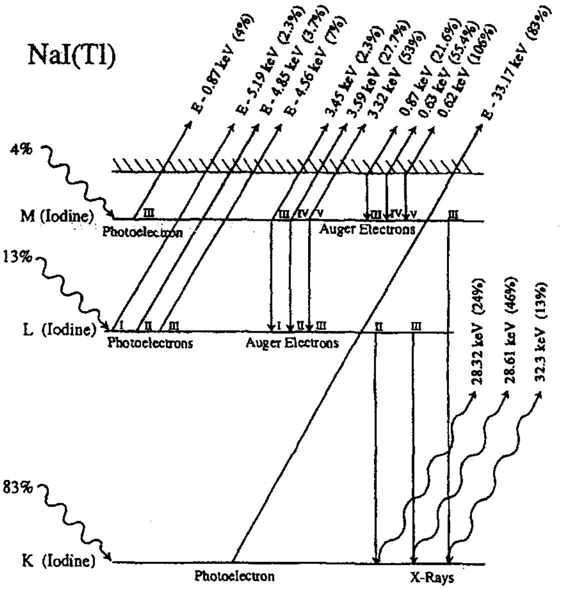

Figure 10.21 Representation of the possible origins of electrons and photons following the photoelectric absorption of an incident X-ray or gamma ray with energy E that is above the K-shell binding energy of 33.17 keV. (From Rooney and Valentine.[27])

K-shell absorption edge, so it is not surprising that the discontinuities in the observed light output also occur near this energy.

D. Detection Efficiency

One of the marked advantages in using scintillation crystals for gamma-ray measurements is the fact that many standard size detectors can be mass produced with virtually identical properties. Because the physical dimensions of these crystals can be controlled to within very small tolerances, the interaction probability for gamma rays will be identical for all crystals of the same size and shape.

One of the common applications of sodium iodide scintillators is to measure the absolute intensity of a given source of gamma rays. From the discussion in Chapter 4, such a measurement based on simple counting data requires a prior knowledge of the efficiency of the radiation detector. Undoubtedly, there are more published data available on the detection efficiency of sodium iodide scintillators for gamma rays than for any other detector type or application. The number of different sizes and shapes of NaI(Tl) crystals in routine use is relatively limited so that reasonably complete data can be compiled on each of the common configurations.

1. CRYSTAL SHAPES

Two general crystal shapes are in widespread use for applications in gamma-ray detection. The solid right circular cylinder is simple to manufacture and encapsulate and can be mounted directly to the circular face plate of most PM tubes. If the height-to-diameter ratio of the cylinder does not greatly exceed unity, the light collection properties are quite favorable in this geometry. If the height-to-diameter ratio is much less than 1, the pulse height resolution can often be improved by interposing a light pipe between the crystal and photomultiplier tube to spread the light more uniformly from each scintillation event over the entire photocathode, averaging out spatial variations of its quantum efficiency.

A *well crystal* is a right circular cylinder into which a cylindrical well has been machined, usually along the cylindrical axis. A significant advantage of this geometry is the very high counting efficiency that can be achieved by placing the samples to be counted at the bottom of the well. In this position, almost all the gamma rays that are emitted isotropically from the source are intercepted by at least a portion of the crystal. For low-energy gamma rays, the counting efficiency in this geometry can therefore approach 100%. At higher energies, some of the advantage is lost because the average path length through the crystal is somewhat less than if the gamma rays were externally incident on a solid crystal. Because the efficiency for sources near the bottom of the well is not a sensitive function of position, well counters can also simplify the counting of multiple samples with different physical properties while providing nearly identical counting efficiency.

2. EFFICIENCY DATA

Data on detector efficiency are commonly presented in the form of a graph of the efficiency value as a function of gamma-ray energy. Some examples are shown in Figs. 10.22 through 10.25. It is important to point out those parameters that must be specified before using this type of data:

1. The specific category of efficiency which is being tabulated must be clearly identified. As defined in Chapter 4, detector efficiencies are classified as either absolute or intrinsic, with the latter being the more common choice. An additional specification must be made that deals with the type of event accepted by the counting system. Here the most common choices are either peak or total efficiencies, with the distinction hinging on whether only full-energy events or all events are accepted (see Chapter 4).

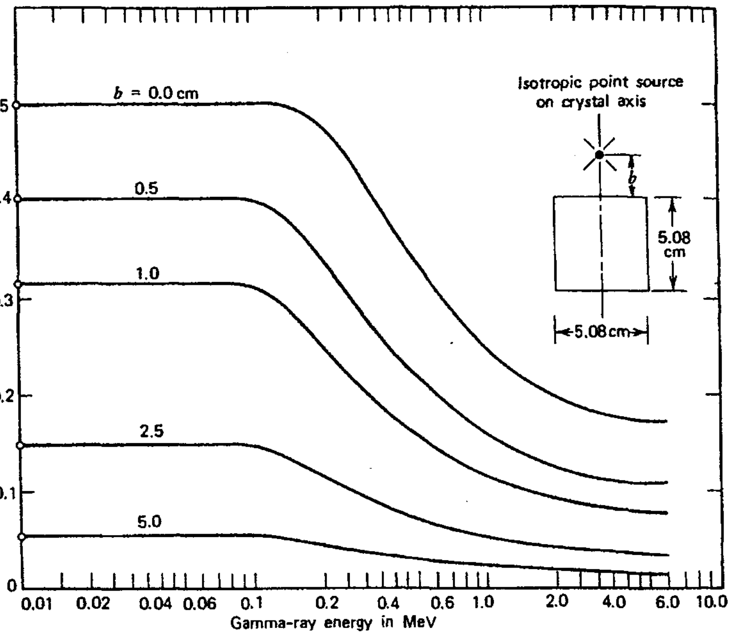

Figure 10.22 The absolute total efficiency calculated for a 5.08 cm × 5.08 cm solid cylindrical NaI(Tl) scintillator. Different values of the source location are shown. (From Snyder.[28])

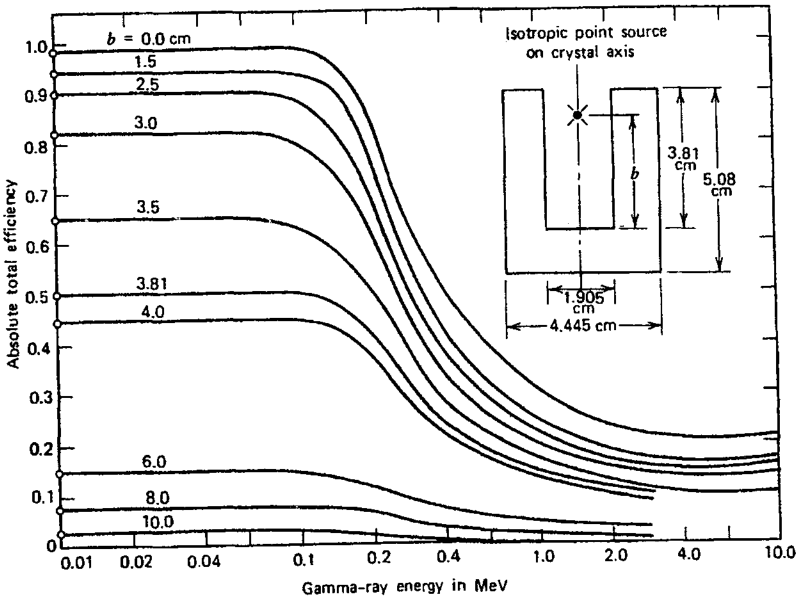

Figure 10.23 The absolute total efficiency calculated for a point gamma-ray source and a NaI(Tl) well-type scintillator with the dimensions shown. The parameter *b* is the source height above the well bottom. (From Snyder.[28])

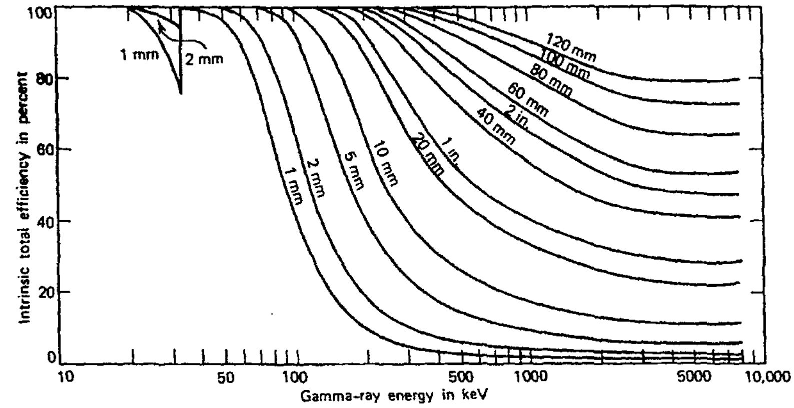

Figure 10.24 The intrinsic total efficiency of various thicknesses of NaI(Tl) for gamma rays perpendicular to its surface.

2. The size and shape of the scintillation crystal have a strong influence on the counting efficiency. Although the major influence on the intrinsic efficiency is the thickness of the crystal in the direction of the incident gamma radiation, mild variation with other detector dimensions should also be expected.
3. The size and physical nature of the source also influence the counting efficiency. Data are widely available for the relatively simple case of an isotropic point gamma-ray source located a specified distance from the detector face along its axis. Although absolute efficiencies are quite sensitive to the source–detector spacing, this dependence is much milder for intrinsic efficiencies and vanishes entirely if the source is sufficiently far from the detector. Other common source conditions for which data can be found include the case of a parallel beam of gamma rays uniformly irradiating one surface of the detector (equivalent to a point source at an infinite distance) and a narrowly collimated beam (a "pencil beam") incident at a specified point on the detector surface. Limited data also are available for distributed sources consisting of disks or volumetric sources under specified source–detector geometries.
4. Any absorption taking place between the point of gamma-ray emission and the scintillation crystal will also influence the detection efficiency. Published data normally neglect the effects of the crystal housing and other material between the source and detector, but some data can be found that account for self-absorption within large-volume gamma-ray sources.

There are two general methods by which efficiency data may be generated. The most straightforward is simply to measure the appropriate counting rate induced by a gamma-ray source of known activity. Sets of "standard" gamma-ray sources can be purchased whose absolute activity can be quoted to about 1% precision. If the experimenter has a set of such sources available covering the energy range of interest, then an efficiency curve can be determined experimentally for the specific detector in use. In many cases, however, a set of absolutely calibrated sources is not available or they do not adequately represent the geometric irradiation conditions of the actual experiment. Then the experimenter must turn to published efficiency data, which can include a greater variety of energies and experimental conditions.

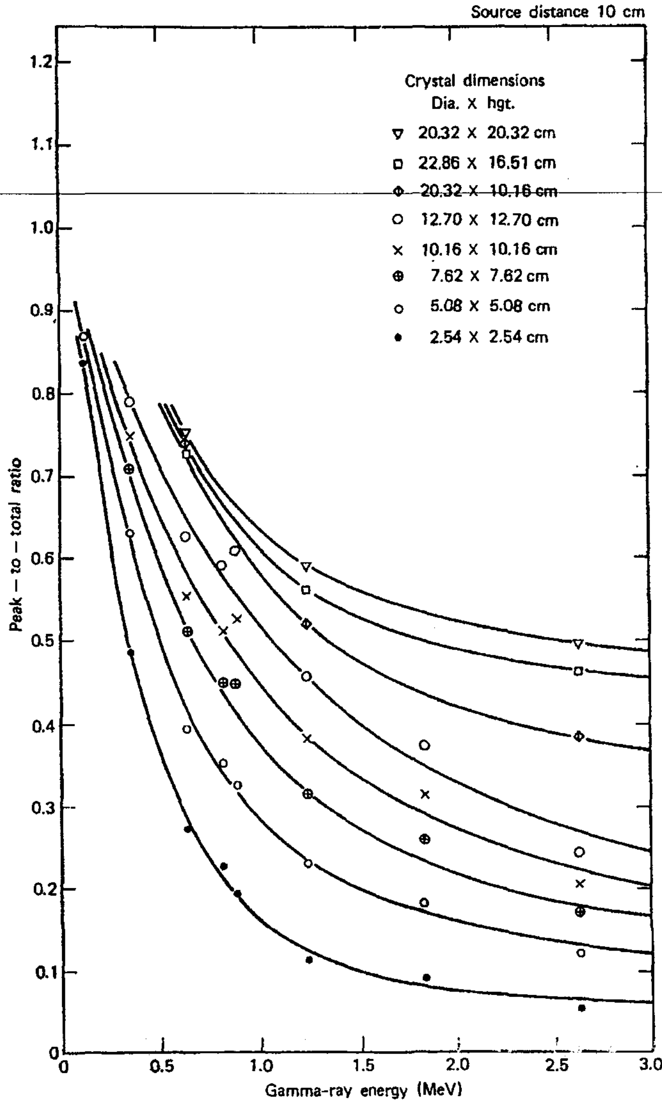

Figure 10.25 Peak-to-total ratio (or the photofraction) for various solid cylinders of NaI(Tl) for a point gamma-ray source 10 cm from the scintillator surface. (Courtesy of Harshaw Chemical Company.)

A second means of obtaining efficiency data is through calculation based on an assumed knowledge of the various gamma-ray interaction probabilities. The simplest case is the total efficiency, which is completely determined by the total linear absorption coefficient μ that characterizes the detector material. The intrinsic total efficiency is just the value of the gamma-ray interaction probability $(1 - e^{-\mu l})$ integrated over all path lengths l taken by those gamma rays that strike the detector. For simple geometries, this integration can be carried out analytically. In most cases, however, the peak efficiency is of greater interest. Because more complex processes involving multiple interactions contribute to full-energy events, the peak efficiency, in general, no longer can be calculated analytically. Instead, recourse must be made to Monte Carlo calculations, which attempt to simulate the behavior of gamma-ray photons based on knowledge of the individual probabilities for photoelectric absorption, Compton scattering, and pair production. Because each Monte Carlo calculation is, in effect, a computer experiment, the results obtained are subject to statistical uncertainties determined by the number of histories that have been calculated. Furthermore, the results are specific to the detector geometry and gamma-ray energy assumed and cannot be generalized further.

Extensive tables and graphs of sodium iodide detector efficiencies can be found in Refs. 5, 6, and 29. A good review of both experimentally determined and calculated efficiencies for solid cylindrical sodium iodide crystals has been published by Grosswendt and Waibel.[30] Extensive references are also tabulated in Refs. 31 and 32 for calculations and measurements of efficiencies for well-type crystals, and in Ref. 33 for other crystal shapes.

When the gamma-ray-emitting sample is not negligibly small, self-absorption effects can substantially reduce the efficiency that would be obtained for point sources. The usual procedure is to apply a multiplicative correction factor to standard efficiencies to account for absorption within the sample itself.[34] This approach gives adequate representation for a wide range of physical situations.[35] Reviews of scintillator efficiencies for absorbing disk sources are given in Refs. 36 and 37.

Most of the available efficiency data concern sources that are located along the axis of symmetry of the detector, and only limited data are available regarding the directional response of scintillation crystals to off-axis sources. One such analysis for cylindrical scintillators is given in Ref. 38, which also contains references to other previously published data on directional characteristics.

Efficiency data can also be found for scintillation materials other than sodium iodide. Some measurements comparing cesium iodide with sodium iodide are shown in Figs. 10.26 and 10.27. CsI(Tl) exhibits both a higher efficiency and a greater photofraction, but its somewhat lower light output (as measured using standard PM tubes) leads to a poorer energy resolution. Corresponding differences are even more extreme in the case of BGO. Figure 10.28 shows that the intrinsic peak efficiency for an equivalent size BGO crystal can be greater by almost a factor of 10 than for sodium iodide at high gamma-ray energies, but

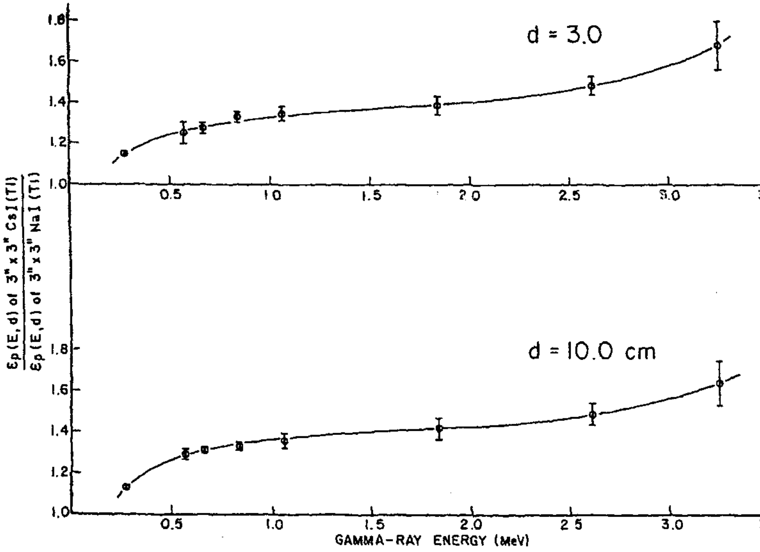

Figure 10.26 Relative intrinsic peak efficiencies of 7.62 cm × 7.62 cm cylindrical crystals of CsI(Tl) and NaI(Tl); *d* is the crystal–source distance. (From Irfan and Prasad.[39])

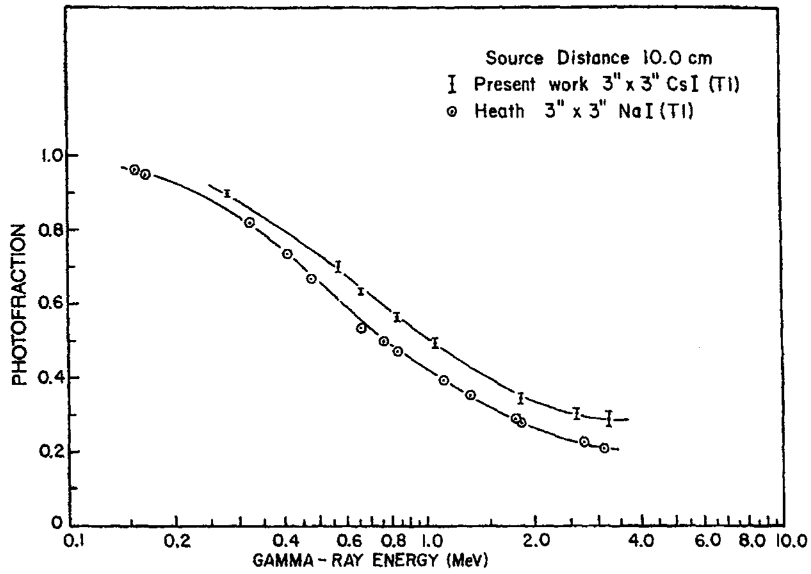

Figure 10.27 Experimental photofractions of 7.62 cm × 7.62 cm cylindrical crystals of CsI(Tl) and NaI(Tl). (From Irfan and Prasad.[39])

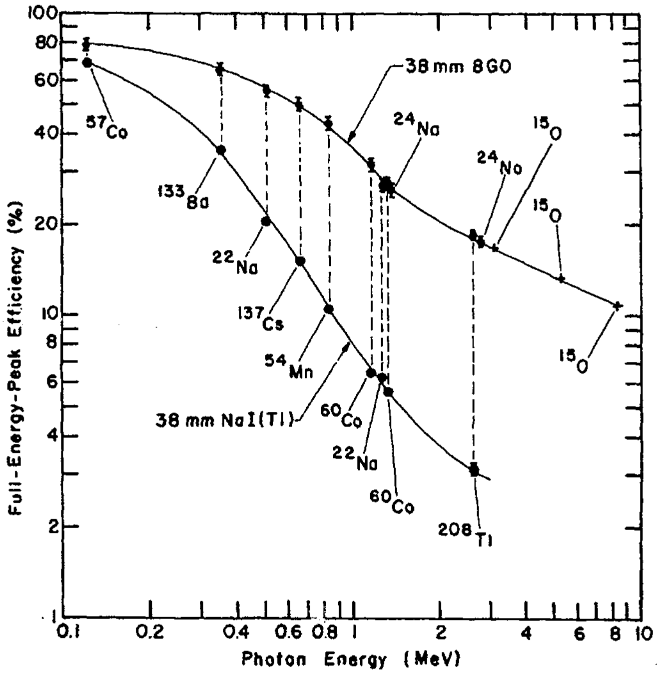

Figure 10.28 Intrinsic peak efficiencies for BGO and NaI(Tl) scintillators of equal 38 mm × 38 mm size. Radioisotope sources used for various photon energies are indicated. (From Evans and Orndoff.[40])

the energy resolution is even poorer than in cesium iodide. Gamma-ray detection efficiencies for NE-213 organic liquid scintillators are given in Refs. 41 and 42, for plastic scintillators in Ref. 43, and for lead-doped plastic scintillators in Ref. 44.

3. PEAK AREA DETERMINATION

To apply the peak efficiency data for any detector, the area under the full-energy peaks that appear in its spectrum must be determined. Even after subtraction of the normal background, nearly all such peaks will be superimposed on a continuum caused by many of the complicating effects described earlier in this chapter. It is therefore not always a simple task to determine the number of events that contribute to a given full-energy peak.

If the peak were a simple isolated one without any superimposed continuum, as shown in Fig. 10.29*a*, its area could be determined by simple integration between the limits shown. When the spectrum is recorded in a multichannel analyzer, the equivalent process is a simple addition of the content of each channel between the indicated limits. If a continuum is also present, as in Fig. 10.29*b*, some additional unwanted counts are included in this process and must be subtracted. Some shape must therefore be assumed for the continuum within the region under the peak, and a number of fitting procedures of varying degrees of complexity can be applied. A linear interpolation between the continuum values on either side of the peak is the easiest approach and will give sufficient accuracy for many purposes.

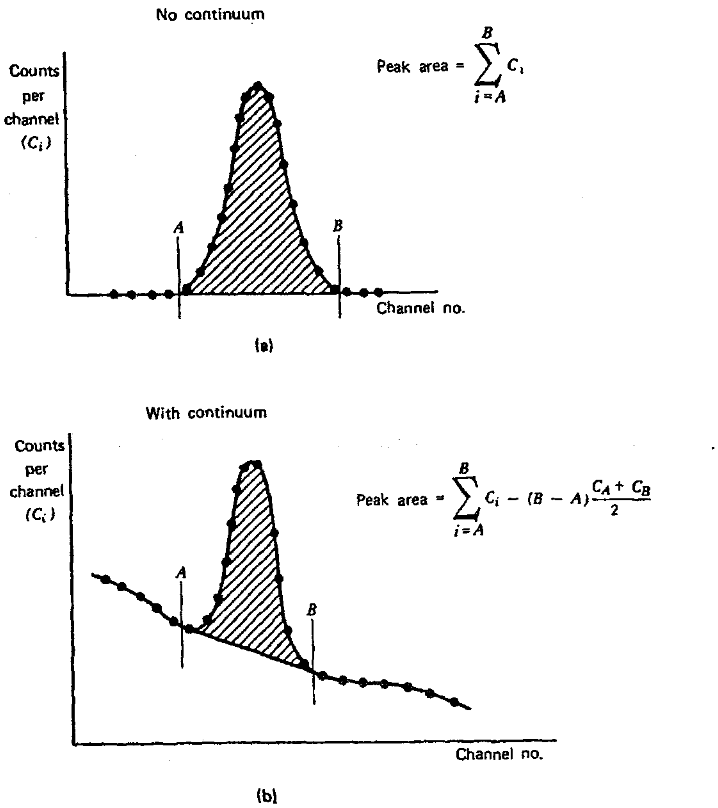

Figure 10.29 Methods of obtaining peak areas from multichannel spectra. In part (*a*) the continuum under the peak present in part (*b*) is negligible.

At times, closely spaced or overlapping peaks do not allow the straightforward summation method to be applied. More complex methods must then be used to separate the individual contributions of each of the closely lying peaks. These methods normally involve fitting an analytic shape to that portion of the peak that can be clearly resolved, and assuming that the remainder of the peak is described by the fitted function. A Gaussian curve fitted to the points that lie within one standard deviation on either side of the peak value adequately represents the shape of the measured photopeak from a NaI(Tl) scintillator over an assortment of source geometry and counting conditions.[45] More complex shapes are sometimes necessary for spectra recorded at high rates or under nonideal circumstances.

V. RESPONSE OF SCINTILLATION DETECTORS TO NEUTRONS

Some types of scintillators specifically designed to be used as neutron detectors are described in Chapters 14 and 15. However, virtually any scintillation material will respond to some extent if exposed to a neutron flux. Fast neutrons are sometimes unavoidably present in gamma-ray measurements made around accelerators or reactors, and the pulses they produce can be an undesirable background. These pulses fall into two general categories: prompt pulses that are produced within a few nanoseconds of the time the neutron enters the scintillator, and pulses that occur after some delay.

In NaI(Tl) and BGO, the prompt pulses are principally caused by the detection of gamma rays produced in inelastic scattering interactions of the neutron with the scintillator.[46] Figure 10.30 shows the detection efficiency corresponding to the prompt pulses in these two materials. BGO has a better gamma ray to neutron sensitivity ratio compared with NaI(Tl).

The delayed pulses can be triggered by two categories of events. A neutron first may be moderated (requiring perhaps 100 μs) and then captured in the detector as a therma neutron. The resulting capture gamma rays may lead to a detected pulse. Pulses that occur after a much longer delay may result if the neutron capture produces a radioactive species that subsequently decays. Examples with their corresponding half-lives are ^{24}Na (15 h) and ^{128}I (25 min) in sodium iodide, and ^{75}Ge (83 min) and ^{77}Ge (11.3 h) in BGO.

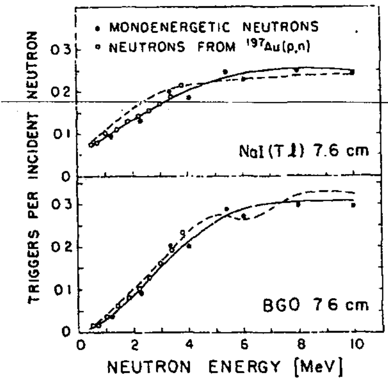

Figure 10.30 The prompt pulse response to fast neutrons in 7.6 cm × 7.6 cm scintillation detectors of NaI(Tl) and BGO. (From Hausser et al. [46])

I. ELECTRON SPECTROSCOPY WITH SCINTILLATORS

Scintillators can also be applied to the measurement of fast electrons (such as beta particles) that are incident on one surface of the crystal. Although it has become more common to use lithium-drifted silicon detectors for this purpose (see Chapter 13), applications sometimes arise in which the size limitation of silicon detectors or other considerations dictate the use of scintillators.

The nature of the electron response function depends on the scintillation material, its physical thickness, and the angle of incidence of the electrons. Electrons from an external source normally must pass through some protective covering and/or light reflector before reaching the surface of the scintillator itself. In the discussion that follows, the energy loss that may occur in these intervening materials is not explicitly considered but may be important if the electron energy is small. We also assume that the scintillators under consideration are thicker than the maximum range of the incident electrons. Even so, the detector may not be totally opaque to the secondary bremsstrahlung photons that will be generated along the path of the electron.

In general, the response functions show a pronounced full-energy peak corresponding to the total absorption of the incident electron energy, together with a tail extending to lower energies. The major cause of such partial energy absorption is backscattering, in which the electron reemerges from the surface through which it entered after having undergone only partial energy loss. Other events that contribute to the tail are those electrons that are fully stopped within the scintillator but that generate bremsstrahlung photons that escape from the front or back surface of the detector.

Both the probability of backscattering and the fraction of the electron energy loss due to bremsstrahlung increase markedly with the atomic number of the scintillator. Because both processes detract from the full-energy peak and add the unwanted tail to the response function, scintillators with low atomic number are generally preferred for electron spectroscopy (just the opposite criterion than that desired for gamma-ray spectroscopy). Therefore, organic scintillators such as anthracene or plastics are most commonly applied in electron measurements. Table 10.1 lists the probability for backscattering of normally incident electrons for some common scintillator materials. The much lower backscattering probabilities for the low-Z materials are evident.

Figure 10.31 shows measured pulse height spectra in both cesium iodide and a plastic scintillator for normally incident 1 MeV electrons. The low-energy tail is more pronounced for cesium iodide because of its higher atomic number. Additional data for other scintillation materials, electron energies, and varying angles of incidence are given in Ref. 47.

ble 10.1 Fraction of Normally Incident Electrons Backscattered from Various Detector Surfaces

	Electron Energy (MeV)				
ntillator	0.25	0.50	0.75	1.0	1.25
stic	0.08 ± 0.02	0.053 ± 0.010	0.040 ± 0.007	0.032 ± 0.003	0.030 ± 0.005
thracene	0.09 ± 0.02	0.051 ± 0.010	0.038 ± 0.004	0.029 ± 0.003	0.026 ± 0.004
I(Tl)	0.450 ± 0.045	0.410 ± 0.010	0.391 ± 0.014	0.375 ± 0.008	0.364 ± 0.007
(Tl)	0.49 ± 0.06	0.455 ± 0.023	0.430 ± 0.013	0.419 ± 0.018	0.404 ± 0.016

rce: Titus.[47]

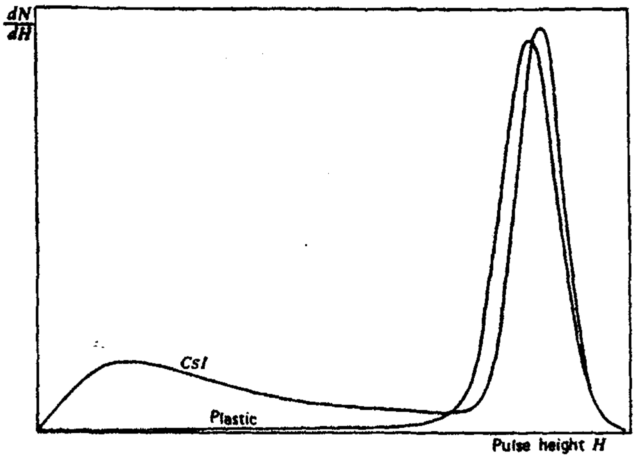

Figure 10.31 Experimental pulse height spectra from CsI(Tl) and plastic scintillators for 1.0 MeV electrons at normal incidence. The spectra are normalized to the same maximum pulse height. (From Titus.[47])

VII. SPECIALIZED DETECTOR CONFIGURATIONS BASED ON SCINTILLATION

A. The Phoswich Detector

The combination of two dissimilar scintillators optically coupled to a single PM tube is often called a *phoswich* (or *phosphor sandwich*) detector. The scintillators are chosen to have different decay times so that the shape of the output pulse from the PM tube is dependent on the relative contribution of scintillation light from the two scintillators. Most applications involve the use of this pulse shape difference to distinguish events that have occurred in only one scintillator from those that occur in both. For example, lightly penetrating radiations can be made to stop fully in the first scintillator, but more penetrating particles may generate light in both. Sodium iodide and cesium iodide are often chosen as the two materials because their decay times are quite different (0.23 versus 0.68 + 3.34 μs), and pulses arising from only one decay are easily distinguished from those with both components, using the pulse shape discrimination methods of Chapter 17. Other common scintillator combinations include BGO and cesium iodide[48,49] or two different plastic scintillators,[50,51] one with a fast decay time and the other with a slow decay. Examples of additional combinations that have been used include CsI(Na) with GSO,[52] BGO with GSO,[53] plastic scintillator with BaF_2,[54–56] and YSO with LSO.[57] Phoswich detectors employing pulse shape discrimination have proved to be useful in suppressing background in the counting of X-rays and beta particles.[58,59]

Alternatively, separate electronic pulses may be derived from the fast and slow components of the PM tube signal.[51,60] Independent measurements of the energy deposited in each scintillator can then be obtained without the need for a second PM tube. Using a thin fast scintillator in front of a thick slow scintillator allows simultaneous measurements of dE/dx and E for particles that penetrate the thin detector. The particle identification techniques described on p. 396 can then be applied to distinguish one type of heavy charged particle from another

A somewhat simpler version of a phoswich detector has been commercially implemented as a combined alpha/beta particle probe. It consists of a thin ZnS(Ag) screen mounted behind a thin aluminum entrance window to serve as the alpha particle detector. This screen is thick enough to stop the alphas, but thin enough so that incident beta particles deposit a very small amount of energy while passing through. A plastic scintillator that is a few millimeters thick is mounted behind this screen and provides the useful response to beta particles. The two scintillators are in optical contact and are viewed by a single photomultiplier tube. The contributions of the alpha and beta particles can be separated by simple amplitude selection because the energy of the alpha particles is generally much larger than the betas, and the scintillation efficiency of the ZnS(Ag) scintillator is much higher than that of the plastic scintillator.

B. The Moxon–Rae Detector

Another type of gamma-ray detector can be built based on the detection of secondary electrons produced by gamma-ray interactions in a converter that is external to the detector. Although the resulting detection efficiency is typically quite low, the efficiency versus energy dependence can be tailored in certain ways to suit the needs of specialized applications. For example, Moxon and Rae[61] first described the properties of a thick low-Z converter used to produce secondary electrons that were then detected by a thin plastic scintillator. By choosing a converter that consisted of graphite with a small component of bismuth, they found that the detection efficiency could be made nearly proportional to the incident gamma-ray energy. This proportionality allows a simplified analysis to be carried out for a class of experiments involving neutron capture because the detection probability of any given radiative capture event becomes independent of the specific de-excitation cascade mechanisms following the capture.[61] The proportionality of efficiency with gamma-ray energy results from the combined probabilities of electron production within the converter and of their escape from the surface facing the electron detector. Detailed analyses of the theory and performance of Moxon–Rae detectors can be found in Refs. 61–63.

. Liquid Scintillation Counters

The liquid scintillation media discussed in Chapter 8 can be applied to avoid some of the difficulties that arise when measuring low-energy beta particles or alpha particles using conventional methods. The approach, sometimes called *internal source liquid scintillation counting*, involves dissolving the sample to be counted directly into the liquid scintillator. Under these conditions, problems relating to sample self-absorption, attenuation of particles by detector windows, and beta backscattering from the detector are completely avoided. These advantages are particularly important for low-energy radiations such as the beta particles emitted by tritium and ^{14}C. The endpoint energies for these beta spectra are 18 and 160 keV, respectively, and average beta energies are about one-third these values. Because these isotopes are particularly important in chemical and biomedical applications, much of the development of the liquid scintillation technique has taken place in connection with these sciences. Several texts have been published[64–66] that thoroughly review the fundamental principles of liquid scintillation counting.

The first step in the technique involves incorporation of the sample within a suitable liquid scintillation solution. Problems can often arise in this step because most liquid scintillation solutions are based on toluene or other organic solvents, whereas many samples are often more conveniently prepared in an aqueous solution. Detailed discussions of various methods for obtaining stable solutions through the use of solubilizing or complexing agents are given in Refs. 67 and 68. A common problem is that the introduction of the sample tends to reduce the scintillation light output compared with the pure scintillator. This phenomenon, commonly called *quenching*, often limits the amount of sample material that can effectively be incorporated within the scintillator solution. The quenching can be due to either alteration of the optical properties of the solution by the sample (*color quenching*) or interference with the energy transfer process within the scintillator itself. Insoluble materials can sometimes be introduced as a suspension of fine particles. In those cases where rapid settling of the suspension is a problem, some methods have been developed that involve converting the solution to a gel immediately after preparation of these suspensions.

After the sample has been prepared, the solution is normally loaded into a glass vial and placed in a light-tight enclosure viewed by one or more PM tubes. Because of the effects of quenching and the fact that typical applications involve radiations of low energy, pulses produced in the PM tube often correspond to no more than a few photoelectrons. Under these circumstances, the measurements are potentially very sensitive to sources of noise that may interfere with accurate and reproducible counting of the sample. Significant sources of noise are thermally generated electrons from the photocathode of the PM tube, long-lived phosphorescence in the scintillator, and chemiluminescence (light generated by chemical reactions within the sample–scintillator solution). Virtually all these noise sources correspond to the generation of only a single electron per pulse, so they can normally be rejected by placing a discrimination level in the signal chain to eliminate those pulses whose amplitude corresponds to a single photoelectron. However, because the signal also consists of only a few photoelectrons, there is a risk that this discrimination process will also eliminate some of the signal.

Because all beta particles emitted by the sample pass through some portion of the scintillator, and the great majority are fully stopped within the solution, the counting efficiency can potentially be close to 100%. The degree to which the few-photoelectron signal can be distinguished from single-electron noise determines the practical counting efficiency. As a gauge of the development of the technique, it is interesting to note the improvement in the counting efficiency for tritium as improvements in PM tube design and other techniques have been implemented. A counting efficiency of about 20% in 1960 was improved to about 60% in 1970 through the use of low-noise bialkali PM tubes, and to a value of about 90% through the application of PM tubes with gallium phosphide high-gain dynodes.[69]

One method of eliminating the PM tube noise is to use two PM tubes to view the scintillator from opposite sides. Only those pulses that are observed in coincidence between the two tubes are counted. Because the noise generated in each tube will be uncorrelated, a true coincidence will not be observed for these events, and the recorded counts will correspond only to events generated within the liquid scintillator. The summed output from both PM tubes can then be used to record the pulse height spectrum for the sample.

Although most commonly applied to samples emitting beta particles or conversion electrons, liquid scintillation counting has also been used to count samples that are alpha active.[70–72] Although the best reported energy resolution[71] of 5–8% is much inferior to that attainable with semiconductor diode detectors, the advantages of high counting efficiency and uniform counting geometry offer some attraction for applications such as counting low-level environmental samples.[72] Because typical alpha energies are several MeV, the light output is much greater than for low-energy beta particle counting, and therefore a counting efficiency that approaches 100% is relatively easy to achieve. Pulse shape discrimination can be applied to eliminate backgrounds due to beta particles or gamma-ray-induced events.[73] By using these techniques, an exceptionally low background level of 0.01 count/min has been reported[71] while maintaining essentially 100% counting efficiency for alpha particles within the sample. To provide an even cleaner separation between the alpha particle events and those from the background, the use of a system with a two-parameter multichannel analyzer[74–76] has been shown to be very effective. Simultaneous measurements are made of the pulse amplitude and rise time that allow a cleaner separation by defining areas of interest in a two-dimensional memory. The background can then be as low as 0.001 counts/min. An illustration of the principle of this technique is given later in Fig. 18.13.

). Position-Sensitive Scintillators

1. ONE-DIMENSIONAL POSITION SENSING

Because the light from a scintillator is generated along the track of the ionizing particle, it is possible to sense the position of interaction by localizing the source of the scintillation light. For sensing position in one dimension, a long rod or bar of scintillation material can be used with PM tubes or photodiodes positioned at either end as in the sketch below:

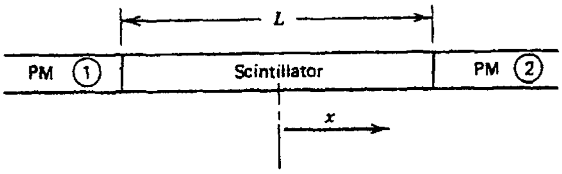

In this type of geometry, it is generally observed that the intensity of the light measured at one end of the rod drops off exponentially with the distance at which the scintillation light is generated. Thus, we can write for the signal from PM tube ①

$$E_1 = \frac{E_\gamma P}{E_0} \exp\left[-\alpha(L/2 + x)\right] \tag{10.18}$$

where E_γ = energy deposited by gamma ray

P = probability that light quantum produced at one end will generate a photoelectron in adjacent tube

E_0 = energy deposited per light photon created in scintillator

α = light attenuation coefficient

Similarly, for PM tube ②,

$$E_2 = \frac{E_\gamma P}{E_0} \exp\left[-\alpha(L/2 - x)\right] \tag{10.19}$$

By dividing one signal by the other, we obtain

$$\frac{E_2}{E_1} = \frac{\exp\left[-\alpha(L/2 - x)\right]}{\exp\left[-\alpha(L/2 + x)\right]} = \exp(+2\alpha x)$$

$$\ln\frac{E_2}{E_1} = 2\alpha x$$

$$x = \frac{1}{2\alpha}\ln\frac{E_2}{E_1} \tag{10.20}$$

Therefore, by electronically deriving the logarithm of the ratio of the two PM tube signals, we obtain a linear indication of the position at which the scintillation occurs.

By multiplying Eq. (10.18) and (10.19), we obtain

$$E_\gamma^2 = E_1 E_2 \left(\frac{E_0}{P}\right)^2 e^{\alpha L}$$

Now taking the square root of both sides, we obtain

$$E_\gamma = \sqrt{E_1 E_2}\,\frac{E_0}{P}\,e^{\alpha L/2} \tag{10.21}$$

Thus, the square root of the product of the two PM tube signals serves as a measure of the total scintillation light, independent of the position within the bar.

For best spatial resolution,[77] the light attenuation coefficient α in the expression above should have an optimal value of $2.9/L$. This light attenuation can be accomplished either by adjusting the reflection conditions at the surface of the scintillator or by allowing some absorption of the light to occur in the bulk of the scintillator. In a typical application of this technique,[77] a spatial resolution of 10 mm was obtained in a 500 mm long sodium iodide rod, using gamma rays of 662 keV energy.

An alternative method of sensing the scintillation position in one dimension is to use the same geometry described above but to exploit the fact that there will be a slight difference in the time of arrival of the scintillation light at the two ends of the bar. This time difference is maximum for an event that occurs at either end of the bar and decreases linearly to zero for an event at the center. The time differences are small, since the velocity of propagation of the light traveling directly from the scintillation site is c/n, where c is the velocity of light and n is the index of refraction of the scintillation medium. For typical scintillators, this corresponds to a flight time of about 5 ps/mm. However, most of the light is reflected many times from the surface of the scintillator as it travels along the length of the bar and therefore the actual flight path and propagation time are substantially extended. In one application of this method using a 250-mm long plastic scintillator rod,[78] a spatial resolution of between 17 and 23 mm was obtained for 511 keV gamma rays.

2. *TWO-DIMENSIONAL POSITION SENSING (IMAGING DETECTORS)*

In nuclear medicine, it is often necessary to form the image of the distribution of gamma-ray-emitting isotopes distributed throughout the patient. The *gamma-ray camera* is a device that senses the two-dimensional coordinates of a gamma-ray photon as it interacts in a large-area detector and forms an image through the accumulation of many such events over the exposure time. A lead pinhole or parallel hole collimator is used to restrict the gamma rays that strike the detector so that the image can be directly interpreted as the spatial distribution of the emitting isotope.

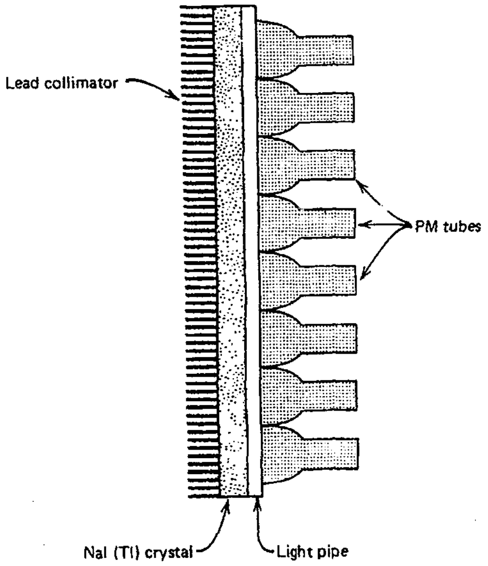

Figure 10.32 Elements of a two-dimensional position-sensitive scintillation detector, commonly called a *gamma camera.*

The most common type of gamma-ray camera is based on an original design by Anger.[79] Its basic elements are diagrammed in Fig. 10.32. The detection medium consists of a flat single scintillation crystal (generally sodium iodide) with length and width up to 50 cm and thickness of about 1 cm. The light generated by gamma-ray interactions in this crystal is sensed by an array of PM tubes that completely cover one of its flat faces. The two-dimensional position of each event across the area of the crystal is deduced from the relative size of the signals produced from these tubes.

Each scintillation event will generate output pulses of significant amplitude from all the PM tubes that are near the location of the interaction. The largest signal will generally be from the tube nearest the position, with smaller pulses from tubes at a greater distance. The "center of gravity" of the light is interpolated from these signals using either a charge division process in which a portion of each signal is coupled to X and Y output lines, or through the use of readout schemes based on delay line encoding of the position.[80] The resulting analog X and Y position signals are typically digitized using fast analog-to-digital

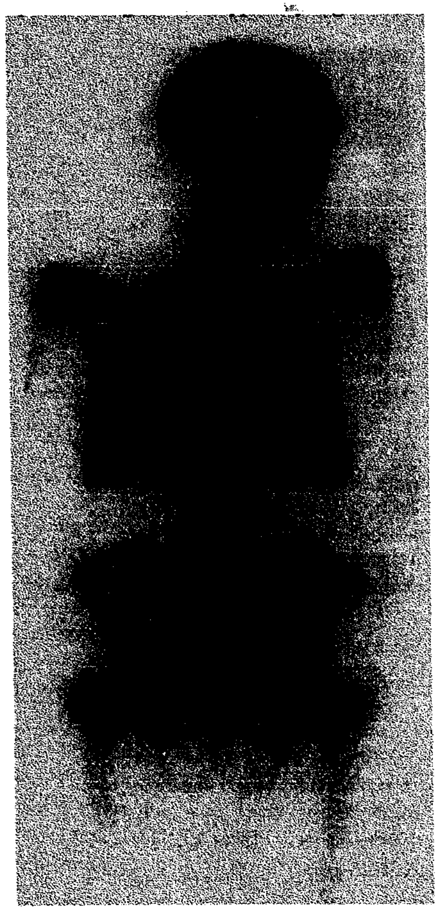

Figure 10.33 Example of a human bone scan produced by using a gamma camera to image the distribution of methylene diphosphonate labeled with ^{99m}Tc. The upper and lower halves of the image each were produced by recording approximately 10^6 counts over a 3-min period. (Courtesy of W. L. Rogers, University of Michigan Medical Center.)

converters and accumulated in a two-dimensional digital memory to form the image. The summed output from all the tubes is a good measure of the total energy deposited in the crystal and is normally passed through a single-channel analyzer to record selectively only those events that correspond to the full source energy. This selection eliminates loss of contrast in the image caused by gamma rays that have initially scattered in the patient or elsewhere before reaching the camera and would therefore give a false position indication.

An example of an image from a typical gamma-ray camera is given in Fig. 10.33. The intrinsic spatial resolution of the camera when recording the most common type of image generated by ^{99m}Tc (140 keV) is limited to about 3-mm FWHM. In practice, additional spatial resolution loss normally occurs due to the geometric uncertainties in the source position when it is some distance from the face of the collimator.

PROBLEMS

10.1 A gamma-ray photon after Compton scattering through an angle of 90° has an energy of 0.5 MeV. Find its energy before the scattering.

10.2 A 2 MeV gamma-ray photon is incident on a detector, undergoes two sequential Compton scatterings, and then escapes. If the angles of scattering are 30° and 60°, respectively, how much total recoil electron energy is deposited in the detector? Does the answer change if the sequence of the scattering angles is reversed?

10.3 Find the maximum energy that can be deposited by a 1 MeV gamma-ray photon if it undergoes two successive Compton scattering events and then escapes the detector.

10.4 Estimate the time that separates two successive gamma-ray scattering interactions that are 3 cm apart in sodium iodide. Compare with the characteristic decay time for the light that is generated in the same material.

10.5 The cross sections for photoelectric, Compton, and pair production interactions in sodium iodide at 2 MeV are in the ratio 1:20:2. respectively. Will the pulse height spectrum from 2 MeV gamma rays incident on a sodium iodide scintillator give a peak-to-total ratio of less than, more than, or about equal to 1/23?

10.6 If the energy resolution of a particular NaI(Tl) scintillation detector is 7% for ^{137}Cs gamma rays (0.662 MeV), estimate its energy resolution for the 1.28 MeV gamma rays from ^{22}Na.

10.7 The mass attenuation coefficient of NaI at 0.5 MeV is 0.955 cm^2/g. Find the intrinsic total efficiency of a slab detector 0.50 cm thick at this energy. If the photofraction is 40% at the same energy, what is the intrinsic peak efficiency?

10.8. **(a)** Find the energy of the Compton edge for the 1.17 MeV gamma rays from ^{60}Co.

(b) Calculate the backscatter peak energies corresponding to incident gamma rays of 1, 2, and 3 MeV.

10.9 Listed below are a number of parameters of interest in gamma-ray spectroscopy using scintillation detectors:

(a) Density of the detector medium.

(b) Kinetic energy required to create a scintillation photon in the crystal.

(c) Average atomic number (Z-value) of the detector medium.

(d) Geometry of the source–detector system.

(e) Gain of the photomultiplier tube.

(f) Quantum efficiency of the photocathode in the photomultiplier.

(g) Gain of the amplifier used between the detector and pulse analysis system.

(h) Fraction of light generated in the crystal that reaches the photocathode of the PM tube (light collection efficiency).

Identify those parameters from this list that have a major influence on the detector *intrinsic peak efficiency.* Repeat, but now identify those that have a major influence on *energy resolution.*

10.10 Calculate the pulse amplitude from the anode of a PM tube used with a NaI(Tl) scintillator under the following conditions: A 1-MeV electron loses all its energy in the scintillator, the light collection efficiency to the photocathode is 50%, the average quantum efficiency of the photocathode is 20%, and 80% of the photoelectrons are collected at the first dynode. Assume that the PM tube has 10 stages with a multiplication factor $\delta = 2.5$ per stage. The anode load resistance is 100 kΩ, and the anode capacitance is 100 pF.

10.11 A particular radioisotope emits two coincident gamma rays, each with 100% yield per decay, with no angular correlation between the photon directions. A sample is placed 10 cm from the surface of a 5 cm radius cylindrical detector along its axis. The intrinsic peak efficiency of the detector for γ_1 is 50%, and for γ_2 it is 30%.

(a) If the sample activity is low enough so that chance coincidences are negligible, calculate the ratio of the counts under the sum peak in the recorded pulse height spectrum to the counts under the γ_1 full-energy peak.

(b) Calculate the rate at which events are recorded in the sum peak if the source activity is 100 kBq. For a detector resolving time of 3 μs, what additional rate should be expected from chance coincidences between γ_1 and γ_2?

10.12 From Fig. 2.14, estimate the range of a 1-MeV electron in sodium iodide. From your answer, calculate the percentage of the total volume of a 5.08 cm × 5.08 cm cylindrical crystal that lies near enough to the surface so that electron escape is possible.

10.13 A radioisotope source is known not to emit any gamma-ray photons with energy of 511 keV, but a peak is observed at this position in the recorded gamma-ray spectrum. Give two possible origins for this peak.

10.14 If the energy resolution of a scintillator is 8.5% at 662 keV, find the standard deviation (in energy units) of the Gaussian curve that would be a fit to the photopeak at that energy.

10.15 Why are materials with low atomic number often preferred as scintillators for electron spectroscopy, while the opposite is true for gamma-ray spectroscopy?

10.16 Explain the major advantage of liquid scintillation counting when applied to low-energy beta emitters compared with conventional solid scintillation detectors.

REFERENCES

1. J. B. Birks, *The Theory and Practice of Scintillation Counting*, Pergamon Press, Oxford, 1964.
2. S. M. Shafroth (ed.), *Scintillation Spectroscopy of Gamma Radiation*, Gordon & Breach, London, 1967.
3. K. Siegbahn (ed.), *Alpha-, Beta-, and Gamma-Ray Spectroscopy*, North Holland, Amsterdam, 1968.
4. C. D. Broyles, D. A. Thomas, and S.-K. Haynes, *Phys. Rev.* **89**, 715 (1953).
5. R. L. Heath, *Scintillation Spectrometry Gamma-Ray Spectrum Catalogue*, IDO-16880, Vols. 1 and 2, 1964.
6. F. Adams and R. Dams, *Applied Gamma-Ray Spectrometry*, 2nd ed. and revision of original publication by C. E. Crouthamel, Pergamon Press, Oxford, 1970.
7. N. A. Wogman, D. E. Robertson, and R. W. Perkins, *Nucl. Instrum. Meth.* **50**, 1 (1967).
8. N. A. Wogman, R. W. Perkins, and J. H. Kaye, *Nucl. Instrum. Meth.* **74**, 197 (1969).
9. B. A. Euler, D. F. Covell, and S. Yamamoto, *Nucl. Instrum. Meth.* **72**, 143 (1969).
10. B. Bengtson and M. Moszynski, *Nucl. Instrum. Meth.* **85**, 133 (1970).
11. M. D. Hasinoff, S. T. Lim, D. F. Measday, and T. J. Mulligan, *Nucl. Instrum. Meth.* **117**, 375 (1974).
12. R. Mueller and D. Maeder, "Single Crystal Spectroscopy," Chap. VII in *Scintillation Spectroscopy of Gamma Radiation* (S. M. Shafroth, ed.), Gordon & Breach, New York, 1967.
13. C. E. Moss et al., *Nucl. Instrum. Meth.* **219**, 558 (1984).
14. R. R. Kiziah and J. R. Lowell, *Nucl. Instrum. Meth.* **A305**, 129 (1991).
15. M. J. Berger and S. M. Seltzer, *Nucl. Instrum. Meth.* **104**, 317 (1972).
16. R. J. D. Beattie and J. Byrne, *Nucl. Instrum. Meth.* **104**, 163 (1972).
17. D. E. Persyk and T. E. Moi, *IEEE Trans. Nucl. Sci.* **NS-25**(1), 615 (1978).
18. P. Dorenbos, J. T. M. de Haas, and C. W. E. van Eijk, *IEEE Trans. Nucl. Sci.* **42**(6), 2190 (1995).
19. J. D. Valentine, B. D. Rooney, and J. Li, *IEEE Trans. Nucl. Sci.* **45**(3), 512 (1998).
20. J. D. Valentine, B. D. Rooney, and P. Dorenbos, *IEEE Trans. Nucl. Sci.* **45**(3), 1750 (1998).
21. J. Berger et al., *Nucl. Instrum. Meth.* **A279**, 343 (1989).
22. J. Zabierowski, *Nucl. Instrum. Meth.* **A338**, 577 (1994).
23. M. Kobayashi et al., *Nucl. Instrum. Meth.* **A337**, 355 (1994).
24. D. Autiero et al., *Nucl. Instrum. Meth.* **A372**, 556 (1996).
25. A. Fyodorov, M. Korzhik, A. Lopatik, and O. Missevitch, *Nucl. Instrum. Meth.* **A413**, 352 (1998).
26. L. R. Wayne, W. A. Heindl, P. L. Hink, and R. E. Rothschild, *Nucl. Instrum. Meth.* **A411**, 351 (1998).
27. B. D. Rooney and J. D. Valentine, *IEEE Trans. Nucl. Sci.* **44**(3), 509 (1997).
28. B. J. Snyder, "Calculation of Gamma Ray Scintillation Detector Efficiencies and Photofraction by Monte Carlo Methods," Ph.D. Dissertation, The University of Michigan, 1965.
29. C. C. Grosjean and W. Bossaert, *Table of Absolute Detection Efficiencies of Cylindrical Scintillation Gamma-Ray Detectors*, Computing Laboratory, University of Ghent, 1965.
30. B. Grosswendt and E. Waibel, *Nucl. Instrum. Meth.* **133**, 25 (1976).
31. P. Holmberg and R. Rieppo, *Int. J. Appl. Radiat. Isotopes* **24**, 99 (1973).
32. R. Rieppo, *Int. J. Appl. Radiat. Isotopes* **27**, 453 (1976).
33. R. Rieppo, *Nucl. Instrum. Meth.* **115**, 541 (1974).
34. R. B. Galloway, *Nucl. Instrum. Meth.* **A300**, 367 (1991).
35. Y. S. Horowitz, S. Mordechai, and A. Dubi, *Nucl. Instrum. Meth.* **122**, 399 (1974).
36. T. Nakamura, *Nucl. Instrum. Meth.* **105**, 77 (1972).
37. M. Belluscio, R. De Leo, A. Pantaleo, and A. Vox, *Nucl. Instrum. Meth.* **118**, 553 (1974).
38. I. Petr, A. Adams, and J. B. Birks, *Nucl. Instrum. Meth.* **95**, 253 (1971).
39. M. Irfan and R. D. G. Prasad, *Nucl. Instrum. Meth.* **107**, 583 (1973).
40. A. E. Evans and J. D. Orndoff, NUREG/CR-1398 (LA-8301), 1980.
41. N. A. Lurie, L. Harris, Jr., and J. P. Wondra, *Nucl. Instrum. Meth.* **129**, 619 (1975).
42. R. De Leo, G. D'Erasmo, and A. Pantaleo, *Nucl. Instrum. Meth.* **129**, 501 (1975).
43. E. V. Bonzi and R. T. Mainardi, *Nucl. Instrum. Meth.* **B72**, 477 (1992).
44. A. Schaarschmidt and H. Durner, *Nucl. Instrum. Meth.* **105**, 504 (1972).
45. T. S. Mudhole and N. Umakantha, *Nucl. Instrum. Meth.* **116**, 401 (1974).
46. O. Hausser et al., *Nucl. Instrum. Meth.* **213**, 301 (1983).
47. F. Titus, *Nucl. Instrum. Meth.* **89**, 93 (1970).
48. E. Costa, E. Massaro, and L. Piro, *Nucl. Instrum. Meth.* **A243**, 572 (1986).

49. L. Piro et al., *Nucl. Instrum. Meth.* **A257**, 429 (1987).
50. M. Bantel et al., *Nucl. Instrum. Meth.* **226**, 394 (1984).
51. F. Lidén, J. Nyberg, A. Johnson, and A. Kerek, *Nucl. Instrum. Meth.* **A253**, 305 (1987).
52. Z. He and D. Ramsden, *Nucl. Instrum. Meth.* **A336**, 330 (1993).
53. T. Kamae et al., *IEEE Trans. Nucl. Sci.* **40**(2), 204 (1993).
54. G. Lanzano et al., *Nucl. Instrum. Meth.* **A323**, 694 (1992).
55. Y. Futami et al., *Nucl. Instrum. Meth.* **A326**, 513 (1993).
56. R. Novotny et al., *IEEE Trans. Nucl. Sci.* **43**(3), 1260 (1996).
57. M. Dahlbom et al., *IEEE Trans. Nucl. Sci.* **44**(3), 1114 (1997).
58. M. R. Mayhugh, A. C. Lucas, and B. K. Utts, *IEEE Trans. Nucl. Sci.* **NS-25**(1), 569 (1978).
59. B. H. Erkkila et al., *IEEE Trans. Nucl. Sci.* **NS-32(1)** , 969 (1985).
60. J. Pouliot et al., Lawrence Berkeley Laboratory Report LBL-24396, Dec. 1987.
61. M. C. Moxon and E. R. Rae, *Nucl. Instrum. Meth.* **24**, 445 (1963).
62. S. S. Malik, *Nucl. Instrum. Meth.* **125**, 45 (1975).
63. S. S. Malik and C. F. Majkrzak, *Nucl. Instrum. Meth.* **130**, 443 (1975).
64. Y. Kobayashi and D. V. Maudsley, *Biological Applications of Liquid Scintillation Counting*, Academic Press, New York, 1974.
65. D. L. Horrocks, *Applications of Liquid Scintillation Counting*, Academic Press, New York, 1974.
66. M. Crook and P. Johnson (eds.), *Liquid Scintillation Counting*, Vol. 4, Heyden and Son, London, 1977.
67. J. H. Parmentier and F. E. L. Ten Haaf, *Int. J. Appl. Radiat. Isotopes* **20**, 305 (1969).
68. B. W. Fox, *Techniques of Sample Preparation for Liquid Scintillation Counting*, North-Holland, Amsterdam, 1976.
69. R. Vaninbroukx and I. Stanef, *Nucl. Instrum. Meth.* **112**, 11[illegible] (1973).
70. J. W. McKlveen, H. W. Berk, and W. R. Johnson, *Int. J. Appl. Radiat. Isotopes* **23**, 337 (1972).
71. J. W. McKlveen and W. J. McDowell, *Trans. Am. Nuc. Soc.* **22**, 149 (1975).
72. W. J. McDowell, *IEEE Trans. Nucl. Sci.* **NS-22**(1), 649 (1975).
73. P. Cross and G. W. McBeth, *Health Phys.* **30**, 303 (1976).
74. W. J. McDowell, *Radioactivity & Radiochemistry* **3**(2), 26 (1992).
75. J. R. Cadieux et al., *Nucl. Instrum. Meth.* **A353**, 534 (1994).
76. S. Hamanaka et al., *Nucl. Instrum. Meth.* **A410**, 314 (1998).
77. J. N. Carter et al., *Nucl. Instrum. Meth.* **196**, 477 (1982).
78. R. Myllyla, H. Heusala, and M. Karras, *IEEE Trans. Nucl. Sci.* **NS-28**(1), 167 (1981).
79. H. O. Anger, *Rev. Sci. Instrum.* **29**, 27 (1958).
80. T. Hiramoto, E. Tanaka, and N. Nohara, *J. Nucl. Med.* **12**, 160 (1971).

Chapter 11

Semiconductor Diode Detectors

In many radiation detection applications, the use of a solid detection medium is of great advantage. For the measurement of high-energy electrons or gamma rays, detector dimensions can be kept much smaller than the equivalent gas-filled detector because solid densities are some 1000 times greater than that for a gas. Scintillation detectors offer one possibility of providing a solid detection medium, and their application to the detection and measurement of various radiations has been described in Chapter 10.

One of the major limitations of scintillation counters is their relatively poor energy resolution. The chain of events that must take place in converting the incident radiation energy to light and the subsequent generation of an electrical signal involves many inefficient steps. Therefore, the energy required to produce one information carrier (a photoelectron) is of the order of 100 eV or more, and the number of carriers created in a typical radiation interaction is usually no more than a few thousand. The statistical fluctuations in so small a number place an inherent limitation on the energy resolution that can be achieved under the best of circumstances, and nothing can be done about improving the energy resolution beyond this point. As detailed in Chapter 10, the energy resolution for sodium iodide scintillators is limited to about 6% when detecting 0.662 MeV gamma rays and is largely determined by the photoelectron statistical fluctuations.

The only way to reduce the statistical limit on energy resolution is to increase the number of information carriers per pulse. As we show in this chapter, the use of semiconductor materials as radiation detectors can result in a much larger number of carriers for a given incident radiation event than is possible with any other common detector type. Consequently, the best energy resolution from radiation spectrometers in routine use is achieved using semiconductor detectors. The fundamental information carriers are *electron–hole pairs* created along the path taken by the charged particle (primary radiation or secondary particle) through the detector. The electron–hole pair is somewhat analogous to the ion pair created in gas-filled detectors. Their motion in an applied electric field generates the basic electrical signal from the detector.

Devices employing semiconductors as the basic detection medium became practically available in the early 1960s. Early versions were called *crystal counters*, but modern detectors are referred to as *semiconductor diode detectors* or simply *solid-state detectors*. Although the latter term is somewhat ambiguous in the sense that technically scintillation counters can also be thought of as solid-state detectors, it has come into widespread use to characterize only those devices that are based on electron–hole pair collection from semiconductor media.

In addition to superior energy resolution, solid-state detectors can also have a number of other desirable features. Among these are compact size, relatively fast timing characteristics, and an effective thickness that can be varied to match the requirements of the application. Drawbacks may include the limitation to small sizes and the relatively high susceptibility of these devices to performance degradation from radiation-induced damage.

Of the available semiconductor materials, silicon predominates in the diode detectors used primarily for charged particle spectroscopy and discussed in this chapter. Germanium is more widely used in the gamma-ray measurements described in Chapter 12, whereas devices that use other semiconductor materials are covered in Chapter 13.

Several comprehensive books are available on the topic of solid-state detectors, including Refs. 1–6. Each of these contains a rather complete citation of the literature up to the time of publication, and the other references in these chapters are largely limited to those that have appeared more recently.

I. SEMICONDUCTOR PROPERTIES

A. Band Structure in Solids

The periodic lattice of crystalline materials establishes allowed energy bands for electrons that exist within that solid. The energy of any electron within the pure material must be confined to one of these energy bands, which may be separated by gaps or ranges of forbidden energies. A simplified representation of the bands of interest in insulators or semiconductors is shown in Fig. 11.1. The lower band, called the *valence band*, corresponds to those outer-shell electrons that are bound to specific lattice sites within the crystal. In the case of silicon or germanium, they are parts of the covalent bonding that constitute the interatomic forces within the crystal. The next higher-lying band is called the *conduction band* and represents electrons that are free to migrate through the crystal. Electrons in this band contribute to the electrical conductivity of the material. The two bands are separated by the *bandgap*, the size of which determines whether the material is classified as a semiconductor or an insulator. The number of electrons within the crystal is just adequate to fill completely all available sites within the valence band. In the absence of thermal excitation, both insulators and semiconductors would therefore have a configuration in which the valence band is completely full and the conduction band completely empty. Under these circumstances, neither would theoretically show any electrical conductivity.

In a metal, the highest occupied energy band is not completely full. Therefore, electrons can easily migrate throughout the material because they need achieve only small incremental energy to be above the occupied states. Metals are therefore always characterized by very high electrical conductivity. In insulators or semiconductors, on the other hand, the electron must first cross the bandgap to reach the conduction band and the

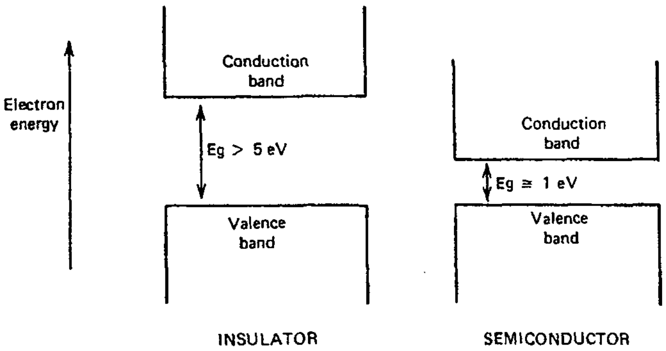

Figure 11.1 Band structure for electron energies in insulators and semiconductors.

conductivity is therefore many orders of magnitude lower. For insulators, the bandgap is usually 5 eV or more, whereas for semiconductors, the bandgap is considerably less.

B. Charge Carriers

At any nonzero temperature, some thermal energy is shared by the electrons in the crystal. It is possible for a valence electron to gain sufficient thermal energy to be elevated across the bandgap into the conduction band. Physically, this process simply represents the excitation of an electron that is normally part of a covalent bond such that it can leave the specific bonding site and drift throughout the crystal. The excitation process not only creates an electron in the otherwise empty conduction band, but it also leaves a vacancy (called a *hole*) in the otherwise full valence band. The combination of the two is called an *electron–hole pair* and is roughly the solid-state analogue of the ion pair in gases. The electron in the conduction band can be made to move under the influence of an applied electric field. The hole, representing a net positive charge, will also tend to move in an electric field, but in a direction opposite that of the electron. The motion of both of these charges contributes to the observed conductivity of the material.

The probability per unit time that an electron–hole pair is thermally generated is given by

$$p(T) = CT^{3/2} \exp\left(-\frac{E_g}{2kT}\right) \tag{11.1}$$

where T = absolute temperature

E_g = bandgap energy

k = Boltzmann constant

C = proportionality constant characteristic of the material

As reflected in the exponential term, the probability of thermal excitation is critically dependent on the ratio of the bandgap energy to the absolute temperature. Materials with a large bandgap will have a low probability of thermal excitation and consequently will show the very low electrical conductivity characteristic of insulators. If the bandgap is as low as several electron volts, sufficient thermal excitation will cause a conductivity high enough for the material to be classified as a semiconductor. [In the absence of an applied electric field, the thermally created electron–hole pairs ultimately recombine, and an equilibrium is established in which the concentration of electron–hole pairs observed at any given time is proportional to the rate of formation.] From Eq. (11.1), this equilibrium concentration is a strong function of temperature and will decrease drastically if the material is cooled.[†]

After their formation, both the electron and the hole take part in a random thermal motion that results in their diffusion away from their point of origin. If all electrons (or holes) were initially created at a single point, this diffusion leads to a broadening distribution of the charges as a function of time. A cross section through this distribution would be approximated by a Gaussian function with a standard deviation σ given by

$$\sigma = \sqrt{2Dt} \tag{11.2}$$

[†] Because the ionization potential for gases is typically 15 eV or more, the probability of a thermally generated ion pair is negligibly small in gas ionization chambers, even at room temperature.

where D is the diffusion coefficient and t is the elapsed time. Values for D can be predicted from the relationship

$$D = \mu \frac{kT}{e} \tag{11.3}$$

where μ is the mobility of the charge carrier, k is the Boltzmann constant, and T is the absolute temperature. At 20°C (293K), the numerical value of kT/e is 0.0253 V.

C. Migration of Charge Carriers in an Electric Field

If an electric field is applied to the semiconductor material, both the electrons and holes will undergo a net migration. The motion will be the combination of a random thermal velocity and a net *drift velocity* parallel to the direction of the applied field. The motion of the conduction electrons is a relatively easy process to visualize, but the fact that holes also contribute to conductivity is less obvious. A hole moves from one position to another if an electron leaves a normal valence site to fill an existing hole. The vacancy left behind by the electron then represents the new position of the hole. Because electrons will always be drawn preferentially in an opposite direction to the electric field vector, holes move in the same direction as the electric field. This behavior is consistent with that expected of a point positive charge, because ~~the hole actually represents the absence of a negatively charged electron.~~

At low-to-moderate values of the electric field intensity, the drift velocity v is proportional to the applied field. Then a *mobility* μ for both electrons and holes can be defined by

$$v_h = \mu_h \mathscr{E} \tag{11.4}$$

$$v_e = \mu_e \mathscr{E} \tag{11.5}$$

where $\mathscr{E}$ is the electric field magnitude. In gases, the mobility of the free electron is much larger than that of the positive ion, but in semiconductor materials the mobility of the electron and hole are roughly of the same order. Numerical values for common semiconductor ~~materials are given in Table 11.1.~~

At higher electric field values, the drift velocity increases more slowly with the field. Eventually, a *saturation velocity* is reached which becomes independent of further increases in the electric field. Figure 11.2 shows the dependence of the drift velocity on field magnitude for silicon and germanium.

Many semiconductor detectors are operated with electric field values sufficiently high to result in saturated drift velocity for the charge carriers. Because these saturated velocities are of the order of 10^7 cm/s, the time required to collect the carriers over typical dimensions of 0.1 cm or less will be under 10 ns. Semiconductor detectors can therefore be among the fastest-responding of all radiation detector types.

In addition to their drift, the charge carriers will also undergo the influence of diffusion mentioned in the previous section. Without diffusion, all charge carriers would travel to the collecting electrodes following exactly the electric field lines that connect their point of origin to their collection point. The effect of diffusion is to introduce some spread in the arrival position that can be characterized as a Gaussian distribution whose standard deviation can be predicted by combining Eqs. (11.2), (11.3), and (11.4)

$$\sigma = \sqrt{\frac{2kTx}{e\mathscr{E}}} \tag{11.6}$$

where x represents the drift distance. In small-volume detectors, a typical value for σ would be less than 100 μm. This diffusion broadening of the charge distribution limits the precision to which position measurements can be made using the location at which charges are collected at the electrodes in semiconductor detectors.

Table 11.1 Properties of Intrinsic Silicon and Germanium

	Si	Ge
Atomic number	14	32
Atomic weight	28.09	72.60
Stable isotope mass numbers	28-29-30	70-72-73-74-76
Density (300 K); g/cm^3	2.33	5.32
Atoms/cm^3	4.96×10^{22}	4.41×10^{22}
Dielectric constant (relative to vacuum)	12	16
Forbidden energy gap (300 K); eV	1.115	0.665
Forbidden energy gap (0 K); eV	1.165	0.746
Intrinsic carrier density (300 K); cm^{-3}	1.5×10^{10}	2.4×10^{13}
Intrinsic resistivity (300 K); $\Omega \cdot$ cm	2.3×10^{5}	47
Electron mobility (300 K); cm^2/V $\cdot$ s	1350	3900
Hole mobility (300 K); cm^2/V $\cdot$ s	480	1900
Electron mobility (77 K); cm^2/V $\cdot$ s	2.1×10^{4}	3.6×10^{4}
Hole mobility (77 K); cm^2/V $\cdot$ s	1.1×10^{4}	4.2×10^{4}
Energy per electron–hole pair (300 K); eV	3.62	
Energy per electron–hole pair (77 K); eV	3.76	2.96
Fano factor (77 K)	0.143 (Ref. 7)	0.129 (Ref. 9)
	0.084 (Ref. 8)	0.08 (Ref. 10)
	$\left.\begin{array}{c}0.085\\ \text{to}\\ 0.137\end{array}\right\}$(Ref. 12)	< 0.11 (Ref. 11)
		$\left.\begin{array}{c}0.057\\ 0.064\end{array}\right\}$(Ref. 12)
	0.16 (Ref. 13)	0.058 (Ref. 14)

Source: G. Bertolini and A. Coche (eds.), *Semiconductor Detectors*, Elsevier-North Holland, Amsterdam, 1968, except where noted.

The collection time of the charges is also spread out by diffusion by an amount that can be estimated from the spatial broadening divided by the drift velocity, or generally less than 1 ns for small volumes. In many cases, these diffusion effects are negligible, and the charges can be pictured as moving along the electric field lines, all with the same drift velocity. However, the consequences of diffusion can become significant for large-volume detectors or when position or timing measurements of high precision are involved.

D. Effect of Impurities or Dopants

1. INTRINSIC SEMICONDUCTORS

In a completely pure semiconductor, all the electrons in the conduction band and all the holes in the valence band would be caused by thermal excitation (in the absence of ionizing radiation). Because under these conditions each electron must leave a hole behind, the number of electrons in the conduction band must exactly equal the number of holes in the valence band.

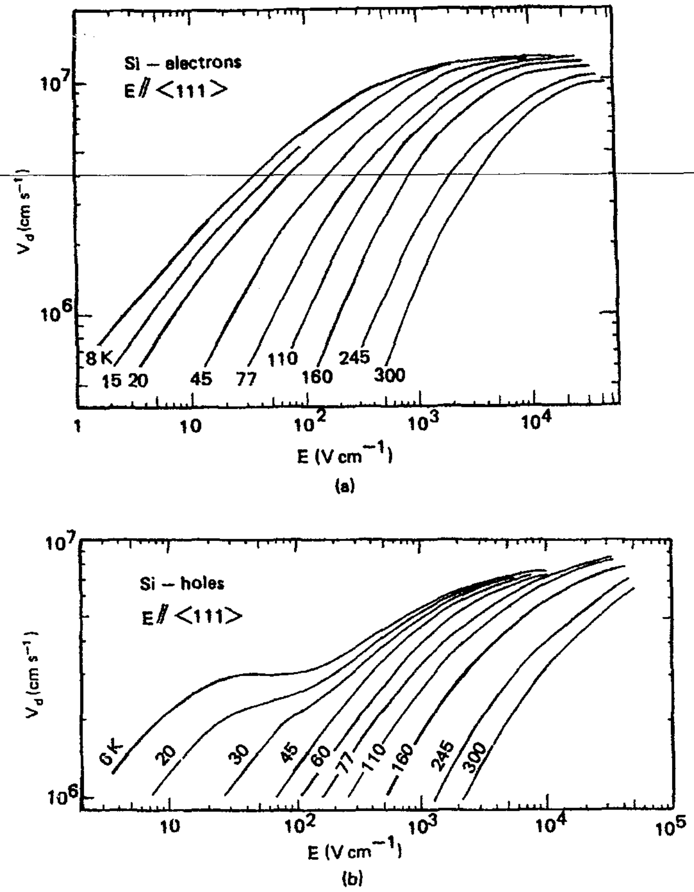

Figure 11.2 Drift velocity as a function of electric field applied parallel to the ⟨111⟩ crystallographic direction. Absolute temperature is the parameter for the different curves. (*a*) Electrons in silicon; (*b*) holes in silicon; (*c*) electrons in germanium; (*d*) holes in germanium. (From Ottaviani et al.[15])

Such material is called an *intrinsic* semiconductor. Its properties can be described theoretically, but in practice it is virtually impossible to achieve. The electrical properties of real materials tend to be dominated by the very small levels of residual impurities; this is true even for silicon and germanium, which are the semiconductors available in the highest practical purities.

[In the discussions that follow, we let n represent the concentration (number per unit volume) of electrons in the conduction band. Also, p represents the concentration of holes in the valence band.] In the intrinsic material (subscript i), the equilibrium established by the thermal excitation of electrons from the valence to conduction band and their subsequent recombination leads to equal numbers of electrons and holes, or

$$n_i = p_i \tag{11.7}$$

The quantities n_i and p_i are known as the intrinsic carrier densities. From Eq. (11.1), it is clear that these densities will be lowest for materials with large bandgap energy and when the material is used at low temperature. [Intrinsic hole or electron densities at room temperature are 1.5×10^{10} cm^{-3} in silicon, and 2.4×10^{13} cm^{-3} in germanium.]

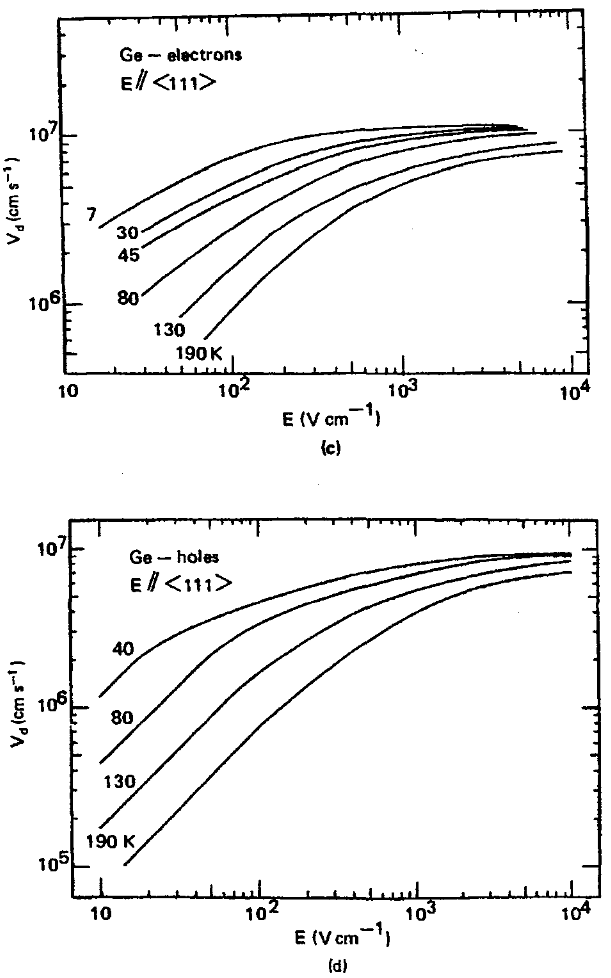

(c)

(d)

Figure 11.2 *(Continued)*

[In a metallic conductor, only the flow of negatively charged electrons contributes to its electrical conductivity. In contrast, the flow of both negatively charged electrons and positively charged holes contribute to the conductivity of an intrinsic semiconductor.]The value of the conductivity (or its inverse, the resistivity ρ) is determined by the intrinsic carrier density n_i and the mobilities μ_h and μ_e of the holes and electrons. If we have a slab of a semiconductor with thickness t and surface area A, the current I that will flow when a voltage V is applied across the thickness is

$$I = \frac{AV}{\rho t} \quad \text{or} \quad \rho = \frac{AV}{It}$$

The current is made up of two separate components: the current due to the flow of holes I_h and that due to the flow of electrons I_e. Note that, although the two types of charge carriers move in opposite directions, the separate currents are additive because of the opposite charges of holes and electrons. Thus an external measurement of the current by itself cannot distinguish between the flow of holes or electrons. The total observed current will be their sum, with each term given by the product of the area, intrinsic carrier density, electronic charge e, and the drift velocity of the charge carrier. Thus

$$I = I_e + I_h = An_i e(v_e + v_h)$$

From Eqs. 11.2 and 11.3

$$I = An_i e\mathscr{E}(\mu_e + \mu_h) = An_i e\frac{V}{t}(\mu_e + \mu_h)$$

Combining

$$\rho = \frac{1}{en_i(\mu_e + \mu_h)} \tag{11.8}$$

Inserting numerical values for intrinsic silicon at room temperature:

$$\rho = \frac{1}{(1.6 \times 10^{-19}C)(1.5 \times 10^{10}/\mathrm{cm}^3)(1350 + 480)\ \mathrm{cm}^2/V \cdot s}$$

$$\rho = 2.3 \times 10^5 \frac{V \cdot s \cdot \mathrm{cm}}{C} = 230{,}000\ \Omega \cdot \mathrm{cm}$$

Presently available silicon material of the highest purity falls short of achieving this resistivity value because of the effect (discussed in the following sections) of residual impurities.

2. *n*-TYPE SEMICONDUCTORS

To illustrate the effect of doping on semiconductor properties, we use crystalline silicon as an example. Germanium and other semiconductor materials behave in a similar way. Silicon is tetravalent and in the normal crystalline structure forms covalent bonds with the four nearest silicon atoms. A sketch of this situation is shown in Fig. 11.3*a*, where each of the dashes represents a normal valence electron involved in a covalent bond. Thermal excitation in the intrinsic material consists of breaking loose one of these covalent electrons, leaving behind an unsaturated bond or hole.

We now consider the effect of the small concentration of impurity that may be present in the semiconductor either as a residual amount after the best purification processes, or as a small amount intentionally added to the material to tailor its properties. We first assume that the impurity is pentavalent or is found in group V of the periodic table. When present

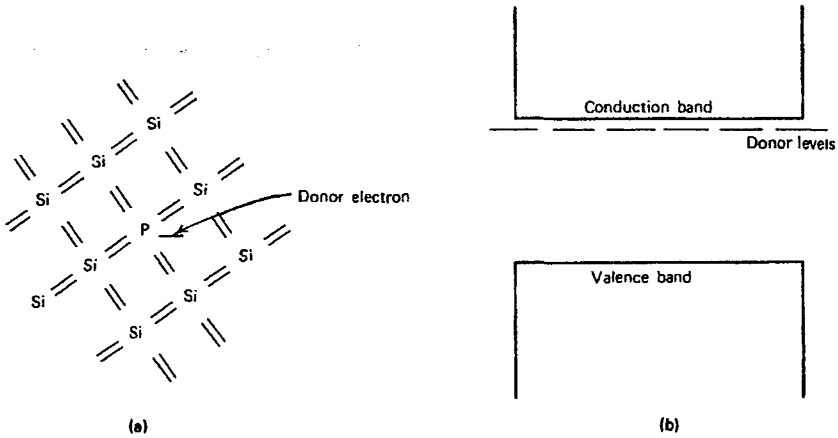

Figure 11.3 (*a*) Representation of a donor impurity (phosphorus) occupying a substitutional site in a silicon crystal. (*b*) Corresponding donor levels created in the silicon bandgap.

in small concentrations (of the order of a few parts per million or less) the impurity atom will occupy a substitutional site within the lattice, taking the place of a normal silicon atom. [Because there are five valence electrons surrounding the impurity atom, there is one left over after all covalent bonds have been formed. This extra electron is somewhat of an orphan and remains only very lightly bound to the original impurity site. It therefore takes very little energy to dislodge it to form a conduction electron without a corresponding hole. Impurities of this type are referred to as *donor impurities* because they readily contribute electrons to the conduction band. Because they are not part of the regular lattice, the extra electrons associated with donor impurities can occupy a position within the normally forbidden gap.] These very loosely bound electrons will have an energy near the top of the gap as shown in Fig. 11.3*b*. The energy spacing between these donor levels and the bottom of the conduction band is sufficiently small so that the probability of thermal excitation given by Eq. (11.1) is high enough to ensure that a large fraction of all the donor impurities are ionized. In nearly all cases, the concentration of impurity N_D is large compared with the concentration of electrons expected in the conduction band for the intrinsic material. Therefore, the number of conduction electrons becomes completely dominated by the contribution from the donor impurities, and we can write

$$n \cong N_D \tag{11.9}$$

The added concentration of electrons in the conduction band compared with the intrinsic value increases the rate of recombination, shifting the equilibrium between electrons and holes. As a result, the equilibrium concentration of holes is decreased by an amount such that the equilibrium constant given by the product of n and p is the same as for the intrinsic material:

$$np = n_i p_i \tag{11.10}$$

For example, in room-temperature silicon, the intrinsic carrier densities are about 10^{10} cm^{-3}. If a donor impurity is present at a concentration of 10^{17} atoms/cm^3 (about 2 parts per million), the density of conduction electrons n will be 10^{17} cm^{-3} and the concentration of holes p will be 10^3 cm^{-3}. Because the *total* number of charge carriers of both types is now much greater (10^{17} cm^{-3} versus 2×10^{10} cm^{-3}), the electrical conductivity of a doped semiconductor is always much larger than that of the corresponding pure material.

Even though conduction electrons now greatly outnumber the holes, charge neutrality is maintained because of the presence of ionized donor impurities. These sites represent net positive charges that exactly balance the excess electron charges. They are not, however, to be confused with holes because the ionized donors are fixed in the lattice and cannot migrate.

[The net effect in n-type material is therefore to create a situation in which the number of conduction electrons is much greater and the number of holes much smaller than in the pure material.] [The electrical conductivity is then determined almost exclusively by the flow of electrons, and holes play a very small role. In this case, the electrons are called the *majority carriers* and holes the *minority carriers*.]

The resistivity of doped material can be calculated from the dopant concentration and the mobility of the majority carrier, since only the flow of majority carriers is important in measured currents. As an example, assume we have silicon with a donor density of 10^{13}/cm^3, which will also be the concentration of conduction electrons. Then the resistivity will be

$$\rho = \frac{1}{eN_D\mu_e} \tag{11.11}$$

$$\rho = \frac{1}{(1.6 \times 10^{-19} C)(10^{13}/\text{cm}^3)(1350\ \text{cm}^2/V \cdot s)}$$

$$\rho = 463\ \Omega \cdot \text{cm}$$

3. p-TYPE SEMICONDUCTORS

The addition of a trivalent impurity such as an element from group III of the periodic table to a silicon lattice results in a situation sketched in Fig. 11.4*a*. If the impurity occupies a substitutional site, it has one fewer valence electron than the surrounding silicon atoms and therefore one covalent bond is left unsaturated. This vacancy represents a hole similar to that left behind when a normal valence electron is excited to the conduction band, but its energy characteristics are slightly different. If an electron is captured to fill this vacancy, it participates in a covalent bond that is not identical to the bulk of the crystal because one of the two participating atoms is a trivalent impurity. An electron filling this hole, although still bound to a specific location, is slightly less firmly attached than a typical valence electron. Therefore, these *acceptor impurities* also create electron sites within the normally forbidden energy gap. In this case, the acceptor levels lie near the bottom of the gap because their properties are quite close to sites occupied by normal valence electrons.

Normal thermal excitation in the crystal ensures that there will always be some electrons available to fill the vacancies created by the acceptor impurities or to occupy the acceptor sites shown in Fig. 11.4*b*. Because the energy difference between typical acceptor sites and the top of the valence band is small, a large fraction of all the acceptor sites are filled by such thermally excited electrons. These electrons come from other normal covalent bonds throughout the crystal and therefore leave holes behind in the valence band. To a good approximation, an extra hole is created in the valence band for every acceptor impurity that is added. If the concentration N_A of acceptor impurities is made to be large compared with the intrinsic concentration of holes p_i, then the number of holes is completely dominated by the concentration of acceptors, or

$$p \cong N_A \tag{11.12}$$

The increased availability of holes enhances the recombination probability between conduction electrons and holes and therefore decreases the equilibrium number of conduction electrons. Again, the same equilibrium constant discussed earlier holds, and $np = n_i p_i$. In *p*-type material, holes are the majority carrier and dominate the electrical conductivity. The filled acceptor sites represent fixed negative charges that balance the positive charge of the majority holes.

The equilibrium that is at work between electrons and holes is illustrated by the nomogram in Fig. 11.5. Two logarithmic scales are shown, on the left the concentration of con-

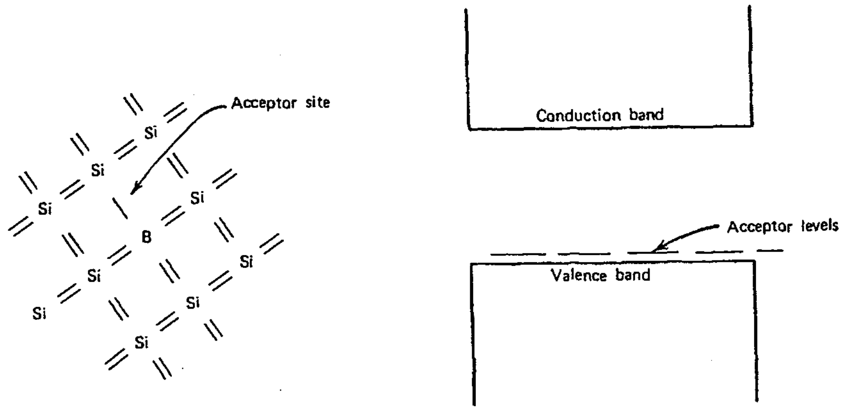

(a) (b)

Figure 11.4 (*a*) Representation of an acceptor impurity (boron) occupying a substitutional site in a silicon crystal. (*b*) Corresponding acceptor levels created in the silicon bandgap.

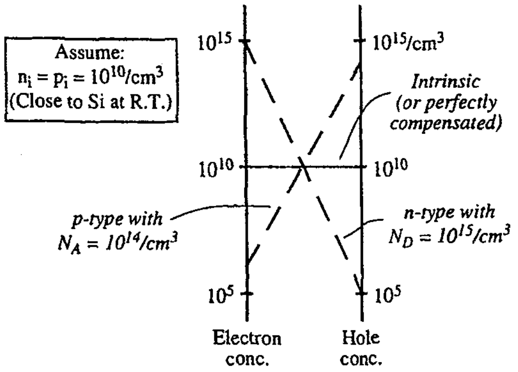

Figure 11.5 Nomogram showing the relationship between electron and hole concentrations in a semiconductor. Lines connecting points on the two logarithmic scales always pass through the center of the diagram for any type or degree of doping.

duction electrons, and on the right the concentration of holes. In intrinsic or perfectly compensated (see following section) semiconductors, the concentrations are equal and have a value given by the intrinsic carrier density. In silicon at room temperature, that value is $1.5 \times 10^{10}/cm^3$. Intrinsic (or perfectly compensated) material can thus be represented as a horizontal line connecting the points on the scales at about $10^{10}/cm^3$. Doping the material will tip the equilibrium so that one carrier dominates, but the product of the concentrations of electrons and holes must still be the same as shown in Eq. (11.10). Since the scales are logarithmic on the nomogram, the two concentrations will be linked by a line that passes through the center of the previous line. The same statement can be made for any level of doping, whether with donors or acceptors, so this point at the center of the nomogram acts as a "pivot point" that is common to all lines. Material that is *n*-type will result in lines with negative slope, while *p*-type material corresponds to lines with positive slope.

Figure 11.5 also illustrates that the total concentration of charge carriers (electrons plus holes) is at a minimum for the intrinsic material. This condition corresponds to a minimum in electrical conductivity if the mobilities of the two carriers are about the same. Tipping the equilibrium in either direction due to the presence of either donors or acceptors will raise the majority carrier concentration by an absolute amount that is always greater than the amount by which the minority carrier concentration is decreased. The effect is shown in Fig. 11.6, where the minimum conductivity occurs for the pure or intrinsic material, and either excess donors or acceptors result in a higher conductivity. Thus one measure of the impurity level of semiconductor materials is the electrical conductivity, or

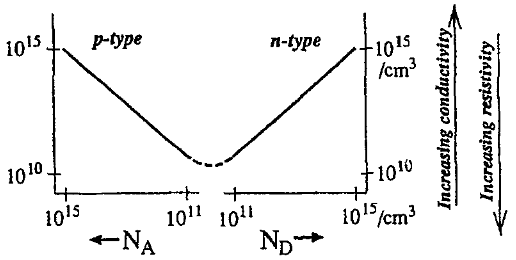

Figure 11.6 Plot using logarithmic scales of the conductivity of a semiconductor as a function of the net concentration of acceptors (N_A) or donors (N_D).

its inverse, the resistivity. For the intrinsic material in which all the charge carriers are produced through thermal excitation, the resistivity value can be calculated from Eq. (11.8) using the intrinsic carrier density and mobilities. The corresponding values for silicon and germanium are listed in Table 11.1. In practice, these theoretical values of resistivity are never observed because of the unavoidable residual impurities. Using the most advanced purification methods available at this writing, silicon resistivity of about 50,000 Ω-cm can be achieved, compared with a theoretical value of over 200,000 Ω-cm.

4. COMPENSATED MATERIAL

If donor and acceptor impurities are present in a semiconductor in equal concentration, the material is said to be *compensated.* Such material has some of the properties of an intrinsic semiconductor because electrons contributed by donor impurities are removed to some extent by their capture at the site of acceptor impurities. Despite the potential confusion with purified intrinsic material, compensated regions in semiconductors are commonly given the designation *i* because of their near intrinsic properties.

In practice, it is impossible to achieve exact compensation at the time of fabrication of the doped material because any small imbalance in the acceptor or donor concentration quickly leads to *n*-type or *p*-type behavior. At present, the only practical means for achieving compensation over large volumes in silicon or germanium is through the lithium ion drifting process after the crystal has been fabricated. This procedure is discussed in Chapter 13.

5. HEAVILY DOPED MATERIAL

Thin layers of semiconductor material that have an unusually high concentration of impurity are often given a special notation. Thus, n^+ and p^+ designate heavily doped *n*- and *p*-type layers that, as a result, have very high conductivity. These layers are often used in making electrical contact with semiconductor devices, because the very low minority carrier density allows their application as "blocking" contacts described later in this chapter.

E. Trapping and Recombination

Once electrons and holes are formed in a semiconductor, they will tend to migrate either spontaneously or under the influence of an applied electric field until they are either collected at an electrode or recombination takes place. There are theoretical predictions[16] that the average lifetime of charge carriers before recombination in perfectly pure semiconductors could be as large as a second. In practice, lifetimes at least three or four orders of magnitude smaller than a second are actually observed that are dominated entirely by the very low level of impurities remaining in the material. Some of these impurities, such as gold, zinc, cadmium, or other metallic atoms occupying substitutional lattice positions, introduce energy levels near the middle of the forbidden gap. They are therefore classified as "deep impurities" (as opposed to acceptor or donor impurities that, because the corresponding energy levels lie near the edges of the forbidden band, are called *shallow impurities*). These deep impurities can act as *traps* for charge carriers in the sense that if a hole or electron is captured, it will be immobilized for a relatively long period of time. Although the trapping center ultimately may release the carrier back to the band from which it came, the time delay is often sufficiently long to prevent that carrier from contributing to the measured pulse.

Other types of deep impurities can act as *recombination centers.* These impurities are capable of capturing both majority and minority carriers, causing them to annihilate. An impurity level near the center of the forbidden gap might, for example, first capture a conduction electron. At a slightly later time, a hole from the valence band might also be captured, with the electron then filling the hole. The impurity site is thus returned to its original state and is capable of causing another recombination event. In most crystals, recombination through such centers is far more common than direct recombination of electrons and holes across the full bandgap.

Both trapping and recombination contribute to the loss of charge carriers and tend to reduce their average lifetime in the crystal. For the material to serve as a good radiation detector, a large fraction (preferably 100%) of all the carriers created by the passage of the incident radiation should be collected. This condition will hold provided the collection time for the carriers is short compared with their mean lifetime. Collection times of the order of 10^{-7} to 10^{-8} s are fairly common, so that carrier lifetimes of the order of 10^{-5} s or longer are usually sufficient.

Another widely quoted specification is the *trapping length* within the material. This quantity is simply the mean distance traveled by a carrier before trapping or recombination and is given by the product of the mean lifetime and the average drift velocity. In order to have an acceptable detector, the trapping length should be long compared with the physical dimensions over which the charge must be collected.

In addition to impurities, structural defects within the crystal lattice can also lead to trapping and charge carrier loss. These imperfections include point defects such as vacancies or interstitials that tend to behave as acceptors or donors, respectively. Carrier loss may also occur at line defects or dislocations that may be produced in stressed crystals. A dislocation represents the slippage of one crystal plane with respect to another, and its intersection with the surface of the crystal leads to a pit upon chemical etching. The density of these etched pits is often quoted as a measure of the crystalline perfection of a semiconductor sample.]

II. THE ACTION OF IONIZING RADIATION IN SEMICONDUCTORS

A. The Ionization Energy

When a charged particle passes through a semiconductor with the band structure shown in Fig. 11.1, the overall significant effect is the production of many electron–hole pairs along the track of the particle. The production process may be either direct or indirect, in that the particle produces high-energy electrons (or *delta rays*) that subsequently lose their energy in producing more electron–hole pairs. Regardless of the detailed mechanisms involved, the quantity of practical interest for detector applications is the average energy expended by the primary charged particle to produce one electron–hole pair. This quantity, often loosely called the *ionization energy* and given the symbol ϵ, is experimentally observed to be largely independent of both the energy and type of the incident radiation. This important simplification allows interpretation of the number of electron–hole pairs produced in terms of the incident energy of the radiation, provided the particle is fully stopped within the active volume of the detector.

When radiation interacts in a semiconductor, the energy deposition always leads to the creation of equal numbers of holes and electrons. This statement holds regardless of whether the host semiconductor is pure or intrinsic, or doped as *p*-type or *n*-type. Just as equal numbers of free electrons and positive ions are created in a gas, every conduction electron produced in a semiconductor must also create a hole in the valence band, leading to an exact balance in the initial number of created charges. It should also be emphasized that the doping levels typical in *p*- or *n*-type semiconductors are so low that these atoms play no significant role in determining the nature of the radiation interactions in the material. Thus *p*-type or *n*-type silicon of equal thickness will present identical interaction probabilities for gamma rays, and the range of charge particles in either type will also be the same.

The dominant advantage of semiconductor detectors lies in the smallness of the ionization energy. The value of ϵ for either silicon or germanium is about 3 eV (see Table 11.1), compared with about 30 eV required to create an ion pair in typical gas-filled detectors. Thus, the number of charge carriers is 10 times greater for the semiconductor case, for a given energy deposited in the detector. The increased number of charge carriers has two beneficial effects on the attainable energy resolution. The statistical fluctuation in the number of carriers per pulse becomes a smaller fraction of the total as the number is increased. This factor often is predominant in determining the limiting energy resolution of a detector for medium to high radiation energy. At low energies, the resolution may be limited by electronic noise in the preamplifier, and the greater amount of charge per pulse leads to a better signal/noise ratio.

More detailed examination shows that ϵ depends on the nature of the incident radiation. Most detector calibrations are carried out using alpha particles, and the values for ϵ shown in Table 11.1 are based on this mode of excitation. All experimental values obtained using other light ions or fast electrons seem to be fairly close,[17–19] but differences as large as 2.2% have been reported[20] between proton and alpha particle excitation in silicon. These observed differences point up the need to carry out detector calibration using a radiation type that is identical to that involved in the measurement itself if precise energy values are required.

A much larger difference is measured for ϵ when heavy ions or fission fragments are involved. The value of ϵ is significantly higher than for alpha particle excitation, leading to a lower than anticipated number of charge carriers. The physical origins of this *pulse height defect* are discussed later in this chapter.

The ionization energy is also temperature dependent. For the most significant detector materials, the value of ϵ increases with decreasing temperature. As shown in Table 11.1, ϵ in silicon is about 3% greater at liquid nitrogen temperature compared with room temperature.[18]

There is also evidence[21–23] that the ionization energy can be dependent on the energy of the radiation, especially in the soft X-ray energy range. It appears that its value increases with decreasing X-ray energy below about 1 keV, and that the Fano factor (described below) also increases significantly with decreasing energy in this range.

B. The Fano Factor

In addition to the mean number, the fluctuation or variance in the number of charge carriers is also of primary interest because of the close connection of this parameter with energy resolution of the detector. As in gas counters, the observed statistical fluctuations in semiconductors are smaller than expected if the formation of the charge carriers were a Poisson process. The Poisson model would hold if all events along the track of the ionizing particle were independent and would predict that the variance in the total number of electron–hole pairs should be equal to the total number produced, or E/ϵ. The Fano factor F is introduced as an adjustment factor to relate the observed variance to the Poisson predicted variance:

$$F \equiv \frac{\text{observed statistical variance}}{E/\epsilon} \tag{11.13}$$

For good energy resolution, one would like the Fano factor to be as small as possible. Although a complete understanding of all the factors that lead to a nonunity value for F does not yet exist, rather sophisticated models have been developed[24] that at least qualitatively account for experimental observations. Some numerical values for silicon and germanium are given in Table 11.1.

There is considerable variation in reported experimental values, particularly for silicon. The Fano factor is usually measured by observing the energy resolution from a given detector under conditions in which all other factors that can broaden the full-energy peak (such as electronic noise or drift) can be estimated and taken into account. The assumption is then made that the residual width can be attributed to statistical effects only. If nonstatistical residual factors remain, however, the Fano factor will appear to be larger than it actually is. This may explain the historical trend toward lower values as measurement procedures are refined. It has also been postulated[13] that the value of the Fano factor may depend on the nature of the particle that deposits the energy. Some measurements[25] suggest that its value in silicon may also vary significantly with radiation energy, especially in the energy range typical of X-ray photons.

III. SEMICONDUCTORS AS RADIATION DETECTORS

A. Pulse Formation

When a particle deposits energy in a semiconductor detector, equal numbers of conduction electrons and holes are formed within a few picoseconds along the particle track. The detector configurations that are discussed in the following sections all ensure that an electric field is present throughout the active volume, so that both charge carriers feel electrostatic forces that cause them to drift in opposite directions. The motion of either the electrons or holes constitutes a current that will persist until those carriers are collected at the boundaries of the active volume. With the simplifying assumption that all charge carriers are formed at a single point, the resulting currents can be represented by the plot at the top of Fig. 11.7. Since the charge collection times are not likely to be the same because of differences in drift distance and carrier mobilities, one of the two currents will persist for a longer time than the other. When these currents are integrated on a measuring circuit with long time constant, the measured induced charge has the time characteristics shown in the lower plot in Fig. 11.7. This time profile will also be that of the rise of the pulse produced by a conventional preamplifier used to process the pulses from the detector. This pulse profile is similar to that derived in Chapter 5 for ion chambers (see Fig. 5.16), with the exception of the time scale. In gases, the collection time for the positive charges (ions) is greater by orders of magnitude than that for the negative (free electron) charges, so the ion motion adds a very long component to the pulse rise and, as a practical matter, does not contribute to the output pulse. In silicon or germanium semiconductor detectors, the hole mobility is within a factor of about 2 or 3 of the electron mobility, so the collection times are much closer to being equivalent. As a result, while pulse-type ion chambers almost never include the motion of the ions in the output pulse, standard silicon and germanium semiconductor detectors rely on complete integration of the currents due to both the electrons and holes. Both carrier types must therefore be completely collected for the resulting pulse to be a faithful measure of the energy deposited by the particle.

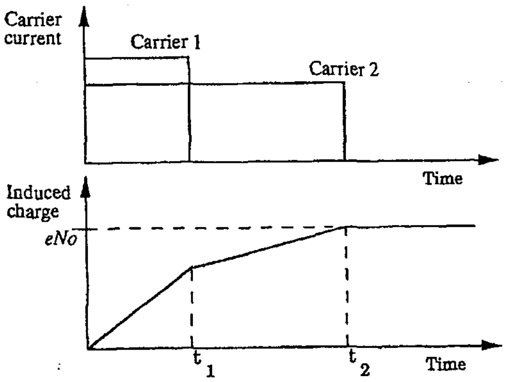

Figure 11.7 The upper plot shows an idealized representation of the electron and hole currents flowing in a semiconductor following the creation of N_0 electron–hole pairs. In the lower plot, t_1 represents the collection time for the carrier type (either electrons or holes) that is collected first, and t_2 is the collection time for the other carrier. If both are fully collected, a charge of eN_0 is induced to form the signal, where e is the electronic charge.

B. Electrical Contacts

In order to construct a practical radiation detector, some means must be provided to collect the electrical charges created by the radiation at either boundary of the semiconductor material. An *ohmic* contact is a nonrectifying electrode through which charges of either sign can flow freely. If two ohmic contacts are fitted on opposite faces of a slab of semiconductor and connected to a detection circuit, the equilibrium charge carrier concentrations in the semiconductor will be maintained. If an electron or hole is collected at one electrode, the same carrier species is injected at the opposite electrode to maintain the equilibrium concentrations in the semiconductor.

The steady-state leakage currents that are observed using ohmic contacts are too high, even with the highest resistivity material available (see following section), to permit their general application to silicon or germanium detectors. Instead, *noninjecting* or *blocking* electrodes are universally employed to reduce the magnitude of the current through the bulk of the semiconductor. If blocking electrodes are used, charge carriers initially removed by the application of an electric field are not replaced at the opposite electrode, and their overall concentration within the semiconductor will drop after application of an electric field. The leakage current can thus be reduced to a sufficiently low value to allow the detection of the added current pulse created by the electron–hole pairs produced along the track of an ionizing particle.

The most appropriate type of blocking contacts are the two sides of a *p-n* semiconductor junction. It is very difficult to inject electrons from the *p* side of this junction because holes are the majority carrier and free electrons are relatively scarce. At the opposite side, electrons are the majority carrier and holes cannot readily be injected. In this chapter, we discuss detectors that are created by placing the *p*- and *n*-type materials in direct contact, forming a *p-n* junction. In Chapters 12 and 13, detectors in which the *p* and *n* regions are separated by an intrinsic or compensated region (the *i* region) are described.

C. Leakage Current

In order to create an electric field large enough to achieve an efficient collection of the charge carriers from any semiconductor detector, an applied voltage of typically hundreds or thousands of volts must be imposed across the active volume. Even in the absence of ionizing radiation, all detectors will show some finite conductivity and therefore a steady-state *leakage current* will be observed. Random fluctuations that inevitably occur in the leakage current will tend to obscure the small signal current that momentarily flows following an ionizing event and will represent a significant source of noise in many situations. Methods of reducing the leakage current are therefore an important consideration in the design of semiconductor detectors.

The resistivity of the highest purity silicon currently available is about 50,000 Ω-cm. If a 1-mm thick slab of this silicon were cut with 1-cm^2 surface area and fitted with ohmic contacts, the electrical resistance between faces would be 5000 Ω. An applied voltage of 500 V would therefore cause a leakage current through the silicon of 0.1 A. In contrast, the peak current generated by a pulse of 10^5 radiation-induced charge carriers would only be about 10^{-6} A. It is therefore essential to reduce this bulk leakage current greatly through the use of blocking contacts. In critical applications, the leakage current must not exceed about 10^{-9} A to avoid significant resolution degradation.

At these levels, leakage across the surface of the semiconductor can often become more significant than bulk leakage. Great care is taken in the fabrication of semiconductor detectors to avoid contamination of the surfaces, which could create leakage paths. Some configurations may also use grooves in the surface or guard rings to help suppress surface leakage (see Chapter 5).

D. The Semiconductor Junction

1. BASIC JUNCTION PROPERTIES

The radiation detectors described in this chapter are based on the favorable properties that are created near the junction between *n*- and *p*-type semiconductor materials. Charge carriers are able to migrate across the junction if the regions are brought together in good thermodynamic contact. Simply pressing together two pieces of the material will not suffice because gaps will inevitably be left that will be large compared with the interatomic lattice spacing. In practice, the junction is therefore normally formed in a single crystal by causing a change in the impurity content from one side of the junction to the other.

As an illustration, assume that the process begins with a *p*-type crystal that has been doped with a uniform concentration of acceptor impurity. In the concentration profile at the top of Fig. 11.8, this original acceptor concentration N_A is shown as a horizontal line. We now assume that the surface of the crystal on the left is exposed to a vapor of an *n*-type impurity that diffuses some distance into the crystal. The resulting donor impurity profile is labeled N_D on the figure and falls off as a function of distance from the surface. Near the surface, the donor impurities can be made to outnumber the acceptors, converting the left portion of the crystal to *n*-type material.

The approximate variation of equilibrium charge carrier concentration is also plotted at the top of Fig. 11.8 and labeled as *p* (hole concentration) and *n* (conduction electron concentration). These profiles are subsequently altered in the vicinity of the *p*-*n* junction because of the effects of charge carrier diffusion. In the *n*-type region at the left, the density of conduction electrons is much higher than in *p*-type. The junction between the two regions therefore represents a discontinuity in the conduction electron density. Wherever such a sharp gradient exists for any carrier that is free to migrate, a net diffusion from regions of high concentration to those of low concentration must take place. Thus, there will be some net diffusion of conduction electrons into the *p*-type material, where they will quickly combine with holes. In effect, this annihilation represents the capture of the conduction electron by one of the vacancies existing in the covalent bonds in the *p*-type material. The diffusion of conduction electrons out of the *n*-type material leaves behind immobile positive charges in the form of ionized donor impurities. A similar and symmetric argument leads to the conclusion that holes (the majority in the *p*-type material) must also diffuse across the junction because they also see an abrupt density gradient. Each hole that is removed from the *p* side of the junction leaves behind an acceptor site that has picked up an extra electron and therefore represents a fixed and immobile negative charge. The combined effect is to build up a net negative space charge on the *p* side and a positive space charge on the *n* side of the junction.

The accumulated space charge creates an electric field that diminishes the tendency for further diffusion. At equilibrium, the field is just adequate to prevent additional net diffusion across the junction, and a steady-state charge distribution is therefore established.

The region over which the charge imbalance exists is called the *depletion region* and extends into both the *p* and *n* sides of the junction. If the concentrations of donors on the *n* side and acceptors on the *p* side are equal, the diffusion conditions are approximately the same for both holes and electrons, and the depletion region extends equal distances into both sides. Usually, however, there is a marked difference in the doping levels on one side of the junction compared with the other. For example, if the donor concentration in the *n*-type material is higher than that of acceptor atoms in the *p*-type, the electrons diffusing across the junction will tend to travel a greater distance into the *p*-type material before all have recombined with holes. In this case, the depletion region would extend farther into the *p* side.

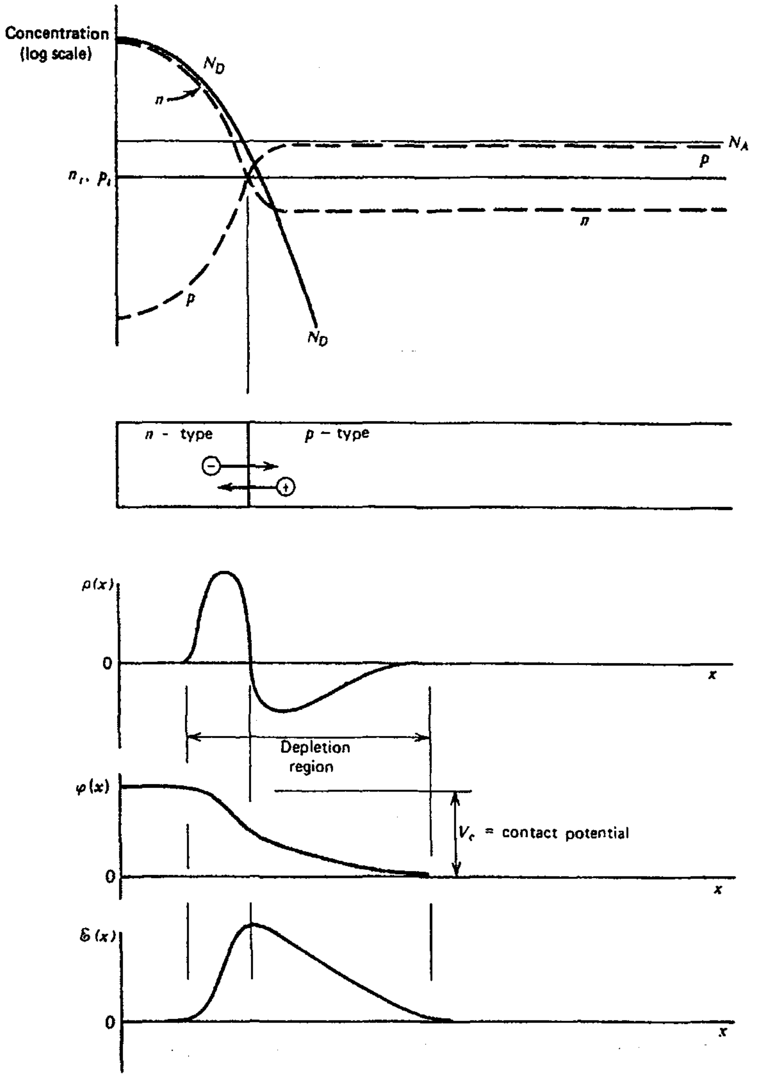

Figure 11.8 The assumed concentration profiles for the *n-p* junction shown at the top are explained in the text. The effects of carrier diffusion across the junction give rise to the illustrated profiles for space charge $\rho(x)$, electric potential $\varphi(x)$, and electric field $\mathscr{E}(x)$.

The buildup of net charge within the region of the junction leads to the establishment of an electric potential difference across the junction. The value of the potential φ at any point can be found by solution of Poisson's equation

$$\nabla^2\varphi = -\frac{\rho}{\epsilon} \tag{11.14}$$

where ϵ is the dielectric constant of the medium, and ρ is the net charge density. In one dimension, Eq. (11.14) takes the form

$$\frac{d^2\varphi}{dx^2} = -\frac{\rho(x)}{\epsilon} \tag{11.15}$$

so that the shape of the potential across the junction can be obtained by twice integrating the charge distribution profile $\rho(x)$. Graphical examples are shown in Fig. 11.8. At equilibrium, the potential difference across the junction (called the *contact potential*) amounts to nearly the full bandgap value of the semiconductor material. The direction of this potential difference is such that it opposes the further diffusion of electrons from left to right and holes from right to left in Fig. 11.8.

Where a difference in electrical potential exists, there must also be an electric field $\mathscr{E}$. Its magnitude is found by taking the gradient of the potential

$$\mathscr{E} = -\text{grad } \varphi \tag{11.16}$$

which, in one dimension, is simply

$$\mathscr{E}(x) = -\frac{d\varphi}{dx} \tag{11.17}$$

The electric field will extend over the width of the depletion region, in which charge imbalance is significant and the potential has some gradient. Its variation is also sketched in Fig. 11.8.

The depletion region exhibits some very attractive properties as a medium for the detection of radiation. The electric field that exists causes any electrons created in or near the junction to be swept back toward the *n*-type material, and any holes are similarly swept toward the *p*-type side. The region is thus "depleted" in that the concentration of holes and electrons is greatly suppressed. The only significant charges remaining in the depletion region are the immobile ionized donor sites and filled acceptor sites. Because these latter charges do not contribute to conductivity, the depletion region exhibits a very high resistivity compared with the *n*- and *p*-type materials on either side of the junction. Electron–hole pairs that are created within the depletion region by the passage of radiation will be swept out of the depletion region by the electric field, and their motion constitutes a basic electrical signal.

The thermal generation of charge carriers will continue to take place in the depletion region, contributing a component sometimes called the *generation current* to the observed leakage current. These charges are swept away typically within a few nanoseconds, however, a time that is many orders of magnitude shorter than the time required to establish thermal equilibrium. Thus, the steady-state concentration of carriers is strongly reduced in the depletion region because the removal of charges is a much faster process than their creation. The small concentration of carriers created by an ionizing particle is therefore easily detected above this highly suppressed, thermally generated concentration.

2. *REVERSE BIASING*

Thus far, we have discussed a semiconductor diode junction to which no external voltage is applied. Such an unbiased junction will function as a detector, but only with very poor performance. [The contact potential of about 1 V that is formed spontaneously across the junction is inadequate to generate a large enough electric field to make the charge carriers move very rapidly. Therefore, charges can be readily lost as a result of trapping and recombination, and incomplete charge collection often results.] The thickness of the depletion region is quite small, and the capacitance of an unbiased junction is high. Therefore, the noise properties of an unbiased junction connected to the input stage of a preamplifier are quite poor. For these reasons, unbiased junctions are not used as pulse mode radiation detectors, but instead, an external voltage is applied in the direction to cause the semiconductor diode to be reverse biased.

The *p*-*n* junction is most familiar in its role as a diode. The properties of the junction are such that it will readily conduct current when voltage is applied in the "forward" direction, but it will conduct very little current when biased in the "reverse" direction. In the configuration of Fig. 11.8, first assume that a positive voltage is applied to the *p* side of the junction with respect to the *n* side. The potential will tend to attract conduction electrons from the *n* side as well as holes from the *p* side across the junction. Because, in both cases, these are the majority carriers, conductivity through the junction is greatly enhanced. The contact potential shown in Fig. 11.8 is reduced by the amount of the bias voltage that is applied, which tends to lessen the potential difference seen by an electron from one side of the junction to the other. This is the direction of forward biasing, and only small values of the forward bias voltage are needed to cause the junction to conduct large currents.

If the situation is reversed, and the *p* side of the junction is made negative with respect to the *n* side, the junction is reverse biased. Now the natural potential difference from one side of the junction to the other is enhanced, as shown in Fig. 11.9*c*. Under these

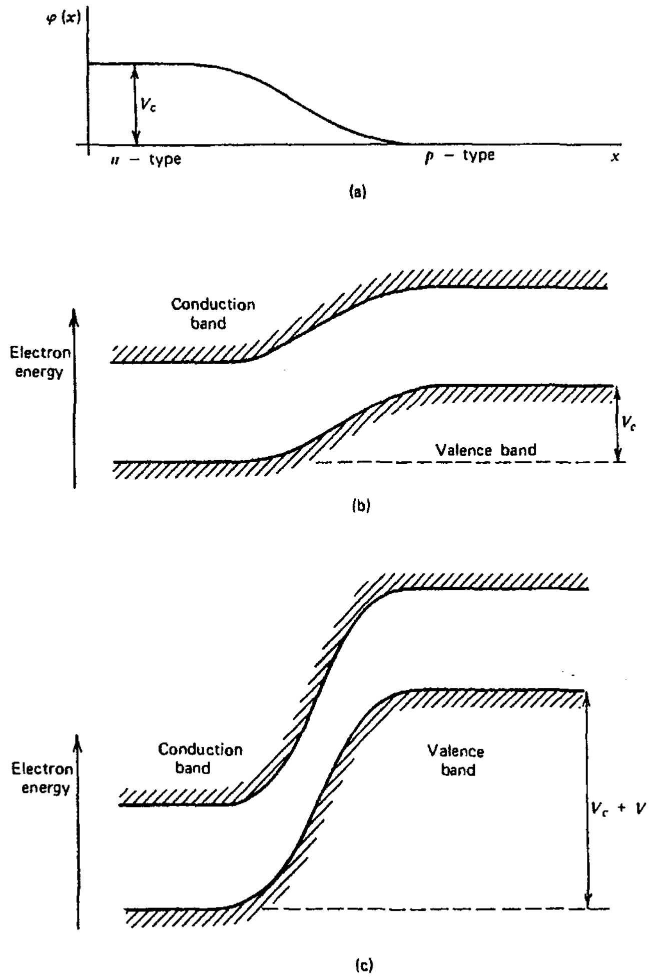

Figure 11.9 (*a*) The variation of electric potential across an *n-p* junction from Fig. 11.8. (*b*) The resulting variation in electron energy bands across the junction. The curvature is reversed because an increase in electron energy corresponds to a decrease in conventional electric potential $\varphi(x)$ defined for a positive charge. (*c*) The added displacement of the bands caused by application of a reverse bias *V* across the junction.

circumstances, it is the minority carriers (holes on the n side and electrons on the p side) that are attracted across the junction and, because their concentration is relatively low, the reverse current across the diode is quite small. Therefore, the p-n junction serves as a rectifying element, allowing relatively free flow of current in one direction while presenting a large resistance to its flow in the opposite direction. If the reverse bias is made very large, a sudden breakdown in the diode will occur and the reverse current will abruptly increase, often with destructive effects.

3. PROPERTIES OF THE REVERSE BIAS JUNCTION

When a reverse bias is applied to the junction, virtually all the applied voltage will appear across the depletion region, because its resistivity is much higher than that of the normal n- and p-type material. Because the effect of the reverse bias is to accentuate the potential difference across the junction, Poisson's equation [Eq. (11.14)] demands that space charge must also increase and extend a greater distance on either side of the junction. Thus, the thickness of the depletion region is also increased, extending the volume over which radiation-produced charge carriers will be collected. Practical detectors are almost always operated with a bias voltage that is very large compared with the contact potential, so that the applied voltage completely dominates the magnitude of the potential difference across the junction.

In the analysis that follows, we first assume that the semiconductor wafer in which the junction is formed is sufficiently thick so that the depletion region does not reach either surface and is contained within the interior volume of the wafer. This condition holds for *partially depleted* detectors in which some portion of the wafer thickness remains undepleted. Many semiconductor detectors are operated with sufficient reverse bias voltage so that the depletion region extends through the full wafer thickness, creating a *fully depleted* (or *totally depleted*) detector. These configurations share many of the properties derived below, except that the depletion region is obviously limited by the physical thickness of the wafer.

Some properties of the reverse bias junction can be derived if we represent the charge distribution sketched in Fig. 11.8 by the idealized distribution shown below:

$$\rho(x) = \begin{cases} eN_D & (-a < x \le 0) \\ -eN_A & (0 < x \le b) \end{cases}$$

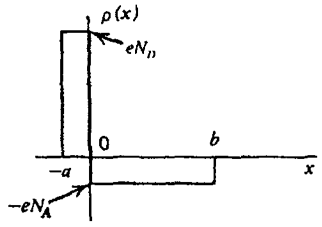

Here the electron diffusion is assumed to result in a uniform positive space charge (the ionized donor sites) over the region $-a < x \le 0$ on the n side of the junction. A corresponding negative space charge (the filled acceptor sites) resulting from hole diffusion is assumed to extend over the region $0 < x \le b$ on the p side. Because the net charge must be zero, $N_D a = N_A b$.

Equation (11.15) applied to this case takes the form

$$\frac{d^2\varphi}{dx^2} = \begin{cases} -\dfrac{eN_D}{\epsilon} & (-a < x \le 0) \\ +\dfrac{eN_A}{\epsilon} & (0 < x \le b) \end{cases}$$

We now carry out an integration and apply the boundary conditions that the electric field $\mathscr{E} = -d\varphi/dx$ must vanish at both edges of the charge distribution:

$$\frac{d\varphi}{dx}(-a) = 0 \quad \text{and} \quad \frac{d\varphi}{dx}(b) = 0$$

The result is then

$$\frac{d\varphi}{dx} = \begin{cases} -\dfrac{eN_D}{\epsilon}(x+a) & (-a < x \leq 0) \\ +\dfrac{eN_A}{\epsilon}(x-b) & (0 < x \leq b) \end{cases}$$

The corresponding shape of the electric field $\mathscr{E} = -d\varphi/dx$ is sketched below:

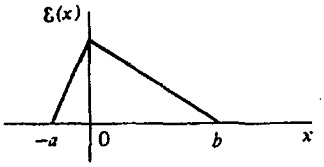

Another integration will now yield the electric potential $\varphi(x)$. The difference in potential from the n side to the p side of the junction, if we neglect the relatively small contact potential, is just the value of the applied reverse bias V. We can therefore apply the boundary conditions

$$\varphi(-a) = V \quad \text{and} \quad \varphi(b) = 0$$

The solution then takes the form

$$\varphi(x) = \begin{cases} -\dfrac{eN_D}{2\epsilon}(x+a)^2 + V & (-a < x \leq 0) \\ +\dfrac{eN_A}{2\epsilon}(x-b)^2 & (0 < x \leq b) \end{cases}$$

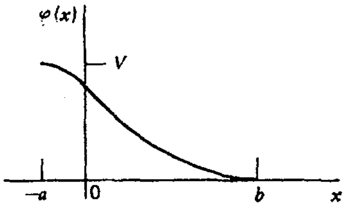

Since the solutions for either side of the junction must match at $x = 0$, we can write

$$V - \frac{eN_D a^2}{2\epsilon} = \frac{eN_A b^2}{2\epsilon}$$

or

$$N_A b^2 + N_D a^2 = \frac{2\epsilon V}{e}$$

Now since $N_D a = N_A b$, the expression above can be rewritten:

$$(a+b)b = \frac{2\epsilon V}{eN_A}$$

The total width of the depletion region d is the entire distance over which the space charge extends, or $d = a + b$.

For purposes of the present example, we have assumed that the n-side doping level is much higher than on the p side, so that $N_D \gg N_A$. Because $N_D a = N_A b$, it follows that $b \gg a$, and therefore the space charge extends much farther into the p side than the n side. Then $d \cong b$ and we can write

$$d \cong \left(\frac{2\epsilon V}{eN_A}\right)^{1/2}$$

If we had started from the opposite assumption that the p-side doping level was predominant, a similar result would be obtained except that N_A in the above expression would be replaced by N_D. A generalized solution for the thickness of the depletion region is therefore

$$d \cong \left(\frac{2\epsilon V}{eN}\right)^{1/2} \tag{11.18}$$

In this expression, N now represents the dopant concentration (either donors or acceptors) on the side of the junction that has the lower dopant level. (For surface barriers described later in this chapter, N is the dopant concentration in the bulk of the crystal.)

The resistivity ρ_d of the doped semiconductor [see Eq. (11.11)] is given by $1/e\mu N$, where μ is the mobility of the majority carrier. Equation (11.18) may thus be written

$$d \cong (2\epsilon V \mu \rho_d)^{1/2} \tag{11.19}$$

Because one often would like the largest depletion width possible for a given applied voltage, it is advantageous to have the resistivity as high as possible. This resistivity is limited by the purity of the semiconductor material before the doping process, because enough dopant must be added to override the nonuniform effects of the residual impurities. A premium is therefore placed on obtaining detectors fabricated from the highest purity material possible.

Because of the fixed charges that are built up on either side of the junction, the depletion region exhibits some properties of a charged capacitor. If the reverse bias is increased, the depletion region grows thicker and the capacitance represented by the separated charges therefore decreases. The value of the capacitance per unit area is

$$C = \frac{\epsilon}{d} \cong \left(\frac{e\epsilon N}{2V}\right)^{1/2} \tag{11.20}$$

Good energy resolution under conditions in which electronic noise is dominant depends on achieving a small detector capacitance and is thus promoted by using the largest possible applied voltage, up to the point that the detector becomes fully depleted.

The maximum electric field will occur at the point of transition between the n- and p-type material. Its magnitude is given by

$$\mathscr{E}_{\max} \cong \frac{2V}{d} = \left(\frac{2VNe}{\epsilon}\right)^{1/2} \tag{11.21}$$

and can easily reach 10^6–10^7 V/m under typical conditions. For partially depleted junctions, the depletion layer thickness d is proportional to $\sqrt{V}$ so that the value of $\mathscr{E}_{\max}$ increases with applied voltage as $\sqrt{V}$.

The interrelation between these parameters is illustrated in the nomogram for silicon detectors given in Fig. 11.10. Also shown are scales corresponding to the ranges of various charged particles to allow selection of conditions required to produce a depletion depth that exceeds the range.

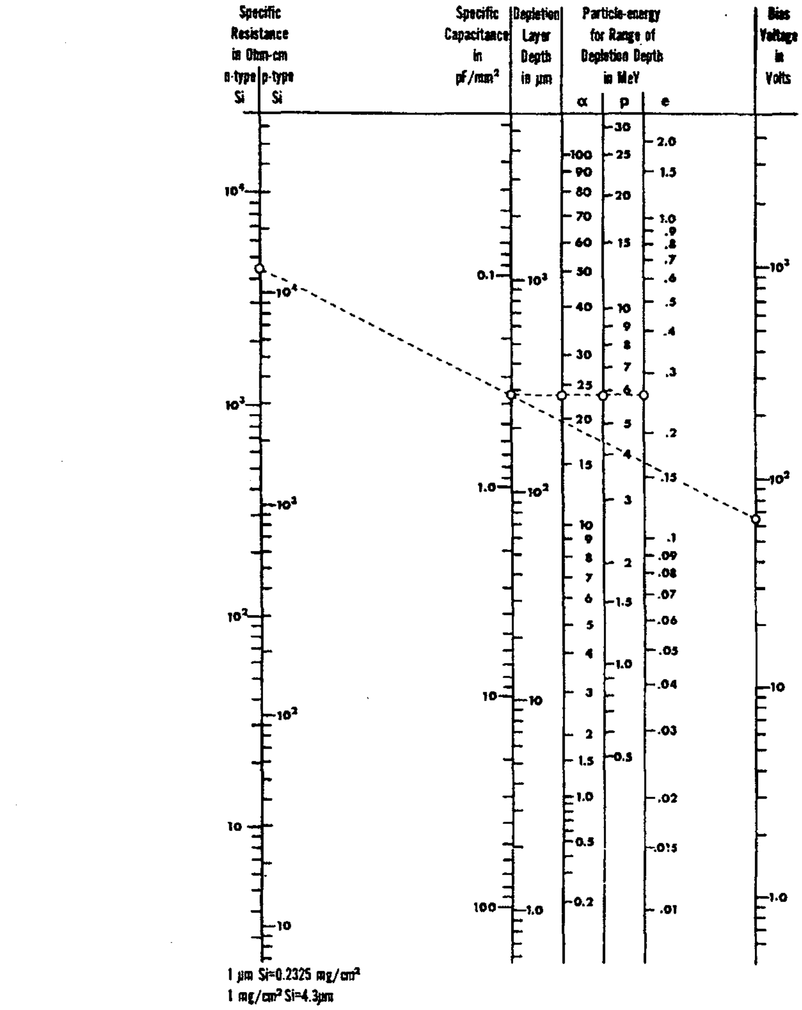

Figure 11.10 Nomogram illustrating interrelation between parameters for silicon junction detectors. (Similar to nomogram originally published by Blankenship.[26])

The maximum operating voltage for any diode detector must be kept below the breakdown voltage to avoid a catastrophic deterioration of detector properties. Commercially manufactured detectors are supplied with a maximum voltage rating that should always be strictly observed. Additional protection can be provided by monitoring the leakage current during application of the voltage (see the discussion later in this chapter).

To summarize, the reverse biased *p-n* junction makes an attractive radiation detector because charge carriers created within the depletion region can be quickly and efficiently collected. The width of the depletion region represents the active volume of the detector and is changed in partially depleted detectors by varying the reverse bias. The variable active volume of semiconductor junctions is unique among radiation detectors and sometimes is used to good advantage. The capacitance of a partially depleted detector also varies with applied voltage, and stable operation therefore requires the use of charge sensitive preamplifiers (see Chapter 17).

IV. SEMICONDUCTOR DETECTOR CONFIGURATIONS

A. Diffused Junction Detectors

One common fabrication method for semiconductor diode detectors starts with a homogeneous crystal of *p*-type material. One surface is treated by exposing it to a vapor of *n*-type impurity (typically phosphorus), which then converts a region of the crystal near the surface from *p*-type to *n*-type material. A junction is therefore formed some distance from the surface at the point at which the *n*- and *p*-type impurities reverse their relative concentration. Typical depths of the diffused *n*-type layer range from 0.1 to 2.0 μm. Because the *n*-type surface layer is heavily doped compared with the *p*-type original crystal, the depletion region extends primarily into the *p* side of the junction. Therefore, much of the surface layer remains outside the depletion region and represents a *dead layer* or window through which the incident radiation must pass before reaching the depletion region. In charged particle spectroscopy, this dead layer can be a real disadvantage because a portion of the particle energy will be lost before the active region of the detector is reached. Methods for experimentally determining its thickness are given later in this chapter.

To avoid the disadvantages of the dead layer, diffused junction detectors have been replaced in many applications by other configurations described in the following sections. Diffused junction detectors are still commercially manufactured, however, and offer some advantage over surface barrier detectors. They are somewhat more rugged and less prone to the problems that can arise due to the accumulation of oil or other foreign matter on the surface of the detector.

B. Surface Barrier Detectors

The role of the *p*-type material in forming the junction can be assumed by a high density of electron traps formed at the surface of an *n*-type crystal. The resulting depletion region behaves in much the same way as discussed earlier for a diffused junction detector. Formation of the surface states is carried out using recipes that have evolved somewhat empirically. One such set of typical procedures is described in Ref. 27. The usual treatment is etching of the surface, followed by evaporation of a thin gold layer for electrical contact. Best results are obtained if the evaporation is carried out under conditions that promote slight oxidation of the surface; the resulting oxide layer between the gold and silicon apparently plays an important role in the resulting properties of the surface barrier. Surface barriers can also be produced by starting with a *p*-type crystal and evaporating aluminum to form an equivalent *n*-type contact. The very thin dead layers that characterize surface barrier detectors are further discussed later in this chapter.

One potential disadvantage of surface barriers is their sensitivity to light. The thin entrance windows are optically transparent, and photons striking the detector surface can reach the active volume. The energy of visible light photons of 2–4 eV is greater than the bandgap energy of most semiconductors, and electron–hole pairs can therefore be produced by photon interactions. A very high noise level is produced by normal room lighting, but the vacuum enclosure required for most charged particle applications usually reduces light-induced noise to insignificant levels. The thin entrance window also makes the detector sensitive to damage from exposure to vapors, and the front surface must never be directly handled.

A cross-sectional diagram of a typical mounting arrangement for a surface barrier detector is shown in Fig. 11.11*a*. The outer housing and front surface are normally grounded, and an electrical lead from the back surface of the semiconductor wafer attaches to the center electrode of the coaxial connector at the rear. Because normal surface barriers are usually created on *n*-type crystals, a positive polarity voltage is required to reverse bias the junction.

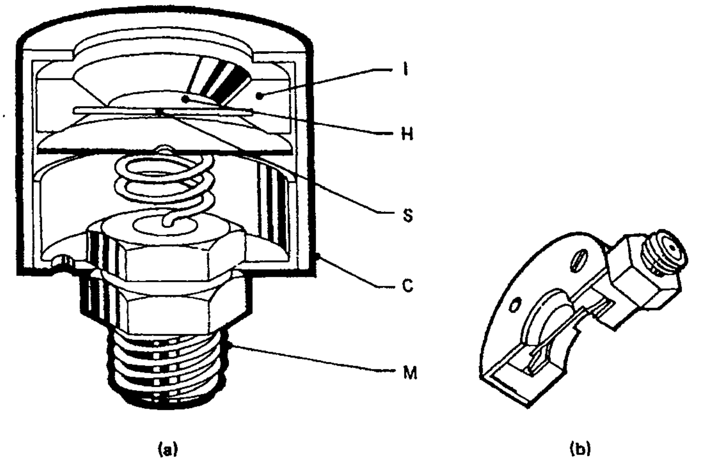

Figure 11.11 Construction and mounting of silicon junction detectors shown in cross-sectional view. (*a*) Surface barrier mount with coaxial connector (M) at rear. The silicon wafer (S) is mounted in a ceramic ring (I) with electrical contact made between either side of the junction and opposite metalized surfaces of the ring. The front surface is connected to the outer case (C) and grounded, whereas the back surface is connected to the center conductor of the coaxial connector. (*b*) Cutaway view of a transmission mount, in which both surfaces of the silicon wafer are accessible. The coaxial connector is placed at the edge of the ceramic ring. (Courtesy of EG & G ORTEC, Oak Ridge, TN.)

C. Ion Implanted Layers

An alternative method of introducing doping impurities at the surface of the semiconductor is to expose that surface to a beam of ions produced by an accelerator. This method is known as *ion implantation* and can be used to form n^+ or p^+ layers by accelerating, for example, either phosphorus or boron ions, respectively. At a fixed accelerator voltage (typically about 10 kV) monoenergetic ions are produced that have a well-defined range in the semiconductor material. By changing the energy of the incident ions, the concentration profile of the added impurity can be closely controlled. Following exposure to the ion beam, an annealing step is normally carried out to reduce the effects of radiation damage caused by the incident ions. One of the advantages of ion implantation is that the annealing temperature required (less than 500°C) is considerably lower than that needed for the thermal diffusion of dopants to form a diffused junction. The structure of the crystal is therefore less disturbed, and carrier lifetimes are not unnecessarily reduced. Compared with surface barriers, ion-implanted detectors tend to be more stable and less subject to ambient conditions. Also, they can be formed with entrance windows as thin as 34 nm silicon equivalent[28,29] and they are available commercially. A review of the use of ion implantation to form radiation detectors can be found in Ref. 30.

D. Fully Depleted Detectors

As shown by Eq. (11.18), the width of the depletion region associated with a *p-n* junction increases as the reverse bias voltage is increased. If the voltage can be increased far enough, the depletion region eventually extends across virtually the entire thickness of the silicon wafer, resulting in a fully depleted (or totally depleted) detector. Because of the several advantages this configuration presents over partially depleted detectors, the fully depleted configuration is the preferred type in most applications.

In the usual case, one side of the junction is made up of a heavily doped n^+ or p^+ layer or, alternatively, a surface barrier. The opposite side of the junction generally consists of high-purity semiconductor material that is only mildly n or p type. (Such material is often designated ν or π respectively.) The reason that high-purity material is important is reflected in Eq. (11.18). For a given applied voltage, the depletion depth is maximized by minimizing the concentration of doping impurities on the higher-purity side of the junction. Thick depletion regions can therefore only be obtained by starting from semiconductor material with the lowest possible impurity concentration. Also, with a large difference in the doping levels, the depletion layer essentially extends only into the high-purity side of the junction. The heavily doped layer can then be very thin, providing an *entrance window* for weakly penetrating radiations.

In Fig. 11.12, we assume that we have such a junction formed between a heavily doped p^+ surface layer and a high-purity n-type silicon wafer. As the reverse bias voltage applied to the detector is raised from zero, the depletion region extends further from the p^+ surface into the bulk of the wafer. For low values of the voltage, the wafer is only partially depleted and the electric field goes to zero at the far edge of the depletion region. Between this point and the back surface of the wafer, a region of undepleted silicon exists in which there is no electric field. This region then represents a very thick dead layer from which charge carriers are not collected. For all practical purposes, partially depleted detectors are therefore only sensitive to charged particles incident on the front surface.

If the applied voltage is increased further, the depletion region may be made to extend all the way to the back surface of the wafer. The voltage required to achieve this condition is sometimes called the *depletion voltage.* Its value is found by setting the depletion depth d in Eq. (11.18) equal to the wafer thickness T:

$$V_d = \frac{eNT^2}{2\epsilon}$$

When this stage is reached, a finite electric field exists all the way through the wafer, and the back dead layer thickness is reduced to that of the surface electrical contact that is employed. This condition is represented by the middle plot in Fig. 11.12. Once the wafer is

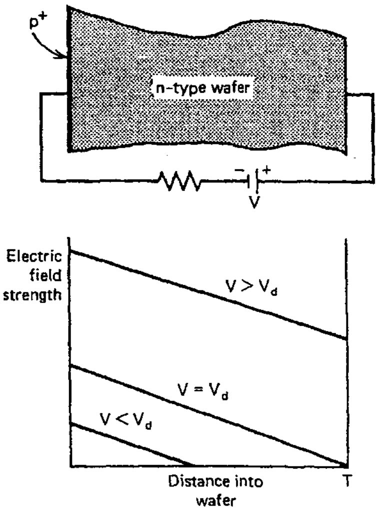

Figure 11.12 The electric field shape in a reverse bias semiconductor detector. Three plots are shown for bias voltages that are below, equal to, and above the depletion voltage V_d.

fully depleted, raising the applied voltage further simply results in a constant increase in the electric field everywhere in the wafer. At voltages much larger than the depletion voltage, the electric field profile therefore tends to become more nearly uniform across the entire wafer thickness. Under these conditions, the detector is sometimes said to be *overdepleted.* Because of the advantages of having a high electric field everywhere within the detector active volume, virtually all totally depleted detectors are operated at sufficient voltage to achieve this condition.

Figure 11.13 shows several configurations that are typical of fully depleted detectors, together with the corresponding electric field profile through the wafer. In order to deplete the wafer fully at as low a voltage as possible, one normally starts with material with the highest available purity, either n or p type. The junction is then formed by providing a heavily doped surface layer of the opposite type. This is often called the *rectifying contact.* Because of its high doping level, it also serves as an excellent blocking contact in which the minority carrier concentration is very low. In the nearly pure bulk of the wafer, however, the minority carriers are not highly suppressed and an additional blocking contact is normally provided at the opposite face of the wafer. If the high-purity silicon is mildly n type, then a thin n^+ layer is provided at this back surface. Since both materials are n type, no semiconductor junction exists at this surface. Instead, the n^+ layer provides the noninjecting conditions necessary to suppress leakage current due to minority carrier motion across the junction.

As shown on the right in Fig. 11.13, the roles of the n^+ and p^+ surface layers are reversed if one starts with high-purity material that is mildly p type. In both cases, the electric field is a maximum at the rectifying contact and decreases linearly to a minimum at the blocking contact. Shown in the center in Fig. 11.13 is the case in which intrinsic or perfectly compensated material is used for the wafer. In this case, the distinction between the two contacts disappears and the electric field is uniform throughout the entire wafer. The detector is fully depleted even for very low values of applied voltage. This *p-i-n* configuration is discussed in connection with lithium-drifted detectors in the next chapter.

Fully depleted silicon detectors are very useful as *transmission detectors* for incident particles that have sufficient energy to pass completely through the wafer. The pulse amplitude then indicates the energy lost by the incident radiation during its transit through the device. Totally depleted silicon detectors are commercially available in thicknesses from about 50 to 2000 μm. Transmission mounts of the type shown in Fig. 11.11*b* allow access to both surfaces of the wafer.

Several properties of totally depleted detectors are of primary importance. The dead layers must be as small as possible at both the front and rear surfaces of the detector if the

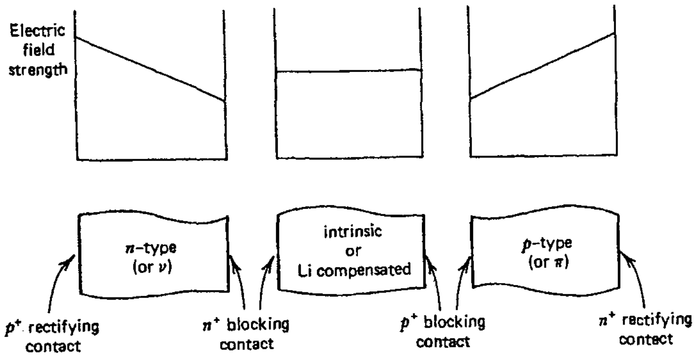

Figure 11.13 The electric field shapes for fully depleted planar semiconductor detectors of different configurations.

pulse is to indicate accurately the energy loss of the particle during its transit. An empirical test is often carried out to determine the minimum bias voltage at which these detectors are totally depleted. The pulse height from a monoenergetic source of charged particles is recorded for the particles incident on both the front and back face of the detector. When the detector is totally depleted, the pulse height should be approximately the same for either orientation. In interpreting such measurements, allowance must be made for the fact that the inherent window thicknesses of the front and back contacts of these detectors are often not the same.

In partially depleted detectors, the thickness uniformity of the crystal from which the detector is fabricated is not critical because the active volume of the detector is determined by the limited depletion depth. In fully depleted detectors, however, the wafer thickness must be kept quite uniform to avoid energy loss variations across the surface of the detector. Consequently, considerable effort is taken to provide uniform crystal wafers when totally depleted configurations are produced.

Fully depleted detectors have other advantages over partially depleted configurations in which there is an undepleted back dead layer. The finite electrical resistance of this dead layer is a source of Johnson noise that can contribute to the degradation of energy resolution. It is eliminated in a fully depleted detector by extending the depletion region all the way to the back contact. Timing properties also tend to be superior in fully depleted configurations. In a partially depleted detector, the electric field drops to zero at the edge of the depletion region. Charge carrier velocities therefore become very low in these low-field regions, slowing the rise of the signal pulse. In a totally depleted detector, the electric field can be maintained at a high value everywhere within the detector volume. Finally, some added stability results from the fact that the active volume and capacitance of a fully depleted detector are no longer functions of the applied voltage as they are in a partially depleted configuration.

The thickness of wafer that can be fully depleted using voltages short of catastrophic breakdown depends on the purity of the semiconductor. In this respect, there is a significant difference between silicon and germanium. Using ultrapure germanium described in the following chapter, a depletion thickness of several centimeters can be achieved. The impurity levels in currently available silicon are somewhat higher, and depletion thicknesses are generally limited to no more than several millimeters. Greater thicknesses in silicon are currently possible only through the use of material compensated by the lithium-drifting process described in Chapter 13.

E. Passivated Planar Detectors

The newest method of fabricating silicon junction detectors combines the techniques of ion implantation and photolithography to produce detectors with very low leakage currents and excellent operational characteristics.[31-33] Methods that were first developed in the semiconductor industry to produce integrated circuits have now been adapted successfully[34,35] to the fabrication of detectors. The techniques described below lend themselves to the batch production of multiple detectors simultaneously starting with a large-area silicon wafer, thus providing potential cost savings. These techniques can also accommodate the type of complex electrode geometry required, for example, in the silicon microstrip detectors described in Chapter 13.

The planar fabrication process generally begins with high-purity silicon that is mildly *n* type due to residual donor impurities. The steps in the fabrication process are shown in Fig. 11.14. After the wafer has been polished and cleaned, the surface is "passified" through the creation of an oxide layer at elevated temperature. Next, the techniques of photolithography are used to remove selectively areas of the oxide where the entrance windows of the finished detectors are to be located. The junction is then formed by converting a very

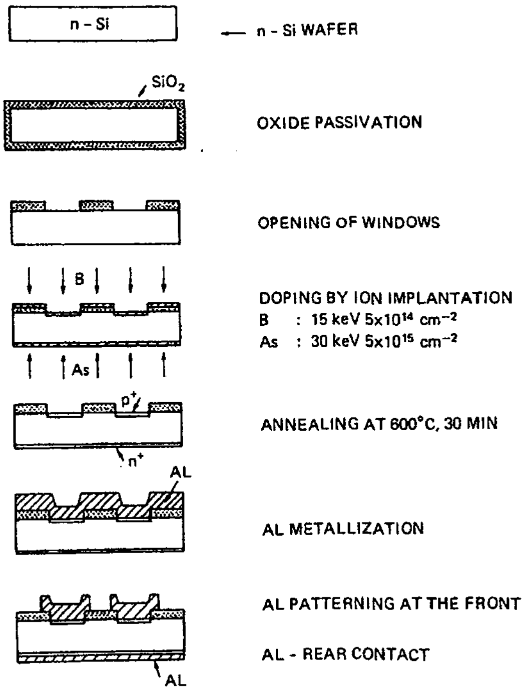

Figure 11.14 Steps in the fabrication of passivated planar silicon diode detectors. (From Kemmer.[34])

thin layer of silicon within the windows into *p*-type material through the implanting of acceptor ions (boron) using an accelerator. To serve as a blocking electrical contact, the rear surface of the wafer is converted into n^+ material through implantation of donor (As) ions. The radiation damage in the implanted layers is next removed through annealing at elevated temperature. Finally, aluminum is evaporated and patterned by photolithography to provide thin ohmic electrical contacts at the front and rear surfaces. The individual detectors are then separated and encapsulated.

One advantage of this planar fabrication process is that the junction edges are defined by the ion implantation pattern and can be kept within the bulk of the wafer. The oxide-passivated surface keeps leakage currents much lower than in surface barrier detectors, where the junction edge extends all the way to the edge of the wafer. Much of the leakage current in these designs then occurs where these edges are encapsulated in epoxy or similar material. Formation of the p^+ layer through ion implantation also provides planar detectors with a very thin and uniform entrance window or dead layer, an important consideration in preserving good energy resolution for the detector. The aluminized front surface is more rugged and less subject to damage compared with the gold front surface used in surface barrier fabrication.

V. OPERATIONAL CHARACTERISTICS

A. Leakage Current

When voltage is applied to a junction detector in the normal fashion, that is, to reverse bias the junction, a small current of the order of a fraction of a microampere is normally observed. The origins of this *leakage current* are related both to the bulk volume and surface of the detector. Bulk leakage currents arising internally within the volume of the detector can be caused by either of two mechanisms.

The direction of the electric field across the depletion region is such that any majority carriers that diffuse from the normal p and n regions of the detector to the edges of the depletion region will be repelled away from the junction. However, the minority carriers in either case are attracted and will therefore be conducted across the junction. Because the minority carriers are generated continuously on both sides of the junction and are free to diffuse, a steady-state current will result that will be roughly proportional to the area of the junction. In most cases, the minority carrier current is small and is seldom an important leakage source.

A second source of bulk leakage is the thermal generation of electron–hole pairs within the depletion region. This rate will obviously increase with the volume of the depletion region and can be reduced only by cooling the material. Silicon detectors of usual dimensions have a sufficiently low thermally generated current to allow their use at room temperature, but germanium detectors, because of the lower gap energy, must always be operated at reduced temperatures.

Surface leakage effects take place at the edges of the junction where relatively large voltage gradients must be supported over small distances. The amount of surface leakage can vary greatly, depending on such factors as the type of detector encapsulation used, humidity, and any contamination of the detector surface by fingerprints, vacuum pump oil, or other condensable vapors. Guard rings analogous to those described in Chapter 5 are sometimes incorporated into the design of semiconductor diode detectors[36,37] to reduce the surface leakage, but in commercial detectors the normal approach is to rely on clean encapsulation techniques to keep the surface leakage within tolerable levels. The introduction of the planar fabrication process has allowed the production of detectors in which the junction edges are buried within the silicon wafer. As a result, leakage current is reduced to a small fraction of that typically observed in either diffused junction or surface barrier devices.

In addition to the effects on energy resolution discussed in the following section, the leakage current has another practical influence on detector operation. The bias voltage to the detector is always supplied through a large-value series resistor (R_L in Fig. 17.5) for signal isolation purposes. Therefore, the true bias voltage applied to the junction is reduced from that of the voltage source by the product of the leakage current and the series resistance. If the leakage current is large enough, the drop across the resistor can appreciably diminish the actual voltage applied to the detector, and the supply voltage must then be raised to compensate for this loss. It is therefore a fairly common practice to monitor the leakage current with an ammeter in series with the voltage supply.

Monitoring the leakage current can also detect the onset of abnormal detector behavior. During steady operation, the leakage should normally maintain a steady value, and any abrupt change or increase in the leakage current can indicate a change in detector performance, which may degrade the energy resolution. Also, it is useful to monitor the leakage current as the bias voltage is first applied to the detector. Normally, the leakage current will increase as the bias voltage is raised. However, any sudden increases can signal the approach of the breakdown of the diode, and the voltage should therefore be reduced to a lower value. Finally, the long-term behavior of the leakage current is often a useful monitor on the degree of radiation damage suffered by a given detector when used under conditions in which such damage is significant.

B. Detector Noise and Energy Resolution

Sources of electronic noise in spectroscopic measurements fall into two main categories: *series noise* and *parallel noise*. A discussion of the distinctions between these categories and their variations with operating parameters such as the choice of electronic shaping time is postponed until Chapter 17. For the type of silicon diode detectors used for charged particle measurements, three main contributors to the electronic noise are most significant:

1. Fluctuations in the bulk generated leakage current, a component of parallel noise.
2. Fluctuations in the surface leakage current, another component of parallel noise.
3. Noise associated with series resistance or poor electrical contacts to the detector, a contributor to series noise.

The relative importance of these sources will depend on the magnitude of the leakage currents for the specific detector, the capacitance of the detector, and whether the diode is partially or fully depleted. The overall peak broadening due to electronic noise is often measured experimentally by injecting the output of a stable pulse generator into the preamplifier input while the detector remains connected. If the pulse generator has negligible spread in the amplitude of its output pulses, then the width of the corresponding "pulser peak" in the recorded spectrum is a direct measure of the electronic noise contribution.

This noise width combines in quadrature with other sources of peak broadening, such as the contributions of charge carrier statistics and fluctuations in particle energy loss in dead layers to determine the peak widths actually observed. Examples of the energy resolution attainable with semiconductor diode detectors are given in the section on alpha particle spectroscopy later in this chapter.

If trapping effects become significant in the detector, it is usually evidenced by the appearance of low-energy tails on the peaks observed from monoenergetic sources of radiation. These tails correspond to pulses in which less than the total amount of charge generated by the radiation has been collected. Because the amount of trapping varies according to the distance traveled by the carriers before reaching the collection electrodes, the amount of energy loss is variable and the full-energy peaks are spread only to the low-energy side.

C. Changes with Detector Bias Voltage

When the bias voltage and electric field are low, the pulse height from radiations that are fully stopped within the depletion layer continues to rise with applied voltage. This variation is caused by the incomplete collection of charge carriers because of trapping or recombination along the track of the incident particle. The fraction that escape collection will decrease as the electric field is increased. Similar losses to recombination are observed in a gas-filled ion chamber at low values of the electric field. Once the electric field is sufficiently high, charge collection becomes complete and the pulse height no longer changes with further increases in the detector bias voltage. This region of operation is called the *saturation region* and corresponds to the region of ion saturation in a gas-filled ion chamber.

If radiations of a single energy and type are involved, it is sometimes possible to operate the detector at a bias voltage that is short of true saturation without significant deterioration in the energy resolution, because the fraction of charge lost for each event is likely to be nearly constant. When measuring radiations of diverse energy and specific ionization, however, it is quite important to ensure that the detector is operating in the region of true saturation to avoid significant deterioration in the energy resolution. To reach the saturation region, somewhat higher electric fields are generally required as the detector undergoes radiation damage.[38]

If the electric field is made sufficiently high, multiplication effects can be induced in a semiconductor detector that are analogous to gas multiplication in proportional counters or Geiger–Mueller tubes. The multiplication arises when electrons liberated in the initial radiation interaction gain sufficient energy from the field to create further electron–hole pairs as they drift toward the collecting electrodes. These multiplication effects are discussed in some detail in Ref. 39 and are the basis of operation for silicon avalanche detectors described in Chapter 13.

D. Pulse Rise Time

Semiconductor diode detectors are generally among the fastest of all commonly used radiation detectors. A general review of theoretical and experimental work on their timing properties is given in Ref. 40. Under normal conditions, the observed pulse rise time is of the order of 10 ns or less. The detector contribution to this rise time is composed of the *charge transit time* and the *plasma time*.

The charge transit time corresponds to the migration of the electrons and holes formed by the incident radiation across the region of high electric field in the depletion region. The rise time of the output pulse is therefore limited by the time required for complete migration of these charges from their point of formation to the opposite extremes of the depletion region. These times are minimized in detectors with high electric fields and small depletion widths. In totally depleted detectors, the depletion width is fixed by the physical thickness of the silicon wafer, and therefore the transit time is decreased as the bias voltage is increased. In partially depleted detectors, however, the depletion width increases with increasing bias [see Eq. (11.18)], and therefore the effect of a larger bias voltage is to increase both the electric field and the distance over which charges must be collected. Furthermore, because the electric field is not uniform, the drift velocity of electrons and holes will vary as they move across the depletion region. The dependence of the charge transit time on bias voltage in these detectors is therefore somewhat more complicated, but it can be shown to be independent of the voltage if certain simplifying assumptions are made.[41] A derivation is given in Chapter 12 (see p. 421) of the time profile of the signal pulse attributable to charge migration in solid-state detectors in which the electric field is uniform.

For the case of a particle range that is much less than the width of the depletion region, all the charge carriers are created near one boundary. The collection time of one type of carrier corresponds to its migration across the entire depletion region and is therefore much longer than that for the other carrier. For a surface barrier on an *n*-type crystal, it is thus the electron collection time that dominates the time response for weakly penetrating particles.

A second component called the *plasma time* is observed when heavy charged particles, such as alpha particles or fission fragments, comprise the incident radiation. For these radiations, the density of electron–hole pairs along the track of the particle is sufficiently high to form a plasma-like cloud of charge that shields the interior from the influence of the electric field. Only those charge carriers at the outer edge of the cloud are subject to the influence of the field, and they begin to migrate immediately. The outer regions are gradually eroded away until the charges at the interior are finally subject to the applied field and also begin to drift. The plasma time is roughly defined as the time required for the charge cloud to disperse to the point where normal charge collection proceeds.

A number of theoretical models have been developed to describe the plasma erosion process;[42–47] it is predicted[42] that the plasma time should vary inversely with the electric field strength at the position of the track and increase as the cube root of the linear carrier density along the track. The effects of the plasma formation are observed to be a fixed delay of several nanoseconds between the time of track formation and the onset of the rise of the output pulse together with a slowing of the rise time of the output pulse. Measurements of the delay time with silicon surface barrier detectors,[48–53] give typical values of 1–3 ns for alpha particles, and 2–5 ns for heavy ions and fission fragments.

The actual rise time observed from a detector–preamplifier combination may also be influenced by the preamplifier properties. The time constant of the equivalent input circuit must be short if the rise time is to be held to that determined by the detector charge collection and plasma time properties only. One contributor to the input time constant is the series resistance of the undepleted region in partially depleted detectors. Therefore, fully depleted detectors in which the series resistance is largely eliminated are often favored in fast-timing situations.

E. Entrance Window or Dead Layer

When heavy charged particles or other weakly penetrating radiations are involved, the energy loss that may take place before the particle reaches the active volume of the detector can be significant. Because the thickness of the dead layer includes not only the metallic electrode but also an indeterminate thickness of silicon immediately beneath the electrode in which charge collection is inefficient, the dead layer can be a function of the applied voltage. Its effective thickness must often be measured directly by the user if accurate compensation is to be made.

The simplest and most frequently used technique is to vary the angle of incidence of a monoenergetic charged particle radiation. When the angle of incidence is zero (i.e., perpendicular to the detector surface), the energy loss in the dead layer is given by

$$\Delta E_0 = \frac{dE_0}{dx} t \tag{11.22}$$

where t is the thickness of the dead layer. The energy loss for an angle of incidence of θ is given by

$$\Delta E(\theta) = \frac{\Delta E_0}{\cos \theta} \tag{11.23}$$

Therefore, the difference between the measured pulse height for angles of incidence of zero and θ is given by

$$E' = (E_0 - \Delta E_0) - (E_0 - \Delta E(\theta))$$

$$E' = \Delta E_0 \left(\frac{1}{\cos \theta} - 1 \right) \tag{11.24}$$

If a series of measurements are made as the angle of incidence is varied, a plot of E' as a function of $(1/\cos \theta - 1)$ should be a straight line whose slope is equal to ΔE_0. Using tabular data for dE_0/dx for the incident radiation, we can calculate the dead layer thickness from Eq. (11.22).

One possible flaw in this method involves the assumption that the energy loss through the dead layer depends only on the total path length traversed and not on the relative orientation of the particle path with respect to the detector axis. There is some evidence that recombination should be more severe for particle paths parallel to the direction of the electric field in the detector compared with paths perpendicular to the field. This recombination would tend to cause a lower than expected response for paths near normal incidence and should be evidenced by a curvature in the plot described above.

The thinnest dead layers are produced in semiconductor detectors of the ion implanted or surface barrier types. Typical values of 100 nm of silicon equivalent correspond to an energy loss of 4 keV for 1 MeV protons, 14 keV for 5 MeV alpha particles, and several hundred keV for fission fragments. Because variations in this energy loss due to straggling or variable angle of incidence will potentially detract from energy resolution, thin dead layers are quite important in high-resolution charged particle spectroscopy. Using special techniques, dead layers of less than 30 nm have been successfully fabricated.[54]

F. Channeling

In crystalline materials, the rate of energy loss of a charged particle can depend on the orientation of its path with respect to the crystal axes.[55] Particles that travel parallel to crystal planes can, on the average, show a rate of energy loss that is lower than that for particles directed in some arbitrary direction. Therefore, these "channeled" particles can penetrate